

# AIAA FLIGHT SIMULATION TECHNOLOGIES CONFERENCE

A Collection of Technical Papers  
Niagara Falls, New York  
June 13-15, 1983



For permission to copy or republish,  
contact the American Institute of Aeronautics and Astronautics  
1633 Broadway, New York, NY 10019





**A COLLECTION  
OF  
TECHNICAL PAPERS**

**AIAA FLIGHT SIMULATION TECHNOLOGIES CONFERENCE**

June 13-15, 1983/Niagara Falls, New York

**Conference Committee**

*General Chairman*

PHILIP REYNOLDS  
Arvin/Calspan Corp.

*Technical Program Chairmen*

ANTHONY M. COOK  
NASA Ames Research Center

*Administrative Chairman*

CHARLES REID  
Arvin/Calspan Corp.

DOMINIC GIBINO  
ASD/YWE

# TABLE OF CONTENTS

AIAA NO.		PAGE NO.
83-1075	Simulator Fidelity and Flight Test Data: Improving the Flight Performance of the B-52H WST Production Unit Flight Station Simulator - D.A. SCAFETTA	1
1076	Indoctrination of Navy Test Pilots to Vectored Thrust Flight in the X-22A In-Flight Simulator - J.L. BEILMAN	14
1078	In-Flight Simulation at the U.S. Air Force and Naval Test Pilot Schools - L. KNOTTS and M. PARRAG	23
1079	Advanced Display Techniques for Training the Multi-Member Tactical Air Crew - G. ALBERS	32
1081	A Visual Cueing Model for Terrain-Following Applications - G.L. ZACHARIAS, A.K. CAGLAYAN and J.B. SINACORI	35
1084	An Investigation of Motion Base Cueing and G-Seat Cueing on Pilot Performance in a Simulator - B.T. McKISSICK, B.R. ASHWORTH and R.V. PARRISH	44
1086	Sinusoidal Integration for Simulation of Second-Order Systems - D.R. ROLSTON	52
1087	Spectral Decontamination of a Real-Time Helicopter Simulation - R.E. McFARLAND	64
1088	Analysis of a Real-Time Application - R. SHASTRI	71
1089	Benchmarks for a Computer System for NASA'S Shuttle Procedures Simulator - A.R. HAJARE	75
1090	Error Sources in Hybrid Computer Based Flight Simulation - R.A. WEEKS	84
1091	Use of Flight Test Results to Improve the Flying Qualities Simulation of the B-52H Weapon System Trainer - J. WEISS	92
1092	Simulator Performance Definition by Cue Synchronization Analysis - S.K. BUTRIMAS and G.B. BROWDER	114
1097	Real Time Simulation of Mission Environments for Avionics Systems Integration - R.A. WEEKS	123
1098	The Man-Vehicle Systems Research Facility: A New NASA Aeronautical R&D Facility - D.C. NAGEL and R.J. SHINER	130
1099	Data Base Considerations for a Tactical Environment Simulation - C.G. HORATTAS and R.P. ADKINS	140
1100	Application of Experimentally Derived Pilot Perceptual Angular Response Transfer Functions - R.J. CROSBIE	146
1101	Design of a Real-Time CGSI System - D.M. BALDWIN, B.F. GOLDIEZ and C.P. GRAF	154
LATE PAPERS		
1080	Compensation for Time Delay in Flight Simulator Visual-Display Systems D.F. CRANE	163



SIMULATOR FIDELITY AND FLIGHT TEST DATA:  
IMPROVING THE FLIGHT PERFORMANCE OF THE B-52H WST  
PRODUCTION UNIT FLIGHT STATION SIMULATOR

by

Dennis A. Scafetta

The Singer Company, Link Flight Simulation Division

Binghamton, New York

#### ABSTRACT

A systematic method of analysis for comparing aircraft simulator flight performance against actual aircraft flight test data is presented as a means of improving the fidelity of the B-52H WST Production Unit Flight Station Simulator. Verification of simulated aircraft performance as designed to reflect an airframe manufacturer's data package is established against flight test data as contained in the aircraft's Category II flight test report and flight performance manual. Discussions are included on the design approaches used for the mathematical modeling of the engine and aerodynamic simulation models as an introduction to the data analysis method. First, a detailed analysis of all available engine and aircraft flight test data is made. Second, simulated engine performance is verified. Third, simulated aircraft performance for the "clean" aircraft configuration is verified. Finally, simulated aircraft performance for the "dirty" aircraft configuration is verified by analyzing each aircraft drag component separately. Based on the analysis, several engine and aerodynamic simulation model changes were made to the original design. As a result, the flight performance of the B-52H WST Production Unit Flight Station Simulator matches aircraft flight test data.

#### INTRODUCTION

A detailed comparison of simulated aircraft performance versus actual aircraft flight test data was conducted on the B-52H Weapon System Trainer Production Unit (WST PU) Flight Station Simulator as installed at Castle Air Force Base, California. The purpose of the analysis was to verify that the simulated aircraft performance designed to satisfy an airframe manufacturer's data package matched corresponding aircraft flight test data. The analysis was conducted using the logical progression of tasks outlined in Figure 1. First, a review was made of all available sources of flight test data on engine and aircraft performance. Second, a comparison was made of simulated

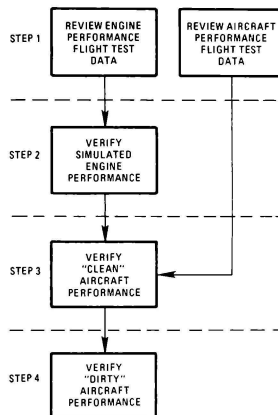


Figure 1 FLIGHT TEST DATA ANALYSIS METHOD

engine performance against available engine flight test data. Third, for the "clean" aircraft configuration, a comparison was made of simulated aircraft performance against similar flight test data. Finally, for the "dirty" aircraft configuration, comparisons were made of simulated aircraft performance against corresponding flight test data for various aircraft configurations. Where discrepancies between simulated performance and flight test data existed, an analysis was undertaken to provide design changes to the original model in order to obtain flight test results on the simulator.



Data for the analysis was obtained in two different ways. The first, and most obvious, was the collection of data directly from the simulator. The amount of data obtained by this method was limited by the time allotted on the simulator for the analysis, by the large amounts of engine and aircraft performance data to be collected, and finally by the unavailability of the simulator while it was being prepared for installation. The second method involved extensive use of the Software Development Facility (SDF) developed at Singer-Link. The SDF computer system allows the engineer to implement, debug, and test software designs in an off-line mode using the same real-time iteration rates and module sequencing used in the simulator load. Software testing begins with the input/output testing of individual modules, progresses to the grouping of modules into a system test, and culminates in the integration testing of two or more systems. This type of systems integration test (i.e., the combining of the engine and aerodynamic simulation models) was used in generating the multitude of flight test data points needed for the analysis. The importance of the SDF system and its relation to the typical engine and aerodynamic simulation development process from data analysis through customer acceptance is shown in Figure 2. The use of the SDF in this manner assures that the simulator software will be ready for the hardware/software integration phase of simulator testing, minimizes the amount of debug necessary during real-time testing, and provides a means of continued simulator testing, analysis, and support once the simulator is delivered.

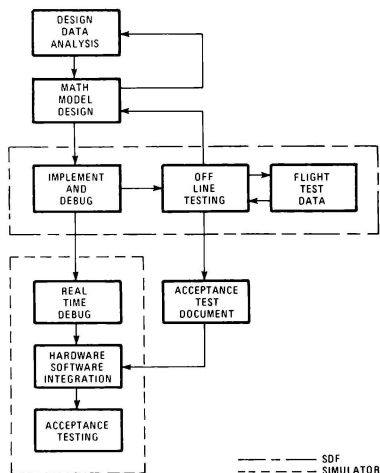


Figure 2 TYPICAL ENGINE/AERODYNAMIC SIMULATION DEVELOPMENT PROCESS

Reference 1 investigates the application and restrictions of using aircraft stability and control flight test data for improving the overall flight handling qualities of the B-52G WST Pilot Production Unit (PPU) simulator. Also contained is an overview of the B-52G aircraft and an excellent description of the B-52G WST PPU simulator complex. The major difference between the B-52G and B-52H aircraft (and, therefore, between the B-52G PPU and B-52H PU Flight Station Simulators) is the powerplant installation change between the two aircraft models. The G model aircraft is powered by the Pratt and Whitney Aircraft (PWA) J57-P-43B turbojet engine equipped with water injection thrust augmentation capability, while the H model aircraft is powered by the PWA TF33-P-3 turbofan engine and has no thrust augmentation capability. This engine change accounts for all performance differences between the two aircraft as well as for longitudinal stability and control differences; lateral-directional characteristics between the two aircraft models remain unchanged. The B-52G PPU/B-52H PU areas of commonality also include the flight control systems, ground reaction characteristics, and the air refueling flying quality characteristics behind the KC-135A tanker aircraft. The B-52H PU unique areas of change center upon the engines and the aircraft performance, stability, and control characteristics with respect to lift and drag forces and pitching moment, the thrust moments in the yaw axis, and the aircraft weight and balance characteristics.

#### ENGINE SIMULATION

As previously noted, the B-52H aircraft is powered by the PWA TF33-P-3 turbofan engine. Engine speed scheduling and power output are controlled by the Hamilton Standard JFC25-14 Fuel Control Unit. In the actual aircraft the engine and the fuel control unit are two independent systems, with the throttle providing the linking interface between them. The fuel control unit schedules the requested power output in response to the pilot's throttle input. The engine responds to the demanded power output scheduled by the fuel control unit. The fuel control unit does this while automatically ensuring (by monitoring various engine parameters) that safe engine operating limits are not exceeded and that engine accelerations and decelerations are surge-free. The simulation approach to the engine and fuel control models treats their operation in the same manner.

The basic computational flow for the simulated engine is shown in Figure 3. It should be noted that this diagram is valid only for steady-state operation at idle and above and excludes engine dynamics, malfunctions, and system bleed load effects. The mathematical model of the fuel control unit simulates its main control functions, which are scheduling engine rotor speed via the speed governor cam schedule and maintaining safe engine operating limits by monitoring burner pressure and fuel flow. For normal operation a throttle movement computes a power lever angle. This, along with ambient pressure and the control's operating limits (burner pressure, maximum and minimum fuel flows, and acceleration and deceleration fuel flows), then determines scheduled rotor speed. Scheduled speed is then compared to actual rotor speed and a rate of

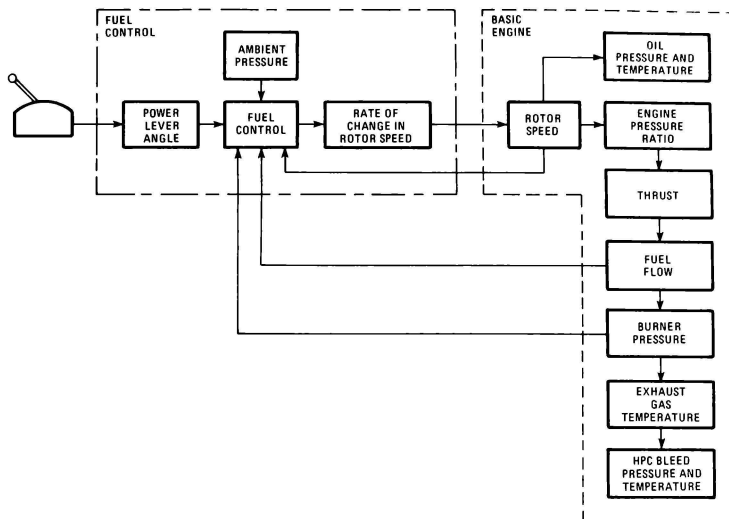


Figure 3 SIMULATED ENGINE COMPUTATIONAL FLOW

change in rotor speed is calculated and then integrated to compute engine rotor speed. Rotor speed is the main input to the basic engine model and is used to derive all the required gas generator performance parameters by relating the parameters to a common base -- engine pressure ratio.

Steady-state engine equations are developed through the use of the parametrized engine data contained in Reference 2, as a function of engine pressure ratio (as well as Mach number, altitude, surge bleed operation, and system bleed loads). Gas generator performance parameters are corrected by the total free stream pressure/temperature ratios to provide engine performance over the entire engine operating regime. Engine pressure ratio, rotor speed, fuel flow, exhaust gas temperature, oil pressure and temperature, high pressure compressor bleed air pressure and temperature, and thrust are simulated to produce the required outputs for interfacing with cockpit instruments and warning lights as well as the necessary aircraft systems. Engine dynamic performance is simulated to provide correct engine transient responses as contained in Reference 2 throughout the entire engine operating envelope. Modeled are pneumatic and cartridge ground starts, engine accelerations and decelerations, ground shutdowns, and in-flight starts and shutdowns. All performance parameters are modeled to reflect system bleed loads, surge bleed valve operation, and simulated malfunctions.

Each related engine system is modeled using actual aircraft wiring diagrams and system operation is simulated to reflect actual aircraft responses.

Figure 4 shows the scheme for integration of the various engine systems (ignition, starter, pneumatic, surge bleed, anti-ice, oil and fire detection), the associated aircraft systems interfaces (fuel and electrical), the applicable flight system interfaces (atmosphere and aerodynamic forces), the simulator training systems interfaces (malfunctions) and the various engine cockpit controls (instruments, switches and warning lights).

The mathematical models developed accurately describe the engine's gas generator performance parameters, realistically duplicate operation and control of the engine from the cockpit, and accurately describe operating characteristics of all the related engine systems. The simulation model was designed to be completely flexible and fully capable of simulating the installed configuration of the engine, its cockpit controls and indicators, and the interfaces required by the related engine systems. The equations used to describe the basic engine performance and the related engine systems characteristics were modeled to simulate engine operation over the entire aircraft flight and engine operating envelopes. A more detailed description of the engine simulation model can be found in Reference 8.

#### AERODYNAMIC SIMULATION

The simplified flow diagram describing the total flight simulation system for the B-52H Flight Simulator is shown in Figure 5. The mathematical model describing this system involves, first, the determination of the forces and moments which act

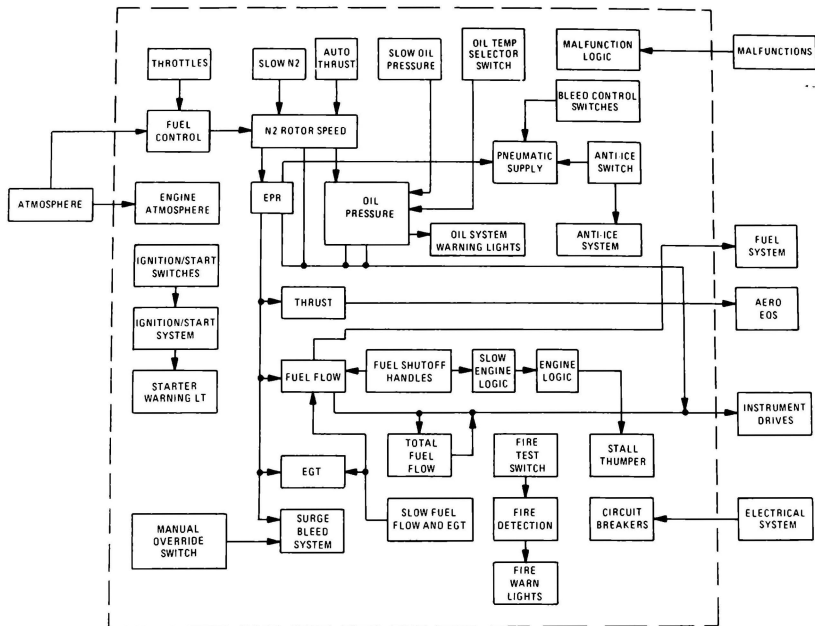


Figure 4 ENGINE AND ENGINE SYSTEMS SIMULATION INTERFACE

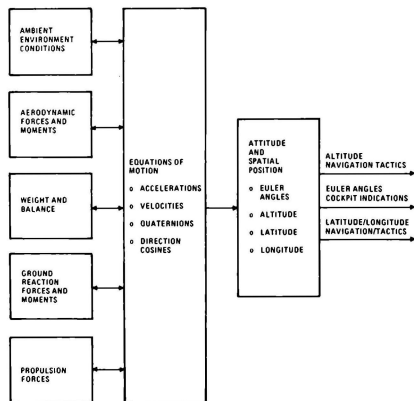


Figure 5 SIMPLIFIED TOTAL FLIGHT SIMULATION SYSTEM FLOW DIAGRAM

upon the aircraft due to the engine and external environmental effects, second, the determination of the translational and rotational accelerations which result from these forces and moments, and, third, the determination of aircraft attitude and relative position from these accelerations. The models developed fully simulate the aircraft's total regime of flight and ground reactions while providing for the full six-degree-of-freedom motion of simulated flight.

The general scheme used in developing the flight simulation model was to first generate the performance for the "clean" aircraft configuration. Then incremental effects for flaps, landing gear, speed brakes, bomb bay doors, ground effects, weapons loadings, airframe icing, control surface deflections, and tanker flow field were added for obtaining the overall aircraft performance and handling qualities under all flight conditions. The continuous solution of the aircraft's ground reaction and flight equations ensures an all-attitude, full-environment simulation model.

As shown in Figure 6, the simulation of the ground and flight characteristics of the B-52H aircraft (ground handling, performance, and stability and control) and the fulfillment of WST

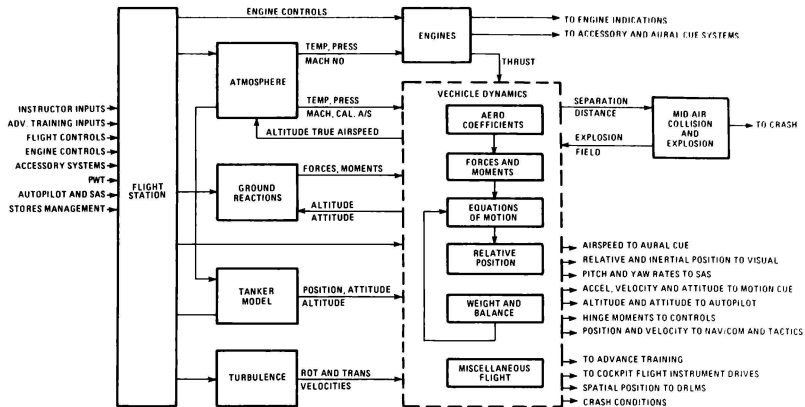


Figure 6 AERODYNAMIC SYSTEMS SIMULATION INTERFACE

PU simulator training requirements (air-refueling capabilities) is complex and involves several simulation models and many systems interfaces. The simulation of vehicle dynamics uses mathematical models for describing the aircraft's aerodynamic coefficients, forces and moments, equations of motion, ground reactions, and weight and balance, while simulating the air-refueling capability requires mathematical models for describing tanker aerodynamics, tanker-receiver relative position, and mid-air collision effects. System interfaces are required from engines, atmosphere, atmosphere turbulence, tanker position, and ground reactions, as well as interfaces from flight controls, flight instruments, weapons loading, flight accessory systems, and instructor inputs. Note that the additional requirements for the integrated mode of simulator operation with the Offensive Station are not shown.

The impact of the flight test data analysis on simulated aircraft performance falls primarily upon the model for the aerodynamic coefficients, in particular, the drag coefficient. The coefficient equations determine the flight performance and handling qualities of the simulator. The all-important "fidelity of simulation," which determines the acceptability of a simulator for training, is a direct function of the amount of detail provided in these equations. The aerodynamic coefficients and stability derivatives for the B-52H PU simulator were modeled using the coefficient data contained in Reference 3. The structure of the simulation model for the coefficients and the required interfaces is shown in Figure 7. The coefficients affected by the incorporation of the turbofan engines on the H model aircraft were the lift, drag, and pitching moment coefficients. All remaining aerodynamic coefficients were unchanged and represent original B-52G PPU design. A more detailed description of the coefficient simulation model can be found in Reference 9.

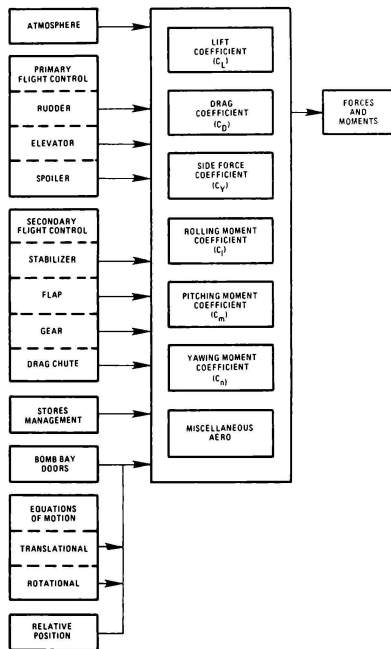


Figure 7 SIMULATED AERODYNAMIC COEFFICIENTS INTERFACE

	CATEGORY II FLIGHT TEST REPORT		SUBSTANTIATING (I) DOCUMENT		FLIGHT (I) MANUAL	
	STATIC	NON- STATIC	STATIC	NON- STATIC	STATIC	NON- STATIC
ROTOR SPEED	✓	✓				
THRUST	✓		✓	✓		
FUEL FLOW	✓	✓		✓		✓ (3)
EXHAUST GAS TEMPERATURE	✓	✓				
POWER SETTING CURVES		✓	✓	✓	✓	✓
THRUST AVAILABLE				✓		
IDLE THRUST			✓	✓		

NOTES: (1) DATA BASIS IS INSTALLED  
(2) DATA BASIS IS ESTIMATED EXCEPT  
WHERE NOTED  
(3) DATA BASIS IS FLIGHT TEST  
STATIC IS MACH = 0  
NON-STATIC IS MACH = 0

Figure 8 ENGINE PERFORMANCE FLIGHT TEST DATA SOURCES

#### FLIGHT TEST DATA

The sources of flight test data available for comparing against simulated engine and aircraft performance are shown in Figures 8 and 9. The major sources for the B-52H aircraft are the Category II Flight Test Report (Reference 4), the aircraft's Flight Performance Manual (Reference 5), and the Substantiating Document (Reference 6) which was used in generating the Flight Performance Manual. The Category II flight test report, although not applicable for comparing simulated aircraft stability and control performance with flight test data because of flight control system differences between the simulated aircraft and the flight test aircraft, does contain applicable engine and aircraft performance flight test data. It should be noted that the data is representative of an early B-52H aircraft and does not account for the additional drag due to the EVS and Phase VI ECM Pod installations found on the simulated aircraft. This is also true of all performance data contained in the Substantiating Document and some of the curves given in the Flight Performance Manual (identifiable from the date when the pod installations occurred). In using the aircraft performance manual where no flight test data was available, the data labeled as "estimated" was used for the data comparison. In using all of the data sources, the hierarchy established in Figure 10 was adhered to.

Available flight test data for comparing engine performance is shown in the data matrix given in Figure 8. Flight test data was available for verifying all the gas generator performance parameters and for verifying engine power setting, idle thrust, and thrust available. The Category II Flight Test Report became the basis for verifying gas generator performance, the Substantiating Document became the basis for verifying engine thrust, and the Flight Performance Manual became the basis for verifying cruise fuel flows.

Available flight test data for comparing aircraft performance for both the "clean" and "dirty" aircraft configurations is shown in the data matrix given in Figure 9. Adequate flight test data was available for verifying the "clean" configuration aircraft performance. The flight test data available for verifying "dirty" aircraft performance was not adequate, however. Enough data (either labeled as "flight test" or "estimated") is available to verify gear down only and flaps down only performance. The only data (all labeled as "estimated") available for verifying airbrake performance is for positions 4 and 6 only. Data for verifying intermediate airbrake positions and various combinations of gear, flaps, and airbrakes was not available. Performance for the intermediate airbrake positions was estimated by normalizing the data available for positions 4 and 6.

#### ENGINE PERFORMANCE

Since the thrust-drag relationship dictates most aircraft performance parameters, analysis of simulated engine performance against available flight test data is the first step in verifying overall simulated aircraft performance. Therefore, verification of the EPR-Thrust relationship over the aircraft's entire flight envelope is critical. Also to be verified are all the steady-state engine gas generator performance parameters. Engine transients were not taken into account because of the lack of flight test data and the insignificant impact of these engine characteristics on aircraft performance.

#### Thrust

The in-flight thrust available curves contained in Reference 6 were found to be significantly less than anticipated for normal and military thrust ratings in the sea level/Mach 0.7 and above region. Further analysis of the installed thrust curve (Reference 6) showed that the simulation model failed to meet the thrust levels defined by the pressure altitude limit lines. This was traced to the fact that the engine's thrust output was being curtailed by the fuel control's burner pressure limiter. The original simulation of the burner pressure limit was taken from a fuel control technical document and was simply stated as 205psia (Reference 7). To find a more accurate model of the limiter, the pressure altitude limit lines on the installed thrust curve were used to calculate the true action of the limiter. The analysis yielded a new model for burner pressure limit as a function of Mach number and altitude. This modification verified the entire thrust available curve and all but the static high-EPR part of the installed thrust curve.

Verification of static thrust was made using the static thrust calibration curves of Reference 4 and the static portion of the installed thrust curve of Reference 6. The sea-level static high-power thrust curve showed that the maximum thrust available was low. This was traced to the rotor speed (and therefore the EPR-Thrust) scheduled at the maximum PLA. The original design for scheduled rotor speed at maximum PLA was through the fuel control unit's speed governor schedule. To meet the maximum static thrust shown in the installed thrust curve, the following performance

	FLAPS UP								FLAPS DOWN							
	GEAR UP				GEAR DOWN				GEAR UP				GEAR DOWN			
	AIRBRAKE POSITION				AIRBRAKE POSITION				AIRBRAKE POSITION				AIRBRAKE POSITION			
	0	2	4	6	0	2	4	6	0	2	4	6	0	2	4	6
	(1) CATEGORY II FLIGHT TEST	SPEED/POWER														
(1) SUBSTANTIATING DOCUMENT	R/C															
(2) FLIGHT MANUAL	R/C				R/C	R/D	R/D	WF	R/C				R/C			WF
	WF	(3)														

NOTES: (1) DATA BASED ON AIRCRAFT BASIC DRAG POLAR WITHOUT EVS AND PHASE VI ECM PODS  
(2) DATA BASIS IS ESTIMATED EXCEPT WHERE NOTED  
(3) DATA BASIS IS FLIGHT TEST

Figure 9 AIRCRAFT PERFORMANCE FLIGHT TEST DATA SOURCES

DATA SOURCE	COMMENTS
CATEGORY II FLT TEST REPORT	CONTAINS ENGINE AND AIRCRAFT PERFORMANCE FLIGHT DATA, NOTING ANY DIFFERENCES BETWEEN FLIGHT TEST AND SIMULATED AIRCRAFT CONFIGURATIONS ARE ESSENTIAL.
SUBSTANTIATING DOCUMENT	CONTAINS MOSTLY "CLEAN" AIRCRAFT DRAG AND PERFORMANCE CHARACTERISTICS AS WELL AS INSTALLED ENGINE DATA.
AIRCRAFT FLIGHT MANUAL	OFTEN USES "ESTIMATED DATA" FOR AIRCRAFT PERFORMANCE CALCULATION, CONTAINS LITTLE ENGINE PERFORMANCE DATA.
MANUFACTURER'S DATA	SIMULATOR ORIGINALLY DESIGNED TO REFLECT THIS DOCUMENT.

Figure 10 HIERARCHY FOR APPLYING FLIGHT TEST DATA TO SIMULATOR FLIGHT PERFORMANCE

conditions must be satisfied by the fuel controller. First, increase the burner pressure limit (already done by the non-static analysis) and, second, increase the scheduled rotor speed at maximum PLA. To satisfy the second requirement the increase in scheduled rotor speed should happen at a PLA greater than 90° (the maximum PLA given in the fuel control design specification) but less than 98° (the full forward hard stop defined by the throttle quadrant). To obtain this scheduled rotor speed it was decided to add another PLA line to the governor schedule. A PLA equivalent to the full-open no-load position on the throttle quadrant was used. This modification verified the static high EPR portion of the installed thrust curve.

Figures 11 and 12 show the results of these design changes on engine thrust flight test data.

#### Gas Generator Parameters

The remaining static gas generator performance parameters were verified using the static thrust calibration curves (Reference 4). The analysis indicated discrepancies for all the static parameters and proved that the original design decision to base static gas generator performance on engine maintenance manual data was incorrect.

This discrepancy was attributed to inlet losses generated by engine test stand inlets and exhaust casings. The performance parameters were modified and static gas generator performance was found to be consistent with flight test data. Non-static gas generator performance was verified using the engine performance curves of Reference 4 and found to be consistent with the flight test data.

#### Cruise Fuel Flows

Reference 5 contains numerous fuel flow charts for the aircraft over its entire airspeed envelope in the cruise configuration at various gross weights. Also contained in the reference are correction factors for including the increased airframe drag effects on cruise fuel flows due to the EVS and Phase VI ECM Pod modifications. An analysis of simulator fuel flows was conducted from sea level to 50,000 feet at three gross weights (minimum, intermediate, and maximum) for several airspeeds (including best endurance and best range airspeeds) and for surge bleed valves both closed and open (where scheduled open). The analysis showed a discrepancy in fuel flows for the low-altitude/low-airspeed/ low-gross-weight flight conditions. These aircraft operating conditions correspond to low engine power settings (i.e., in the EPR range of 1.0 to 1.1). Since the flight conditions are for low power and in a region where the EPR-Wf map was extrapolated because of incomplete data, it was decided to investigate the low-power part of the EPR-Wf maps. Also, it was decided that it would be easier to modify the low-EPR fuel flows rather than try to adjust the aircraft's basic drag polar in the Mach 0.3 and below region in order to match the flight test data. Modifying the low-EPR fuel flow relationship was accomplished by taking the EPR values obtained from the trim flight condition and matching it to the flight test fuel flows contained in Reference 5. This modification as well as expanding the linear function interpolator (LFI) data tables to incorporate



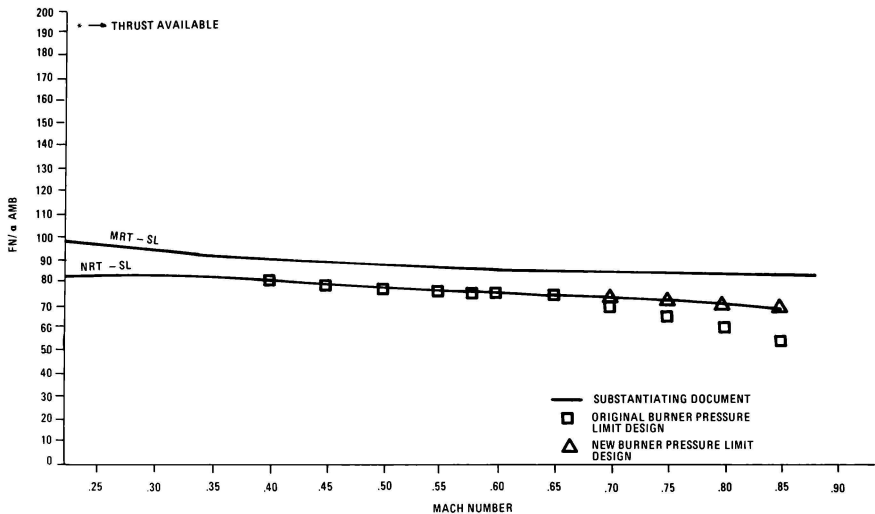


Figure 11 RESULTS OF DESIGN CHANGES ON THRUST AVAILABLE

additional EPR and Mach number break points verified that simulator fuel flows matched flight test data. Figure 13 shows the results of the design change on a typical flight manual fuel flow curve.

#### "CLEAN" AIRCRAFT PERFORMANCE

Analysis of simulated aircraft performance for the "clean" aircraft configuration was established as the second step in verifying overall simulated aircraft performance. Available performance tests based on flight test data included aircraft speed/power trims and rates of climb and descent.

#### Speed/Power Trims

Comparison of the speed/power flight test data contained in Reference 4 with the simulator's speed/power characteristics indicated discrepancies in engine power levels for given flight test conditions. Since the EPR-thrust relationship had already been verified, it was decided to investigate the aircraft's basic drag polar. The previous analysis done on available flight test data sources uncovered the fact that the flight test aircraft drag polar was reduced by the lack of the 1969 EVS and Phase VI ECM pod installations. The design data used to implement the basic drag polar in the simulation model was taken from Reference 3 and was found to include drag due to the pod installations. Replacing the design drag polar of Reference 3 with the flight test drag polar of Reference 6 verified all the flight test speed/power data. Further analysis of aircraft performance and available flight test data (especially the data contained in Reference 5) will have to take into account which aircraft

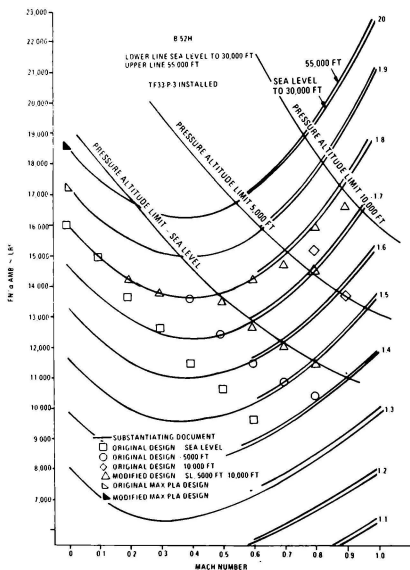


Figure 12 RESULTS OF DESIGN CHANGES ON INSTALLED THRUST

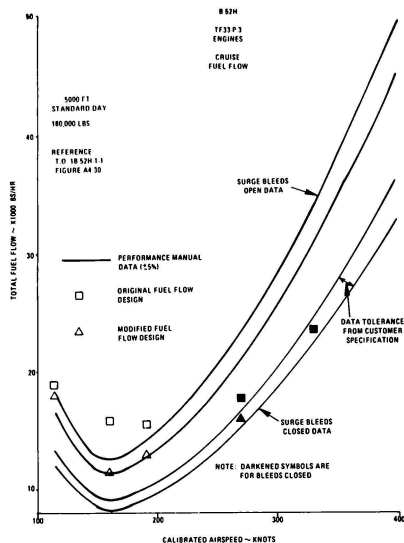


Figure 13 RESULTS OF DESIGN CHANGE ON FUEL FLOW

basic drag polar is to be used. Figure 14 shows the results of using the correct drag polar on the speed/power flight test data.

#### Rates of Climb/Descent

Analysis of the rate of climb data contained in References 4, 5, and 6 was verified using the flight test aircraft drag polar. Figure 15 shows the results of using the correct drag polar on the rate-of-climb flight test data. Analysis of the limited rate of descent data from Reference 5 indicated discrepancies in simulator performance even though the applicable drag polar was being used. Since aircraft drag was verified in the previous analysis, attention was turned to idle thrust performance. Analysis of available data on idle thrust from Reference 6 indicated errors throughout the aircraft's flight envelope. Modifying idle thrust with a delta thrust term to the levels given in Reference 6 verified simulator rate of descent. Figure 16 shows the results of using correct idle thrust on the "estimated" rate of descent data.

#### "DIRTY" AIRCRAFT PERFORMANCE

Analysis of simulated aircraft performance for the "dirty" aircraft configuration (i.e., landing gear down and/or flaps down and/or airbrakes extended) is the final step in verifying overall simulated aircraft performance. The analysis was done by separating out tests for individual drag components and verifying each component. Based on the flight test data available, the aircraft drag components were separated by landing gear

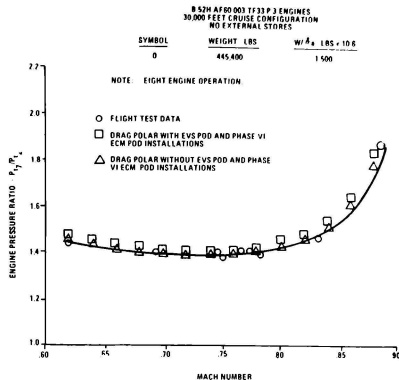


Figure 14 RESULTS OF CORRECT DRAG POLAR ON SPEED/POWER TRIMS

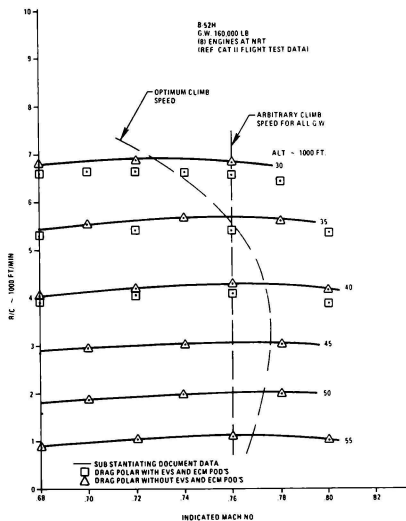


Figure 15 RESULTS OF CORRECT DRAG POLAR ON RATES OF CLIMB

only, flaps only, and landing gear, flaps, and airbrakes. The data for landing gear only was used to verify landing gear drag as designed, the data for flaps only was used to verify flap drag as designed, and the data for landing gear, flaps, and airbrakes was used to verify airbrake drag as designed.

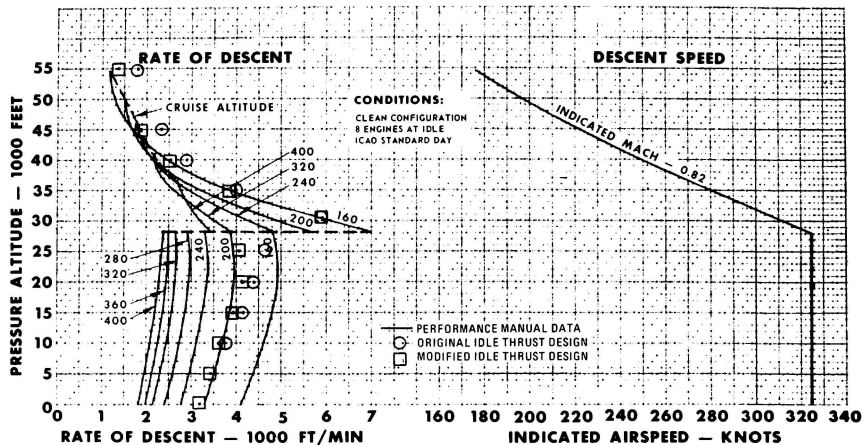


Figure 16 RESULTS OF IDLE THRUST MODIFICATION ON "ESTIMATED" RATES OF DESCENT

#### Landing Gear Drag

Analysis of simulator performance with landing gear down only was done using the estimated gear-down rates of climb curves of Reference 5. The analysis verified that the landing gear drag polars as originally designed match the available data.

#### Flap Drag

Analysis of simulator performance for flaps down only indicated that the maximum rates of climb did not match the estimated flaps down rates of climb curves of Reference 5. The analysis disproved the validity of the original flaps-down drag polar data given in Reference 3. A new flaps-down drag polar was derived by calculating a drag coefficient for each rate of climb data point given in the flight manual curve. The analysis increased flap drag and Figure 17 shows the results of the new drag polar on the maximum rate of climb data.

#### Airbrake Drag

Analysis of simulator performance with airbrakes extended indicated that the rates of descent did not match the estimated normal and emergency configuration rates of descent of Reference 5. Also, the fuel flows obtained from the simulator did not match the estimated power approach configuration fuel flows of Reference 5. This disproved the validity of the basic flaps-up and flaps-down drag polars due to spoilers given in Reference 5 and necessitated the inclusion of spoiler blowdown in the original design. To match the above estimated data the following approach was implemented:

First, match the normal descent rates. This data is for airbrakes at position

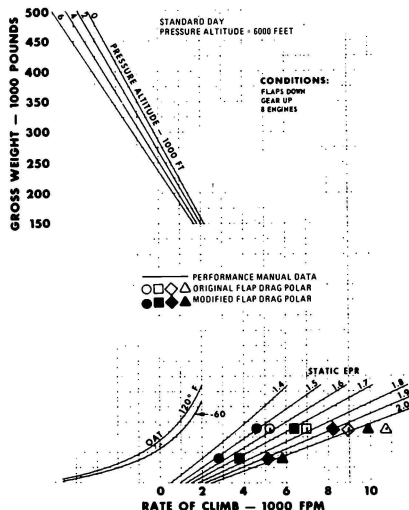


Figure 17 RESULTS OF MODIFIED FLAPS DOWN DRAG POLAR ON ESTIMATED RATES OF CLIMB

4, landing gear down, flaps up, and, because it is below 250 knots, has no spoiler blowdown effects.

Second, match the flaps-up approach fuel flows. This data is for airbrakes at position 6, landing gear down, flaps up, and also has no spoiler blowdown effects.

The first two steps will generate a new flaps-up drag polar due to spoilers that will meet the estimated data for normal descent rates and approach fuel flows. The data will be normalized for airbrake position so that it will be applicable to all airbrake positions.

Third, match the emergency descent rates. This data is for airbrakes at position 6, landing gear down, flaps up, and, because it is above 250 knots, contains spoiler blowdown effects.

This step will modify the flaps-up drag polar for spoiler blowdown effects at high airspeeds and will match the estimated data for emergency descent rates. Again, the data will be normalized for all airbrake positions.

Finally, match the flaps-down approach fuel flows. This data is for the airbrakes at position 6, landing gear down, flaps down, and has no spoiler blowdown effects.

This step will generate a new flaps-down drag polar due to spoilers that will meet the estimated flaps-down approach fuel flows. Again, normalizing the data will make it applicable to all airbrake positions.

#### STEP ONE

AIRBRAKE = 4 (NO BLOWDOWN)

CONSTANT INDICATED AIRSPEED

The spoiler drag contribution for airbrakes at position 4 for a constant indicated airspeed was developed by analyzing the data contained in the normal rate of descent performance curve from Reference 5. A new flaps-up drag polar for airbrakes at position 4 was derived by calculating a drag coefficient for each rate of descent data point given in the flight manual

curve. This data was then plotted as a function of lift coefficient and Mach number and is part of the new flaps-up drag polar due to spoiler.

#### CONSTANT INDICATED MACH NUMBER

The spoiler drag contribution for airbrakes at position 4 for constant indicated Mach number was developed by analyzing the data contained in the normal descent curve at constant Mach number. The same procedure which was used to analyze the constant airspeed data was again used to analyze the constant Mach number data. The data was then plotted as a function of lift coefficient and gross weight and becomes another part of the flaps-up spoilers drag polar.

Figure 18 shows the results of the new flaps-up drag polar for airbrakes at position 4 on the estimated normal rate of descent data.

#### STEP TWO

AIRBRAKE = 6 (NO BLOWDOWN)

The spoiler drag contribution for airbrakes at position 6 was developed by analyzing the data contained in the low-altitude/low-airspeed fuel flow curves from Reference 5. The data is used for determining approach fuel flows and is well below the 250 knot spoiler blowdown airspeed given in Reference 3. A new flaps-up drag polar for airbrakes at position 6 was derived by calculating a drag coefficient for each fuel flow data point given in the flight manual curve. The data was then plotted as a function of lift coefficient and Mach number and becomes the final part of the new flaps-up spoilers drag polar. Figure 19 shows the results of the new flaps-up drag polar for airbrakes at position 6 on the estimated approach fuel flow data.

The data derived to generate the new flaps-up drag polar due to spoilers showed a discontinuity in the Mach data range between the airbrakes 4

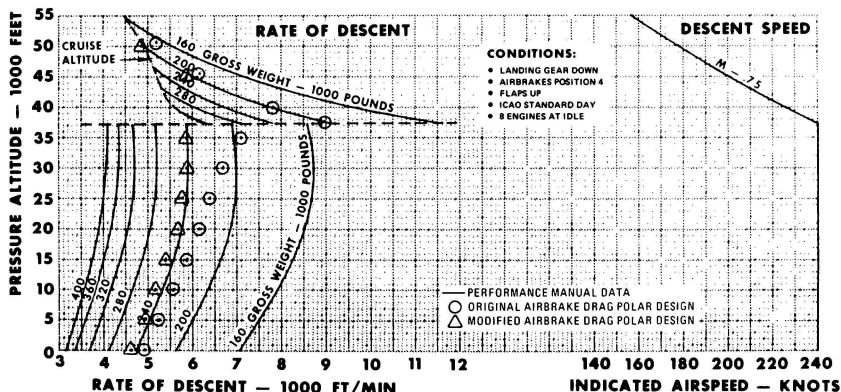


Figure 18 RESULTS OF MODIFIED FLAPS UP DRAG POLAR DUE TO SPOILERS ON ESTIMATED NORMAL RATE OF DESCENT DATA

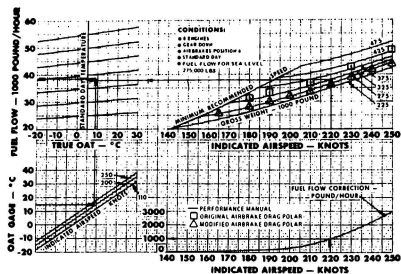


Figure 19 RESULTS OF MODIFIED FLAPS UP DRAG POLAR  
DUE TO SPOILERS ON ESTIMATED APPROACH  
FUEL FLOW DATA

and airbrakes 6 data. As implemented in the linear function interpolator (LFI) this discontinuity was minimized by the choice of the Mach breakpoints. The overall effect on simulator performance was minimal and was within performance tolerances.

### STEP THREE

## BLOWDOWN EFFECT

The slowdown effect on spoiler drag was developed by analyzing the data contained in the estimated emergency rate of descent curve (Reference 5). The data is at a constant indicated airspeed of 305 knots and is well above the 250 knots spoiler slowdown speed. A change in drag coefficient due to spoiler slowdown was derived by calculating a delta drag coefficient for meeting the airbrake 6 rate of descent data points given in the flight manual curve. The delta was plotted as a function of lift coefficient and airspeed and is applied at 305 knots (data basis) up to 600 knots

(maximum spoiler blowdown effect) with the additional stipulation of 0 delta at 250 knots (minimum spoiler blowdown effect). A multiplier was developed to implement the change for all airspeeds above 250 knots for meeting the emergency descents. The results of implementing the spoiler blowdown effect on the estimated descent rates is shown in Figure 20.

## STEP FOUR

## FLAP EFFECTS

The effect of flaps down on spoiler drag was developed by analyzing the data contained in the low-altitude/low-airspeed approach fuel flow curve contained in Reference 5. A new flaps-down drag polar for airbrakes extended was derived by calculating a drag coefficient for each fuel flow data point given in the flight manual. The data was normalized for all flap positions and then plotted as a function of lift coefficient and Mach number. Because of the difference in Mach number breakpoints between this data and the flaps-up data it was decided to implement the flaps-down data as a separate drag polar instead of flaps-up data with a flap position factor. Figure 21 shows the results of the new flaps-down drag polar due to spoilers on estimated approach fuel flows.

The overall impact of the software design changes incorporated to simulate airbrake drag was that some emergency rates of descent obtained from the simulator (mainly at low altitudes) deviate slightly from the performance manual values. This is due to the fact that the rates of descent and approach fuel flow data with airbrakes extended contained in the performance manual overlapped in the associated Mach regions and did not agree. It was decided that it would be more important to match the performance manual approach fuel flows because they provide more meaningful information to the pilot than low-altitude emergency descent rates.

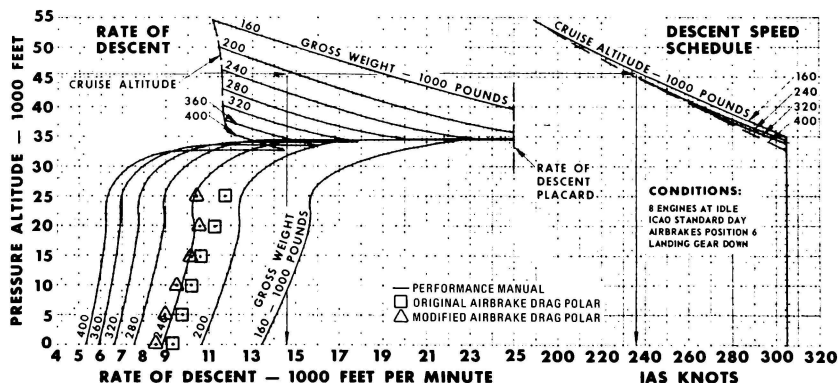


Figure 20 RESULTS OF SPOILER BLOWDOWN EFFECT ON ESTIMATED EMERGENCY RATE OF DESCENT DATA

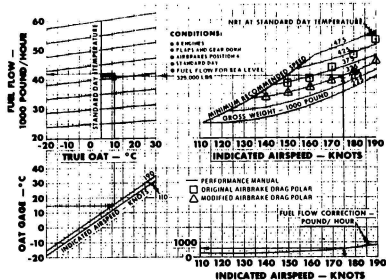


Figure 21 RESULTS OF MODIFIED FLAPS DOWN DRAG POLAR DUE TO SPOILERS ON ESTIMATED APPROACH FUEL FLOW DATA

### CONCLUSIONS

Based on the above analysis several software modifications were made to the engine and the aerodynamic simulation models. Changes in burner pressure limit and fuel control scheduling increased thrust at the high-airspeed/higher-power settings. This validated the thrust-available curves contained in the substantiating document. Modifying idle thrust verified the clean aircraft rates of descent contained in the flight performance manual. A slight bending of the EPR-Fuel Flow Map in the low power region satisfied the low airspeed/low gross weight/low altitude regime of the fuel flow charts contained in the aircraft flight manual. Noting dates for airframe modifications for EVS and Phase VI EMC pods and using the correct aircraft drag polar in analyzing certain flight test data verified all clean aircraft performance. The simulation model for landing gear down only was correct as designed, but the flaps-down drag polar was modified to meet the maximum rates of climb curves contained in the aircraft flight manual. Changes were made to the flaps-up and the flaps-down drag polars due to spoilers as well as adding a term to account for spoiler blowdown effect. These modifications assured meeting the normal and emergency descent rates as well as the powered approach fuel flows contained in the flight manual.

Analysis of flight simulator results against available flight test data proved to be a valuable means of verifying simulated aircraft performance and enhancing overall simulator fidelity. A definite understanding of aircraft configuration during the flight test program and of modifications made to the aircraft which are not reflected in the manufacturer's design data is essential for understanding the scope of flight test data available and its applicability to simulator results.

### REFERENCES

1. Richardson, W. S. and Rockwell, C., "CAN FLIGHT TEST RESULTS IMPROVE SIMULATOR REFINEMENT? PROOF AND EXCEPTIONS USING B-52 WEAPON SYSTEM TRAINER TEST RESULTS."
2. Boeing D3-9776-3, "B-52G/H PROPULSION CHARACTERISTICS - MISSION SIMULATORS (U)." Prepared under contract number F34601-74-C-1785, 1975.
3. Boeing D3-9776-2, "B-52G/H AERODYNAMIC CHARACTERISTICS - MISSION SIMULATORS (U)." Prepared under contract number F34601-74-C-1785, Revision B, 21 June 1977.
4. Adolph, Charles E., Cole, Frank E., Worthington, Forrest W., and Sturmthal, Emil, "B-52H CATEGORY II PERFORMANCE AND STABILITY TESTS." FTC-TR-63-16, November 1963.
5. T.O. 1B-52H-1-1, "B-52H FLIGHT MANUAL PERFORMANCE DATA," 1 February 1961, Change 61, 1 November 1979.
6. Lewis, Perkins, and Wintz, "SUBSTANTIATING DATA REPORT B-52H FLIGHT MANUAL STANDARD AIRCRAFT CHARACTERISTICS CHARTS." Boeing D3-3211, 26 January 1961.
7. T.O. 6J3-4-55-3, "OVERHAUL INSTRUCTIONS - TURBINE ENGINE MAIN FUEL CONTROL - MODEL NO. JFC25-14," 15 December 1968.
8. Link SDMR 128012, "B-52H ENGINE AND ENGINE SYSTEMS," January 1982.
9. Link SDMR 111011-1, "B-52H AERODYNAMIC COEFFICIENTS," January 1982.



John L. Beilman  
Arvin/Calspan Advanced Technology Center  
Buffalo, New York

### Abstract

Under contract to the U.S. Naval Test Pilot School, the Calspan Corporation has been conducting special flight demonstrations with the Navy X-22A V/STOL Research Airplane. These flight demonstrations are part of a curriculum designed to acquaint the student test-pilot with an unconventional means of flight control: thrust vectoring. In addition to the flight demonstrations, the curriculum includes lectures on the basic aerodynamic considerations of V/STOL flight, flight control systems, information display systems, X-22A systems and ground simulation.

The X-22A flight demonstrations, conducted by Calspan engineering test-pilots, consist of two flights:

- Flight One -- a flight under visual meteorological conditions to demonstrate short takeoff and landings, inbound and outbound transitions and vertical landings and takeoffs.
- Flight Two -- a flight under simulated instrument meteorological conditions (amber windscreen plus blue visor on student pilot) using the X-22A Programmable Head Up Display (HUD) to perform decelerating, descending approaches to a hover.

The guidance information for these approaches is obtained from a dedicated, portable, scanning beam tactical landing system (TLS). TLS position and derived velocity information is blended with aircraft accelerometer data in complementary filters to obtain smoothed data for both the flight control and display systems.

After the lectures and ground-school, in preparation for the flight demonstrations, the student pilots receive about four hours of training via ground simulation.

The fixed-based ground simulator consists of the X-22A itself coupled into a six-degree-of-freedom digital computer simulation at the basic X-22A aerodynamics, with all significant non-linearities included in the model. The cockpit flight control inputs disturb the model, the response variables are fed back through the X-22A variable-stability system to the X-22A flight control surfaces and the simulated aircraft motion variables are displayed to the pilot on a head-up-display (HUD).

For use in both ground simulation and in-flight demonstrations, a variety of HUD formats for the instrument landing approach are stored in the airborne digital computer. The computer is addressable by the pilot from a cockpit terminal.

The level of information in the HUD is variable from status only, to status plus velocity, to status and velocity plus flight or control directors.

The approach profile, under simulated instrument conditions, requires continuously decelerating and descending from about 100 knots and 1100 ft AGL, at 8000 ft from the landing pad, to a hover at 100 ft altitude over the landing pad. Thrust vectoring during this transition can be done manually or automatically.

In addition to the variety of displays, a variety of flight control systems are available. Because of the brevity of the Navy TPS flight demonstrations, only rate command and attitude command systems are demonstrated, in conjunction with selected HUD formats.

The TPS students and faculty who have participated in the X-22A V/STOL demonstration program have all acknowledged it to be a very educational experience. Most participants have performed better in flight than in the ground simulator, indicating the importance of proprioceptive cues.

### Introduction

Under contract to the U.S. Naval Test Pilot School, the Flight Research Department of the Calspan Corporation has conducted a series of flight demonstrations with the Navy X-22A V/STOL Research Airplane at Buffalo, N.Y. The purpose of the demonstrations is to introduce selected TPS student pilots to the use of thrust-vectoring as a means of flight control.

While thrust-vectoring is not a new concept for flight-control, it has seen very limited application to date, the Harrier and its various derivatives being the only operational V/STOL airplanes. It is anticipated that thrust-vectoring will see greatly increased application in the future. Thus, it is important to the training of future engineering test pilots that they be exposed to the impact of this ability to simultaneously control the magnitude of thrust and its direction, independent of aircraft attitude.

Accordingly, beginning in 1981, the faculty of the Navy TPS designated four pilots from each TPS class to participate in the X-22A demonstration program at Calspan. For each group of four TPS students, the X-22A program represented their "Special Projects" assignment, a tutorial-like part of the Navy TPS curriculum. Each group of four TPS students assigned to the X-22A Special Project comprised two pilots with fixed-wing experience and two pilots with rotary-wing experience. In no case to date has any of these TPS students had any previous flight time in an airplane with vectored thrust capability.

The five main elements of the Navy TPS/X-22A Special Project, as conducted by Galapán, are:

1. A series of lectures on the basics of V/STOL aerodynamics, flight control and displays.
2. A ground school on the X-22A, its systems and flight characteristics, including egress training (the X-22A has rocket fired ejection seats).
3. Ground-based simulation, using the X-22A itself coupled to a six-degree of freedom digital computer model.
4. One one-hour flight under visual meteorological conditions (VMC) and one one-hour flight under simulated instrument meteorological, conditions (IMC), using the Head-Up-Display and Microwave Landing System.
5. A Special Projects Report by the Navy TPS students.

Figure 1 shows the schedule for the X-22A V/STOL Training Program.

WEEK	DAY	AM	PM
1	WEDNESDAY		CALSPAN PERSONNEL TRAVEL TO NATC
1	THURSDAY	V/STOL CLASS, SIMULATOR BRIEFING	
1	FRIDAY	~ X-22A GROUND SCHOOL ~	
			CALSPAN PERSONNEL RETURN TO BUFFALO
2	MONDAY	PILOTS 1 AND 2 AT CALSPAN FOR GROUND SIMULATION TRAINING	
2	TUESDAY	PILOTS 3 AND 4 AT CALSPAN FOR GROUND SIMULATION TRAINING	
2	WEDNESDAY	CONVERSION OF X-22A SYSTEMS FROM GROUND SIMULATOR TO FLIGHT MODE	
2	THURSDAY	X-22A FUNCTIONAL TEST FLIGHT	
2	FRIDAY	POST-FLIGHT, PRE-FLIGHT INSPECTIONS	
		AM	
3	MONDAY	FLT. 1, PILOT 1	FLT. 2, PILOT 2
3	TUESDAY	FLT. 3, PILOT 3	FLT. 4, PILOT 2
3	WEDNESDAY	FLT. 5, PILOT 3	FLT. 6, PILOT 4
3	THURSDAY	FLT. 7, PILOT 3	FLT. 8, PILOT 4
3	FRIDAY	RESERVE FOR CONTINGENCY	
3	SATURDAY	RESERVE FOR CONTINGENCY	
NOTES: (1) X-22A FLIGHTS 1 AND 2 SAND 6 BASIC V/STOL INDOCTRINATION (X-22A FLY-BY WIRE)			
(2) X-22A FLIGHTS 3 AND 4 7 AND 8 ADVANCED FCS AND DISPLAYS (X-22A VSS, HUD, MLI)			

Fig. 1 USN/TPS X-22A V/STOL Training Program Schedule.

### Lectures

#### V/STOL Aerodynamics

A brief overview of the current status of V/STOL aircraft development is presented, with the X-22A representing a disc loading intermediate to the XV-15 (low disc loading) and the AV-8A/B (high disc loading), as shown in Figure 2. The full range of V/STOL aircraft configurations is given in Figure 3, with representative vehicles for each configuration also listed.

Every V/STOL aircraft has its "transition corridor", i.e., a limited range of airspeeds which can be flown at any particular angular setting of its thrust vectoring system. Figure 4 shows the transition corridor for the X-22A. Even within the preferred corridor, the pilot must deal with

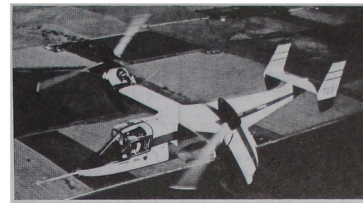
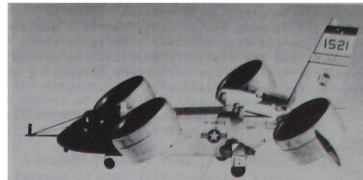


Fig. 2 Representative V/STOL aircraft.

- TILT WING – VERTOL VZ-2, Vought XC-142, CANADAIER CL-84
- TILT THRUST: JETS, PROPELLERS, ROTORS – DOAK VZ-4, BELL ATV, XV-3, X-22A, XV-15, CURTISS X-19
- DEFLECTED SLIPSTREAM – RYAN VZ-3, FAIRCHILD VZ-5
- DEFLECTED JET – BELL X-14A, HAWKER-SIDDELEY XV-6A, AV8A/B, LOCKHEED XV-4A/B, MIRAGE 3
- SUBMERGED FANS, FAN IN WING – RYAN XV-5A
- DIRECT THRUST, SEPARATE THRUST AND LIFT DEVICES – SHORT SC 1, DORNIER DO31, ENTWICKLUNGSRING – SUEB VJ-101, FLOGGER (USSR)

Fig. 3 V/STOL technology.

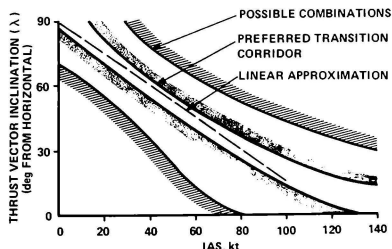


Fig. 4 X-22A transition corridor.

continuously changing flying qualities; the frequency and damping of the characteristic motions of the unaugmented aircraft vary widely, as shown in Figure 5, and the stability augmentation system (SAS)—at best—reduces the variations in damping of the angular degrees of freedom).

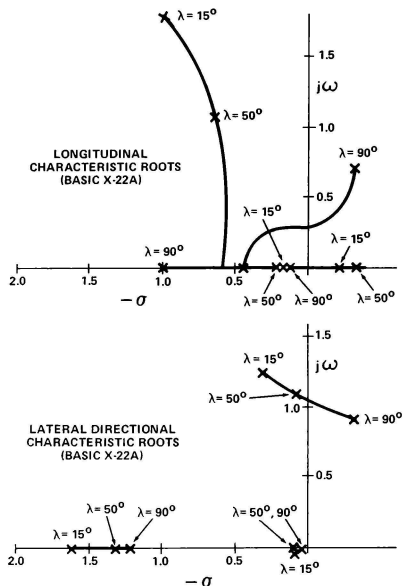


Fig. 5 Locus of characteristic roots (basic X-22A).

The lecture then proceeds to discuss the characteristics of response coupling in VTOL aircraft (i.e., pitch-vertical in forward flight versus pitch-translational in hover). The viewgraphs used with this part of the lecture are given in Figures 6, 7 and 8,

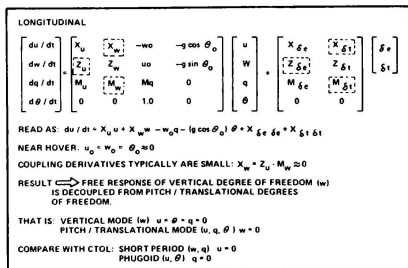


Fig. 6 Linear/small perturbation equations of motion for V/STOL ( $\lambda = \text{constant}$ )

IF CONTROL COUPLING DERIVATIVES ARE ALSO SMALL ( $X_{\delta t} = Z_{\delta e} = M_{\delta t} \approx 0$ ), THEN FORCED RESPONSES ALSO DECOUPLE INTO A VERTICAL MODE AND A PITCH/TRANSLATIONAL MODE

RESULT ⇒ CAN WRITE LONGITUDINAL EQUATIONS OF MOTION AS TWO INDEPENDENT SETS.

PITCH / TRANSLATIONAL

$$\begin{bmatrix} du/dt \\ dq/dt \\ d\theta/dt \end{bmatrix} = \begin{bmatrix} X_u & 0 & -g \\ M_u & M_q & 0 \\ 0 & 1.0 & 0 \end{bmatrix} \begin{bmatrix} u \\ q \\ \theta \end{bmatrix} + \begin{bmatrix} X_{\delta e} \\ M_{\delta e} \\ 0 \end{bmatrix} \begin{bmatrix} \delta e \end{bmatrix}$$

VERTICAL

$$dw/dt = Z_w w + Z_{\delta t} \delta t$$

Fig. 7

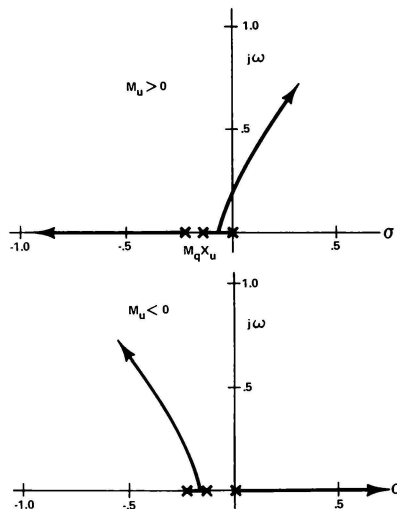


Fig. 8 Characteristics equation  $\Delta(S) = S(S-X_u)(S-M_q) + M_u g$  typical root locus with  $M_u$  varying.

With this background, the considerations leading to flying qualities difficulties of V/STOL aircraft in decelerating transitions are briefly summarized:

- Constraints tighten (smaller window) as range decreases (like flying into funnel). Although V/STOL's can stop, back-up etc. ground obstacles still require precise flight path control at low speed.
- Inherent stability tends to deteriorate - aerodynamic surfaces less effective.

- Additional controller (conversion)
- Flight path, speed control strategy changes
 

Frontside	{	Pitch attitude controls $\gamma$ (or h)
		Thrust controls V
Backside	{	Pitch attitude controls V
		Thrust controls $\gamma$ (or h)
- Control of monotonically decreasing velocity vector
- Trim changes
- Transition corridor
- Wake from ground obstacles
- Ground effect - height "stiffness" may be positive or negative
  - Unusual force and moment derivatives
- IFR.

#### Flight Control Systems and Displays

It has long been recognized that, due to the inherently poor dynamics of most V/STOL aircraft during powered-lift flight, some stability and control augmentation is required.

In addition, if the full capabilities of V/STOL aircraft are to be exploited, difficult flying tasks must be performed, such as the simultaneously decelerating and descending transition under IMC to a minimum hover altitude prior to landing. The safe performance of such a task will surely require assisting the pilot with displays of integrated information.

It can be seen that a "systems" approach to any V/STOL flying task, such as the instrument landing approach, must consider that the displayed information, as well as the flight control system and aircraft response are in the overall pilot/airplane closed loop. This situation is depicted in Figure 9. As with any closed-loop system, phase-shifts, time-lags or excessive gain in any element can drive the system unstable. The design of the display is very complex because it demands that any abstract symbology chosen be as "intuitive" as possible and that, at the same time,

its dynamic and static characteristics (gain or sensitivity) be compatible with the stability of the closed loop pilot-airplane, combination. For example, a pilot-induced-oscillation (PIO) in pitch can be produced under IMC by too much sensitivity in the display of pitch attitude, i.e., by having the motion of the pitch attitude symbol create too great an angular change at the pilot's eye per unit pitch angle of the airplane.

A number of years ago, it was hypothesized (Reference 1) that flight-control system sophistication and display sophistication could be exchanged or "traded-off" for constant pilot workload. Putting the hypothesis in other words: a very advanced display system could compensate for a degraded flight control system and a very advanced flight control system would minimize the requirements for displayed information.

In the context of this hypothesis, control sophistication is an unquantified concept measured by the role of the pilot and the degree to which he is relieved of lower level tasks:

1. At the lowest level, the pilot acts as a servo mechanism controlling inner loops such as attitude stabilization.
2. At an intermediate level, the pilot acts as an autopilot controlling outer loops such as guidance and navigation.
3. At the highest level, the pilot acts as a manager, monitoring status and intervening only as required.

Display sophistication is also an unquantified concept, defined to increase as the need for interpretation or estimation on the part of the pilot is reduced:

1. At the lowest level, the display provides status information. All inner loop closures are made either implicitly through estimating motions of the symbols or indirectly through force and motion cues.
2. At an intermediate level, translational velocity and velocity commands are added. Only innermost attitude command loops now require implicit or indirect information.
3. At the highest level, control commands are added. Ideally, no implicit or indirect information is required; the pilot may act as a pure gain to null the displayed control commands.

Figure 10 shows the original hypothesis graphically (and adds the practical consideration of cost, which obviously increases with sophistication). The results of an earlier X-22A research program (Reference 2) essentially validated the original hypothesis, as indicated by the pilot rating data in Figure 11 (taken from Reference 2, pg. 157).

It is important for the student pilot to have all the above background on control systems and displays because the X-22A Special Project will introduce him, at least for the instrument landing approach, to more sophisticated systems than he is likely to have previously encountered.

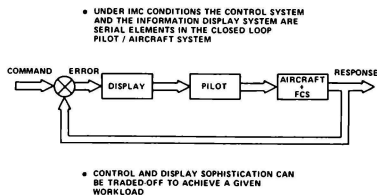


Fig. 9 Control and display interaction.

**DIRECTORS/PREDICTORS**

**SITUATION**

**INTEGRATED INCREASING DISPLAY SOPHISTICATION**

**INCREASING CONTROL SOPHISTICATION**

**WORKLOAD**

**EQUIPMENT COST**

**INCREASING COST**

**SATISFACTORY**

**ACCEPTABLE**

**INTOLERABLE**

**COUPLED GUIDANCE**

**Fig. 10** Possible relationship between control and display sophistication.

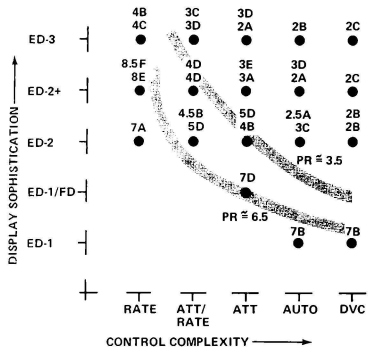


**Fig. 11 Pilot rating data for primary matrix (no crosswinds, with thrust vectoring commands)**

### X-22A Ground Simulator-Specific Tasks and Displays

The lecture then focuses on the basics of the X-22A Ground Simulator, its capabilities and limitations. This includes operational details, discussion of the profile of the descending, decelerating landing approach, the various selectable flight control systems and the library of display formats available through the X-22A cockpit computer terminal. All of these items will be discussed in detail later in this paper in connection with ground and in-flight simulation.

## X-22A Ground School

The preparation of the TPS students is completed with instruction on the X-22A, its systems, operating procedures and flight characteristics. This part of the classroom work is in the nature of a review and open book

examination since the students are required to read through the X-22A Utility Flight Manual in advance of the class.

Only an outline of the topics covered in the ground school is given here because of the specialized nature of the material:

## X-22A Ground School Lecture Syllabus

1. Operational Procedures
2. Power Plant
3. Fuel System
4. Power Transmission and Propellers
5. Lubrication System
6. Hydraulic System
7. Electrical System
8. Wheel Brakes
9. Master Caution Panel
10. Communication Systems
11. Cockpit Displays - Conventional
12. Flight Envelope and Limitations
13. Data Acquisition System
14. VSS and FBW Flight Control System
15. Head-Up-Display System (HUD)
16. Microwave Landing System (MLS)

Following the classroom session and prior to flight, each student spends several hours at the airplane and in the cockpit being drilled in emergency procedures and becoming familiar with the cockpit environment.

### Ground Simulation

Each student pilot receives 3-4 hours of ground simulation, "flying" the approach profile to be used later in flight.

## Mechanization

For ground simulation, the X-22A airplane is connected to the PDP11/20 digital computer which is part of the data acquisition and flight-safety monitoring system in the X-22A telemetry van. The PDP11/20 is programmed with a six-degree-of-freedom model having the non-linear aerodynamics of the X-22A at duct angles from zero to ninety degrees and airspeeds from zero through one-hundred-twenty knots. The six degrees of freedom input/output produce appropriate responses from the computer model which are presented to the pilot through motion of the symbols or changes in the numerics on the head-up-display (Figure 12).

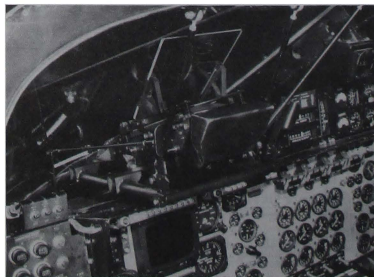


**Fig. 12 X-22A HUD**

In this ground simulation mode the X-22A flight control system, variable stability system and on-board analog and digital computers operate the same as in flight. The actual motion of the X-22A flight controls become inputs to the PDP11/20 computer and the computed response signals from the PDP11/20 are substituted for the X-22A airborne sensors for groundspeed\*, airspeed, linear and angular accelerations, angular rates, etc.

#### Evaluation Task

The student's task during ground simulation is to "fly" the approach profile shown in Figure 13\*\*. Because of the limited time, the student is restricted to using only two types of flight control systems: rate command and attitude command. However, the student is permitted to explore the full library of display formats and to concentrate on two or three for further practice in ground simulation and later use in actual flight.

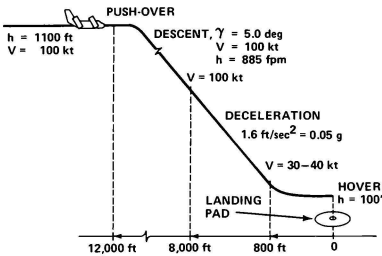


Fig. 13 Evaluation task.

#### Display Formats

The on-board computer library of landing approach display formats contains two generic formats, one designated "AV8" type and the other designated "ED2" type. These formats were designed and programmed in the X-22A airborne digital computer as part of the experiment reported in Reference 5. (The AV8 format is patterned after an original British Harrier format and the ED2 format was developed at Calspan). Seven variations of the AV8 format are available, designated AV8-0 through AV8-6. Three variations of the ED2 format are available, designated ED2-0, ED2-1 and ED2-2. On all of the formats, a flashing of the aircraft symbol calls for duct (thrust vector) rotation until the flashing stops. On any of the formats, digital or analog tape readouts of airspeed may be selected and the AV8 pitch ladder scaling can be selected as 5° or 10° per rung. The miniature computer terminal in the cockpit, used for calling up the various displays, and the safety pilot's HUD monitor are shown in Figure 14.

\* All inertial range and velocity signals used for guidance in the X-22A are derived by combining MLS data with aircraft accelerometer signals in Kalman filters (Reference 3)

\*\* The detailed rationale, synthesis and systems mechanization for this task are given in Reference 2, Sections III & IV. A summary of the same task design is given in Reference 4.



Fig. 14 X-22A Cockpit computer terminal & hud monitor.

Only one example of each generic format will be discussed here. (Complete details of all the formats are given in Reference 5). It should be noted that in these formats the horizontal and vertical situations are necessarily collapsed into the single plane of the HUD. The AV8-5 format is shown in Figure 15 with nomenclature and in Figure 16 as viewed on the HUD. The ED2-0 format is shown in Figure 17 with nomenclature and in Figure 18 as it is viewed on the HUD.

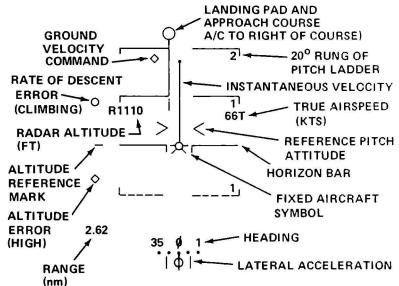


Fig. 15 AV8-5 format.

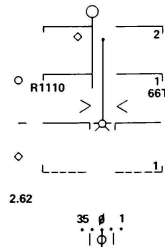


Fig. 16 AV8-5 format.



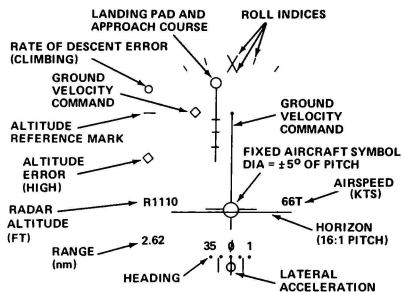


Fig. 17 ED2-0 format.

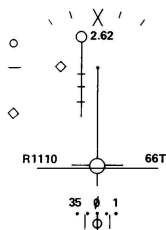


Fig. 18 ED2-0 format.

A very minor appearance detail of the ED2 aircraft symbol, the "tail" shown at 6 o'clock on Figures 17 and 18, is very important and offers a significant advantage over the AV8 display for hovering flight: When the velocity vector is near zero, the "tail" enables the pilot to determine his heading relative to the approach course.

### Simulated Approaches

Each student pilot then flies 30-40 "approaches" (Figure 13) with various HUD formats and either rate command or attitude command types of flight control systems. During the approach he observes on the HUD a continuous decrease in numerical and analog range to the landing pad (from a starting value of 2.62 nm) accompanied by a growth in pad symbol size as he approaches it (the pad symbol also migrates down the field of view toward the fixed aircraft symbol until, at hover, the aircraft symbol is centered over the pad symbol). Also during the approach, the radar altitude decreases to 100 ft AGL and airspeed is

reduced to zero or the headwind value. The approach is made with automatic turn coordination operative until, at a few hundred feet from the pad and at an airspeed of about 20 kts, heading hold is selected. Simultaneously the display is switched from approach course "up" to aircraft heading "up", making interpretation of the display symbology in hover more natural for the pilot, since the approach course and pad move the same way relative to him as if he were looking out a window at them in the real world. This display situation is shown pictorially in Figure 19. Without the switching of the display reference system if the pilot should overshoot the pad and turn 180° in order to return to it, he would have to push forward on the stick to fly backwards on the approach course—a very unnatural procedure on the course-referenced display.\*

AT GLIDE SLOPE INTERCEPT,  $V = 100$  kt,  
~1000 ft TO LEFT OF APPROACH COURSE;  
HEADING PARALLEL TO APPROACH COURSE;  
NORMAL SCALING, ATC SELECTED.  
PILOT NEEDS TO TURN TO RIGHT TO PLACE  
HEAD OF VELOCITY VECTOR IN COMMAND  
DIAMOND

(a)

LEVEL APPROACH TO HOVER,  $V = 20$  kt,  
~100 ft TO LEFT OF APPROACH  
COURSE WITH ~200 ft TO TOUCHDOWN  
POINT; HEADING 030 WITH RESPECT  
TO APPROACH COURSE; NORMAL SCALING,  
ATC SELECTED

(b)

SAME SITUATION AS (b);  
HH SELECTED

(c)

Fig. 19

During these simulated approaches the student becomes familiar with the sequential features of the task, the airplane response characteristics and the proper duct rotation and flight control strategies. The student pilot may select between a throttle handle or collective stick for power management. Typically, the fixed-wing pilots select the throttle handle and the rotary-wing pilots select the collective stick. Thus the student is able to concentrate more on the overall task without having to adapt to an unfamiliar controller.

In the early part of the approach, power is used to control airspeed and pitch attitude is used to control altitude. As the thrust vector is

\* The differences between approach course-up and heading-up display symbology can be illustrated by the following analogy. The interpretation of the approach course-up format is similar to that required in driving North guided by a road-map. Provided that the orientation of the road is generally north-south, no particular difficulty is encountered in determining direction or relative bearing of landmarks such as towns or access roads. However, if the road has large changes in direction; i.e., 90 degrees or more, the interpretation is much more difficult. For example, if the road turns to the south, left turns off the road take you to the right on the map and vice-versa. By continuously rotating the map, so that the direction you are driving is always up on the map, the interpretation difficulty can be eliminated. This latter situation is analogous to the heading-up format, in which the orientation of the longitudinal axis of the aircraft is always vertical in the display. As on the rotating road-map analogy, thus display always shows the true bearing of landmarks such as the landing pad.

rotated toward the vertical and the airplane slows down, power controls altitude and pitch attitude controls airspeed. This is a drastic change in control strategy and the pilot's only cues are the motion of the displayed symbols.

Most pilots learn to perform the approach task quite well in the ground simulator with the attitude command systems. They tend to have considerable difficulty with the rate command systems, so much so that until the spring 1983 class no student pilot attempted to use the rate command system in flight. It is notable that pilots from this class achieved an acceptable performance level in flight with the rate command systems although they too found them to be almost "unflyable" in the fixed-base ground simulator. The obvious inference is that the additional proprioceptive cues of force and motion are crucial to the task performance since the displayed information is identical in each case.

### In-Flight Simulation

#### Preparation for Flight

At the conclusion of the ground simulation phase the TPS students return to the Naval Air Test Center and the X-22A is re-converted to the flight mode. This takes one day, with all pre-flight checks, as shown on the schedule of Figure 1. The following day a functional check flight is performed by Calspan engineering test pilots to verify proper operation of all systems, including the microwave landing system. After post-flight and pre-flight inspections are completed, the Navy pilots are notified to return to Calspan, ready to begin the flight phase of the program.

#### Demonstration Flight Outline

Each student is then given two one-hour demonstration flights by the Calspan Instructor Pilot.

The first flight includes:

1. Basic X-22A handling qualities with full SAS, 1/2 SAS and SAS OFF,
2. Partial conversions from wing-borne to powered-lift flight,
3. Normal landing approaches and wave-off, and
4. Full conversions, inbound to hover and outbound from hover.

The second X-22A flight includes:

1. Demonstration of rate-command and attitude-command flight control systems during visual hover/low speed flight, and

2. Approaches to hover under simulated IMC\* using the combinations of flight-control systems and HUD formats selected by the student during the ground simulation phase.

### Winds and Turbulence

No attempt is made during the ground simulation to simulate winds and/or turbulence. However, in the flight phase, winds and turbulence are not controllable and may become a significant factor. The only way to avoid excessive turbulence is not to fly when it is known to be present. However, head winds up to 25 knots are accounted for in the guidance system by delaying the deceleration commands until the actual ground speed matches the commanded ground speed. This brings the deceleration command point closer to the landing pad in a headwind than in a zero wind condition, as shown in Figure 20.

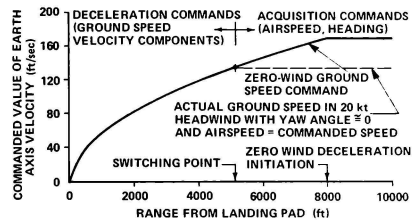


Fig. 20 Effect of headwind on deceleration profile.

Since the duct (thrust-vector) rotation commands begin when airspeed matches commanded ground speed, the delay in initiation of duct rotation caused by a headwind leaves the thrust vector rotated less than  $90^\circ$  at zero ground speed. This is approximately the duct angle required to maintain a fuselage level hover in the particular value of headwind. This situation is shown in Figure 21.

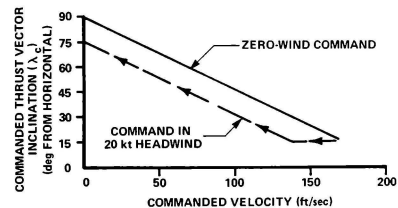


Fig. 21 Effect of headwind on duct rotation schedule.

\* To simulate IMC, the X-22A student pilot uses the blue visor on his helmet, which passes the 5 micron wavelength of the HUD CRT with little attenuation. However, the outside world is blocked from his view by the additional amber windscreen and canopy of the X-22A (L.H. side of aircraft only).

### Pre-flight and Post-flight Meetings

Each flight is preceded by a meeting of all the personnel involved to discuss and/or execute the following:

Aircraft maintenance status

Configuration of airborne research systems

Status of special systems

Detailed Flight Plan, Procedures

Location of MLS and approach course

Weather, especially winds, airport traffic conditions, hover areas etc.

Crew assignments and stations

Government approvals and flight releases

Alerting Buffalo Air Traffic Control to the specific time and details of the imminent X-22A flight.

An X-22A flight operation requires two pilots in the X-22A airplane, two pilots in the chase helicopter, three mechanics, and an inspector. Additionally, in the telemetry van there are a communicator and a minimum of three engineers to monitor all aspects of the flight of this unique aircraft via the telemetry down-link and digital data system.

After the flight, all operational details are reviewed, reports are received on aircraft status and on the performance of the various systems involved (including any observed anomalies). Then the student pilot reviews the flight with his observations and evaluations, especially with respect to flight control, displays, flying qualities, workload and any problem areas. Emphasis is given to comparison of his task performance in flight compared with his performance in the ground simulator.

#### Conclusions

1. The Navy TPS/X-22A program has been a unique and valuable learning experience for the students who have participated, (according to their own reports).
2. In general, the pilots have found it easier to perform the descending, and decelerating approach task under IFR in actual flight than in the ground simulator. In particular, some pilots were able to make acceptable approaches with a rate-command flight-control system in actual flight even though they were unable to do so in the ground simulator.
3. In spite of its lack of motion, the ground simulator was essential in familiarizing the student test pilots with flying the instrument approach task, using vectored thrust, during their second flight and second hour in the X-22A. (The first flight is conducted entirely under visual flight conditions). On an earlier X-22A program -- simulating the AV8-B -- two experienced USMC AV8-A pilots were the evaluation pilots. Despite their prior experience, they had no AV8 instrument time and there was no X-22A ground simulator available. After two one-hour, simulated IMC flights, these AV8 pilots were not as proficient as the Navy TPS students have become on their first approach in actual flight.

4. A more subtle but equally important conclusion is this; Calapan has been developing and using electronic display symbology in the X-22A for eight years. Much basic data on flight experiments involving controls and displays has been collected and reported. However, the subject pilots in these experiments have always been Calapan engineering test pilots who helped develop and "grew up" with the symbology. The ease with which pilots both from rotary wing and fixed wing backgrounds adapted to this complex VTOL task attests to the general applicability of these experimental results.

#### References

1. Anon. "Displays for Approach and Landing of V/STOL Aircraft," AGARD Advisory Report No. 51, November 1972.
2. J.V. Lebacqz and E.W. Aiken, "A Flight Investigation of Control, Display, and Guidance Requirements for Decelerating Descending VTOL Instrument Transitions Using the X-22A Variable Stability Aircraft," Vol. I, Technical Discussion and Results, AK-5336-F-1, Naval Air Systems Command, September 1975.
3. Beilman, J.L. and Till, R.D. "Implementation of a Unique Air Data System for In-Flight Investigations of Advanced VTOL Flight Control & Display Concepts. Proceedings of 1978 Air Data Systems Conference, U.S. Air Force Academy Colorado Springs Colorado, May 1978.
4. J.V. Lebacqz and E.W. Aiken, "Experimental Investigation of Control-Display Requirements for VTOL Instrument Transition," Journal of Guidance and Control, Vol. 1, Nov. 4, July-August 1978, pp. 261-268.
5. J.V. Lebacqz, R.C. Radford, and J.L. Beilman, "An Experimental Investigation of Control-Display Requirements for a Jet-Lift VTOL Aircraft in the Terminal Area," Final Report, NADC-76099-60, also AK-5985-F-1, Naval Air Development Center, July 1978.

Louis Knotts  
Michael Parrag  
Arvin/Calspan Advanced Technology Center  
Buffalo, New York

### Abstract

In-flight simulation is used at the U.S. Naval and Air Force Test Pilot Schools to enhance academic instruction and broaden the flight experience of student test pilots and engineers. The vehicles used to provide this training are the Calspan variable stability Learjet, the Air Force NT-33A, the Navy NCH-46A variable stability helicopter, and the Navy V/STOL X-22A. The in-flight simulation program at the Test Pilot Schools can be divided into two areas—routine training flights and special projects. During their course of study each student test pilot receives at least five flights in variable stability aircraft. These flights are used to demonstrate aircraft statics, dynamics, and control system characteristics, provide instruction in handling quality evaluations, and expose the pilots to new technology such as current control system designs, side stick controllers, and Head-Up-Displays. The special projects which make use of variable stability aircraft are diverse in subject matter, but in general enable the students to apply their academic and flight training to a specific airborne investigation. These projects consist of an NT-33A handling quality study and a Learjet flight control system design project performed at the Air Force Test Pilot School. At the Naval Test Pilot School the test pilots perform an NT-33A Head-Up-Display evaluation and a Learjet handling quality evaluation.

augmented aircraft. The two Test Pilot Schools now use up to four different variable stability aircraft (Figure 1)—a modified Learjet, an NT-33A jet trainer, an NCH-46A helicopter, and a V/STOL X-22A. Flights in these aircraft comprise a routine instructional program of at least five flights, and a series of special research projects performed by the students near the end of their training. A description of the variable stability aircraft used at the Test Pilot Schools, the content of the training flights, and the special projects which make use of in-flight simulators are discussed in this paper.

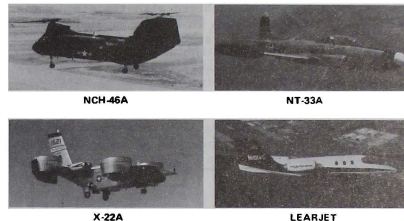


Fig. 1 US Air Force, US Navy and Calspan in-flight simulators.

### Introduction

The earliest variable stability aircraft were created by NASA Ames and the Cornell Aeronautical Laboratory during the mid 1940's. These aircraft, also known as in-flight simulators, have evolved over the years from the original F4U Corsair with a servo controlled auxiliary rudder, to the USAF Total In-Flight Simulator (TIFS), which has 6—degree of freedom simulation capability. In-flight simulators were originally created for use in research and aircraft development, and are still flown extensively for these reasons.<sup>1</sup> In addition, for the past twenty years they have contributed significantly to the training of test pilots and flight test engineers.

In-flight simulation was first used as a training tool at the U.S. Naval Test Pilot School (NTPS) in 1960. In 1963, in-flight simulation was added to the U.S. Air Force Test Pilot School (AFTPS) curriculum. The Cornell Aeronautical Laboratory (now Calspan Corp.) variable stability B-26 was then used as a 'flying classroom' to provide instruction in aircraft stability, dynamics, and handling qualities. Over the years the use of in-flight simulation at the Test Pilot Schools has changed to reflect a growing interest in flight control system design, artificial feel system characteristics, and the evaluation of highly

### Variable Stability Aircraft

All the variable stability aircraft used at the Test Pilot Schools are equipped with two sets of cockpit controls. One set of these controls comprises the original flight control system for that aircraft and is flown by the safety pilot. It is the safety pilot's job to fly the aircraft when the variable stability system (VSS) is not engaged, monitor operation of the VSS to ensure flight safety, program the VSS in flight, and instruct the student test pilots.

The second set of controls consists of a fly-by-wire system. Stick force or stick position command signals from the pilot's stick are sent to a VSS computer, which in turn drives the control surfaces. The student test pilot or 'evaluation pilot' uses this set of controls. With a response-feedback type of variable stability system, aircraft responses such as attitude, rates, and accelerations are measured by on-board sensors and sent to the VSS computer through adjustable feedback gains. Changes to these feedback gains modify the inherent responses of the vehicle to create new forms of aircraft response.

Since the fly-by-wire system does not provide the evaluation pilot with any feel of aerodynamic

control loading, an artificial feel system is necessary. On many of the variable stability aircraft, this feel system is programmable to vary related characteristics such as stick motion, friction, and breakout forces.

A brief description of each in-flight simulator currently used at the Naval and Air Force Test Pilot Schools now follows.

**NT-33A:** The USAF/Flight Dynamics Laboratory NT-33A aircraft is a Lockheed T-33 jet trainer which has been extensively modified and has been operated by Calspan since 1954.<sup>2</sup> The front seat control system has been replaced by a full authority fly-by-wire flight control system and a variable artificial feel system. The evaluation pilot, who sits in the front cockpit, controls the aircraft through a conventional center stick and rudder pedal or through a sidestick controller installed on the right console. The three axis response feedback variable stability system utilizes both analog and digital computers. This system enables the airplane to simulate the stability, dynamic responses, and control effectiveness of a wide range of other aircraft. In addition, the flight control laws of a specific aircraft can be programmed exactly and combined with the simulated airframe dynamics as shown in Figure 2. In-flight operation of the variable stability system is accomplished by the safety pilot using a large number of manual potentiometers located in the rear cockpit.

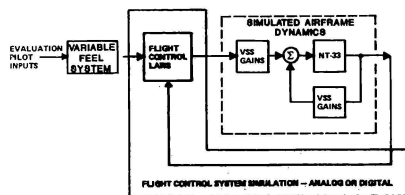


Fig. 2 Bare airframe and flight control system simulation concept used by NT-33A.

A recent addition to the NT-33A is the Display Evaluation Flight Test (DEFT) system, which provides the front seat pilot with a fully programmable Head-Up-Display (HUD). The HUD has two primary formats - a conventional display, much like that in the F-18, and a pictorial Klopstein display for use during instrument approaches. In addition to these two main HUD format options, the individual display elements can be altered as desired to create an almost unlimited variety of HUD formats.

**Learjet:** The newest in-flight simulator used at the Test Pilot Schools is a variable stability Learjet Model 24.<sup>3</sup> As with the NT-33A, this aircraft is equipped with a 3-axis response feedback variable stability system which enables the safety pilot to alter the aircraft's inherent stability and control characteristics in flight. The right seat cockpit controls in the Learjet consist of a center stick and rudder pedals

equipped with a variable feel system, and a side stick controller with fixed feel characteristics. The evaluation pilot uses this set of controls to send inputs to the fly-by-wire flight control system. The left seat cockpit controls are operated by the safety pilot and consist of the original unboosted Learjet yoke and rudder pedals connected to the control surfaces via cables.

The most significant advance in the more modern Learjet variable stability system over that of the other Calspan-operated VSS airplanes is that the many variable gain settings required for a simulation are set digitally by means of a Configuration Control System (CCS). The CCS is capable of storing a large number of preset flight configurations each of which requires up to 64 gain settings. These configurations can be recalled in flight by selecting a single configuration number rather than manually setting all the gains individually. This system offers a significant saving in the time required to change a configuration in-flight, and is especially important in a training situation when a large number of characteristics are demonstrated during a single flight.

**NCH-46A:** Of the two U.S. military test pilot schools, only the Naval school at Patuxent River, Md., possesses a rotary wing test pilot curriculum. A variable stability helicopter is therefore an essential training vehicle at the Naval Test Pilot School to supplement flights in the normal inventory of military helicopters. In 1972 the Hover Augmentation System (HAS) of a Navy CH-46A helicopter was modified by Sperry to create a variable stability capability.<sup>4</sup> The modified NCH-46A helicopter control system uses limited authority series servos in the longitudinal and lateral axes. This allows variations in control sensitivity, rotational damping, control lag, attitude feedback, control cross coupling, and attitude rate cross coupling in both the pitch and roll axes. The NCH-46A does not possess a variable feel system. In 1981, the VSS computer and the method of controlling the system in flight were modified by Calspan. These improvements increased the reliability of the system and eliminated the requirement for an on-board engineer to operate the variable stability system.

**X-22A:** Unlike the other variable stability aircraft which are modifications of existing airframes, the Navy/Calspan X-22A was designed at the outset by Bell to possess an in-flight simulation capability. The X-22A is a V/STOL aircraft capable of hovering flight as well as conventional forward flight. The aircraft attains this capability by means of four variable-tilt ducted propellers powered by four jet engines. The left seat of the X-22A is equipped with a variable feel system and provides inputs to the response feedback variable stability system. The evaluation pilot may fly the aircraft using the center stick controller and either a collective control as in a helicopter or a throttle control as with a fixed wing aircraft. The safety pilot sits in the right seat where the flight controls are mechanically linked to the control surfaces. Like the NT-33A, the X-22A has a programmable Head-Up-Display which can be used to evaluate variations of V/STOL HUD formats and flight directors. An important capability from a training point of view is the

ability to easily configure the X-22A to a ground simulator mode. This enables new evaluation pilots to become familiar with HUD symbology and V/STOL flight procedures before beginning an X-22A flight program.

#### Variable Stability Flight Program

The variable stability program at the Naval and Air Force Test Pilot Schools consists of at least five flights per pilot with an equal number of classroom lecture hours and preflight briefings.<sup>4,5</sup> The sorties are performed in the variable stability Learjet, the NT-33A, and the NCH-46A. This curriculum provides an essential link between academic instruction and airborne experience. Because of the broad repertory of possible aircraft dynamics or control system characteristics which can be reproduced by in-flight simulators, many of the academic concepts discussed in the classroom can be demonstrated to the student in flight. In addition, because these aircraft can be programmed to provide handling qualities ranging from excellent to unflyable, they can be used to practice the techniques of performing handling quality evaluations. Accordingly, the test pilot school variable stability syllabus emphasizes the use of these special aircraft to demonstrate aerodynamic or control system characteristics, and to instruct the techniques required to perform handling quality evaluations. A third use of these aircraft is to introduce to the pilots new equipment such as Head-Up-Displays or side stick controllers, and to show new concepts in flight control system design. These three general aspects of the variable stability flight program are now discussed in depth. The specific content of each variable stability flight is summarized in Table 1.

**Flight Demonstrations:** Academic instruction at the Test Pilot Schools thoroughly cover aircraft equations of motion and the dynamic modes of response. Stability derivatives and their influence on aircraft motion are also discussed at length. However, on a purely classroom basis, it is difficult to relate the mathematics to what is experienced in flight. It is in this area of flight demonstration that the variable stability aircraft is of great training value.

One of the reasons that variable stability concepts are so useful in clarifying aeronautical concepts is that they can show the pilots a much wider range of aircraft response on a single flight than is possible from the entire spectrum of conventional aircraft. For example, the short period damping ratio ( $\zeta_{sp}$ ) of the tactical aircraft flown at the schools is usually in the 0.4 to 0.7 range. That is, the pilot is able to see at most only a few oscillations in the aircraft's free response following an abrupt elevator input. On a typical longitudinal variable stability flight, the short period response is varied from an over damped condition ( $\zeta > 1$ ) which produces no overshoots, to a dynamically unstable system (negative  $\zeta$ ), which grows in amplitude with every oscillation.

The ability to change only one airplane characteristic at a time is beneficial in helping a pilot or engineer to understand the effect that characteristic has on flying the aircraft. This capability is used throughout the variable stability syllabus to isolate the different properties of the classic response modes. For example, the Dutch roll mode of response is characterized by a frequency, a damping ratio, and a roll-to-yaw ratio. To show the importance of

Table 1 Test Pilot School Variable Stability Flights

<u>Aircraft</u>	<u>Flight #</u>	<u>School</u>	<u>Student*</u>	<u>Content</u>
Learjet	1	NTPS	Pilot/Pilot	Modes of Response, Test Inputs; Intro. to HQ Evals
	2	AFTPS, NTPS	Pilot/Engineer	Longitudinal statics & dynamics; Feel system characteristics; Practice HQ Evals (Long. only)
	3	AFTPS, NTPS	Pilot/Engineer	Lateral/Directional statics and dynamics; Practice HQ Evals (Lat/Dir only)
	4	AFTPS, NTPS	Pilot/Engineer	Review of Long./Lat./Dir. dynamics; Control System aspects; Practice HQ Evals (All axes)
	5	AFTPS, NTPS	Engineer/-	Review of all demonstrations with emphasis on pilot-in-the-loop feel
NCH-46A	1	NTPS	Pilot/-	Long./Lat./Dir. characteristics during hover
	2	NTPS	Pilot/-	Long./Lat./Dir. characteristics during forward flight
NT-33A	1	AFTPS	Pilot	Responses at higher accelerations, Advanced FCS's, Sidestick
	2	AFTPS	Pilot	HUD demonstration with format variations
	3	NTPS	Pilot	Advanced FCS's, Sidestick, HUD demonstration

\*In those aircraft equipped with a jumpseat two students are often flown on a single flight. The student listed first is at the fly-by-wire controls; the student listed second is in the jumpseat.

each of these characteristics by itself, two are held fixed while the third is changed through a wide range of values. At each demonstration point the response characteristic is first identified by checking the free response to a test input, and then the pilot performs a control task, such as air-to-ground tracking, to determine the effect of that parameter on pilot-in-the-loop performance.

A useful attribute of in-flight simulation to training demonstrations is the ability to exaggerate flight characteristics which are particularly subtle or difficult to observe without instrumentation. An example of one such characteristic which is demonstrated on the lateral/directional variable stability flights is an oscillatory roll rate ( $\rho_{osc}$ ), produced by the roll component of the Dutch roll mode superimposed on the first order roll mode response. To make this effect easily observable, a configuration is set with a large amount of adverse yaw due to lateral control as well as strong dihedral effect. When the pilot attempts to smoothly roll the aircraft from one angle of bank to another, the Dutch roll is excited and the desired roll rate, which the pilot is trying to hold constant, speeds up and slows down with every cycle of the Dutch roll.

Another advantage of demonstrating certain flight characteristics on an in-flight simulator is that difficult to fly, or even dangerous, configurations can be flown without risk. The variable stability aircraft can be taken off and landed as a normal aircraft with benign flight characteristics. It is only when at a safe altitude that the fly-by-wire system is engaged to demonstrate the unflyable configurations. Loss of control at this time causes minimal concern because either of the two pilots, or the automatic safety trip circuitry, can disengage the fly-by-wire system and instantly return control of the aircraft to the safety pilot. An example of such a demonstration is the effect of center of gravity location on longitudinal dynamics. During this demonstration the students are shown the effect of moving the center-of-gravity aft to the neutral point, the maneuver point, and finally far into the unstable region. This configuration provides the evaluation pilots with an appreciation of the benefits of positive static stability!

One area of aircraft flying quality characteristics which is difficult to appreciate from academic instruction alone is the significance of stick feel system characteristics. As with the dynamic response demonstrations, single characteristics of the pilot's artificial feel system are varied while all other properties remain fixed. This is done to show the strong influence that stick force, stick motion, control system friction, and break out forces have on a pilot's ability to perform a task with the aircraft. It is emphasized that these qualities can overshadow the significance of aircraft response and should not be considered to be secondary in importance. One demonstration that makes this point very clear is to provide the student test pilot with an aircraft which has excellent dynamics, a nominal stick force per g gradient, but with no stick motion. The pilot may even overlook the fact that the control stick doesn't move as he puts in his command

inputs. When told to perform an aggressive air-to-ground tracking task he quickly finds that he has difficulty in precisely controlling the aircraft, and that his inputs can lead to pilot-induced-oscillations.

These discussions have illustrated the benefits of demonstrating aircraft response and control characteristics using in-flight simulators. Because of their importance, over half of the variable stability flight time is dedicated to the demonstration role.

**Pilot Handling Quality Evaluations:** When we refer to 'handling qualities' we are concerned with the closed-loop, pilot-plus-vehicle system. The pilot, a non-linear, time-variant element in this system, uses a variety of feedback cues which affect his flight control inputs (Figure 3). Because of this he changes the overall system dynamics in a complex, often unpredictable way. His gain varies significantly from task to task and within a certain range his compensation can change to accommodate variations of the other elements in the pilot-airplane system. For these reasons a well-behaved type of response of the open-loop airplane can exhibit an entirely different character when the pilot is continuously applying control inputs to perform a task. The ultimate criteria for acceptable closed loop response is whether the pilot can perform the task with reasonable effort. This determination is made by performing a handling quality evaluation which produces a number, usually a Cooper-Harper rating<sup>6</sup> (Figure 4), indicative of the 'goodness' of the airplane's flight characteristics, and a set of pilot comments which expound upon the specific traits of the closed-loop aircraft system. Because of the importance of handling quality evaluations, techniques for performing them are taught at the test pilot schools. A large part of the variable stability program is therefore devoted to instructing the student test pilots on how to methodically perform concise and consistent handling quality evaluations.

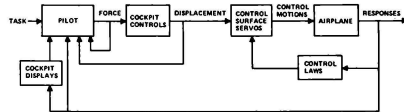


Fig. 3 The pilot-plus-vehicle dynamic system.

ADVISORY FOR SELECTED TASK OR REQUIRED OPERATION*	AIRCRAFT CHARACTERISTICS IN SELECTED TASK OR REQUIRED OPERATION*	DEMANDS ON THE PILOT IN SELECTED TASK OR REQUIRED OPERATION*	PILOT RATING
Is adequate without compensation?	Excellent	Pilot compensation not a factor for desired performance	1
	Good	Pilot compensation not a factor for desired performance	2
	Fair	Minor pilot compensation required for desired performance	3
	Major deficiencies	Desired performance requires moderate pilot compensation	4
Is adequate with a moderate pilot compensation?	Minor deficiencies	Desired performance requires moderate pilot compensation	5
	Major deficiencies	Desired performance requires moderate pilot compensation	6
	Major deficiencies	Desired performance requires moderate pilot compensation	7
	Major deficiencies	Desired performance requires moderate pilot compensation	8
Is adequate?	Minor deficiencies	Desired performance requires moderate pilot compensation	9
	Major deficiencies	Desired performance requires moderate pilot compensation	10
	Major deficiencies	Desired performance requires moderate pilot compensation	11
	Major deficiencies	Desired performance requires moderate pilot compensation	12

Fig. 4 Handling qualities rating scale.

Part of the process of learning to critique an aircraft's flight characteristics is exposure to aircraft which handle differently from the one or two aircraft the pilots are familiar with through their operational tours of duty. This broadening of experience is one of the basic instructional goals of a test pilot school, and is accomplished by giving the student test pilots the opportunity to fly a wide variety of aircraft - from gliders, transport aircraft and fighters, to a host of guest aircraft from all the services. The variable stability aircraft serve in this role as well, by providing widely varying handling qualities not available on any operational aircraft.

As the student test pilot gains exposure to a wide range of aircraft, he learns that the same piloting techniques cannot be used to fly each aircraft - some require more pilot compensation than others to produce the same precision of control. One of the hardest things to learn at this point is the ability to recognize and describe what is required of the pilot to fly a particular aircraft. By making use of the variable stability aircraft, flying qualities can be quickly changed, allowing the pilot to fly a new configuration while the old one is still fresh in his mind. This enables the pilot to more easily recognize how his own piloting techniques change from one aircraft to another. He is coached into describing these changes on each practice evaluation by referring to a pilot comment card which questions him about all aspects of the pilot-in-the-loop aircraft system. He must respond to queries about such things as the system's initial response, final response, tendency to overshoot, and the type of compensation required to obtain the desired results. As the student test pilot practices numerous evaluations throughout the variable stability program, a noticeable improvement in his ability to recognize and describe these aspects is readily apparent.

"Variable stability" instruction on the subject of handling qualities allows the students to practice using the full range of the Cooper-Harper rating scale. Configurations can be programmed which intentionally direct the student test pilot toward a particular segment of the scale. This can be used to clarify definitions on the card as well as to emphasize the method necessary to arrive at consistent pilot ratings. For example, an almost unflyable aircraft can be simulated which requires the pilot to determine the degree to which controllability is in question. The pilot's decision will then direct him to assigning a Cooper-Harper rating of either 7, 8, or 9. Likewise he can be provided with an aircraft configuration which has very good flying qualities, which forces him to work his way through the decision tree format of the Cooper-Harper scale to a rating of either 1, 2, or 3. Then he must determine if the aircraft has deficiencies and the magnitude of any minor deficiencies.

An enjoyable and educational exercise usually reserved for the later variable stability flights involves an evaluation of a poor aircraft design which is then 'fixed' as the exercise progresses. After the student test pilot evaluates the closed loop tracking performance of the configuration by assigning a Cooper-Harper rating and commenting on its deficiencies, he tries to identify characteristics which contribute to the poor pilot-

in-the-loop performance. These deficiencies are then fixed by changing gains in the variable stability system. The improved design is reevaluated and the whole process is repeated until an acceptable airplane results. The process provides practice in using the entire rating scale, describing the adverse closed loop characteristics, and relating the problems to possible open loop or control system characteristics which the student had observed during the demonstration phase of the variable stability syllabus.

**New Technology:** The last aspect of the Test Pilot School variable stability program which will be discussed is the use of the in-flight simulator aircraft to demonstrate new technology. This includes the Head-Up-Display (HUD) demonstration flights, the side stick controller demonstrations, and the demonstrations of different generic flight control system designs.

The NT-33A programmable Head-Up-Display can provide a display format similar to that of the F-18 HUD. Student test pilots, who have not flown HUD equipped aircraft, are thereby offered the opportunity to perform acrobatic maneuvers as well as approaches and landings using a HUD. Because the HUD format is programmable and can be varied in flight, the pilots can sample variations to the basic display format such as different pitch scalings, a fixed pitch marker versus a flight path marker, or a display caged in sideslip versus one which moves with sideslip. In the landing configuration the pilots can compare this conventional HUD format (Figure 5) to an innovative symbolic format (Figure 6) which presents instrument approach information without the use of numeric displays.

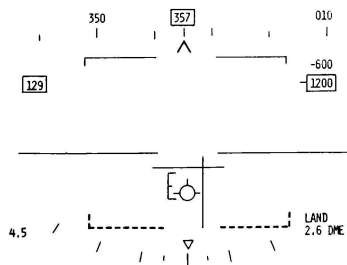


Fig. 5 Conventional HUD format.

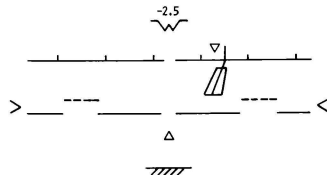


Fig. 6 Klopstein HUD format.



The NT-33A aircraft contains a side stick controller with variable feel capability in addition to a conventional center stick. Thus, the students are able to experience the generic feel of sidestick control for maneuvering tasks as well as for approach and landing. They can relate these experiences to characteristics attributed to aircraft such as the F16. The NT-33A variable stability flight also provides a demonstration of advanced flight control systems such as pitch rate command and g-command systems.

Finally, the Learjet incorporates an analog computer in which new forms of flight control system designs can be easily incorporated. This feature is currently used primarily for the special flight control design projects.

#### Special Projects

In addition to the routine variable stability flights in the Test Pilot School curriculums, special projects are performed by each TPS class using the variable stability aircraft. These projects are assigned to groups of student test pilots and test engineers late in their course of study as practical exercises requiring the students to draw from many areas of their test pilot school academic and flight instruction. To date, projects have been performed using the NT-33A, X-22A, and the Learjet variable stability aircraft. The Learjet projects have been concerned with the flight evaluations of student control system designs. The NT-33A projects have consisted of handling quality flight evaluations or Head-Up-Display evaluations. The X-22A projects have been concerned with the evaluation of HUD display formats during decelerating, descending approaches to a hover using microwave landing system (MLS) guidance. The X-22A program is discussed in a separate paper<sup>7</sup> and will not be covered here. The NT-33A and Learjet student projects will be discussed at some length since they make a significant contribution to the training provided by variable stability aircraft at the Test Pilot Schools.

AFTPS NT-33A Handling Quality Project: A handling quality evaluation project utilizing the NT-33A has been an integral part of the AFTPS syllabus for many years. A student team consisting of 2-3 flight test engineers and 2-4 test pilots from each class take part in the project. The topic of investigation is a relevant area of handling quality research approved by the Flight Dynamics Laboratory, who are sponsors of the project. Recent NT-33A project topics have included:

- An investigation of the lower Level 1 short period frequency boundary for center stick controlled aircraft with various stick force and deflection gradients<sup>8</sup>
- A comparison of center stick and side stick controllers<sup>9</sup>
- An investigation into variations of HUD flight director dynamics<sup>10</sup>
- The most recent project compares handling quality evaluations for various short period frequencies obtained in a ground simulator to those obtained in-flight in

the NT-33A. In both cases, an identical pitch tracking task consisting of step and ramp changes in commanded pitch attitude serves as the evaluation task.

After the general structure of the NT-33A project is specified to the student team, they design the experiment, write the test plan, prepare for the safety review board, and define the procedures to be carried out on each project flight. Throughout this period of preparation they are assisted by the AFTPS staff and by the Calspan engineering pilots.

Once the test configurations called for in the test plan are defined, the NT-33A variable stability system is calibrated to produce the desired aircraft dynamics and control system characteristics. When the aircraft arrives at Edwards AFB, the students fly calibration flights to verify these characteristics. In the process they gain practical experience in collecting and reducing flight data. Several flights may then be flown to familiarize the evaluation pilots with in-flight procedures and the evaluation tasks. Evaluation task procedures and criteria for 'desired' and 'adequate' performance are standardized so as to ensure consistency among evaluation pilots in their use of the Cooper-Harper rating scale.

The data collection phase of the project typically consists of twenty NT-33A flights. During this phase the student project engineers prepare flight cards for use by the NT-33A pilots and detailed comment cards describing what observations must be taken during each evaluation. A test matrix is constructed to ensure that the different configurations are distributed evenly among the evaluation pilots and throughout the data flights. Repeat evaluations of a configuration are given to each evaluation pilot to ensure that the pilots are consistent in their comments and use of the rating scale. The same configuration is also given to more than one pilot to check for standardization, or rating trends, among the different pilots. In this regard the Calspan safety pilot is useful in ensuring that each pilot performs the evaluation task in the same manner and with a similar level of aggressiveness. Periodically, an aircraft configuration with known good handling qualities is given to the evaluation pilots. This serves the purpose of recalibrating them to the way an aircraft with good flying qualities performs. Following the project data flights, the handling quality ratings are collated and analyzed. A written report is prepared which summarizes the test method and discusses the results.

NTPS NT-33A HUD Evaluation Project: A recent addition to the NTPS syllabus is an NT-33A flight to evaluate a Head-Up-Display. Several pilots in each class are assigned to this project. The pilots select for study either the conventional numeric display format (Figure 5) or the Klopstein format (Figure 6). They are then assigned the preparation of a comprehensive set of procedures to check the display in flight during approaches and landings. One sortie in the NT-33A is flown by each pilot to carry out the evaluation. During the flight they perform multiple instrument approaches and check such HUD features as field of view,

brightness, required head position, legibility of symbols, location of symbols, and ease of interpretation. Following the flight the student test pilots summarize their findings in a written report.

**AFTPS Learjet Flight Control System Project:** Two years ago the AFTPS added a unique project to their flight control systems course.<sup>11</sup> By using the variable stability Learjet as a control system testbed, a student design team can experience the complete aircraft flight control system design process. The project progresses from a specified set of airframe dynamics, to analysis and refinement of a set of flight control laws, through ground simulation, and finally to flight evaluation of the design in the Learjet.

The student test pilots and engineers are prepared academically for the design project by receiving classroom instruction in classical aircraft stability and control. Instruction in this area is aided by the use of the variable stability Learjet during routine curriculum flights. The students receive follow-on academic instruction in linear control theory and aircraft simulation. This leads up to the flight control systems course which completes the flying qualities sequence of academic instruction. The course emphasizes the effect of a flight control system on an aircraft's handling qualities. Instruction in various feedback strategies, control system elements, block diagram algebra, and test techniques are included in the course. The project then provides practical experience in the application of principles taught in these courses, through the analysis, simulation, and flight test of an actual flight control system.

To conduct the flight control system project, the AFTPS class is divided into four groups. Each group is provided with a guideline document which presents background information on the problem, lists general guidelines for working the problem, and provides recommended test procedures. Included in the document is the block diagram of a longitudinal flight control system for a hypothetical 'F-X' aircraft. The F-X airframe is statically unstable in the longitudinal axis and has dynamics similar to that of the unaugmented F-16. The F-X flight control system compensates for the instability, but is intentionally designed by the Test Pilot School staff to have significant handling quality defects. Figure 7 shows the F-X flight control system which was used on a previous student project. The student design teams are charged with improving the flight control system by changing gain values or selecting among several options which modify the structure of the control system. Completion of the control system design project consists of three phases - analysis, during which the augmented F-X dynamics are made to conform to handling quality specifications; ground simulation, which is used to refine the flight control system design and set the control sensitivities; and airborne simulation, during which the designs are flown and evaluated while performing approaches and landings.

The first phase of the project involves analysis of the original flight control system, and modification of gains or control system components.

Root locus, Bode, and time response analysis techniques are used to create an aircraft response which meets the short period requirements of the military handling quality specification<sup>12</sup> as well as the proposed bandwidth criteria.<sup>13</sup> Figure 8 shows the characteristics of the original F-X design and the four student designs plotted with respect to the Mil-F-8785C short period frequency and damping ratio requirements. Figure 9 shows the same designs plotted on the bandwidth criteria requirements.

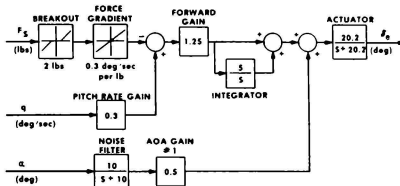


Fig. 7 Proposed F-X power approach flight control system configuration.

#### CONTRACTOR AND STUDENT CONFIGURATIONS PLOTTED AGAINST MIL-F-8785C REQUIREMENTS (CATEGORY C FLIGHT PHASE)

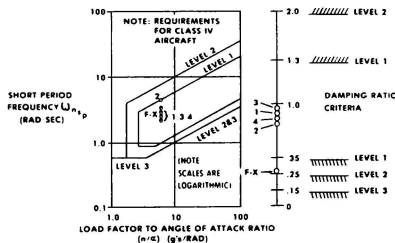


Fig. 8 Original and 4 group FCS designs plotted against MIL-F-8785C requirements (category C flight phase).

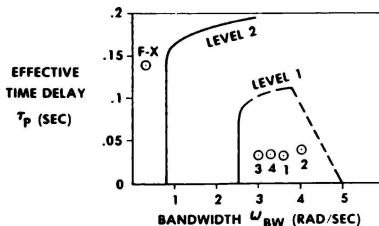


Fig. 9 Original and 4 group FCS designs plotted against bandwidth criteria (category C flight phase).

The second phase of the project consists of testing and refining the proposed student configurations on two ground simulators. Each group begins with the AFTPS fixed-point simulator to determine if their design has reasonably good flying qualities. This first simulation allows the students to adjust the control sensitivity characteristics, which cannot be accurately set using analysis alone. The design is then implemented on the AFPTC Simulator for Aircraft Flight Test Development (SAFTD) to further refine the design. On this more advanced simulator, the students are able to fly instrument approaches and perform more realistic tracking tasks than is possible using the AFTPS simulator.

The third phase of the project is airborne testing of the student designs in the variable stability Learjet. A generic longitudinal flight control system with all the design options made available to the students is programmed on a special analog computer in the Learjet. The gain values of the original F-X design as well as the four student designs are stored in the Configuration Control System for instant recall in flight. Each student test pilot on the project team receives a flight during which he evaluates his own team's design as well as several other designs. The evaluation tasks performed for each configuration consist of horizon tracking, an instrument approach, and a visual approach and landing. During the horizon tracking exercise the pilot moves the nose of the aircraft away from the horizon and then quickly and accurately tries to reacquire a particular aimpoint on the horizon. This is a fairly aggressive maneuver which enables the pilot to judge a configuration's pitch attitude predictability. The second evaluation task, of flying an instrument approach, allows the evaluation pilot to draw conclusions about the aircraft's flight path control. In addition the presence, or lack of, stick force cues due to airspeed changes can be evaluated during the approach. The visual approach task requires the pilot to land the aircraft within a specified distance on the runway, at a prescribed airspeed, and without excessive pitch attitude changes close to the ground. Because the pilot's gain tends to be higher in close proximity to the ground, any tendency of a configuration toward Pilot-Induced-Oscillations (PIO's) are most apparent during this last evaluation task. After all of the pilots complete their project evaluation flight, the Cooper-Harper ratings and comments received by the five designs are compared to determine the overall best design.

**NTPS Learjet Handling Quality Project:** This year a handling quality project for aircraft with advanced flight control systems has been added to the NTPS curriculum. The project team consists of three pilots and an engineer who prepare and execute a flight evaluation effort followed by an analysis of the evaluation results. The first phase of this project consists of in-flight evaluation of four different longitudinal flight control system designs during the approach and landing flight phase. Five evaluation flights are flown in the VSC Learjet. The evaluation task consists of pitch tracking at altitude, instrument approaches, and precise visual approaches utilizing the Fresnel lens visual landing system. Cooper-Harper ratings and pilot comments are used to evaluate each

aircraft configuration. The configurations simulated were chosen to test the characteristics of current flight control augmentation schemes such as pitch rate feedback with proportional plus integral forward path. The Learjet data collection flights teach the project team the importance of carefully structuring an evaluation program with well defined task and performance criteria.

After the handling quality data is collected the project team is provided with block diagrams, transfer functions, frequency response data and closed loop analyses for all the configurations. The students can then compare these data to a variety of criteria such as MIL-F8785C<sup>12</sup> as well as several alternate longitudinal criteria such as the Neal-Smith criteria<sup>14</sup> and the bandwidth criteria.<sup>13</sup> The flying qualities level that these criteria predict are then compared to the actual in-flight evaluation data. The students therefore gain an appreciation for the advantage of using more than one method of analyzing a flight control system design and the limitations of any particular analysis in predicting all aspects of an aircraft's handling qualities.

### Conclusions

In-flight simulation plays an important role in the training of test pilots and flight test engineers at the U.S. Naval and Air Force Test Pilot Schools. During the routine variable stability program they are exposed to a wide variety of aerodynamic and feel system characteristics which they would not otherwise be able to experience in the flight environment. Each of the demonstrated characteristics can be exaggerated to clarify the instruction, or changed individually to isolate their effect. Widely differing aircraft designs from nearly unflyable to excellent can be generated to provide practice in performing handling quality evaluations. Advanced concepts in flight control system design, and new airborne systems such as Head-Up-Displays can also be demonstrated to the evaluation pilots.

The special projects fulfill an equally important role in the test pilot's training. The nature of these projects require the students to draw on all their flight test training to analyze, design, and carry out the research projects or pilot evaluations. Because of the flexible nature of in-flight simulators, it is possible to provide a wide variety of project topics ranging from evaluations of aerodynamic, feel system, or cockpit display characteristics to analysis and design of advanced flight control systems.

### References

1. Knotts, Louis H.; Rogers E. Smith, "The Role of In-Flight Simulation in Aircraft Test and Evaluation," Conference on Simulation, NATC, Patuxent River, Md., March 1982.
2. Eulrich, B.J.; N.C. Weingarten, R.E. Bailey, "Capabilities of the NT-33A Variable Stability Aircraft," Flight Research Memorandum No. 558, Calspan Corp., Buffalo, N.Y., June 1982.
3. Brooks, Maj. William J.; Capt. James W. Smolka; LCDR R. Michael Norman; Arno E. Shelhorn, "Acceptance Testing of the Calspan Variable

- Stability Learjet," Society of Experimental Test Pilot's Symposium, Los Angeles, Ca., September 1981.
4. Miller, R.V., "Simulation at the U.S. Naval Test Pilot School," Conference on Simulation, NATC, Patuxent River, Md., March 1982.
  5. Ball, J.; C. Berthe; L. Knotts; M. Parrag; R. Smith, "Flight Syllabus and Background Material for the U.S. Air Force/U.S. Navy Test Pilot School Variable Stability Programs," Calspan Corp., Buffalo, N.Y., April 1981.
  6. Cooper, G.E.; R.P. Harper, "The Use of Pilot Ratings in the Evaluation of Aircraft Handling Qualities," NASA TN-D-5153, April 1969.
  7. Beilman, John L., "Indoctrination of Navy Test Pilots to Vectored Thrust Flight in the X-22A In-Flight Simulator," AIAA Flight Simulation Technologies Conference, Niagara Falls, N.Y., June 1983.
  8. Pearson, Maj. W.D.; Capt. T.J. Hudson; Capt. D.L. Weiss; Capt. W.G. Kuller, "Limited Evaluation of Longitudinal Flying Qualities of a Centerstick Controlled Aircraft with Various Stick Force and Deflection Gradients and Longitudinal Dynamics," USAF Test Pilot School, Edwards Air Force Base, Ca., November 1982.
  9. Smith, Capt. G.E.; et. al., "Limited In-Flight Handling Qualities Comparison of Centerstick and Sidestick Controllers in the NT-33A," USAF Test Pilot School, Edwards Air Force Base, Ca., December 1980.
  10. Rootman, Capt. Haim R.; et. al., "NT-33A Limited Display Evaluation Flight Test of Director Integrated Commands," USAF Test Pilot School, Edwards Air Force Base, Ca., May 1981.
  11. Engel, Maj. Richard L.; Capt. James W. Smolka; Louis H. Knotts, "Advanced Flight Control Instruction at the Air Force Test Pilot School," Society of Experimental Test Pilot's Symposium, Los Angeles, Ca., September 1982.
  12. Military Specification, Flying Qualities of Piloted Airplanes, MIL-F-8785C, 5 November 1980.
  13. Hoh, Roger H., et. al., Proposed MIL Handbook - Handling Qualities of Pilot Airplanes, Systems Technology, Inc., Hawthorne, Ca., December 1981.
  14. Neal, T.P.; R.E. Smith, "An In-Flight Investigation to Develop Control System Design Criteria for Fighter Airplanes," AFFDL-TR-70-14, Vol. I & Vol. II, December 1970.

Dr. Gerry Albers  
 Manager, Crew Systems Engineering  
 General Electric Company  
 Simulation and Control Systems Department  
 Daytona Beach, Florida

Training the multi-member crew in a single simulator creates a multi-faceted training problem. Each crew station must include the appropriate hardware and functional capability to train the respective crew member. However, the one aspect of multi-member training which is especially challenging is that which they all share in common; that is, the view of the outside world. This paper discusses the visual simulation system requirements which must be met to accommodate the needs of all crew members and it provides specific examples of how these needs can be met with today's visual simulation technology.

In this regard, the first thought is usually that of field of view (FOV). Each crew member may require simulated imagery to provide visual cues for his mission tasks. This may mean accommodating standing crew members as well as those seated. This does not necessarily require having imagery everywhere; it means having a cost-effective selection of mission related display capabilities. There are, however, other considerations just as important as field of view.

First of all, there is the scene content. Each crew member needs certain visual cues to realistically achieve his sortie objectives. These cues may be runway markings or VASI lights or power lines, roads, rivers, lakes, drop zones and even other aircraft. Furthermore, these cues must be correlated with other mission related cues such as navigation aids, radar, formation flight and station keeping equipment. A pilot, a copilot, and a navigator will all be looking for different visual cues for their respective parts of the mission. The data base must contain all of the cues for all of the crew members. However, if the data base contains only the essential cues the mission can become trivial. There must be a "context" in which the visual cues are placed. This context provides the realistic environment in which the crew trains. Hills, farms, roads, lakes and other real world artifacts may not appear on the navigational JOG chart but are an essential part of providing a realistic setting--a type of clutter from which checkpoint navigational information must be extracted.

Tactical operations are tending to be lower and lower--in altitude, that is, not in priority. Because of the threat of AAA and SAM's, a low level navigation route and tree-top ordnance and supply deliveries are now typical. To practice these missions in a simulator the visual system must have both the quality and quantity of surface features to make this difficult type of training effective. As the mission gets closer and closer to ground objects the ability of the crew to quickly judge altitude, distance and the rate of change of these parameters becomes extremely important. This concept leads to the

requirement for a great number of small artifacts and the ability to detect or resolve these details in the scene. The ability to resolve the important cues at an appropriate range must be supported by the image generator and the display--easily said but difficult to accomplish. Similarly, populating a scene with a sufficient amount of detail can be extremely costly, not only in terms of dollars, but in terms of system performance as well. Therefore, some cost-effective form of textural relief combined with a high resolution display is necessary so that the training missions can be flown as close to the ground as necessary.

Tactical air crews are a lot like physicians and lawyers--they keep on practicing until they get it perfect. None of them, however, can afford to keep practicing the same thing over and over again. There must be an adequate variety of mission profiles to challenge the air crew from the standpoint of departure and recovery points, routes and waypoints, delivery areas, and tactical situations. Furthermore, a drop zone is not likely to be close to the deployment area but more likely to be hundreds of miles away, much of which must be traversed at low altitude. Therefore, the size of the data base geographically and logistically plays a key role in practical air crew training.

A tactical operational need is a lot like a medical need--it doesn't wait for daylight or good weather to happen. Thus, bad weather and night operations are an essential part of a realistic training program. This places an added requirement on the visual simulation system, especially where night operations are concerned. Not only must it produce a wide dynamic range of brightness, hue and saturation, but it must be capable of producing realistic blackness. Now blackness, being the absence of light, might seem easy to achieve. But alas, it takes a lot of time (relatively) to take an amplifier or CRT out of cut-off (total darkness) into an operational state. Thus, if we are to produce runway lights, street lights and other point sources for the crew we must keep the CRT and its associated circuitry in a linear mode (and stable tool). In the past, whatever night scene the visual system could produce was acceptable; runway lights (the only lights that really mattered) tended to make the dark areas appear darker than they really were. However, the tactical air crew must be capable of flying into unlit and sometimes unprepared areas with and without landing lights. They must practice navigation, assaults and drops in as little as 5% moonlight, which amounts to an overcast, moonless night. The displays must exhibit an unusual dark level capability and the multiple display sources around the cockpit must have extremely good stability to ensure identical dark levels over long periods of time. Furthermore, it is necessary for some air crews to practice the use of special devices such as night vision goggles (NVG's). All of this amounts to specially designed visual system components, particularly the display.

\*Manager, Crew Systems Engineering  
 Member AIAA

Figure 1 summarizes the forementioned system requirements. Each one in its own right is a challenge to the visual system designer. When these items are taken in total, however, the task of training the Tactical Air Crew becomes an extremely great challenge. The recent development and installation of the C-130 Weapon System Trainer Visual System for the Military Airlift Command at Little Rock AFB is an outstanding example of how all of these requirements can be met with ingenuity and advanced techniques. Let's address these requirements individually and show examples of the solution in each case.

- Field of View
- Visual Content (Cues)
- Visual Context (Environmental)
- Visual Correlation (Nav/Radar/SKE)
- Textural Relief
- Resolution
- Geographic Size of Data Base
- Logistic Size of Data Base
- Realistic Night Operations
- Night Vision Goggle Capability

Figure 1 Visual System Requirements

Figure 2 illustrates the field of view which was determined to be a critical parameter in accomplishing the mission. Small gaps in this coverage were considered to be a rational trade-off, provided that essential areas were covered. Note the "T"-shaped coverage area at the side windows. During air drops and low altitude parachute extraction system (LAPES) maneuvers, the navigator must use the lower portion of this coverage to pick up timing panels and other ground references. The pilot (or copilot on the right side) must use the middle display coverage enroute and the upper coverage in the traffic pattern. Since these requirements were not simultaneous, they could be addressed serially by a moveable display. Figure 3 shows the pilot's side of the C-130 simulator with the moveable display (first display from the right) located in the No. 2 (mid-range) position. During selected portions of the mission, the display is moved to the appropriate position for the upcoming leg and the image generator "view window" definition is adjusted accordingly. This task is accomplished from the instructor's console and takes about one minute. The net result is a six window display system with 10 window positions--an exceptionally cost-effective solution to a tough problem.

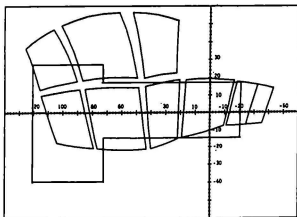


Figure 2 C-130 FOV Requirements, Pilot's Side

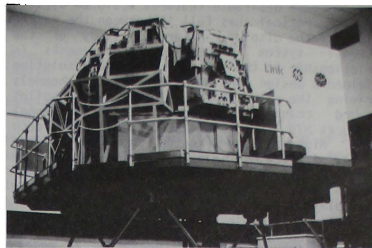


Figure 3 Moveable Display, Pilot's Side of C-130 Simulator

The C-130 visual data base could be anywhere in the world but has been initially set up around the Little Rock AFB area. In order to ensure radar simulation correlation, Defense Mapping Agency (DMA) data was used to generate the data base. Even so, it had to be supplemented with key ground references from navigational JOG charts. In order to efficiently create these "contextual" and environmental embellishments, a library of universal features was created and employed to give the user frequent occurrences of houses, barns, trees and other likely visual effects. These universal features could be quickly and easily placed in the data base anywhere, in any orientation, size and color. This is an extremely useful tool for cost-effective data base generation.

For quite some time, the effect of texture has been well understood but unattainable in visual simulators on a realistic basis. Stripes and lines could be modeled in the scene in order to break up large fields and hillsides but at the expense of the overall system performance. One of the most significant CIG techniques developed was that of hardware generated texture. Each CIG face has certain information associated with it such as its color; now a texture code has been added which keys circuitry in the output stages of the image generator. Therefore, a highly textured runway, as illustrated in Figure 4, greatly improves scene quality and mission capability without loading the system down in any way.



Figure 4 Hardware Generated Texture Patterns on Runway

All of these desirable features would be useless if the critical cues fell in between the raster lines of the display. A careful study of the overall system processing requirements in relationship to the field of view and resolution yielded a design consisting of five CIG channels driving the six windows (pilot and copilot forward channels are common). Each channel produces 875 lines with 1000 pixels on each line. High quality (Kratos) monitors are the sources for the infinity displays which have individual fields of view ranging from 30° X 40° to 36° X 48°. These design criteria resulted in a display with better than 2.7 arc minutes of resolution and six foot Lamberts of brightness covering nearly 12,000 square degrees of the field of view.

As mentioned above, the training area could be anywhere in the world but is presently located near Little Rock AFB so that crews can quickly transition from simulator to real world. In order to accommodate the need for a realistic mission in length, variety and flexibility, the data base covers an irregular area encompassing a total of over 33,000 square nautical miles! Please realize that this is highly detailed terrain, any part of which could be used for low level navigation. There are three airstrips including Little Rock AFB itself, five drop zones, a combat training zone, an infinite variety of routes and waypoints and seven independent moving models. Incidentally, the visual simulator system provides one thing that central Arkansas does not--active SAM and AAA sites.

Many of the above mentioned requirements and their associated solutions are illustrated in Figures 5, 6 and 7. The aspects of visual content, visual context, textural relief, resolution and data base geographic size and logistics become apparent when these scenes are observed. Figure 8 illustrates a few of the attributes of the C-130 night scene capability. The original CRTs in the Kratos displays were replaced during the initial operational phase with newly designed Panasonic tubes. With this change, the improvement in night-time scene quality was no less than dramatic. Stability, power consumption and dark level all improved significantly. The uniform, night-like quality of the display system now permits the use of night vision goggles with realistic effect. Figure 8 illustrates some of the dynamic range of this display from the pitch-black sky through the horizon glow to the highly illuminated runway. The realistic landing light simulation was also a significant development on this program.

The C-130 system at this writing is undergoing the final stages of the USAF final operational test and evaluation (FOT&E) process. The system is scheduled 7 days a week to provide enhancement of the data base, training and testing of the device, and has received a high degree of pilot acceptance, primarily due to the improvement in flight hour efficiency that is being achieved.



Figure 5 Rural Area illustrating Visual Context, Textural Relief and Data Base Geography

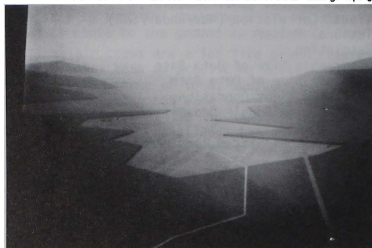


Figure 6 Approach to Drop Zone illustrating Visual Context, Textural Relief, and Data Base Geography



Figure 7 Combat Training Zone illustrating Visual Context, Textural Relief, Resolution, and Data Base Logistics



Figure 8 Night Runway Scene illustrating Dark Level Point Source Response of Display along with Landing Light Effect

Greg L. Zacharias\*, Alper K. Caglayan\*, John B. Sinacori\*\*

\*Bolt Beranek and Newman, Inc.  
Cambridge, MA 02238\*\*J.R. Sinacori Associates  
Hollister, CA 95023

### Abstract

A model is described to account for the pilot's processing of visual flow-field cues, during low-level flight over uncultured terrain. The model is predicated on the notion that the pilot makes noisy, sampled measurements on the spatially distributed visual flow-field surrounding him, and, on the basis of these measurements, generates estimates of his own linear and angular terrain-relative velocities which optimally satisfy, in a least-squares sense, the visual kinematic flow constraints. A subsidiary but significant output of the model is an "impact time" map, an observer-centered spatially-sampled scaled replica of the viewed surface. Simulation results are presented to demonstrate the potential for modelling relevant human visual performance data, and for evaluating candidate simulator configurations, in terms of expected impact on the perceptual performance of the terrain-following pilot. Additional model applications are discussed, including interfacing with other human performance models and modelling other types of visually-driven human task performance.

### Introduction

The current trend towards visual "stimulus realism" in flight simulators has been made possible by rapid advances in computer generated image (CGI) technology. Because of its appeal, we see a continuing trend in this direction, but it is not at all clear to us that such a strategy will guarantee effective training at reasonable cost. We see, for example, efforts directed toward development of 200,000 polygon systems [1], when it is possible that a more "cartoon-like" image will focus a trainee's attention on the critical task cues, and result in more rapid training and efficient transfer. Even if enhanced training is not achieved with such an impoverished (but directed) display, it may be possible to achieve significant system cost savings, and thus improve overall simulator cost-effectiveness, if not absolute level of training effectiveness. In short, we are skeptical of the ultimate efficacy of full visual stimulus realism for training.

The development of effective "non-realistic" displays requires, of course, an understanding of not only human visual processing capabilities and limitations, but also an understanding of "downstream", task-related capabilities (such as flight control), as well as learning behavior in training situations. We recognize that research advancements in these areas have not kept pace with the technological advances in CGI systems, and that the resulting "knowledge vacuum" is perhaps as

responsible for the trend towards realism as is the supporting technology itself. This trend, however, does not obviate the need for pushing forward in our effort to understand the pilot's perceptual capabilities.

To this end, we have undertaken an effort directed at understanding human visual processing in one specific flight task: terrain-following flight. We have deliberately limited the domain of applicability to assure a reasonable probability of success in modelling the processing function; we have chosen the specific flight task both on the basis of its current operational relevance and on its potential for tractable functional modelling.

### Terrain-Following Flight

Terrain-following flight is performed when entering or leaving air space containing ground-to-air threats. The intent is the timely movement toward an objective while using the terrain for masking. This difficult and dangerous task results in high crew workload, and demands a continuing awareness of one's own position and velocity with respect to the ground.

An informal review of "classical" visual cueing mechanisms [4] identifies few candidates which might subserve the required terrain-relative positioning function. The "apparent/familiar size" mechanism can provide cues to absolute distance, but in uncultured terrain with tree, shrub, and grass cover, there are few, if any, objects that are familiar enough to support absolute distance estimation. A further examination of real terrain samples for interposition, texture density, and texture gradient cues showed us that these were strikingly weak and/or sparse also. Furthermore, while shading effects and aerial perspective effects are commonly seen, they are not associated with mechanisms that permit the perception of absolute distance; also, flight at low level is easily performed without them.

It is well-known, however, that pilots are able to fly low-level over unfamiliar terrain that they have never seen before. Indeed, they report no unusual difficulty except over "unfavorable" terrain, such as snowscapes, desert sand dunes, and open, glassy water. This suggested to us that visual texture was an important factor. Since the static attributes of texture density and texture gradient did not appear to us to adequately subserve the required distance cueing function, we

---

\*devoid of man-made objects

† This work was performed under USAF Contract F33615-81-C-0515; technical monitor was Dr. Grant R. McMillan of USAF AMRL.



turned our attention to the dynamic attributes of visual texture, or the "flow-field".

### Flow-Field Cueing

Flow-field cues arise when an observer moves through a fixed visual world, causing lines-of-sight to viewed objects to change dynamically in response to the changing geometry between observer and object. These lines-of-sight, and their corresponding rates-of-change, define the observer's visual flow-field: a dynamic "map" which reflects the observer's translational and rotational motion with respect to the static visual world. Our concerns here are not so much with the generation of this map, but rather with the use of the information implicit in it relevant to the pilot's requirement for ongoing terrain-relative positioning information.

Gibson's early pictorial representation [4] of the flow-field initiated a series of studies directed at a better understanding of the field characteristics. These studies (summarized and critiqued in detail by Warren [20]) provide significant insight into the basic cueing problem, but are limited by a lack of (mathematical) formalism and/or generality. Thus, some deal only with field speed and fail to recognize field velocity as a vector quantity (e.g., [8], [21]); some present mathematically incorrect results (e.g., [6]); some are restricted to the viewing of a single flat plane in the visual field (e.g., [5], [7]); and most are restricted to considering only non-rotating rectilinear observer motion (e.g., [5], [8], [11], [21]).

More recent work has focused on determining the flow-field's "informational content", and how to extract it. Several studies have demonstrated, in principal at least, that flow cues alone can be used to determine not only observer (translational and rotational) velocity with respect to a fixed visual world, but also the geometric shape of that world. However, these studies also suffer from various shortcomings. Specifically, some deal only with non-rotating rectilinear motion (e.g., [3]); some tie a proposed algorithm to a specific projection geometry (e.g., [9], [18]), when, in fact, the flow-field is independent of projection planes; some demand advanced computational capabilities for accomplishing what appears to be a relatively straightforward estimation function (e.g., using first and second spatial gradients of the flow-field to estimate surface shape [3], [9], [14] when an interpolated "impact time" surface would seem to do as well); some focus concern on the "observability" or "solvability" of impoverished visual scenes having few visual objects (e.g., [16], [18]); when, in fact, most non-contrived scenes are likely to be characterized by an object count which is many orders of magnitude larger than the minimum required; and, finally, most fail to deal with the fundamental issue at hand: making accurate and reliable motion/surface estimates with what we know will be "noisy" flow-field cues.

We have thus directed our attention to the development of a model of flow-field cue processing, centered on a computational approach designed to overcome most of the above

shortcomings. Our goal is for it to be quantitative, applicable to general viewing geometries and observer motions, independent of projection geometry, and rational in its treatment of "redundant" and "noisy" flow-field cues. Our motivation stems from the terrain-following flight problem, but we are optimistic that such an approach has applicability to the larger family of viewer locomotion problems. We thus summarize here the preliminary results of this effort.

### Definition of Flow-Field

We begin our definition of the flow-field by assuming that the external visual world can be modeled as an array of fixed, rigid, and opaque surfaces, which may or may not be connected together in some fashion to form visual "objects". Thus, the visual world may be a single surface, such as the rolling ground plane viewed by a pilot flying low-level over the desert, or it may be a complex of connected flat surfaces, such as the array of building faces one might encounter in the center of a city.

For an observer moving with respect to this visual world, the problem geometry is as illustrated in figure 1. The observer's position  $P$  is referenced to a surface-fixed coordinate system, as are his linear and angular velocities,  $\underline{v}$  and  $\underline{\omega}$ . He is shown "viewing" a point on the surface  $P_1$ , defined by an observer-relative position vector  $\underline{\rho}_1$ , and an associated unit-length line-of-sight (LOS) vector,  $\underline{u}_1$ , where

$$\underline{u}_1 = \underline{\rho}_1 / \rho_1 \quad (1)$$

In the observer's frame of reference, this LOS vector will appear to change with time, at a rate given by

$$\dot{\underline{u}}_1 = \underline{\omega}_1 \times \underline{u}_1 \quad (2)^{**}$$

where the apparent rotation rate is given by [22]

$$\underline{\omega}_1 = \underline{u}_1 \times (\underline{u}_1 \times \underline{\omega}) - \frac{1}{\rho_1} (\underline{u}_1 \times \underline{v}) \quad (3)$$

which reflects the fact that the observer is both translating and rotating with respect to the fixed visual world.

We can consider the visual "flow" associated with a single point  $P_1$  and LOS vector  $\underline{u}_1$  to be simply the associated LOS rate vector  $\dot{\underline{u}}_1$ . The vector couple  $(\underline{u}_1, \dot{\underline{u}}_1)$  thus defines single point location and flow. By direct extension, the "flow-field" associated with a set of  $N$  viewed points can be defined by the set of  $N$  corresponding LOS and LOS rate couples, or  $\{(\underline{u}_i, \dot{\underline{u}}_i); i=1, \dots, N\}$ . As  $N$  increases, this spatially-sampled field gradually approximates our intuitive notion of a (spatially continuous) visual flow-field.

\* In this case, the conventional north-east-down local navigation frame.

\*\* We denote the magnitude of a vector  $\underline{r}$  by  $r$ .

Figure 2 gives a perspective rendition of the visual flow associated with observer motion over flat (textured) terrain, horizon, and (untextured) sky.

For simple translation (with no rotation), figure 2a shows the zero flow rate "expansion point", whose associated LOS vector is collinear with the observer's linear velocity vector  $\underline{v}$ . The "flow" of every other point  $P_i$  is radially outward from this expansion point\*, with a flow rate given by the magnitude of the corresponding LOS rate vector, or, from (3):

$$\omega_i = \left| -\frac{1}{\rho_i} (\underline{u}_i \times \underline{v}) \right| = \frac{v}{\rho_i} \sin \beta_i \quad (4a)$$

where  $\beta_i$  is the eccentricity of  $P_i$  relative to the expansion point (i.e., the included angle between  $\underline{u}_i$  and  $\underline{v}$ ). Thus, an observer undergoing pure translation sees a radial flow-field, where flow rate increases with expansion point eccentricity.

For simple rotation (with no translation), figure 2b shows the zero flow-rate "rotation point", whose associated LOS vector is collinear with the observer's angular velocity vector  $\underline{\omega}$ . The "flow" of every other point  $P_i$  is normal to the corresponding radial which emanates from this rotation point\*, with a flow rate again given by the magnitude of the corresponding LOS rate vector, or, from (3):

$$\omega_i = \left| \underline{u}_i \times (\underline{u}_i \times \underline{\omega}) \right| = \omega \sin \beta_i \quad (4b)$$

where, in this case,  $\beta_i$  is the eccentricity of  $P_i$  relative to the rotation point (i.e., the included angle between  $\underline{u}_i$  and  $\underline{\omega}$ ). Thus, an observer undergoing pure rotation sees a circumferential flow field, where the flow rate increases with point eccentricity.

Even with these simple constrained motions, the flow-field can show considerable richness and complexity. For example, a simple dive towards flat terrain can give rise to a complex distribution of flow rates within the field-of-view, and this distribution, in turn, will be a sensitive function of the dive angle itself [22]. Likewise, straight-and-level flight over hilly terrain can result in very complicated flow patterns; a graphic example is provided in [2]. Finally, if we consider combined translational and rotational motions associated with normal aircraft maneuvers, we can generate corresponding flow-fields which undergo dramatic and complex "deformations" over the course of the maneuver,

\*This assumes observer motion is toward the surface being viewed; if away, flow will be radially inward toward the "contraction point".

\*\*Clockwise flow is illustrated, under the assumption that the observer is undergoing a left roll ( $\underline{\omega}$  out of page); counterclockwise flow would result from an oppositely-directed rotation.

even for simple maneuvers conducted over flat terrain [22].

The potential complexity associated with these and other factors suggests that any self-motion estimator based on flow-field pattern recognition is likely to fail, except for fairly trivial and artificially constrained cases. Although qualitative discussions of flow-fields and their interpretation in terms of the generating self-motion are useful in providing insight into the cueing situation, it does not appear that such an approach can provide a quantitative basis for self-motion estimation, given the wide scope of potential field patterns one might encounter during terrain-following flight. We are thus motivated to adopt a strategy which does not focus on flow-field patterns, per se, but rather on local flow-field measurements; measurements which directly reflect the observer's motions through the cueing geometry involved.

#### Proposed Visual Cue Processing Strategy

We can specify a measurement strategy by assuming, quite simply, that the observer is limited to making only angular measurements on the visual world, and hence, on the flow-field. In particular, we assume that he can measure, for each visible point  $P_i$ , only the LOS vector  $\underline{u}_i$ , and its angular rate of change,  $\dot{\underline{u}}_i$ . We specifically assume he is incapable of measuring the relative point range  $\rho_i$ .

For an N-point measurement set, the observer's self-motion estimation problem then becomes one of "solving" the set of N LOS rate equations given by (3), for the (unknown) linear and angular observer velocities,  $\underline{v}$  and  $\underline{\omega}$ , and the (N unknown) relative point ranges  $\{\rho_i\}$ , given the (N known) visual LOS measurement couples  $\{\underline{u}_i, \dot{\underline{u}}_i\}$ .

Direct inspection of (3) shows that it is not possible to "solve" for the unknowns  $\underline{v}$  and  $\dot{\underline{u}}_i$ , since they enter only as the ratio  $(\underline{v}/\rho_i)$ , and thus can be known only to within a common scale factor. This motivates the introduction of two new unknowns, a heading vector  $\underline{u}$  and an "impact time"  $\tau_i$ , defined for a non-stationary observer by:

$$\underline{u} \equiv \underline{v}/v \quad ; \quad \tau_i \equiv \rho_i/v \quad (5)$$

The unit-length heading vector thus defines only the direction of the observer's motion, but not his speed. The impact time is so named because this would be the elapsed time before observer impact with the surface at point  $P_i$ , if the observer were to head directly at  $P_i$ , at his current speed  $v$ .

These variables allow us to express the  $(\underline{v}/\rho_i)$  ratio of (3) as:

$$(\underline{v}/\rho_i) = (v/\rho_i)\underline{u} = (1/\tau_i)\underline{u} \quad (6)$$

Clearly, this term will be determined by the  $(\underline{u}, \tau_i)$

\*For a stationary observer,  $v$  is zero, and these variables are undefined. This (degenerate) case is treated in more detail in [23].

values, and will be indifferent to the particular  $(\underline{u}, \rho_i)$  values, as long as they vary according to:

$$\underline{v} = c\underline{u} \quad ; \quad \rho_i = c\tau_i \quad (7a,b)$$

where  $c$  is an arbitrary (positive) common scale factor. The observer-related unknowns of absolute velocity and point range  $(\underline{u}, \rho_i)$  are thus fundamentally "non-observable" from the flow-field measurements alone; we are consequently motivated to focus our attention on the flow-related unknowns of heading and impact time  $(\underline{u}, \tau_i)$ .

With the definitions for  $(\underline{u}, \tau_i)$  given by (5), the measurement equation (3) becomes

$$\tau_i (\underline{A}_i \underline{u} + \underline{\omega}_i) = \underline{u} \times \underline{u}_i \quad (8)$$

where we have introduced the  $(3 \times 3)$  rotation matrix

$$\underline{A}_i \equiv \underline{I} - \underline{u}_i \underline{u}_i^T \quad (9)$$

where  $\underline{I}$  denotes the  $(3 \times 3)$  identity matrix, and the superscript  $T$  denotes a transpose. The observer's motion estimation problem thus becomes one of solving the set of  $N$  LOS rate equations given by (8), for the unknown heading and angular velocity,  $\underline{u}$  and  $\underline{\omega}$ , and the  $(N)$  unknown impact times  $\{\tau_i\}$ , given the  $(N)$  known visual LOS measurement couples  $\{\underline{u}_i, \underline{\omega}_i\}$ .

The structure of this three-dimensional vector measurement equation becomes clearer by decomposing it into its three scalar components. If we choose an orthogonal coordinate system defined by the point-specific orthonormal triad  $(\underline{u}_i^L, \underline{u}_i^M, \underline{u}_i^N)$ , where

$$\underline{u}_i^L \equiv \underline{u}_i \quad ; \quad \underline{u}_i^M \perp \underline{u}_i^L \quad ; \quad \underline{u}_i^N \equiv \underline{u}_i^L \times \underline{u}_i^M \quad (10)$$

then (8) can be decomposed into three L-, M-, and N-axis scalar equations [22]:

$$\text{L:} \quad 0 = 0$$

$$\text{M:} \quad \tau_i = (\underline{u}_i^N \cdot \underline{u}) / \underline{u}_i^M \cdot (\underline{\omega} + \underline{\omega}_i) \quad (11a,b,c)$$

$$\text{N:} \quad \underline{u} \cdot (\underline{A}_i \underline{\omega} + \underline{\omega}_i) = 0$$

Thus, the vector measurement equation is equivalent to: a) a trivial identity; b) an impact time equation which defines  $\tau_i$  in terms of the other variables; and c) a "residual" measurement equation constraining the observer velocity states  $\underline{u}$  and  $\underline{\omega}$ . This separation of the point-dependent unknown,  $\tau_i$ , from the point-independent unknowns,  $\underline{u}$  and  $\underline{\omega}$ , immediately suggests a stepwise solution: first, by some means, "solve" the  $N$  measurement residual equations of (11c), for  $\underline{u}$  and  $\underline{\omega}$ ; then, with these

\*These joint constraints are of course central to the design of any terrain-board visual simulation: the speed scale factor used in driving the camera gantry,  $c_{\text{gantry}}$ , must closely match the terrain map scale factor,  $c_{\text{map}}$ , if the flow-field cueing seen by an in-simulator pilot is to closely match that seen by an in-flight pilot.

and the triad vectors found from (10), directly compute a  $\tau_i$  for each of the  $N$  viewed points, using (11b).

Once impact time is found in this manner, we can compute a corresponding impact time vector, from:

$$\underline{\tau}_i \equiv \tau_i \underline{u}_i \quad (12)$$

From (1) and (5), this is merely the speed-scaled observer-relative range vector to the viewed surface  $(\rho_i/v)$ . Thus, the set of impact time vectors  $\{\underline{\tau}_i\}$  provides us with an observer-centered spatially-sampled and scaled replica of the viewed surface. Simply stated, viewed surface shape is potentially available from the flow-field cues.

### Least-Squares Estimator

Since computation of the impact time map is straightforward once we know  $\underline{u}$  and  $\underline{\omega}$ , the basic estimation problem reduces to finding a solution  $(\underline{u}, \underline{\omega})$  to the  $N$  residual equations of (11c), an overdetermined equation set in any normal viewing situation (where  $N$  is normally very large). Since there will be errors in the measurements  $(\underline{u}_i, \underline{\omega}_i)$ , this equation set will not be satisfied exactly, and, in fact, will take on the form:

$$\underline{u} \cdot (\underline{A}_i \underline{\omega} + \underline{\omega}_i) = \epsilon_i \quad (13)$$

where  $\epsilon_i$  is the measurement residual associated with the  $i$ th measurement couple  $(\underline{u}_i, \underline{\omega}_i)$  and the estimate  $(\underline{u}, \underline{\omega})$ . The set of  $N$  residuals thus provides a natural measure of how well the single estimate fits the  $N$  "noisy" measurements. With this view of the problem, we are thus motivated to take a least-squares approach, and generate an estimate which minimizes the sum of the squared residuals, by choosing  $(\underline{u}, \underline{\omega})$  to minimize the cost  $J$  where

$$J \equiv J(\underline{u}, \underline{\omega}) \equiv \frac{1}{2} \sum_i \epsilon_i^2 \quad (14)$$

where, from (13)

$$\epsilon_i \equiv \underline{b}_i \cdot \underline{u} \quad ; \quad \underline{b}_i \equiv \underline{A}_i \underline{\omega} + \underline{\omega}_i \quad (15a,b)$$

A graphical interpretation of this formulation of the problem is given in figure 2, which we used earlier to illustrate two simple flow patterns arising from uncoupled observer motion over flat terrain. The radial flow pattern of figure 2a suggests that the expansion point (or heading vector  $\underline{u}$ ) may be estimated from the intersection point of a number of backwards-traced flow vectors. Figure 2c shows how this might work for a three-point noisy measurement case. Errors in specifying point location (LOS  $\underline{u}_i$ ) and flow rate (LOS rate  $\underline{\omega}_i$ ) preclude a single point intersection of the three extended flow vectors, or "flow-lines"; instead, we obtain a triangular region of uncertainty. As shown, any estimate will, in general, be some residual distance away from each of the three flow-lines. A reasonable estimation strategy would then

\*The summation ranges from 1 to  $N$ .

choose the estimate to minimize some joint metric of the residuals: the sum of the squared distance residuals naturally comes to mind. Since it is a direct matter to show that the distance residuals are proportional to the measurement residuals of (13), minimizing the cost  $J$  of (14) becomes roughly equivalent to choosing a heading estimate which is "optimally near" all of the observed flow-lines, in a least-squares sense.

The circumferential flow pattern of figure 2b suggests a similar strategy for estimating the rotation point, here based on the intersection of the flow radials normal to the flow vectors themselves. Again, it is straightforward to show that this strategy (illustrated in figure 2d) yields distance residuals which are proportional to the measurement residuals of (13), so that minimizing  $J$  in this situation is roughly equivalent to finding a rotation estimate which is "optimally near" all the flow radials. Note, however, that this graphic strategy provides no direct means of inferring total angular velocity  $\underline{\omega}$ , but only spin direction  $\underline{\omega}/\omega$ . Additional features of the field must be considered to estimate spin magnitude.

This discussion has attempted to provide a graphical interpretation of the formal minimization problem we introduced with (14). It should be recognized that the illustrations presented here have been limited to simple uncoupled observer motion (pure translation or pure rotation), have considered only a 3-point measurement solution, rather than the general  $N$ -point solution, and have lacked somewhat in rigor, because of the use of perspective geometry projections in place of a more appropriate projection-free spherical geometry representation. The formal minimization problem, of course, suffers from none of these limitations.

We have thus specified a least-squares estimator, which generates an estimate  $(\underline{u}, \underline{\omega})$  to minimize the sum-squared measurement residual cost function of (14). The particular method by which this minimizing estimate is generated formally defines the estimator, but we will not go into the details here as these are covered in [23] and [24]. We will note, however, that the estimator "solves" the  $n$ - $N$ -linear constrained least-squares problem by direct minimization of the residual cost. It does this recursively by, in effect, taking alternating minimizing steps in the individual  $\underline{u}$  and  $\underline{\omega}$  solution subspaces, to arrive at a total solution  $(\underline{u}, \underline{\omega})$  which globally minimizes the residual cost. Because the algorithm depends on simple matrix functions (e.g., inverse, eigenvalue) which operate on matrices no larger than  $(3 \times 3)$ , convergence of the algorithm is rapid and reliable.

It is worth noting again that once we have obtained an estimate  $(\underline{u}, \underline{\omega})$ , we are then in a position to directly calculate, from (11b) and (12), the set of impact time vectors  $\{\underline{t}_i\}$ . As noted, these define an observer-centered spatially-sampled and scaled replica of the viewed surface. Because of noise in the measurements  $(\underline{u}_i, \underline{\omega}_i)$  and

errors in the estimates  $(\underline{u}, \underline{\omega})$ , the impact time vector set, and thus the impact time surface, will be a noisy approximation to a perfect surface replica. The accuracy of the approximation will of course depend on the level of the driving measurement noise and the viewing geometry.

Figure 3 illustrates the construction of this map, for the special case in which an observer is flying straight-and-level over rolling terrain. Figure 3a sketches the viewing geometry, in the plane containing  $\underline{y}$  and the position vector  $\underline{r}_i$  to the  $i$ th viewed point  $P_i$ . The heading eccentricity  $\beta_i$  is determined from the LOS  $\underline{u}_i$  and the estimated heading  $\underline{u}$ ; eccentricity rate  $\dot{\beta}_i$  is the flow rate and is determined by (3), which, from (4a), simplifies to the expression shown. From this we can solve for the impact time  $\tau_i$ , which, with  $\underline{u}_i$ , lets us compute the impact time vector  $\underline{t}_i$ , as shown.

Figure 3b sketches the situation for a number of coplanar viewed terrain points, each associated with an observer-referenced position vector  $\underline{r}_i$ . For each we can compute, via the process just outlined, an impact time vector  $\underline{t}_i$ . The resulting "map" of this set  $\{\underline{t}_i\}$  is shown in figure 3c. Note that each terrain point  $P_i$  becomes a projected point  $P'_i$  in impact time space, although perfect registry of the two point sets is precluded by errors in the estimated vector set  $\{\underline{t}_i\}$ , due to flow-field measurement errors. Note also that we have indicated in figure 3c, via a solid line, an interpolated or continuous impact time surface; such interpolation naturally requires some sort of surface model, a modelling issue which goes beyond the scope of the estimation problem under discussion.

#### Simulated Estimator Performance

The performance of the estimator has been investigated through digital simulation. We present here some preliminary results which demonstrate estimation performance trends over various problem factors of interest.

Noisy observation of the visual flow was simulated by additive measurement noise corrupting the LOS measurement vector couple  $(\underline{u}_i, \underline{\omega}_i)$ . Vector noise magnitudes were normally distributed with zero mean; directions were uniformly distributed, with the LOS noise constrained to ensure a unit-length "noisy" measurement vector. Standard deviation (SD) of the LOS noise magnitude,  $\sigma_{\omega_0}$ , was set at 1 mrad, based on human static threshold considerations [17]. The SD of the LOS rate noise magnitude,  $\sigma_{\omega_1}$ , was defined as a composite of a fixed value and a value proportional to actual LOS rate  $\omega_i$ , or

$$\sigma_{\omega_1} = [\sigma_{\omega_0}^2 + (f\omega_i)^2]^{1/2} \quad (16)$$

where  $\sigma_{\omega_0}$  was set at 1 mrad/sec, and the rate noise/signal (N/S) ratio  $f$  was set at 10% or -20dB, based on human dynamic threshold considerations [17].

Results presented here were obtained by computing the ensemble statistics of the estimation errors, across 100 Monte Carlo simulation runs.

\*For small residuals.

## Sensitivity to Display Parameters

Simulations were conducted for a pilot flying straight-and-level at 400 kts 100 ft above flat featureless textured terrain. Out-the-window field-of-view (FOV) was nominally limited to  $\pm 24$  deg laterally, 24 deg down, and 12 deg up. A finite distance horizon was modelled, to keep the textural point count finite; this distance was about 3500 ft, based on an assumption of a maximum 5 sec preview or "look-ahead" distance. A number of surface decoration and visual sampling strategies were studied; the results shown here assume the observer visually samples the terrain surface in such a manner as to ensure that the resulting LOS vectors are uniformly spherically distributed over the solid angle subtended by the viewable terrain.

Figure 4 shows the standard deviation of the error in estimated heading or "aim point",  $\Delta$ . Error trends with N, the number of points viewed, are sketched in, for lateral (left/right) error, vertical (up/down) error, and total error. As might have been expected from the least-squares structure of the estimator, significant error reductions are to be had as viewed point count N increases over the range from 10 to 1000. Note however that the rate of these reductions diminishes rapidly with increasing N. The implication for CGI design would seem to be that, in simulating this task, diminishing returns are to be had in terms of improving the simulator pilot's perception of heading, for counts much greater than about 1000. Naturally, the use of such a low edge count to represent a high density visual scene will lead to a considerable lack of "simulator realism"; the model results would indicate however that this shortcoming in appearance would have little impact on the perceptual performance of the simulator pilot (for this task, terrain type, etc.)

Figure 5 shows the standard deviation of the error in estimating the total angular rate, and the error breakdown by body axis. The trends with point count are similar to those just seen for heading error, and would imply a similar point of diminishing returns in the scene density, in terms of potential improvements in perceiving angular rates.

Figures 6 and 7 show heading estimation performance as a function of lateral and vertical FOV limits. Viewed point count N was maintained at approximately 500 points, across all FOV conditions indicated.

Figure 6 shows the effect of lateral (half-

\*Point counts less than 10 occasionally led to algorithm convergence problems, when certain "solvability conditions" were violated [22]; counts greater than 1000 were not run to conserve computational resources.

\*\*The conventional axis assignment is assumed, with roll along X, yaw pointing down to the surface, and pitch normal to the other two.

width) FOV variations. As the curves indicate, once the FOV exceeds roughly the nominal 24 deg half-width, the opposite trends of lateral and vertical heading estimation errors yield a total heading error function which is fairly insensitive to lateral FOV. For the geometry we are considering, this suggests that aim-point can be fairly well localized in the absence of the peripheral visual flow provided by wide FOV displays, assuming, as we have in these simulations, that the FOV is centered on the aim point.

Figure 7 shows the effect of variations in the vertical (downward) FOV. As seen, vertical errors grow directly with increasing FOV, throughout the FOV range; lateral errors also increase with FOV, but only for the larger FOV limits. Because of the relative minimum in the lateral error curve, both errors combine to yield a total heading error function which is minimized for a FOV of about 36 deg. We suspect that this behavior reflects the fact that a too small FOV overly constrains the viewing geometry and provides an inadequate measurement sample for accurate estimation, whereas a too large FOV encompasses very high-rate, and thus, high-noise, measurements, which degrade the overall heading estimate; an intermediate vertical FOV limit should thus ensure the best estimation performance.

## Human Performance Simulation

We are currently conducting model simulations of human estimation performance. We report here the results of one such simulation of a psychophysical experiment conducted by Warren [19].

Subjects were "flown" over flat terrain decorated by a uniformly random array of luminous dots. The flight path was straight and level, with an altitude of  $d$  units and speed  $1.25d$  units/sec, where  $d$  was the average interdot spacing of the terrain texture. Lateral FOV was  $\pm 26$  deg; vertical FOV was 26 deg below the displayed horizon, which was depressed about 1.2 deg below the true horizon to maintain a finite texture point count (of about 1100 viewable points). After viewing the display, subjects were asked to indicate their lateral heading aim point, and were able to do so with an accuracy of 1.5 deg standard deviation (across subjects).

Figure 8 shows the results of a model simulation of this experiment. Using the above problem parameters, and visual thresholds of  $1 \text{ min}$  and  $1 \text{ min/sec}$ , heading estimation performance was "swept out" as a function of N/S ratio  $f$ , as shown. In modelling terms, the observed lateral pointing accuracy of 1.5 deg is simply explained by a -22dB rate noise ratio, or, equivalently, a dynamic discrimination capability of about 8%. This is in remarkable agreement with a demonstrated 10% figure obtained by independent threshold measurements [17].

## Model Applications

These model-based predictions of perceptual performance allow us to start identifying the significant visual factors in a given flight simulation, but they do not fully address the

problem of task-relevant cueing. For this we need a model of the pilot's task performance, which functionally relates the perception of vehicle/terrain states to the overt actions characterizing the flight task. With a flow-field perceptual model defining the functional transformation from stimulus set to perceived state, and a task performance model defining the functional transformation from perceived state to overt action, we are then in a position to predict the overall input-output function characterizing the pilot operating in the given cue environment and imposed task structure.

For the task of terrain-following flight, this means that we must have a task performance or flight control model, which transforms terrain-relative state information into timely and effective manual flight control commands, which, in flight, eventually drive the actuating surfaces of the aircraft, and result in the desired terrain-following path control. Fortunately, the manual control community has focused considerable attention on this problem, and there are a number of control models which could be "interfaced" with the perceptual model we are proposing (e.g., the crossover model [15], the optimal control model (OCM) [10], etc.). The major effort we see in this area is in ensuring an appropriate interface; i.e., ensuring that the perceptual model generates, in an appropriate format, all the state measurements required by the control model for terrain-following flight.

We have begun an effort in this direction using the OCM [13]. In essence, we use the perceptual model to generate error statistics (as above) for heading, angular velocity, impact time, and terrain-relative attitude. These are then converted, via the aircraft speed, to state-related uncertainties, which, in the OCM context, are interpreted as "residual display noise" [12]. This, in turn, allows us to use the OCM to predict closed-loop flight path control performance, in the visually-driven terrain-following task. We are currently using this approach to design validation experiments and interpret the resulting simulation data.

We do not see this visual cueing model as limited, however, to the specific task of terrain-following flight, nor even to the general task family of visually-guided path control. For example, we see potential applications in the areas of monitoring for flight path management (during an approach, for example), in identifying the three-dimensional shapes of ground features (e.g., during a flyover of camouflaged ground equipment), and in

other related areas of visually-driven situation assessment requiring shape recognition.

### Conclusions

We have developed and exercised a model of visual flow-field cue processing, for direct application to low-level flight. Our consideration of the terrain-following cueing environment allowed us to focus specifically on flow-field cueing and develop a mathematical description of the kinematic flow constraints. A least-squares solution satisfying these constraints was proposed as the basis for the estimator model, which we showed was capable of estimating not only observer motion states, but viewed surface shape as well.

The least-squares estimator formulation of the cueing model is applicable to general observer motions and viewing geometries, is projection-plane independent, and is rational in its treatment of redundant and noisy flow cues. Simulations of its performance demonstrate its utility in investigating the sensitivity of task-relevant perceptual performance to simulator-related visual display parameters, such as edge count and field-of-view. Preliminary simulation results of human visual performance are encouraging, and have motivated an ongoing experimental validation effort. Additional applications of visually-driven task performance are currently being pursued, in an effort to widen the scope of applicability of the flow-field cueing model.

### References

1. ----, Boeing Imagery Apes Reality, Photonics Spectra, January 1983, pp. 73-74.
2. Ballard, D.H. and Brown, C.M., Computer Vision, Prentice-Hall, Inc., Englewood Cliffs, NJ, 1982.
3. Clocksin, W.F., Perception of Surface Slant and Edge Labels from Optical Flow: A Computational Approach, Perception, 1980, 9, pp. 253-269.
4. Gibson, J.J., The Perception of the Visual World, Houghton Mifflin, Boston, 1950.
5. Gibson, J.J., Olum, P., and Rosenblatt, F., Parallax and Perspective During Aircraft Landings, American Journal of Psychology, 1955, 68, pp. 372-385.
6. Gordon, D.A., Static and Dynamic Visual Fields in Human Space Perception, Journal of the Optical Society of America, 1965, 55, pp. 1296-1303.
7. Harker, G.S., and Jones, P.D., Depth Perception in Visual Simulation (AFHRL-TR-80-19), Air Force Human Resources Laboratory, Brooks Air Force Base, TX, August 1980.

---

\*Although not as much as we would wish on the "preview control" problem which characterizes the terrain-following task.

\*\*These last two are computed by a terrain estimator module appended to the basic flow-cueing model; its function is to transform the spatially-sampled impact time set  $\{I_i\}$  into a spatially continuous terrain surface.

8. Havron, M.D., Information Available from Natural Cues During Final Approach and Landing (Tech. Rep. HSR-RR-62/3-MK-X), Human Sciences Research Inc., Arlington, VA, March 1962.
9. Hoffman, D.D., Inferring Shape from Motion Fields (AI Memo 592), Artificial Intelligence Laboratory, MIT, Cambridge, MA, December 1980.
10. Kleinman, D.L., Baron, S. and Levison, W.H., An Optimal Control Model of Human Response: Theory and Validation, *Automatica*, 1970, 6, pp. 357-369.
11. Lee, D.N., A Theory of Visual Control of Braking Based on Information About Time to Collision, *Perception*, 1976, 5, pp. 437-459.
12. Levison, W.H., The Effects of Display Gain and Signal Bandwidth on Human Controller Remnant (AMRL-TR-70-93), Air Force Aeromedical Research Laboratory, Wright-Patterson Air Force Base, OH, March 1971.
13. Levison, W.H., Zacharias, G.L. and Sinacori, J.B., Design of an Experiment to Study the Pilot's Use of Visual and Motion Cues in a Height-Regulation Task (Rept. No. 5028), Bolt Beranek and Newman, Inc., Cambridge, MA, December 1982.
14. Longuet-Higgins, H.C., and Prazdny, K., The Interpretation of a Moving Retinal Image, *Proceedings of the Royal Society of London*, 1980, B-208, pp. 385-397.
15. McRuer, D.T., Graham, D., Krendel, E.S. and Reinsner, W., Human Pilot Dynamics in Compensatory Systems: Theory, Models, and Experiments with Controlled-Element Forcing Function Variations (AFFDL-TR-65-15), Air Force Flight Dynamics Laboratory, Wright-Patterson Air Force Base, OH, July 1965.
16. Prazdny, K., Egomotion and Relative Depth Map from Optical Flow, *Biological Cybernetics*, 1980, 36, pp. 87-102.
17. Statler, I.C., Characteristics of Flight Simulator Visual Systems, (AVRADCOM Tech. Rept. 81-A-8), AVRADCOM Research and Technology Laboratories, NASA Ames Research Center, Moffett Field, CA, April 1981.
18. Ullman, S., The Interpretation of Visual Motion, MIT Press, Cambridge, MA, 1979.
19. Warren, R., The Perception of Egomotion, *Journal of Experimental Psychology: Human Perception and Performance*, 1976, 2, pp. 448-456.
20. Warren, R., Optical Transformation During Movement, (RF 762591/713616), Ohio State University Research Foundation, Columbus, OH, October 1982.
21. Whiteside, T.C.D., and Samuel, G.D., Blur Zone, *Nature*, 1970, 225, pp. 94-95.
22. Zacharias, G.L., Flow-Field Cueing Conditions for Inferring Observer Self-Motion, (Rept. No. 5118), Bolt Beranek and Newman, Inc., Cambridge, MA, September 1982.
23. Zacharias, G.L. and Caglayan, A.K., A Model for Flow-Field Cueing and Self-Motion Estimation, (Rept. No. 5306), Bolt Beranek and Newman, Inc., Cambridge, MA, April 1983.
24. Zacharias, G.L., Caglayan, A.K., and Sinacori, J.B., "A Model for Visual Flow-Field Cueing and Self-Motion Estimation", (to be published in) *Proceedings of 1983 American Control Conference*, San Francisco, CA, 1983.

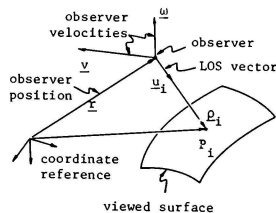


Fig 1: Viewing Geometry

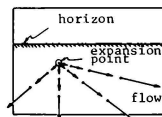


Fig 2a: Translational Flow

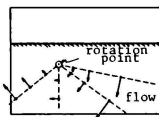


Fig 2b: Rotational Flow

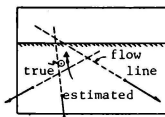


Fig 2c: Aim Point Estimation

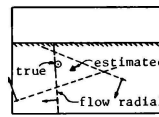


Fig 2d: Spin, Axis Estimation

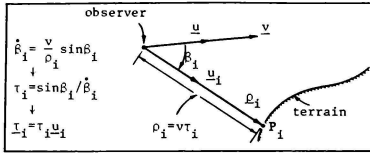


Fig 3a: Viewing Geometry for Flight Over Rolling Terrain

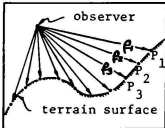


Fig 3b: Terrain Surface

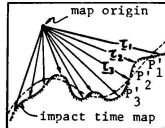


Fig 3c: Impact Time Map

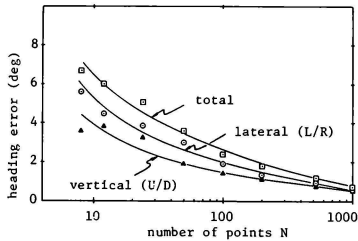


Fig 4: Heading Error vs. Array Size

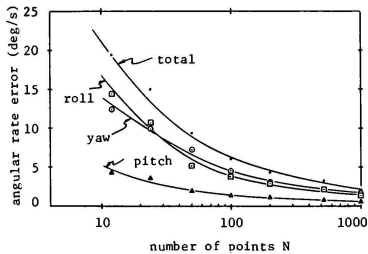


Fig 5: Angular Rate Error vs. Array Size

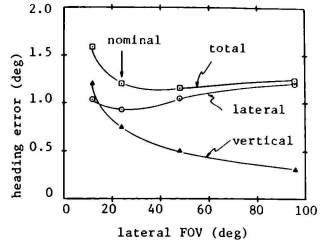


Fig 6: Heading Error vs. Lateral FOV

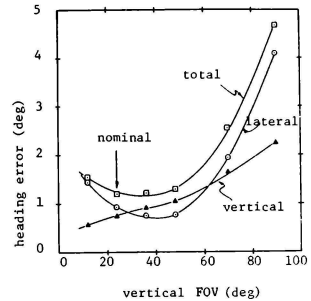


Fig 7: Heading Error vs. Vertical FOV

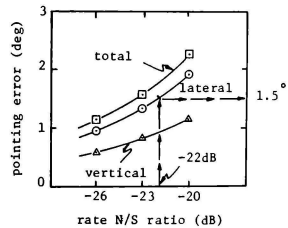


Fig 8: Pointing Error vs. Noise Level



B. T. McKissick\*

B. R. Ashworth\*\*

R. V. Parrish\*

NASA Langley Research Center, Hampton, Va.

Abstract

That portion of the simulation community involved in tactical fighter simulation has been concerned over the utility of both G-seat cueing devices and platform motion systems for several years. In order to measure and analyze the effects of the motion plus G-seat cueing system, a manned flight simulation experiment was conducted utilizing a pursuit tracking task, a F-16 simulation model and Langley's Visual Motion Simulator. The performance results are presented as standard root mean square error measures while the analysis utilized standard univariate statistical techniques. This experiment provided the information necessary to answer the primary question, "Do motion and G-seat cues have an accumulative effect on the performance of this task?" The answer is yes with respect to the lateral tracking error and roll control stick force. In this paper it is shown that presenting the two cues simultaneously caused significant reductions in lateral tracking error and that the G-seat and motion base when used separately provide essentially equal reductions in the pilot's lateral tracking error.

Introduction

That portion of the simulation community involved in tactical fighter simulation has been concerned over the utility of both G-seat cueing devices and platform motion systems for several years. The literature is voluminous, with articles by proponents and antagonists of each or both (12). Recent experiences at Langley Research Center in separate applications of a representative of each cueing system have been quite favorable (1,5).

In spite of the successful application and pilot acceptance at Langley, deficiencies in motion-cueing exist with each system. The Langley-designed G-seat (11) has been most effective in presenting normal acceleration cues, particularly sustained cues. It is less effective in its presentation of rotational and translational onset cues, and sustained side-force and surge cues. The conventional, six-degree-of-freedom, synergistic platform motion system, Langley's Visual Motion Simulator (VMS) (4), has no capability for sustained normal acceleration cueing, and very limited capability for transient vertical cueing. In fact, the vertical axis is used primarily for turbulence and buffet cueing. The other degrees of freedom are effectively presented by the platform-washout system, a system which was also developed at Langley Research Center (3). Intriguingly, the meshing of the two systems to provide an augmented system for six-degree-of-freedom motion cueing was desirable.

\* Aero-Space Technologist, Flight Operations Research Branch, Flight Control Systems Division.

\*\*Aero-Space Technologist, Analysis and Simulation Branch, Analysis and Computation Division.  
Member AIAA.

This paper is declared a work of the U.S. Government and therefore is in the public domain.

In order to measure and analyze the effects of the motion plus G-seat cueing system, a simulation experiment was designed utilizing a pursuit tracking task and an F-16 simulation model with the standard fixed side arm controller. This paper will present the comparative effects on simulated pursuit tracking performance of the following combinations of motion cueing: no motion (fixed-base operation), G-seat only, platform motion only, and platform motion augmented by G-seat. The performance results are presented as standard root mean square (RMS) error measures while the analysis tools utilized standard univariate statistical techniques.

Simulation Facility

The experiment was conducted using LaRC's real-time simulation system. This system, consisting of a CYBER 175 with associated interface equipment, solved the programmed mathematical model 32 times a second. The average time delay from input to output was approximately 47 milliseconds (1.5 times the same period). The simulation hardware and software utilized are described below.

G-Seat

One of the Langley-designed and fabricated seat cushions (1,11) was installed in the VMS. The four-cell seat, (fig. 1) using a thin air cushion with highly responsive pressure control, attempts to reproduce the same events which occur in an aircraft seat under acceleration loading. The seat is initially biased such that it conforms to the pilot to support most of his weight. The initial air pressure allows the two main support areas, the ischial tuberosities, to touch a wood surface, and thus begin to compress the flesh near these areas. As accelerations increase (positive g), air is removed from the seat giving the effect of compressing the cushion material. For negative g, sufficient air is added to the seat to remove all contact with the wood and, thus, uniformly support the body weight. The seat cushion steady-state time lags are about 35 msec, yielding a total average delay, including computational throughput, of slightly more than 80 msec.

Motion System

The Langley Visual Motion Simulator, VMS, (fig. 2) is a six-degree-of-freedom, synergistic platform motion system with acceleration, velocity, and positional limits. These limits are presented in Table I. Time lags of less than 15 msec are achieved by driving the base with lead compensation (2). Thus, the average total motion delay, including computational throughput, is less than 70 msec and is quite compatible with the rest of the system, including visual delays. The washout system used to present the motion-cue commands to the motion base is nonstandard and was conceived and developed at Langley Research Center (3). The basis of the washout is the continuous adaptive change of parameters to (1) minimize a cost functional through continuous

steepest descent method; and (2) produce the motion cues in translational accelerations and rotational rates within the motion envelope of the synergistic base.

#### Visual Display

The Langley VMS is provided with an "out-the-window" virtual image system of the beam splitter, reflective mirror type. The system, located nominally 1.27 m (4.17 ft) from the pilot's eye, presents a nominal  $48^\circ$  width by  $36^\circ$  height field of view of a 525 TV line raster system and provided a  $46^\circ$  by  $26^\circ$  instantaneous field of view. The system supplies a color picture of unity magnification with a resolution on the order of 9 minutes or arc.

The scene depicted in the virtual image display was obtained by video-mixing a terrain model board (4) picture with a target aircraft and a reticle display. The composite scene presented to the pilot is as shown on a monitor in figure 3 with about  $70^\circ$  right-wing down and the target aircraft at 1000 ft. in the 4 o'clock position of the reticle outer circle. The target aircraft display was generated by a computer graphics system with a second order filter added to match the reticle response to the servo response of the terrain board and target aircraft. Total visual delay, including computational throughput delay, was less than 70 msec on the average.

#### Cockpit Hardware

The general purpose transport cockpit of the VMS was modified to represent a fighter by removing the wheel and column and installing a side-arm force-actuated controller. The rudder pedals were configured as force-actuated pedals. Primary instrumentation consisted of an attitude indicator, vertical speed indicator, an altimeter, angles-of-attack and sideslip meters, an airspeed indicator, a Mach meter, a turn and bank indicator, and a compass card.

#### Aircraft Mathematical Model

The equations used to describe the motions of the F-16 were nonlinear, six-degree-of-freedom, rigid-body equation referenced to a body-fixed axis system. The mass and geometric characteristics of the simulation aircraft are presented in Table II. Complete details of the model are documented in reference 6.

#### Experimental Design and Statistical Analyses

A  $2^2 \times 8$  factorial design with a six-degree-of-freedom pursuit tracking task formed the environment within which the data were gathered. Univariate analyses of variance were performed on the performance measures.

#### Experimental Design and Task

The factors of the  $2^2 \times 8$  factorial design were motion (on or off), G-seat (on or off), and test subjects (8 active F-15 pilots stationed at Langley Air Force Base). Each cell within the design was replicated 10 times. The tracking task was two minutes and forty-three seconds in length. At the beginning of the tracking task, 20 seconds was used to phase in the sum of sines followed by 15 seconds for pilot stabilization. The target aircraft was flown at a constant airspeed of 285 knots, and constant altitude of 2500 feet. The pursuit

aircraft (simulated F-16) was required to track the target while maintaining a 1000 foot range. Range information was provided by a standard reticle range analog bar scaled for 2000 ft. (fig. 4). This causes the required 1000 foot range to appear at the 6 o'clock tab. During the task, the pursuit pilot's tracking reference (reticle) was driven in vertical aircraft body axis by a sum of 13 sinusoids in order to provide a source of tracking error. The sinusoids had a fixed set of amplitude and frequencies, but randomly chosen phases (between  $-180^\circ$  and  $+180^\circ$ ). The phases were randomly chosen so that the test subjects would not learn the movements of the reticle. Table III presents the amplitudes and frequencies in the sum of sine waves. In order to track the target, the pursuit aircraft was required to keep the target in the center of the reticle. This provides the same type of tracking task that the pilot would normally encounter in gun tracking with a lead angle computing gunsight.

#### Performance Measures

The Root Mean Squares (RMS) of the vertical height error (EV), lateral displacement error (EL), stick force for roll (TSP) and stick force for pitch (TAP) were computed as measures of performance. The measures are presented in Table IV.

#### Statistical Analysis

Univariate analysis techniques were applied to the performance measures. The statistical techniques are described in most standard texts on the subject, such as references 7 and 8.

#### Results

The primary question to be addressed is: Do motion and G-seat cues have an accumulative effect on the performance of this task? Tables V and VI show mean RMS error, standard deviation and standard error for the lateral and vertical tracking errors (EL & EV) and the roll and pitch control inputs (TAP & TSP) for the four combinations of G-seat and motion conditions. These results are plotted in figures 4 through 7. Tables VII and VIII show the results of an analysis of variance on these four measures.

Table V and figure 4 exhibit highly significant ( $\alpha < 1$  percent) differences between the fixed-base and G-seat/motion conditions for lateral tracking error. Mean RMS error is reduced from 9.04 feet (fixed base) to 7.55 feet by G-seat cues and to 7.75 feet by motion-base cues, respectively a 16.5% and 14.3% reduction. However, the two cues combined provide a significantly lower lateral tracking error (6.42 feet and 29% lower). The analysis of variance for EL (Table VII) shows that there is a highly significant effect on the lateral tracking error due to pilot, motion, G-seat, pilot by motion, and pilot by G-seat effect; however, there is no effect due to the motion by G-seat interaction. Similar results are shown for roll control stick force (TAP). The plots (fig. 5) for roll control stick force show a highly significant lowering of the control input (TAP) for motion conditions (F value of 158 vs. 6.74 for  $\alpha = 1$  percent) with a lesser, but still significant (F value of 9.8 vs. 6.74 for  $\alpha = 1\%$ ) lowering of TAP for G-seat conditions. This lowering of the aileron control force is associated with a lowering of the lateral tracking error for both conditions.

The results of the analysis of variance on the vertical tracking error (EV) and pitch control force (TSP) are presented in Table VIII. The pilot, G-seat, pilot by motion, and pilot by G-seat effect are all significant ( $\alpha < 1\%$ ) for EV. No significance with respect to EV is recorded for the motion and motion by G-seat effects. The same trends hold for TSP. Visual presentations of the data for EV and TSP are in figures 6, 7, and 12-15. Figures 12 through 15 show the individual pilot differences.

#### Discussion

From these results, the G-seat and motion cues have their greatest effect on the pilot's lateral tracking error, even though the reticle is only driven vertically. This fact was unexpected since previous experience with tracking tasks (1,9,10) showed statistically significant effects for vertical tracking error and pitch control input, as well as for the lateral error and roll control input. However, it should be noted that the tasks were not the same as the one used in this study and that the aircraft dynamics were not the same either. A 3-g wind-up turn with the reticle driven by a square wave was used as a task in references 1 and 10, while the study of reference 9 used a single pitch axis degree-of-freedom task with the reticle driven by a sum of sines. Simulated airplanes in reference 1 and 10 were F-14's. A linearized F-8 was used as airplane dynamics for the study presented in reference 9. An interpretation of the lateral tracking error results is as follows: the pilots' first task, in this 6 degree of freedom task, is to correct for lateral error so that he is in the same body-axis vertical plane as the target. Once he is in "in-plane", the pilot can then attempt to reduce the vertical tracking error.

As far as the lateral measures of performance are concerned, the data (fig. 4 and table V) shows that the G-seat and motion when used alone, provides cues that lead to approximately the same reduction in lateral tracking error. But the amount of stick force for roll control (figure 5) was lower for the motion platform. This effect would correspond to the fact the motion platform is very effective in presenting rotational onset cues which prevent the pilots from over control with respect to roll. As far as the G-seat is concerned, it does not give rotational cues but does provide a normal acceleration cue, which tells the pilot he is going "out of plane" before he can see that he is "out of plane". Hence, the G-seat cue can reduce over control in roll but not as much as the motion platform. Moreover, the data also shows in additive effect (evidenced by figure 4 and a non-significant motion by G-seat interaction) since the combined cues lower the lateral error over each used alone. It is apparent that the two cues (roll motion and normal acceleration) when used together provide the pilot with information which he uses to lower his lateral error by an amount almost equal to the sum of the amount each individual cue case differs from the fixed base case. The same trend holds for stick force for roll control.

For the vertical tracking error (EV) and pitch control (TSP), the motion platform shows no first order effect (figs. 6 and 7, and tables VI and VII). This is to be expected since the motion drive algorithms (1,2) provide very little vertical cue. However, a further look at the data (figs. 8-11) and

knowledge that there are significant pilot interactions leads to the conclusion that possibly the pitch rate cue, presented by the motion platform, does affect pilot performance, but not in a uniform manner across all pilots. Motion cueing improves the performance of pilot 3, 4, and 8 (fig. 12) but degrades the vertical performance of all the other pilots. Therefore, the effect of motion in some individual pilots is significant (pilots 2, 3, 4 and 6 by a t-test) but the pilot effect washes out any first order motion effect.

The vertical situation with respect to the G-seat is much clearer. In figure 13, pilots 1, 2 and 5 show the G-seat cues leading to slightly larger vertical errors. However, none of these pilots show any statistically significant difference when tested with a t-test between G-seat on or off performance with respect to EV. For the remainder of the pilots, the G-seat cues leads to improved performance in vertical tracking t-test results. Overall, the G-seat produces a significant reduction of the vertical error (F value 9.85 vs. 6.74) for  $\alpha = 1\%$  by providing normal acceleration cues which relate directly to the error (EV) when the pilot is "in-plane" with the target.

#### Concluding Remarks

In order to measure and analyze the effects of the motion plus G-seat cueing system, a manned flight simulation experiment was conducted utilizing a pursuit tracking task and an F-16 simulation model in the NASA Langley Visual Motion Simulator. This experiment provided the information necessary to answer the primary question, "Do motion and G-seat cues have an accumulative effect on the performance of this task?"

The answer is yes with respect to the lateral tracking error and roll control stick force. When used separately, the motion platform and G-seat provide information that the pilot uses to prevent overcontrol in roll and, therefore, is able to reduce his lateral tracking error. When used together, the information provided has an effect of lowering the amount of roll control stick force used and lateral tracking error generated by an amount almost equal to the sum of the amounts each individual cue case differs from the fixed base case. For the vertical tracking error, the G-seat significantly lowers the error whether motion is used or not. The motion may have an effect on an individual pilot's vertical performance, but overall, motion does not appear to have a consistent effect on the vertical tracking error. Neither the G-seat nor the motion platform effect the amount of pitch control stick force used.

#### References

1. Ashworth, Billy R.; McKissick, Burnell T.; and Martin, Dennis J., Jr.: Objective and Subjective Evaluation of the Effects of a G-Seat on Pilot/Simulator Performance During a Tracking Task. Tenth NTEC/Industry Conference, Orlando, FL, November 15-17, 1977.
2. Parrish, Russell V.; Dieudonne, J. E.; Martin, Dennis J., Jr., and Copeland, James L.: Compensation Based on Linearized Analysis for Six-Degree-of-Freedom Motion Simulator. NASA TN D-7349, November 1973.

<sup>3</sup>Parrish, Russell V.; Dioudonne, J. E.; Bowles, Roland L.; and Martin, Dennis J., Jr.: Coordinated Adaptive Washout for Motion Simulators. Journal of Aircraft, Vol. 12, No. 1, pp. 44-50, January 1975.

<sup>4</sup>Rollins, John D.: Description and Performance of the Langley Visual Landing Display System. NASA TM 78742, August 1978.

<sup>5</sup>Parrish, Russell V.: Platform Motion for Fighter Aircraft--Let's Be Realistic. AIAA Paper No. 78-1574. Presented at the AIAA Flight Simulation Technologies Conference, September 1978.

<sup>6</sup>Gilbert, W. P.; Nguyen, L. T.; and Van Gunst, R. W.: Simulator Study of the Effectiveness of an Automated Control System Designed to Improve the High Angle-of-Attack Characteristics of a Fighter Airplane. NASA TN D-8176, May 1976.

<sup>7</sup>Hicks, Charles R.: Fundamental Concepts in the Design of Experiments. Second Edition, Holt, Rinehart and Winston, 1973.

<sup>8</sup>Cochran, W. G.; and Cox, G. M.: Experimental Designs. Second Edition, John Wiley and Sones, Inc., January, 1968.

<sup>9</sup>Ashworth, Billy R.; McKissick, Burnell T.; and Parrish, Russell V.: The Effects of Simulation Fidelity on Air-to-Air Tracking. Fifteenth Annual Conference on Manual Control. Wright State University, Dayton, OH, March 20-22, 1979.

<sup>10</sup>Ashworth, Billy R.; and McKissick, Burnell T.: Effects of Helmet Loader Cues on Simulator Pilot Performance. Journal of Aircraft, Vol. 16, No. 11, November 1979, p. 787.

<sup>11</sup>Ashworth, B. R.: A Seat Cushion to Provide Realistic Acceleration Cues for Aircraft Simulators. NASA TM X-73954, 1976.

<sup>12</sup>Puig, Joseph A.; Harris, William T.; and Ricard, Gilbert L.: Motion In Flight Simulation: An Annotated Bibliography. Naval Training Equipment Center Technical Report: NAVTRAEQUIPCEN IH-298, July 1978.

TABLE II.- MASS AND DIMENSIONAL CHARACTERISTICS OF SIMULATED F-16

Weight, N (lb).....	73 480 (16 519)
Moments of inertia,	
kg-m <sup>2</sup> (slug-ft <sup>2</sup> ):	
I <sub>X</sub> .....	12 662 (9339)
I <sub>Y</sub> .....	53 147 (39 199)
I <sub>Z</sub> .....	63 035 (46 492)
I <sub>XZ</sub> .....	179 (132)
Wing dimensions:	
Span, m (ft).....	8.84 (29.0)
Area, m <sup>2</sup> (ft <sup>2</sup> ).....	26.0 (280)
Mean aerodynamic chord,	
m (ft).....	3.335 (10.94)
Surface deflection limits:	
Horizontal tail -	
Symmetric (w <sub>h</sub> ), deg.....	±25
Differential (w <sub>D</sub> ), deg.....	+5 per surface
Ailerons (flaperons), deg.....	±20
Rudder, deg.....	±30

TABLE I.- VMS LIMITS

Displacement	Velocity	Acceleration
Pitch +30°, -20°	±15°/sec	±50°/sec <sup>2</sup>
Roll +22°, -20°	±15°/sec	±50°/sec <sup>2</sup>
Yaw +32°	±15°/sec	±50°/sec <sup>2</sup>
Vert. ±39, -30 in	±24 in/sec	±0.8g
Lat. ±48 in	±24 in/sec	±0.6g
Long. ±48 in	±24 in/sec	±0.6g

TABLE III.- PARAMETERS OF SUM OF SINES USED TO DRIVE RETICLE

Frequencies (rad/sec)	Relative Amplitudes
0.245	1.150
.540	.747
.933	.319
1.424	.121
2.013	.051
2.896	.022
4.074	.009
5.547	.004
8.001	.002
10.946	.001
16.248	.0003
22.040	.0001
32.094	.00006

TABLE IV.- PERFORMANCE MEASURES

<u>State</u>	<u>Units</u>	<u>Mnemonic</u>
Pilot's pitch input	pounds	TSP
Pilot's roll input	pounds	TAP
Vertical height error	feet	EV
Lateral displacement error	feet	EL

TABLE V.- LATERAL PERFORMANCE MEASURES

Variable	Motion Cond.	G-seat Cond.	Freq. #Runs	Mean RMS	STD	STE
EL	OFF	OFF	80	9.043	2.883	0.324
	OFF	ON	80	7.555	2.117	.238
	ON	OFF	80	7.746	1.973	.222
	ON	ON	80	6.420	1.603	.180
EL	OFF	±-	160	8.299	2.630	
	ON	±-	160	7.083	1.911	
EL	±-	OFF	160	8.394	2.547	
	±-	ON	160	6.987	1.957	
TAP	OFF	OFF	80	2.119	0.263	.029
	OFF	ON	80	2.064	.249	.028
	ON	OFF	80	1.862	.209	.023
	ON	ON	80	1.783	.209	.023
TAP	OFF	±-	160	2.092	.257	
	ON	±-	160	1.822	.212	
TAP	±-	OFF	160	1.991	.270	
	±-	ON	160	1.923	.269	

\* - combined on and off

TABLE VI.- VERTICAL PERFORMANCE MEASURES

Variable	Motion Cond.	G-seat Cond.	Freq. #Runs	Mean RMS Error	STD	STE
EV	OFF	OFF	80	18.498	3.860	0.434
	OFF	ON	80	17.621	2.981	.335
	ON	OFF	80	18.470	3.072	.346
	ON	ON	80	17.702	3.522	.396
EV	OFF	±-	160	18.060	3.466	
	ON	±-	160	18.086	3.316	
EV	±-	OFF	160	18.484	3.477	
	±-	ON	160	17.662	3.253	
TSP	OFF	OFF	80	4.010	0.215	.024
	OFF	ON	80	3.988	.224	.025
	ON	OFF	80	4.004	.279	.031
	ON	ON	80	3.968	.252	.028
TSP	OFF	±-	160	3.999	.219	
	ON	±-	160	3.986	.265	
TSP	±-	OFF	160	4.007	.248	
	±-	ON	160	3.978	.238	

\* - combined on and off

TABLE VII

Results of F-Tests on Lateral Performance Parameters

Variation	Source of Variation	F-Value	F-Value for α = 5%	F-Value for α = 1%
EL	Pilots	23.70	2.04	2.72
	Motion	41.26	3.88	6.74
	Pilot*Motion	5.01	2.04	2.72
	G-seat	55.28	3.88	6.74
	P*GS	4.79	2.04	2.72
	M*GS	.18	3.88	6.74
	P*M*GS	1.74	2.04	2.72
	Rep	.57	1.91	2.48
TAP	Pilots	11.93	2.04	2.72
	Motion	158.51	3.88	6.74
	Pilot*Motion	3.56	2.04	2.72
	G-seat	9.85	3.88	6.74
	P*GS	3.21	2.04	2.72
	M*GS	0.319	3.88	6.74
	P*M*GS	7.24	2.04	2.72
	Rep	1.10	1.91	2.48

TABLE VIII

Results of F-Tests on Vertical Performance Parameters

Variation	Source of Variation	F-Value	F-Value for	
			$\alpha = 5\%$	$\alpha = 1\%$
EV	Pilots	39.55	2.04	2.72
	Motion	.01	3.88	6.74
	Pilot*Motion	5.95	2.04	2.72
	G-seat	9.85	3.88	6.74
	P*GS	3.02	2.04	2.72
	M*GS	.04	3.88	6.74
	P*M*GS	3.45	2.04	2.72
	Rep	1.46	1.91	2.48
TSP	Pilots	80.80	2.04	2.72
	Motion	.74	3.88	6.74
	Pilot*Motion	9.06	2.04	2.72
	G-seat	3.68	3.88	6.74
	P*GS	4.00	2.94	2.72
	M*GS	.25	3.88	6.74
	P*M*GS	9.34	2.04	2.72
	Rep	2.95	1.91	2.48



Fig. 1 - G-Seat

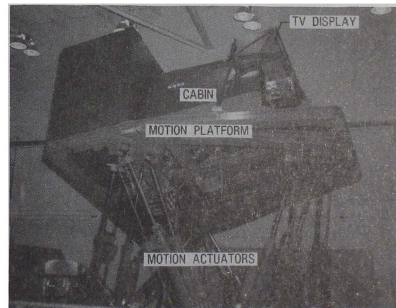


Fig. 2 - Motion Base

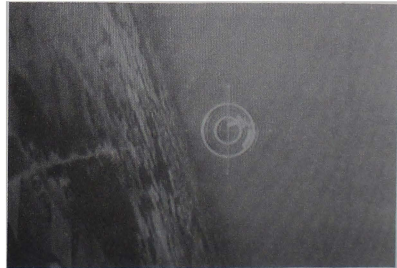


Fig. 3 - Pilot's Visual Scene

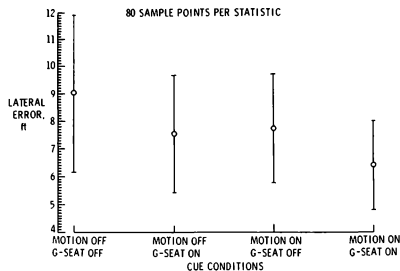


Fig. 4 - Lateral Tracking Error

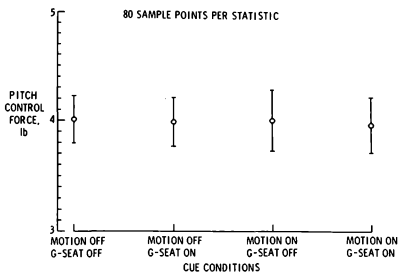


Fig. 7 - Stick Force for Pitch Control

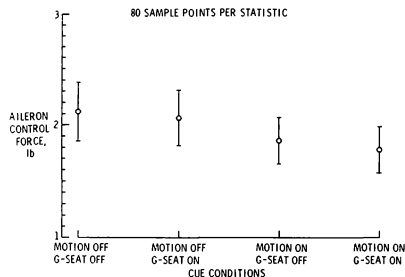


Fig. 5 - Stick Force for Roll Control

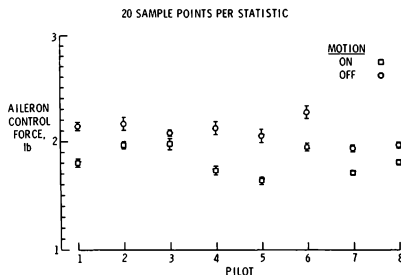


Fig. 8 - Effect of Motion Pilots' Roll Command

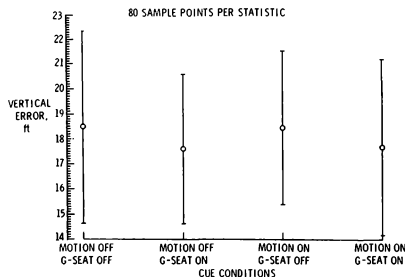


Fig. 6 - Vertical Tracking Error

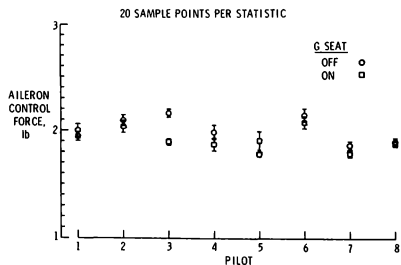


Fig. 9 - Effect of G-Seat on Pilots' Roll Command

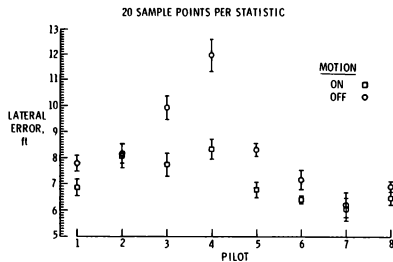


Fig. 10 - Effect of Motion on Pilots' Lateral Error

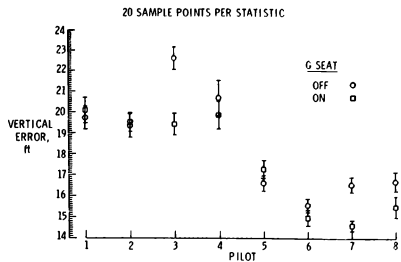


Fig. 13 - Effect of G-Seat on Pilots' Vertical Error

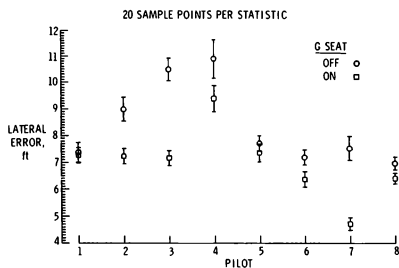


Fig. 11 - Effect of G-Seat on Pilots' Lateral Error

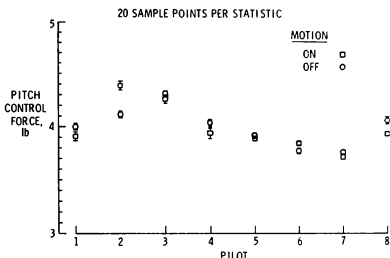


Fig. 14 - Effect of Motion on Pilots' Pitch Command

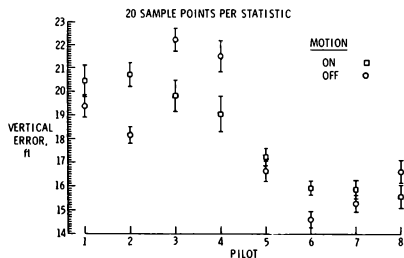


Fig. 12 - Effect of Motion on Pilots' Vertical Error

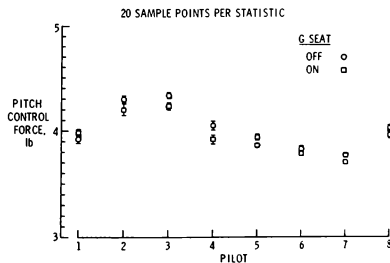


Fig. 15 - Effect of G-Seat on Pilots' Pitch Command



David R. Rolston  
Section Chief  
McDonnell Aircraft Company  
McDonnell Douglas Corporation  
St. Louis, Mo.

### Abstract

Many classical numerical methods for differential equations are based on the exact integration of polynomial functions; However, methods based on sinusoidal functions may be better suited to analysis of oscillatory systems. Discrete time difference equations have been developed for sinusoidal extrapolation, predictor integration, and corrector integration and tested in the equations of motion of real-time flight simulation. The computational stability and accuracy were significantly improved when a sinusoidal function frequency was chosen to match the natural frequency of the aircraft.

### 1. Introduction

This paper presents a new engineering solution to an old engineering problem. The emphasis on engineering is intentional, as the approach throughout is as straightforward as possible. The derivations are elegant only in their simplicity, but the results are satisfying because they are original and they work.

#### 1.1 The Problem

The "old" problem is one which began to show up during the 1960's as the digital computer was incorporated into the man-in-the-loop flight simulation efforts of the space program. The digital computer was introduced to take advantage of its vast storage capacity, accuracy, and repeatability, but its computing power is limited to basic operations. Other mathematical operations, such as integration and differentiation must be performed by approximate numerical methods, and therein lies the difficulty.

In real-time computation simple difference-equation approximations are usually used to perform an integration. However errors introduced by these approximations can have significant effects on accuracy and computational stability. There are numerous methods available based on different theories and differing in programming complexity and computation time. All of these methods have one thing in common, and that is that they all approach the continuous time solution as the sample interval is decreased toward zero. However, in real-time computation the critical factor is the performance of these approximate numerical methods as the sample interval is not decreased, but rather increased toward the natural period of oscillation of the dynamic system being modeled.

Man-in-the-loop simulation imposes some rigid constraints on computer operation. First, and foremost, it must perform its analog-to-digital conversion, math flow computation and digital-to-analog conversion in real-time, and at a sample rate that is fast enough to represent adequately the input and output waveforms. The maximum sample time is therefore, determined by

the response characteristics of the dynamic system being simulated, including its human elements.

The usual rule of thumb is no fewer than 10 samples per cycle for the highest frequency of interest; so this maximum will generally be between .1 and .01 second (10 to 100 samples/second) for a typical piloted flight simulation. The computation time required for the math flow during each iteration fixes the minimum sample interval. The ever increasing scope and sophistication of real-time simulation programs ensures that the computation requirement will push the sample time to the maximum limits of acceptable operation.

Figure 1 shows the results of using the classical Adams-Bashforth method to integrate the equations of motion of a high performance aircraft at a critical flight condition (minimum gain and phase margin). The sample interval for the first run was .005 second, giving results equivalent to the continuous-time system. The second run was made with the .05 second sample interval desired for real-time operation. Note that it demonstrates an unstable oscillation which is a result of the additional (erroneous) gain and phase lag contribution from the numerical integration scheme.

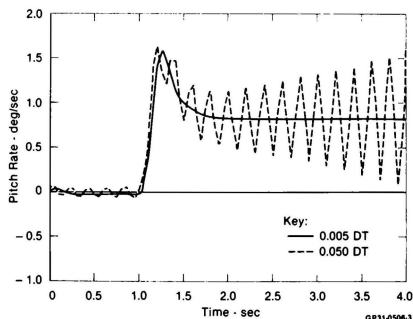


Fig. 1 Computational Instability

In this example, the sample interval had to be reduced to .04 second to obtain stable computation of sufficient accuracy. Thus when using classical methods the sample interval required for computational stability can be less than that required for adequate sampling of the input and output waveforms!

This requirement for faster sampling increases cost or reduces simulation capability by eliminating cycle time that should be available for performing computations.

The numerical methods developed in this paper represent an attempt to recover that lost capability by stretching the sample interval to the practical limits without inducing computational stability or accuracy problems.

## 1.2 The Solution

The usual "brute force" alternative to insufficient computation capability is to buy a bigger, faster computer which would do the computations desired in the time available. That may have been the "American Way" of the 60's, but the economics of the 80's demand something a bit more subtle.

1.2.1 Fowler's Method. Several important developments in numerical methods have been directed to this problem in recent years. The work of Naury Fowler (1), (2) accomplishes a root locus match between the discrete and continuous time systems by the adding of lead compensation and gain adjustments to the difference equations that are used to simulate the various elements of the dynamic system. Although this method has scored some spectacular successes, it has not achieved wide acceptance. The reason can be found in Fowler's words in the summary of his paper (1) where he claims that "the major advantage of the method, in addition to speed of computation, is that a detailed analysis of the system is carried out during the development of the simulation." Unfortunately, this "detailed analysis" is required for every mode of control system operation and every time there is a change in control system design or in the data describing the vehicle response dynamics (mass and inertia properties, aerodynamic data, etc.). The algebraic manipulations required are excessive and require additional special purpose programs to compute the root locus points and  $Z$  - transforms (1).

In summary this method has much to recommend it in simulation programs such as training devices, where the system is completely defined and not subject to frequent change or modification. But it is clearly unsuitable for application to a research and development program where the control laws and response dynamics can change on an almost daily basis.

1.2.2 Tuneable Integrators. B. J. Nigro has developed "optimally stable" integration methods based on perturbations of classical methods (3), (4). Although the conclusions are impressive, a successful application of the method is not documented. The mathematics involved are somewhat tedious and require a solution for the eigenvalues of the Jacobian matrix describing the system differential equations. This requirement is a major drawback for aircraft simulation, as those differential equations are nonlinear, time-varying, and coupled.

A less rigorous approach is taken by J. H. Smith in his development of "tuneable" integrators which are based on variable phase-gain digital filters (5). These integrators have error controlling parameters through which the phase and amplitude of the integrator transfer function is "tuned" to the system of equations being integrated. The tuning is accomplished empirically by adjusting the phase and gain parameters to match a check case.

This method has been widely used but it has several shortcomings. First, the tuning process must be accomplished over the whole range of flight conditions to insure correct compensation. Also, the gain adjusting parameter causes an error in the integral solution if the value of the integrand is not zero in the steady state. This could cause a problem in integrating velocity to obtain position in the equations of motion.

In considering the two alternatives of the preceding paragraphs, the contrast is striking. Fowler's method suffers from overkill in the detailed analysis required for compensation of each dynamic element in the system. The simpler method of compensating the entire system by tuning only the integration element accomplishes similar results but suffers, in a sense, from "under-analysis", in that the tuning process is entirely empirical and does not utilize any prior knowledge of the system dynamics. This paper presents a method between these two extremes, which takes advantage of the known response characteristics of the system being modeled, but does not require additional analysis.

1.2.3 The Thesis. Without exception there is considerable analysis that goes into the design and development of a dynamic system before it is programmed for testing in real-time simulation. This analysis may be linearized, small perturbation, three-degree-of-freedom computations or it may be a full-scale nonlinear simulation done in non-real-time.

In the case of second-order systems (such as aircraft aerodynamics) the results almost always include information on the open and closed loop natural frequency and damping of the system at various conditions. These systems tend to respond with sinusoidal motion at the damped natural frequency. This simple fact suggests a solution to the problem: an integration scheme should be devised which reduces or eliminates the errors for sinusoidal motion at a known frequency.

Many classical methods of numerical integration are devised to provide an exact response for an input of a particular polynomial shape. The thesis of this paper is that for simulating systems whose response is predominantly second order. It is more appropriate to employ an integration scheme that provides an exact response to a sinusoidal input. The fact that we always have knowledge of the damped natural frequency for a simulated aircraft provides the basis for a practical application of the suggested sinusoidal methods.

## 2. Background

There are two general categories of numerical methods for the digital simulation of a simple integrator. First, there are the "self-starting" methods which are distinguished by the fact that they do not require storage of the independent and dependent variables from preceding time intervals. The classic example of this category is the Taylor Series method of numerical integration. Runge-Kutta integration is another method widely used. Both of these methods are usually unsuitable for real-time simulation.

The second class of numerical methods for digital integration is the linear recursion formula, or "multi-step" methods, which, in the difference equation format of serial digital computation, take the form:

$$X(mT) = \sum_{i=1}^j a_i X((m-1)T) + T \sum_{i=0}^k b_i \dot{X}((m-1)T) \quad (2-1)$$

where  $\dot{X}(mT)$  and  $X(mT)$  are the  $m$ th in the sequence of integrand and integral, and  $T$  is the integration step size (sample interval).

The "multi-step" methods are particularly suitable for real-time applications, as they employ fixed step size and require minimum computation time. The storage required for saving past values is generally insignificant and the "nonself-starting" feature is not a problem when the simulation is to be started from a known equilibrium state. The sinusoidal method and other methods used for comparison in this paper are in the form described by (2-1).

The coefficients  $a_i$  and  $b_i$  of (2-1) are usually chosen to satisfy accuracy criteria based on truncation error. Notice that if  $b_0 \neq 0$  then the current value of the integrand  $\dot{X}(mT)$  is required for evaluation of  $X(mT)$ . This property defines a sub-class of integration schemes referred to as the "corrector" (or closed) formulas. In circumstances where  $\dot{X}(mT)$  is not available a "predictor" (or open form) integration method ( $b_0 = 0$ ) must be used.

The approximations involved in many numerical integration schemes can be compared with a truncated Taylor Series, and the magnitude of the terms discarded is a measure of the error which is introduced at each step. Unfortunately, most developments in numerical integration methods have been almost totally preoccupied with controlling the truncation error (perhaps because it is one of the few sources of error which can be elegantly analyzed). This concern for accuracy is well founded in most digital computations, but is not a stringent requirement for most real-time hybrid applications where the errors already inherent in the dynamic model and the analog-to-digital and digital-to-analog conversion process are significant. Accuracy is important, but a precisely defined measure of error is not!

For the methods developed in this paper, an attempt has been made to give equal weights to computational stability and the frequency domain effects of the numerical integration process

**2.1 Polynomial Based Methods.** Of the numerous predictor type multi-step methods available for comparison the ones most often employed in real-time simulation are the ones which can be derived from a polynomial extrapolation. That is, in performing numerical integration the increment of area to be added at each iteration is that which would fall under a one interval extrapolation of the unique polynomial of order "n" which can be fit through the preceding  $n+1$  samples of the integrand (see Figure 2).

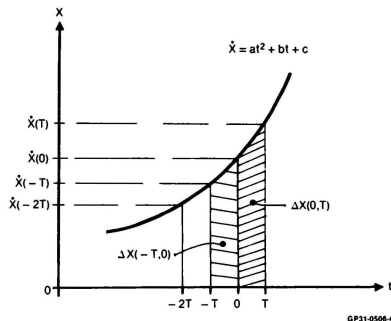


Fig. 2 Graphical Interpretation of Polynomial Integrand Approximation

For reasons of computational efficiency and stability it is desirable to keep the order of the polynomial extrapolations as low as possible and still have a good incremental approximation to the shape of the function describing the input. A second order polynomial is therefore the highest order approximation normally employed in integration of the second order dynamics of flight motion.

Now, if the shape of the integrand,  $\dot{X}$ , between sample points is to be approximated by a second order polynomial, the general expression would be:

$$\dot{X}(t) = at^2 + bt + c \quad (2-2)$$

let the time increment  $\Delta t = T$  and  $c = \dot{X}(0)$ .

For the first past time increment:

$$\dot{X}(-T) = a(-T)^2 + b(-T) + \dot{X}(0) \quad (2-3)$$

For the second past time increment:

$$\dot{X}(-2T) = a(-2T)^2 + b(-2T) + \dot{X}(0) \quad (2-4)$$

Solving (2-3) and (2-4) for  $a$  and  $b$

$$b = \frac{\dot{X}(-2T) - 4\dot{X}(-T) + 3\dot{X}(0)}{2T} \quad a = \frac{\dot{X}(-2T) - 2\dot{X}(-T) + \dot{X}(0)}{2T^2}$$

Now extrapolating to the next future time increment:

$$\dot{X}(T) = aT^2 + bT + c \quad (2-5)$$

Substitute for  $a$ ,  $b$  and  $c$  and collect terms,

$$\dot{X}(T) = 3\dot{X}(0) - 3\dot{X}(-T) + \dot{X}(-2T) \quad (2-6)$$

Thus (2-6) provides a recursion formula for a second order polynomial extrapolation based on the present value of the integrand and two past values. In fact, the coefficients for a recursion formula extrapolation of a polynomial of any order can be written by inspection from the binomial coefficients of  $(X-1)^n$ .

$$\begin{aligned}
n = 0, & \quad \dot{X}(T) - \dot{X}(0) = 0 \\
n = 1, & \quad \dot{X}(T) - 2\dot{X}(0) + \dot{X}(-T) = 0 \\
n = 2, & \quad \dot{X}(T) - 3\dot{X}(0) + 3\dot{X}(-T) - \dot{X}(-2T) = 0 \\
n = 3, & \quad \dot{X}(T) - 4\dot{X}(0) + 6\dot{X}(-T) - 4\dot{X}(-2T) + \dot{X}(-3T) = 0 \\
& \text{etc.} \qquad \qquad \qquad \text{etc.}
\end{aligned}$$

To find the increment of area under the extrapolation of the 2nd order polynomial,

$$\Delta X(0, T) = \int_0^T (at^2 + bt + c) dt = a \frac{T^3}{3} + b \frac{T^2}{2} + cT$$

substituting for a, b and c and collecting terms as before,

$$\Delta X(0, T) = T \left( \frac{23}{12} \dot{X}(0) - \frac{4}{3} \dot{X}(-T) + \frac{5}{12} \dot{X}(-2T) \right) \quad (2-7)$$

Thus, an open form predictor integration is obtained by successively summing the increment approximated by (2-7).

$$X(T) = X(0) + \Delta X(0, T).$$

The formula obtained in (2-7) is the familiar and widely used Adams-Bashforth method. A first order polynomial (linear) extrapolation for  $X(0, T)$  produces the Trapezoidal Predictor integration method and a zero order extrapolation results in Euler integration.

Closed form corrector integration methods can be developed in a way similar to those of Paragraph 2.1 by integrating the approximating polynomial over the interval  $-T$  to 0 to obtain  $\Delta X(-T, 0)$ .

Table 1 summarizes the methods described in this and the preceding section; it also includes the sinusoidal methods developed in the next section.

### 3. Derivation of Sinusoidal Methods

The derivations proceed along simple lines as suggested by the derivations of polynomial methods in Section 2.

#### 3.1 Sinusoidal Extrapolation

Consider the general sinusoid of Figure 3,  $\Omega$  is known from characteristics of the system being simulated. The three remaining unknown parameters are "A" (amplitude), "a" (offset), and  $\theta$  (phase). It should then be possible to write three equations in terms of known values of  $\dot{X}(t)$ ,  $\dot{X}(0)$ ,  $\dot{X}(-T)$ ,  $\dot{X}(-2T)$  to solve for a, A and  $\theta$  from which an extrapolation,  $\dot{X}(T)$ , of  $\dot{X}(t)$  can be obtained.

First, note that it is perfectly general to locate the origin of the time axis,  $t = 0$ , at the present instant as long as the expression for the assumed sinusoidal function includes the unknown phase angle " $\theta$ " which locates the origin of the sine function at an arbitrary distance in time from the present instant.

Table 1 Summary of Integration Methods

	Difference Equation	Z-Transform	Truncation Error (First Term)	Remarks
<b>Predictor Methods</b>				
Adams-Bashforth	$X(T) = X(0) + \frac{T}{12}(23\dot{X}(0) - 16\dot{X}(-T) + 5\dot{X}(-2T))$	$\frac{T(23Z^2 - 16Z + 5)}{12Z^2(Z - 1)}$	$\frac{3}{8} T^4 \ddot{\ddot{X}}$	2nd order polynomial
Trapezoidal Predictor	$X(T) = X(0) + \frac{T}{2}(3\dot{X}(0) - \dot{X}(-T))$	$\frac{T(3Z - 1)}{2Z(Z - 1)}$	$\frac{5}{12} T^3 \ddot{X}$	Linear
Euler	$X(T) = X(0) + T\dot{X}(0)$	$\frac{T}{Z - 1}$	$\frac{T^2}{2} \ddot{X}$	Zero order
Sinusoidal Predictor	$X(T) = X(0) + P_0\dot{X}(0) + P_1\dot{X}(-T) + P_2\dot{X}(-2T)$	$\frac{P_0Z^2 + P_1Z + P_2}{Z^2(Z - 1)}$	—	$P_0, P_1, P_2$ depend on $\Omega T$
<b>Corrector Methods</b>				
Reddy Parabolic	$X(0) = X(-T) + \frac{T}{12}(5\dot{X}(0) + 8\dot{X}(-T) - \dot{X}(-2T))$	$\frac{T(5Z^2 + 8Z - 1)}{12Z(Z - 1)}$	$-\frac{T^4}{24} \ddot{\ddot{X}}$	2nd order polynomial
Tustin	$X(0) = X(-T) + \frac{T}{2}(\dot{X}(0) + \dot{X}(-T))$	$\frac{T(Z + 1)}{2(Z - 1)}$	$-\frac{T^3}{12} \ddot{X}$	Linear
Rectangular (Advanced Euler)	$X(0) = X(-T) + T\dot{X}(0)$	$\frac{TZ}{(Z - 1)}$	$-\frac{T^2}{2} \ddot{X}$	Zero order
Sinusoidal Corrector	$X(0) = X(-T) + C_0\dot{X}(0) + C_1\dot{X}(-T) + C_2\dot{X}(-2T)$	$\frac{C_0Z^2 + C_1Z + C_2}{Z(Z - 1)}$	—	$C_0, C_1, C_2$ depend on $\Omega T$

GP31-0556-1



where:

$$P_0 = \frac{\Omega T \sin(\Omega T) - 2(1 - \cos(\Omega T)) (1 - 2 \sin^2(\Omega T))}{2 \Omega \sin(\Omega T) (1 - \cos(\Omega T))} \quad (3-14a)$$

$$P_1 = \frac{-\Omega T \cos(\Omega T) - \sin(\Omega T) (1 - 2 \cos(\Omega T))}{\Omega (1 - \cos(\Omega T))} \quad (3-14b)$$

$$P_2 = \frac{\Omega T \sin(\Omega T) + 2 \cos(\Omega T) (\cos(\Omega T) - 1)}{2 \Omega \sin(\Omega T) (1 - \cos(\Omega T))} \quad (3-14c)$$

The Sinusoidal Predictor integration method follows from the successive summation:

$$X(T) = X(0) + \Delta X(0, T);$$

$$X(T) = X(0) + P_0 \dot{X}(0) + P_1 \ddot{X}(-T) + P_2 \ddot{X}(-2T) \quad (3-15)$$

It should be noted that although the expressions for  $P_0$ ,  $P_1$  and  $P_2$  are somewhat complex they need only be computed once for a given  $\Omega$  and  $T$  and not at each iteration. Equation (3-15) corresponds to equation (2-1) with  $j=1$ ,  $k=3$ ,  $a_1=1$ ,  $b_0=0$ ,  $b_1=P_0/T$ ,  $b_2=P_1/T$  and  $b_3=P_2/T$ . The coefficients  $P_0/T$ ,  $P_1/T$  and  $P_2/T$  all reduce to 0/0 for  $\Omega=0$ . L'Hospital's rule states that if  $f(a) = g(a) = 0$  then:

$$\lim_{\Omega \rightarrow a} \frac{f(\Omega)}{g(\Omega)} = \lim_{\Omega \rightarrow a} \frac{f'(\Omega)}{g'(\Omega)}$$

where  $a=0$  and " $'$ " denotes differentiation with respect to  $\Omega$ . Four successive applications of L'Hospital's rule to the numerator " $f(\Omega)$ " and denominator " $g(\Omega)$ " of the expressions for  $P_0/T$ ,  $P_1/T$  and  $P_2/T$  proves that for  $\Omega=0$ ,

$$P_0/T = 23/12 \\ P_1/T = -4/3$$

and  $P_2/T = 5/12$

These are the coefficient values for the second order polynomial or Adams-Bashforth method developed in Equation (2-7). This result was anticipated from the fact (noted at the end of Paragraph 3.1) that the Sinusoidal Extrapolator reduces to second order polynomial extrapolation for  $\Omega=0$ . The sinusoidal methods form infinite sets as  $\Omega$  can take on any value between 0 and  $\pi/T$ .

It is, therefore not surprising to find that the sinusoidal methods include other methods as special cases but it is not immediately obvious why a sinusoid of zero frequency should be equivalent to a second order polynomial. For  $\Omega=\pi/T$ , or half sample frequency, the method blows up as  $P_0=-2/0$ ,  $P_1=1/2$  and  $P_2=-2/0$ . This anomaly is of little importance as the practical limit for  $\Omega$  lies well under that theoretical limit. The useful range of  $\Omega T$  (sinusoidal function frequency,  $\Omega$ , normalized to sample rate,  $1/T$ ) is investigated in Section 5.

### 3.3 Sinusoidal Corrector Integration

The development of this method exactly parallels that of the Sinusoidal Predictor method in the preceding paragraphs. Referring to Figure 3,  $\dot{X}(-2T)$ ,  $\dot{X}(-T)$  and  $\dot{X}(0)$  are given and it is desired to determine the integral of the function  $\dot{X}(t)$  for the segment  $(-T, 0)$ .

Assume that the trajectory of the integrand  $X(t)$  is best represented on the interval  $(-2T, 0)$  by the postulated sinusoidal function:

$$\dot{X}(t) = a + A \sin(\Omega t + \theta)$$

The integral segment would be:

$$\Delta X(-T, 0) = \int_{-T}^0 (a + A \sin(\Omega t + \theta)) dt \quad (3-16)$$

Expand and separate terms;

$$\Delta X(-T, 0) = a \int_{-T}^0 dt + \frac{A \sin \theta}{\Omega} \int_{-T}^0 \cos(\Omega t) dt + \frac{A \cos \theta}{\Omega} \int_{-T}^0 \sin(\Omega t) dt \quad (3-17)$$

Hence,

$$\Delta X(-T, 0) = at + \frac{A \sin \theta}{\Omega} \sin(\Omega T) + \frac{A \cos \theta}{\Omega} (\cos(\Omega T) - 1) \quad (3-18)$$

which is identical to (3-13), except for the sign of the third term. Again substitute (3-8), (3-9), and (3-10) for " $A \sin \theta$ ", " $A \cos \theta$ ", and " $a$ " and collect terms to obtain an equation of the form:

$$\Delta X(-T, 0) = C_0 \dot{X}(0) + C_1 \dot{X}(-T) + C_2 \dot{X}(-2T) \quad (3-19)$$

$$C_0 = \frac{\Omega T \sin(\Omega T) - 2 \cos(\Omega T) (1 - \cos(\Omega T))}{2 \Omega \sin(\Omega T) (1 - \cos(\Omega T))} \quad (3-19a)$$

$$C_1 = \frac{-\Omega T \cos(\Omega T) + \sin(\Omega T)}{\Omega (1 - \cos(\Omega T))} \quad (3-19b)$$

$$C_2 = \frac{\Omega T \sin(\Omega T) - 2(1 - \cos(\Omega T))}{2 \Omega \sin(\Omega T) (1 - \cos(\Omega T))} \quad (3-19c)$$

Thus, the Sinusoidal Corrector integration method follows from the successive summation of:

$$X(0) = X(-T) + \Delta X(-T, 0)$$

$$X(0) = X(-T) + C_0 \dot{X}(0) + C_1 \dot{X}(-T) + C_2 \dot{X}(-2T) \quad (3-20)$$

Equation (3-20) corresponds to equation (2-1) with  $j=1$ ,  $k=2$ ,  $a_1=1$ ,  $b_0=C_0/T$ ,  $b_1=C_1/T$  and  $b_2=C_2/T$ . For  $\Omega=0$ ,  $C_0/T$ ,  $C_1/T$  and  $C_2/T$  all reduce to 0/0. Again, four successive applications of L'Hospital's rule are required to prove that for  $\Omega=0$ :

$$C_0/T = 5/12 \\ C_1/T = 2/3$$

and

$$C_2/T = -1/12$$

which are, as expected, the coefficients for the closed form second order polynomial, or the Reddy parabolic integration method.

#### 4. Error Considerations

Brief remarks in Section 2 briefly noted the general preoccupation with truncation error as a measure of the accuracy of numerical integration methods and alluded to numerical stability and frequency domain characteristics which should receive primary consideration in real-time applications. This section is devoted to developing comparisons which reflect those considerations in a practical and understandable format.

##### 4.1 Truncation Error

The classical methods based on polynomials have truncation errors (listed in Table 1) which are derived from a comparison with the Taylor Series.

Application of similar reasoning to the sinusoidal methods produced an equation of the form:

$$\text{ERROR} = \frac{1}{2} \epsilon_1 \epsilon_2 T^5 \sin \epsilon + \frac{1}{24} \epsilon_1 \epsilon_2^3 \cos \epsilon + \frac{1}{24} \epsilon_1^3 T^5 \sin \epsilon + \frac{1}{24} \epsilon_1^3 T^5 \cos \epsilon \quad (4-1)$$

Note that for  $\omega T < 1.0$  the error expression will tend to be small, due to the powers of  $\omega T$ , but for  $\omega T > 1.0$  the error will grow rapidly for the same reason. This quality suggests a practical limit for sample interval such that  $\omega T < 1.0$  for the highest frequency ( $\omega$ ) to be handled.

For aircraft simulation this translates to a requirement for at least  $2\pi$  samples per cycle of the highest natural frequency. Also note that this limit would apply to all integration formulas considered here, as their truncation errors are expressed in a form similar to (4-1), differing only in the number of terms and values for  $\gamma$ .

The derivation of the error coefficients ( $\gamma$ 's) involves exceedingly complex trigonometric functions of  $\Omega$ . When function frequency,  $\Omega$ , equals the test input frequency,  $\omega$ , the ERROR equation should go to 0. Due to the complexity of the mathematics this proof remains incomplete.

The absence of this mathematical proof was not a concern since test cases with sinusoidal inputs proved that the integral did, in fact, agree exactly with the analytical solution for sinusoidal methods, using the same function frequency as the input signal frequency. Furthermore, the classical Taylor Series approach to determining truncation error is inappropriate to the frequency approach to numerical analysis suggested in Section 1.2.3. A sensible alternative to the Taylor Series is the Fourier Series, with which we can exactly represent some integrable function  $\hat{X}(t)$  on the interval  $0 \leq \Omega t \leq 2\pi$  by an infinite trigonometric series of the form:

$$\hat{X}(t) = \frac{a_0}{2} + \sum_{k=1}^{\infty} (a_k \cos(k\Omega t) + b_k \sin(k\Omega t)) \quad (4-2)$$

For  $\omega = \Omega$ ,  $\hat{X}(t) = \hat{X}(t)$  and the truncation error,  $\hat{X}(t) - \hat{X}(t)$ , goes to zero as expected. However, for  $\omega \neq \Omega$  the coefficient formulas for  $a_0$ ,  $a_k$  and  $b_k$  become quite involved. The complexity of these equations makes the interpretation of

error difficult even for  $\omega$  near  $\Omega$ . The graphical presentation of frequency response (Bode plots) undertaken in Section 4.3 is a much more useful format for error interpretation.

##### 4.2 Stability From Z-Domain Considerations

The study of discrete systems is greatly facilitated by the use of Z-transform calculus in the same way that Laplace transforms are the standard tool of continuous systems analysis. In fact, the Z-transform is a special form of the Laplace transform which maps the complex S-plane into the complex Z-plane through the definition:

$$z = e^{sT} \quad (4-3)$$

where T is the discrete system sample period and z and s are complex variables which are the Z-transform and Laplace operators respectively.

The theory and application of Z-transforms are well covered in the literature but several pertinent features bear repeating here. First, note that the Z variable functions as a unit time advance operator. Negative powers of Z correspond to units (T) of time delay. This property of the Z operator can be employed to transform difference equations into Z-domain transfer functions.

For instance the Sinusoidal Predictor integration difference equation (3-15)

$$X(T) = X(0) + P_0 \dot{X}(0) + P_1 \dot{X}(-T) + P_2 \dot{X}(-2T)$$

is written in terms of past, present, and future values in the sequences of X and  $\dot{X}$ . Using the Z operator to translate those variables in time the equation becomes:

$$zX(z) = X(z) + P_0 \dot{X}(z) + P_1 z^{-1} \dot{X}(z) + P_2 z^{-2} \dot{X}(z) \quad (4-4)$$

Collect terms and cross-divide to obtain an output, input ratio  $X(z)/\dot{X}(z)$ , or Z-domain transfer function.

$$X(z)(z-1) = \dot{X}(z) (P_0 + P_1 z^{-1} + P_2 z^{-2})$$

$$\frac{X(z)}{\dot{X}(z)} = \frac{(P_0 + P_1 z^{-1} + P_2 z^{-2})}{(z-1)} = \frac{P_0 z^2 + P_1 z + P_2}{z^2(z-1)} \quad (4-5)$$

This equation and the other discrete time transfer functions which approximate the continuous time transfer function for the integrator (1/s) are included on Table 1 for comparison.

##### 4.3 Frequency Response

The frequency domain performance of the various digital integration methods is simply obtained by substituting  $e^{j\omega t}$  for Z in the Z-domain transfer functions in the same way one would use  $j\omega$  for S in an S-domain transfer function. Again,  $\omega$  is the frequency of a sinusoidal test input signal, in radians/second. Figure 4 is a Bode plot of phase and gain versus  $\omega T$  for the methods considered. The expression  $\omega T$  is used instead of  $\omega$  to provide normalized curves for more general comparison.

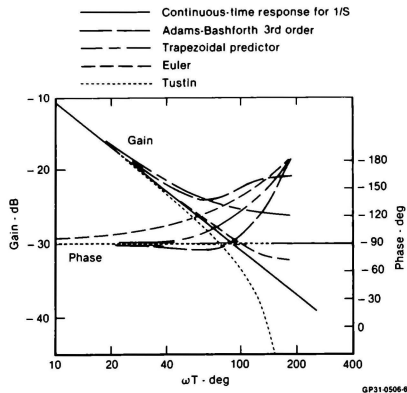


Fig. 4 Frequency Response of Classical Methods

4.3.1 Classical Methods. The results are interesting; first note that in the Euler integration the amplitude response shows only a minor gain at a larger  $\omega T$ . However, the phase error is the worst of the lot. The Trapezoidal Predictor shows a rather high gain and phase lag for increasing  $\omega T$ . The corresponding corrector form, Tustin's Method (6), shows zero phase error and little amplitude error until  $\omega T$  approaches  $180^\circ$  (half sample frequency), where the gain drops sharply to zero.

This is potentially a very useful characteristic as it would attenuate the half sample frequency noise which is inherent from round-off errors and analog-to-digital conversion. The accuracy should be sufficient (gain error less than 1 db) up to  $\omega T = 60^\circ$  (6 samples per cycle). The second order polynomial predictor method (Adams-Bashforth) provides  $180^\circ$  of phase lag at  $\omega T = 180^\circ$ . The Adams-Bashforth has a strong gain increase starting in the area of  $\omega T = 60^\circ$  which corresponds to the break point in truncation error discussed in Section 4.1.

4.3.2 Sinusoidal Methods. The Sinusoidal Methods are shown on Figures 5 and 6 for a family of  $\Omega T$  (sinusoidal function frequency times sample period). It is clear from the Bode plots that both gain and phase pass through the correct value for  $\omega T = \Omega T$ . This characteristic is the whole object of this method and results from the derivation which produces an exact integral value for an integrand waveform of the specified sinusoidal frequency.

Economical computation dictates using the slowest sample rate which is adequate to simulate the highest frequency of interest with stability and reasonable accuracy. By judicious choice of the function frequency,  $\Omega$ , the Sinusoidal Methods should permit some improvement in that direction. However, as the normalized sinusoidal function frequency,  $\Omega T$ , increases, the phase lag below that frequency rises significantly (see

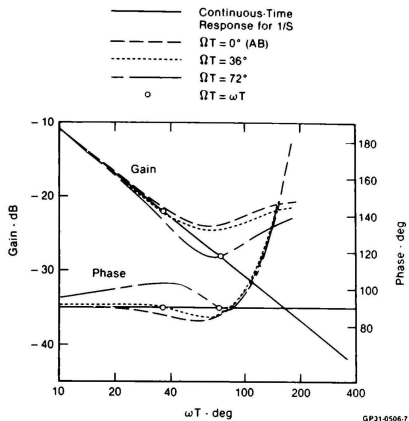


Fig. 5 Frequency Response of Sinusoidal Predictor

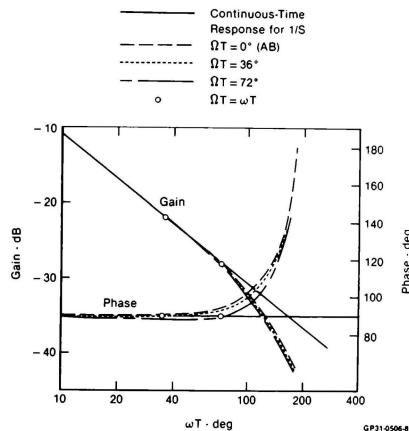


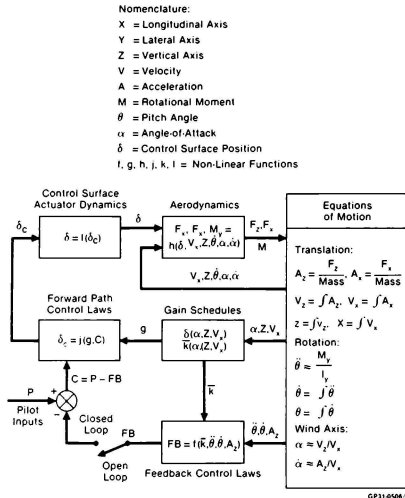
Fig. 6 Frequency Response of Sinusoidal Corrector

Figure 5). Also the phase lag and gain above that frequency break more sharply as  $\Omega T$  is increased. Although the response can theoretically be exact for an arbitrarily large  $\Omega T$  (up to  $\Omega T = 180^\circ$ ) the increasing distortion at adjacent frequencies is sure to impose practical limits on  $\Omega T$  which are to some extent dependent on response characteristics of the dynamic system being simulated. These limits are investigated in the following section.



## 5. Application

The development of the sinusoidal methods in the preceding sections promises greater stability and accuracy for the integration of the equations of motion of a dynamic system in real-time. The test of that thesis is the application of the new methods to a man-in-the-loop simulation of a high performance fighter aircraft. Figure (7) presents a simplified block diagram of the longitudinal axis of the flight dynamics.



### 5.1 Simulation Program Description

A currently operational aircraft development simulation program was chosen as a test case for several reasons:

- a) The aircraft is a high performance vehicle with a wide variation of natural frequency over the flight envelope (less than 2 radians to greater than 15 radians).
- b) The control system represents state-of-the-art design, incorporating high order dynamic elements plus acceleration and rate feedback.
- c) The program was suffering from computational instability at critical flight conditions for the .05 second sample interval required for full mission simulation.

This program then presented a most challenging example of the "problem" and an opportunity for immediate practical application.

The simulator software program was arranged as follows:

- 1) Beginning of interval; analog-to-digital, sample pilot inputs (aircraft state variables known from end of previous interval)
- 2) Control system
- 3) Aerodynamic forces and moments, valid for beginning-of-interval
- 4) Extrapolation of accelerations to end-of-interval; Integration for Velocity and Position.
- 5) Computation of complete state for end-of-interval
- 6) Aircraft systems; simulator systems
- 7) Digital-to-analog output
- 8) Wait for end-of-interval; go to 1

This outline is greatly simplified, but it specifies the sequence of computation employed in the program. The most important elements are described in more detail in the following Sections.

**5.1.1 Aircraft Model.** The aircraft aerodynamic model included full flight envelope six-degree-of-freedom nonlinear (tabular) data with flexibility effects. The mass and inertia properties included all gyroscopic and crosscoupling terms as well as time varying effects from fuel and payload expenditure. For simplicity this paper treats only the longitudinal axis.

As is usual for real-time simulation, the aircraft was modeled as a point mass so that the high frequency dynamics of structural modes such as body bending and control surface flutter were not present. A sample rate high enough to handle those frequency components would be incompatible with real-time operation.

The control system simulation incorporated a complete digital model of each element in the loop, including nonlinear elements such as mode switching, scheduled gain and limit functions, and load dependent actuator rate and position limits. All of the dynamic elements such as filters, accelerometers, rate gyros, and compensation networks were modeled using Tustin's Method (6). Briefly, Tustin's Method involves the substitution of the inverse of the Z-transform of the Tustin integrator (see Table 1) for the Laplace operator "S" in the transfer function being modeled. The resulting "Z" transfer function is transformed to an approximating discrete-time difference equation using the properties of the Z operator as described in Section 4.2.

Each difference equation approximating a continuous transfer function will contribute some gain and phase error which increases with increasing sample interval. However, Tustin's Method is a corrector type (closed form) which will, in general, produce a stable accurate simulation for time constants as small as one-half

the sample interval. Thus, if the dynamic elements in the control system are programmed with care, the predictor (open form) integrator required in the equations of motion remains as the most significant source of error in the loop.

**5.1.2 Equations of Motion.** In the test program a laboratory "standard" equations of motion subroutine was originally employed. This routine, typical of many in use today, utilized Adams-Bashforth integration (second order polynomial predictor).

The first attempt at testing the Sinusoidal Methods involved simply substituting the Sinusoidal Predictor coefficients for the Adams-Bashforth coefficients. The results were encouraging but a new equations-of-motion subroutine was programmed to provide flexibility for testing the various integration methods and for implementing modes of operation which might eliminate some of the problems with transport delays and compounding predictor errors.

## 5.2 Check Case Objectives

The primary objective of the check case program was to verify the thesis that sinusoidal integration could extend the sample interval for stable computation. The secondary objective was to investigate the effect of acceleration extrapolation.

Additional data was evaluated for "off-optimum" sinusoidal function frequency at the critical flight condition. The use of the critical condition function frequency at other flight conditions was also investigated.

## 5.3 Check Case Description

The primary flight condition selected for evaluating of computational stability was a critical high Mach, high altitude point where the closed loop natural frequency was at a maximum (approximately 15 radian/second) and the gain and phase margins were low (approximately 3 dB and 30 degrees). Sample intervals as long as  $T = .06$  second were attempted; this puts the operations very near that limit suggested by the consideration of truncation error in Section 4.1. That is,  $\omega T = (15)(.06) = 0.9$ , just under the limit of 1.0. The investigation of computational accuracy required check cases spanning a wide range of system response, so flight conditions with a closed loop natural frequency as low as 1.75 radians per second were also included.

Check cases were evaluated for step inputs in longitudinal (pitch), lateral (roll), and directional (yaw). The results were comparable for all axes so only the longitudinal axis check cases are included for comparison and documentation.

All of the results obtained from these check cases were verified in real-time operation with the pilot in the loop to test large amplitude maneuvers in all three axes. In no case was the pilot able to drive aircraft into false instability for a configuration which showed a stable, non-oscillatory response in the check case.

## 5.4 Results

The check case program was extensive, covering many combinations of numerical methods for a wide range of system response frequency. The evaluation of those check cases was tedious but rewarding in that the results clearly demonstrated the practical applicability of the postulated methods.

Acceleration extrapolation was incorporated to avoid the errors caused by using a beginning-of-interval value for acceleration in the computation of end-of-interval data. This transport delay is a certain problem area where acceleration feedback is included in the control law, but it is also present in the open loop case (no feedback) as acceleration is a factor in the angle-of-attack-rate term, which has an important transient effect on aerodynamic lift and pitching moment.

Acceleration extrapolation resulted in only a slight improvement in the accuracy of the load factor response (translational acceleration) at the critical high frequency flight condition, but the improvement was dramatic at lightly damped lower frequency conditions for both open and closed loop check cases. Figure 8 illustrates the accuracy improvement in phase and damping.

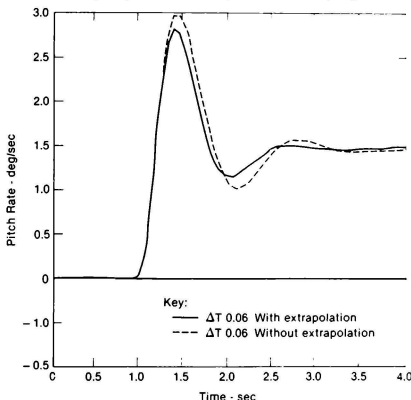


Fig. 8 Effect of Acceleration Extrapolation

The most effective program arrangement started with an acceleration extrapolation to the end-of-interval. Then two closed form (corrector) integrations on that extrapolated acceleration produced velocity and position valid for the end-of-interval. The extrapolator and corrector integration in series are mathematically equivalent to a predictor integration. If the predictor integration method is used, additional computations must still be made to obtain extrapolated acceleration.

It must also be noted that all of the extrapolation methods employed in this study tend to amplify signals at half sample frequency, and this characteristic can degrade stability. The use of a Tustin integrator after the extrapolator reduces the destabilizing effect of the extrapolator.

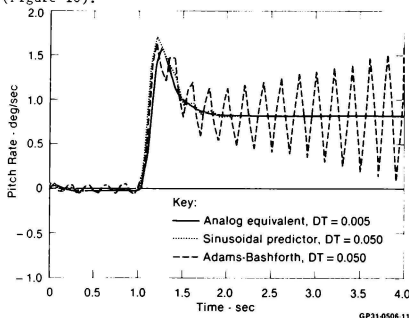
The implementation of sinusoidal methods effects an additional improvement in stability and accuracy for large  $\Omega T$ . Note from Table 2 that the sinusoidal methods extend the maximum sample interval by almost .02 second or 50 percent.

Table 2 Maximum Sample Interval Comparison

Method	Maximum Usable Sample Interval (sec)
Euler	0.01
Trapezoidal Predictor	0.03
Adams-Bashforth	0.04
Sinusoidal Predictor	0.05
Sinusoidal Extrapolator and Sinusoidal Corrector	0.06(-)
Sinusoidal Extrapolator and Tustin (Corrector)	0.06

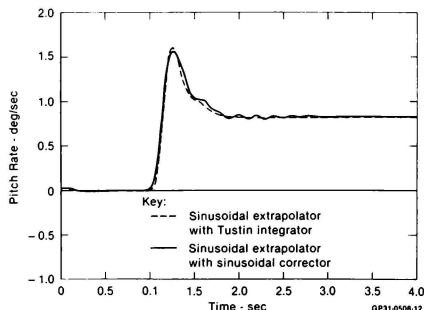
GP31-0506-2

This result was based on the critical closed loop condition (Figure 9) but the improvement was similar for a non-critical open loop check case. The best response is obtained with a Sinusoidal extrapolator followed by a Tustin integrator (Figure 10).



GP31-0508-11

Fig. 9 Sinusoidal Predictor vs Adams-Bashforth



GP31-0508-12

Fig. 10 Tustin vs Sinusoidal Corrector

To summarize the results, it is fair to say that the main objectives of this thesis were accomplished with a high degree of success. The implementation of: 1) acceleration extrapolation, and 2) sinusoidal numerical methods has extended the maximum useful sample interval for a stable, accurate computation from .04 second to .06 second. This 50 percent increase in usable computation time represents a major improvement in simulation capability. It extends the time available for additional computations such as simulator special effects, vehicle subsystems, or multiple vehicle programs. Other constraints (computer output signal stepping, etc.) may not permit operation at the maximum usable sample interval, but the improvements in accuracy obtained at shorter sample intervals still make the incorporation of these methods a worthwhile effort.

A final word of caution is in order: the methods outlined above do not "guarantee" stability or accuracy, as the integration algorithm does not compensate for gain and phase errors in the numerical approximation of other dynamic elements in the loop. This should not be a problem if proper closed form numerical approximations are used and sound programming practices are followed throughout.

## 6. Discussion

### 6.1 Summary

The understanding that many classical methods of numerical integration are based on a polynomial curve fit through past values of the integrand suggested the thesis that a sinusoidal fit might provide more accurate results in the simulation of a system whose response tends to be sinusoidal.

The derivations of the Sinusoidal Extrapolator, Sinusoidal Predictor integration, and Sinusoidal Corrector integration have been accomplished in a straightforward manner (Section 3) suggested by the derivation of polynomial based classical methods (Section 2). The resultant difference equations are simple to apply but the coefficients for the integration formulas are somewhat complex functions involving the sine and cosine of  $\Omega T$  (sinusoidal function frequency,  $\Omega$ ; sample interval,  $T$ ). This complexity is not a serious drawback since the coefficients need only be computed when  $\Omega T$  changes.  $T$  is fixed for the duration of any run in real-time and in some cases a fixed  $\Omega$  can also be used.

In any case the penalty in computation time required for updating the integration coefficients in real-time is very small in comparison to the total sample interval. Furthermore, the consideration of truncation error and frequency response characteristics in Section 4 indicated that the implementation of sinusoidal methods should result in a significant increase in the maximum usable sample interval for stable, accurate computation.

This thesis was tested by incorporating sinusoidal extrapolation and sinusoidal integration into the equations of motion of a large scale fighter aircraft simulation program (Section 5). The usable computation interval was increased 50% over the best classical method.

## 6.2 Conclusion

The ultimate goal of this development was a practical solution to the problem of computational instability in real-time simulation. The initial premise was that polynomials were being sent to do a sinusoid's job. The sinusoidal methods developed to remedy that situation did a credible job but the actual system does not generally respond with pure sinusoidal motion; it may be that numerical methods based on a damped second order system response would be even better!

### References

1. Fowler, Maury E., A New Numerical Method for Simulation, Simulation, Volume 4, May 1965, pp. 324-330.
2. Hurt, James M., New Difference Equation Technique for Solving Nonlinear Differential Equations, American Federation Information Proceedings, Vol. 25, 1964, Spring Joint Computer Conference, pp. 169-179.
3. Nigro, Bart J., An Investigation of Optimally Stable Numerical Integration Methods with Application to Real Time Simulation, Simulation, November, 1969, pp. 253-264.
4. Nigro, Bart J., Study of Numerical Integration Techniques for Real-Time Digital Flight Simulation, Aerospace Medical Research Laboratories, Publication TR-67-4, Wright-Patterson Air Force Base, Ohio, March, 1967.
5. Smith, J. M., Recent Developments in Numerical Integration, Transactions of the ASME, Journal of Dynamic Systems, Measurement and Control, March, 1974.
6. Tustin, A., A Method of Analyzing the Behavior of Linear Systems in Terms of Time Series, Journal of the IEE, Proceedings of Convention on Automatic Regulators and Servomechanisms, Vol. 94, Part II, August, 1947, pp. 130, 142.

R. E. McFarland\*

NASA Ames Research Center, Moffett Field, California

Abstract

Nonlinear mathematical models of a rotor system, referred to as rotating blade-element models, produce steady-state, high-frequency harmonics of significant magnitude. In a discrete simulation model, certain of these harmonics may be incompatible with realistic real-time computational constraints because of their aliasing into the operational low-pass region. However, the energy in an aliased harmonic may be suppressed by increasing the computation rate of an isolated, causal nonlinearity and using an appropriate filter. This decontamination technique is applied to Sikorsky's real-time model of the Black Hawk helicopter, as supplied to NASA for handling-qualities investigations.

I. Introduction

During a typical dynamic check, Sikorsky's real-time model of the Black Hawk helicopter<sup>1</sup> produces the vehicle angular acceleration histories shown in Fig. 1(a), where the cycle time is 20 msec, and the velocity is 100 knots. The steady-state frequency content is a consequence of real, nonlinear physical relationships, but may be destructive to real-time simulation, especially because of the aliasing phenomenon. In addition to high frequencies of dubious value to real-time, man-in-the-loop simulation, the model's performance is degraded by the appearance of folded  $N/\text{rev}$  rotor harmonics in the operational low-frequency region. These harmonics may cause problems ranging from fictional tracking tasks to deterioration of simulator hardware. Conventional filter techniques are not directly applicable to frequencies superimposed on the operational region. The computer scientist is therefore put in the embarrassing position of creating pilot workload where none should exist.

A "decontamination algorithm" is discussed here that takes advantage of the known harmonic positions of these signals relative to the rotor's rpm, prior to aliasing. "Decontamination" rather than "filtering" occurs because aliased frequencies are purged whereas coincident important frequencies are not altered.

In this presentation, certain simplifying operations have been initially performed, as manifest in Fig. 1(b). An  $N/\text{rev}$  notch filter (where  $N$  is the number of blades) was used on the total rotor system outputs, and certain high-frequency terms in the inertial dynamics were deleted. The yaw axis remains contaminated by a 1.5-Hz limit cycle (Fig. 1(b)), and this signal is used to illustrate the decontamination algorithm.

Direct application of the algorithm to the yaw limit cycle produced the traces shown in Fig. 1(c). Frequencies of interest remain intact, but the rotor generated harmonic at 1.5 Hz is purged.

---

\*Research scientist.

This paper is declared a work of the U.S. Government and therefore is in the public domain.

II. Aliasing

Figure 2 displays the aliased location of the first four multiples of  $N/\text{rev}$  as a function of cycle time. Any contaminating frequency observed in the model may be computed from its harmonic origin via the given aliasing equation, where the half-bracket operation is the "least integer" or "floor" operator. Although all frequencies in a discrete model are contained within the envelope given by the Nyquist hyperbola,  $N/\text{rev}$  multiples are of special interest in a rotor model. In particular, at the 20-msec cycle time, the  $3N/\text{rev}$  frequency folds to 1.5 Hz. This aliased frequency constitutes the real-time, low-frequency problem when the cycle time is 20 msec.

From a mathematical point of view, a feasible cycle time is closely associated with the convergence features of these harmonics. If  $N/\text{rev}$  power is known to be negligible beyond the fourth harmonic, for instance, a cycle time of 24 msec would most probably be superior to a cycle time of 20 msec. Aliased frequency content would then remain above about 7 Hz (beyond the bandwidth of most simulation hardware and pilot responses).

III. Rotor-Generated Power

"Rotor-generated power" occurs at multiples of the rpm for each blade as a consequence of the blade's periodic physics. The fact that the total rotor system displays this power only at multiples of  $N/\text{rev}$  is a consequence of the orthogonality of sines applied to the periodic physics of blades with equal spacing.

When an unrealistically small cycle time, such as 5 msec, is used to examine this power, the  $N/\text{rev}$  spectral windows are quite clear, as shown in Fig. 3. The spectral peaks in this figure conform to the aliasing equation, and are designated according to their origins up to the astonishing value of  $12N/\text{rev}$ , or 206 Hz.

If the real-time model could be executed and drive all simulation subsystems at a cycle time of 5 msec, the aliased frequency content would be reduced to the status of a minor annoyance in the low-frequency region. Nonetheless, aliasing occurs even with this unrealistically small cycle time.

IV. Realistic Cycle Times

At realistic cycle times, the low-frequency region is contaminated by frequency content of significant magnitude, as shown in Fig. 4. For the 20-msec example (Fig. 4(a)), the  $3N/\text{rev}$  harmonic appears at the predicted aliased frequency of 1.5 Hz. For the 30-msec example (Fig. 4(b)), the low-frequency contamination is more severe because its major source is the energetic  $2N/\text{rev}$  signal. Both superposition of harmonics and computational degradation distort the model with large cycle times.

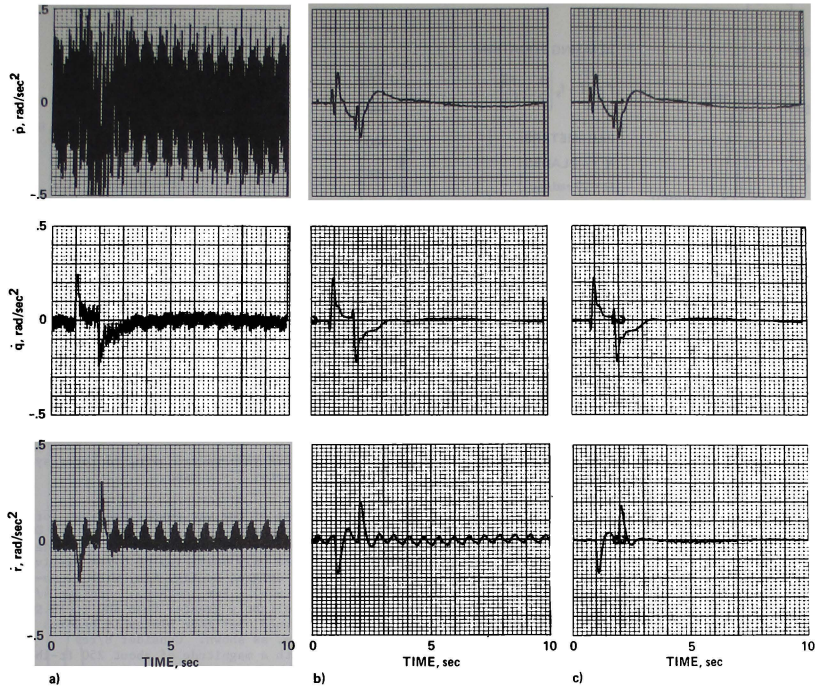


Fig. 1 Angular accelerations: vehicle velocity  $V = 100$  knots, cycle time  $T = 20$  msec.  
a) Original model; b) after simplifying operations; c) final model.

The 20-msec case (Fig. 4(a)), is the spectrum of the original model's yaw acceleration, shown in the time-histories of Fig. 1. Only the 1.5-Hz signal is pertinent to this discussion; it alone survives the postprocessing procedure of filtering the region around  $N/\text{rev}$ .

#### V. Problem Source

In an investigation of the spectrum of various system variables, the lag damper was isolated as the major source of the  $3N/\text{rev}$  signal. The lag damper functionality is a saturation element, and harmonics may be predicted from an idealized representation. The axial rate of the lag damper arm for each blade is the input to the nonlinearity, and this rate consists of rapidly decreasing harmonics of the rpm, as will be shown. An  $m$ th harmonic (of the rpm) component in the axial rate may be represented by

$$\dot{f}_{m,n,k} = r_m \sin(m\psi_{n,k}) \quad (1)$$

where the azimuth angle of a particular blade is

$$\psi_{n,k} = k\omega T + 2\pi(n-1)/N \quad \begin{cases} (n = 1, 2, \dots, N) \\ (k = 1, 2, \dots) \end{cases} \quad (2)$$

Because of the input of this harmonic signal alone, the damper will output an infinite set of odd harmonics of it, for example,

$$g_{m,n,k} = \sum_{i>0} R_{m,i-1} \sin[(2i-1)m\psi_{n,k}] \quad (3)$$

For each individual blade, these signals provide damping to the differential equations describing lagging and flapping motion. However, the summed damper contribution to the total rotor torque has selective spectral windows for rpm multiples,

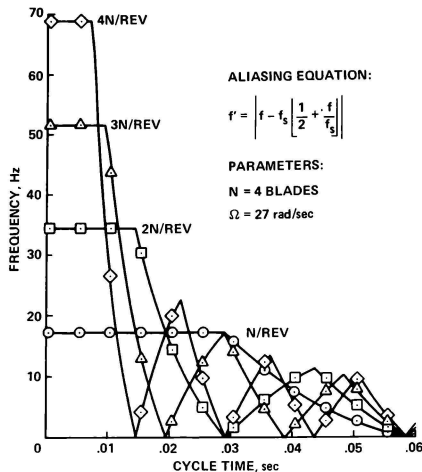


Fig. 2 Black Hawk N/rev aliasing.

that is,

$$h_{m,k} = \sum_{n=1}^N g_{m,n,k}$$

$$= \begin{cases} \sum_{i>0} R_{m,zi-1} \sin[(2i-1)mk\pi T] & (2i-1)m/N \text{ integer} \\ 0 & \text{otherwise} \end{cases} \quad (4)$$

Integer multiples of the rpm that are not also multiples of the number of blades  $N$  do not survive this summation process. Since  $N$  is even, only odd harmonics of the surviving  $N/\text{rev}$  signals are transmitted.

## VI. Observed Spectra

Using the full simulation model, the generation of harmonics by the lag damper is spectrally illustrated in the next two figures. In Fig. 5(a), the lag damper axial rate spectrum is shown for any given blade, as input to the lag damper function, where the multiples of the rotor's rpm are indicated. The lag damper force output (Fig. 5(b)) contains significant power at odd multiples of the input frequencies. This power is a consequence of the lag damper nonlinearity, and propagates throughout the rotor model. Of particular concern to us here, however, is the direct summation of damper signals over the blade index. After multiplication by the moment arm, as shown in Fig. 6, the spectrum is not altered.

As shown in Fig. 6(a), the spectrum is essentially unchanged with the conversion from force to moment summing. After summation over the blade index

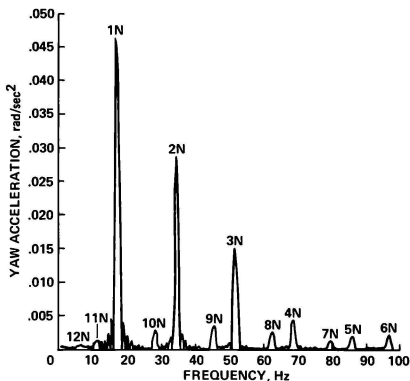


Fig. 3 Black Hawk yaw spectra owing to rotor system:  $V = 100$  knots,  $T = 5$  msec.

(Fig. 6(b)), most of the yaw output spectrum for the total rotorcraft may be identified; 1/rev, 2/rev, and 3/rev in Fig. 6(a) have vanished under summation. Since only multiples of  $N/\text{rev}$  survive, we can identify origins in Fig. 6(a) with consequences in Fig. 6(b). For instance, consider 4/rev<sup>1</sup> with magnitude slightly greater than 400 ft-lb. When this is summed over four blades it becomes 4 times as large, as shown. Consider 8/rev (Fig. 6(a)), with a magnitude of about 250 ft-lb. When this is summed it also becomes 4 times as large, as shown. Since only odd multiples of the input  $N/\text{rev}$  harmonics survive the summation, the 3N/rev signal is identified as the first surviving odd multiple of  $N/\text{rev}$ , which would appear at about 51.5 Hz if aliasing did not occur.

The magnitude of the 3N/rev signal may be compared with that of a well-known nonlinear function. In particular, if the saturation element was a Coulomb friction or bang-bang system, the amplitude of this harmonic would be exactly one-third of the  $N/\text{rev}$  signal. This is effectively a close approximation to the saturation system in the model, because the 3N/rev signal is just slightly less than this value.

Blade frequencies that are rpm multiples of the number of blades have unusual significance in the summation process, and 4/rev produces the fundamental  $N/\text{rev}$  output, along with its harmonic 3N/rev. This energetic harmonic is then folded to the annoying 1.5-Hz position in conformance with the Shannon sampling theorem. The 8/rev signal also survives the summation process, and is aliased to the approximate position of the  $N/\text{rev}$  signal, as shown in Fig. 6. However, it may be conveniently suppressed, because when the total rotor-system outputs are operated upon by the  $N/\text{rev}$  notch filter,

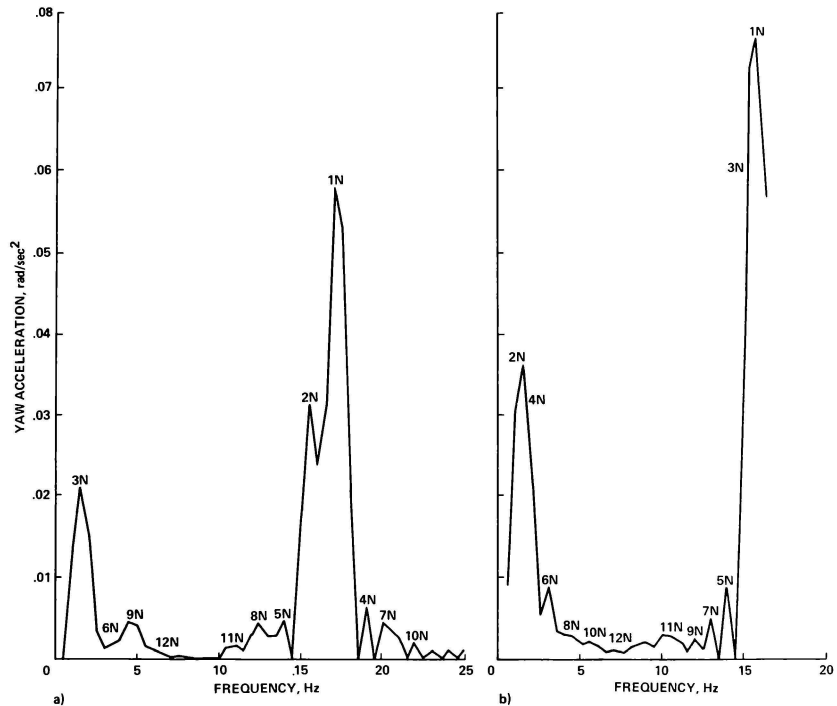


Fig. 4 Black Hawk yaw spectra at realistic cycle times. a)  $T = 20$  msec; b)  $T = 30$  msec.



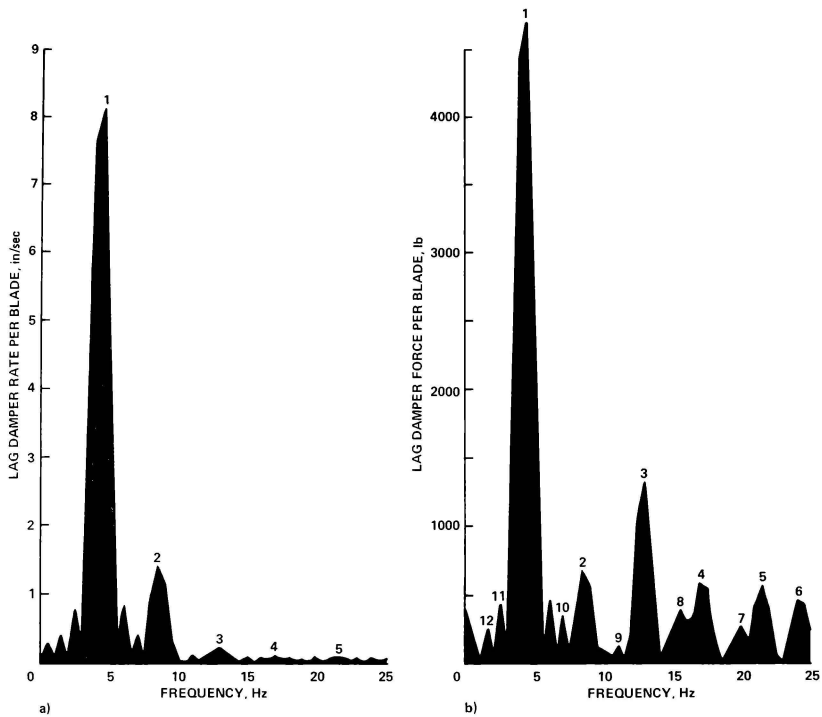


Fig. 5. Saturation element spectra:  $V = 100$  knots,  $T = 20$  msec. a) Input spectrum; b) output spectrum.

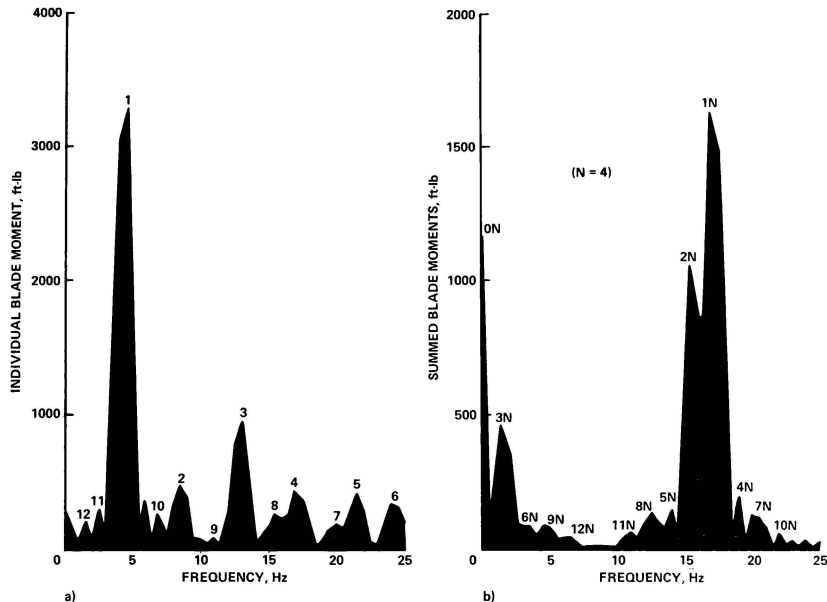


Fig. 6 Lag damper moment spectra:  $V = 100$  knots,  $T = 20$  msec. a) Individual blade moments; b) summed blade moments.

both  $N$  and  $2N/\text{rev}$  are attenuated. Thus, using the 20-msec cycle time, only the  $3N/\text{rev}$  signal constitutes significant contamination of the low-frequency region.

#### VII. Subsystem Interpolation

In real-time simulation, a cycle time of 20 msec implies an actual computer workload of something slightly less than this value. Hence, the option of decreasing the cycle time by any significant amount is not available. However, if just some minor subsystem or element of the model required solution at a higher rate, then perhaps this could be accomplished without materially influencing the computer workload. This interpolation scheme may be called "quasi-cycles," and it has been used with good results when the numerical stability of some partially closed-loop subsystem required it. Since this technique decreases computational degradation in the subsystem, it more accurately creates the high-frequency content which manifests itself as a low-frequency problem. The quasi-cycle technique does not address the aliasing problem because the final outputs of the interpolated system must be decimated in order to communicate with the rest of

the simulation model, and this is the operation that aliases the harmonics.

#### VIII. The Nested Subsystem

When the causal nonlinearity can be identified and isolated, as in the Black Hawk model, the decontamination algorithm makes use of the quasi-cycle technique. This is shown in Fig. 7, where the notch frequency is 3 times  $N/\text{rev}$ , and the effective quasi-cycle Nyquist frequency has been increased to the inverse of the original cycle time, given by  $1/T$ .

The nested subsystem requires interpolation of inputs, which in this case doubles the Nyquist frequency. The nonlinear operation, here performed at the expanded rate, creates the harmonics. Since the nonlinearity is an odd function, the first harmonic of  $N/\text{rev}$  is  $3N/\text{rev}$ , with a relative magnitude of about one-third. By expanding the Nyquist frequency to include this harmonic without serious aliasing problems, the harmonic may be operated upon by a conventional filter. This filter is designed to eliminate the power in the  $3N/\text{rev}$  harmonic so that when the decimation occurs to the original Nyquist frequency (shown here at the point

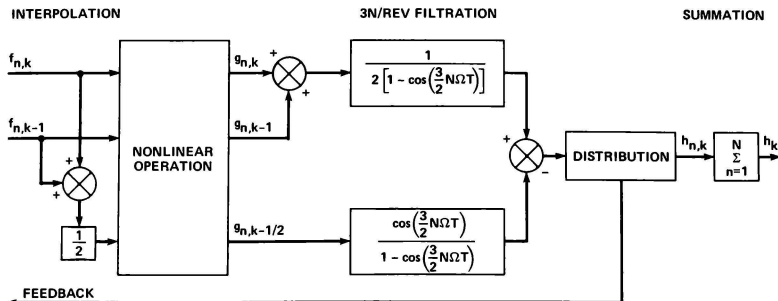


Fig. 7 Implementation of the decontamination algorithm.

of distribution), the operational region is decontaminated.

### IX. Notch Filter

The discretely designed notch filter used in the decontamination algorithm requires that the notch frequency be located within the interval between one-half and three-halves of the Nyquist frequency of the quasi-cycle. For our particular example, the quasi-cycle has the expanded Nyquist frequency of 50 Hz, or twice the original, and the 3N/rev frequency is about 51.5 Hz. Hence, the interval criterion is satisfied, and remains satisfied for large rpm variations. Using three sequential inputs at the expanded computation rate, given by  $g(k-1)$ ,  $g(k-1/2)$ , and  $g(k)$ , the filter output relationship is

$$h(k) = \frac{\frac{1}{2} g(k) + \frac{1}{2} g(k-1) - \cos\left(\frac{1}{2} HT\right) g\left(k - \frac{1}{2}\right)}{1 - \cos\left(\frac{1}{2} HT\right)} \quad (5)$$

where  $H$  is the notch frequency in radians per second (function of rpm), and  $T$  is the original cycle time. The filter response to a sine wave of frequency  $w$  is thus,

$$g(k) = \frac{\cos\left(\frac{1}{2} wT\right) - \cos\left(\frac{1}{2} HT\right)}{1 - \cos\left(\frac{1}{2} HT\right)} \sin\left[\left(k - \frac{1}{2}\right)wT\right] \quad (6)$$

The gain of this filter is shown in Fig. 8, where multiples of rpm are indicated. In the operational region, limited by a very few hertz, the attenuation is negligible.

The decimation process is indicated by a dashed line in Fig. 8; rpm multiples higher than five are aliased to positions below the Nyquist frequency of 25 Hz, but the filter provides attenuation prior to aliasing. In particular, the operational region is cleared of rotor-generated contamination.

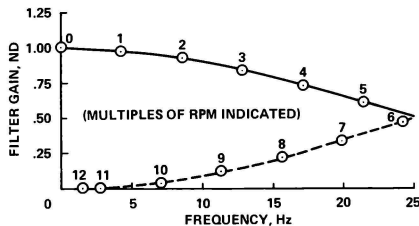


Fig. 8 Filter gain with decimation.

### X. Conclusion

For real-time simulation, high-frequency content is not generally addressed, owing to bandwidth limitations, although the modeled physical entity may itself suppress these frequencies by some such phenomenon as structural damping. The decontamination algorithm provides a technique for eliminating these frequencies, while preserving input-output relationships that are considerably more important to man-in-the-loop operations.

### Reference

- <sup>1</sup>Howlett, J. J., "UH-60A Black Hawk Engineering Simulation Program. Volume I - Mathematical Model," NASA TM-166309, Dec. 1981.

Rajan Shastri  
Gould Inc., S.E.L. Computer Systems Division  
Fort Lauderdale, Florida

### Abstract

In most real-time applications such as simulation and process control, the scope of the project at its onset is usually much smaller than what it turns out to be downstream into the project. As the project progresses, additional requirements are specified and a situation is reached wherein the programs expand to consume all available compute power and/or resources. This paper describes the characteristics of a real-time application in the field of simulation and process control, explores the nature of the problem and suggests some implementation considerations that should be adapted in the initial design phase. In doing so, down-the-line enhancements are readily accommodated and, if necessary, resources may be added incrementally, such that the system as a whole never reaches a performance or resource threshold.

### Characteristics of a Real-Time Application

A typical application in simulation, lab/comp, or process control involves a computer system in a feedback control loop. (Figure 1) The feedback control loop involves a set of inputs that are operated upon by programs executing in the computer system(s), resulting in a set of outputs that control the process.

The formal representation of the problem could be as follows:

$$\begin{bmatrix} O_1 \\ O_2 \\ \vdots \\ O_{M-1} \\ O_M \end{bmatrix} = \begin{bmatrix} P_{11} & \dots & P_{1N} \\ P_{21} & & P_{2N} \\ \vdots & & \vdots \\ P_{M-11} & \dots & P_{M-1N} \\ P_{M1} & \dots & P_{MN} \end{bmatrix} \begin{bmatrix} I_1 \\ I_2 \\ \vdots \\ I_{N-1} \\ I_N \end{bmatrix}$$

$$\begin{matrix} O \\ MX1 \end{matrix} = \begin{matrix} P \\ MXN \end{matrix} \times \begin{matrix} I \\ NX1 \end{matrix}$$

where:

$O$  is the set of Outputs

$M$

$I$  is the set of Inputs

$N$

$P$  is the set of processing elements

$MN$

(processes) which are sub-components of the software

$i=M$

$j=N$

$$\text{i.e. } \sum_{i=1}^M \sum_{j=1}^N P_{ij} = \text{Programs that control the process. (Tasks)}$$

### Traditional Solutions

Traditionally, because of the hardware expenses involved, the processing elements were all incorporated into one monolithic task that analyzed all the inputs, processed them, determined the set of outputs that controlled the process and performed output. This approach has the natural tendency to make the task overly complicated. If the number of inputs and outputs are many and the frequency at which input samples are collected is high, a situation may arise where the speed of the processor becomes a limiting factor. At this point an upgrade of the processor to one that has a higher computing capacity would be necessitated. The assumption here is that the investment in software is so heavy that to redo all the software and distribute it over multiple processors would be uneconomical.

### Shared Memory Implementation

With the reduction in hardware costs and with multiprocessed shared memory configuration, (Figure 2) it became possible to vertically decompose the problem such that one processor handled all the inputs and after doing scaling and some pre-processing, formatted the results in shared memory. A second processor would analyze these inputs and proceed to provide the outputs or invoke a third processor to perform the output functions. At times it was possible to partition the inputs and outputs further, if for example, it was found that a certain subset of the inputs determined a certain subset of outputs, and had no relation whatsoever to other subsets of inputs that determine a separate set of outputs. This form of horizontal partitioning along with vertical partitioning brought about a further decomposition of the problem. Shared memory configurations, however, tend to be limiting because of interconnection complexity. A majority of multiprocessor configurations involving shared memory have no more than four processors configured.

### Common Bus Implementation

Multiprocessor configurations whereby more than one processor share the same memory via a common system bus is an elegant way in which incremental performance is attainable at relatively low cost. (Figure 3) However, it has been experienced that, the marginal performance improvement per additional processor drops off significantly because of bus contention. Moreover, such an architecture is currently limited by the amount of addressable memory that is available to the system. In the future this will not necessarily be a constraint, but currently, memory becomes the limiting factor before the performance threshold is reached.

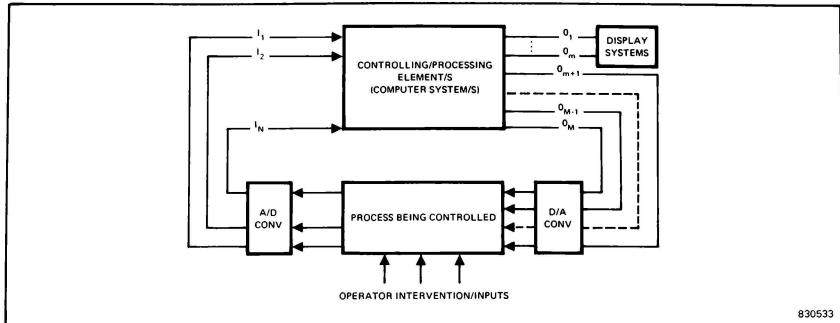


Figure 1. Typical Application in Simulation, Lab/Comp, Process Control

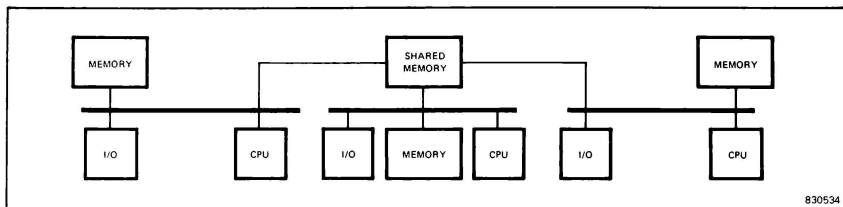


Figure 2. Shared Memory Configuration

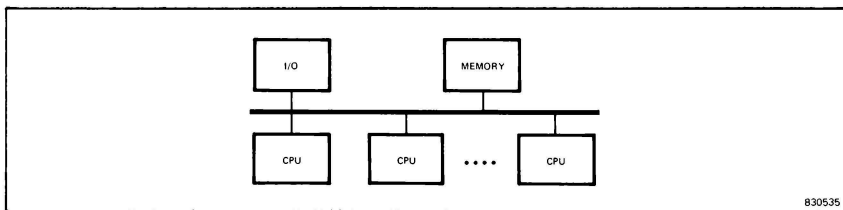


Figure 3. Common Bus Configuration

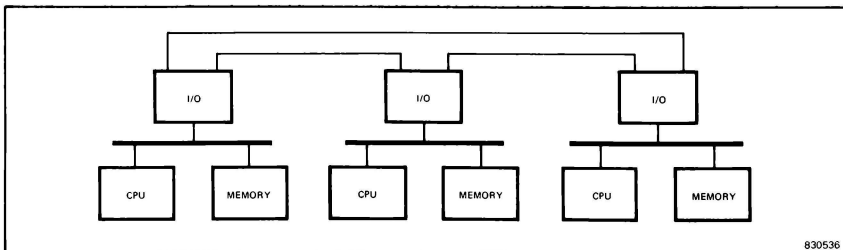


Figure 4. Distributed Processing Configuration

### Distributed Implementation

The availability of high-speed I/O devices has been instrumental in implementations wherein tasks executing on different computers interact with one another via a communication link. (Figure 4) Often these computers exist in the form of a tight cluster and are dedicated to the application. This implementation has virtually no limiting factor as far as resources or compute power is concerned.

However, system performance expectations may not be met due to inherent communication delays.

### Other Limiting Factors

The common limiting factor with most implementations involving shared memory and distributed processing is that adding more CPU's and partitioning the existing processes over the expanded configuration is not an easy chore from the software viewpoint.

### Suggested Solution

In order to achieve a solution that can be easily adapted to multiprocessor configurational changes, it is necessary to decompose the problem along functional lines.

This form of decomposition involves partitioning the processing elements into sub-groups rather than by inputs and outputs. A formal representation of this partitioning would be as follows:

$$\begin{bmatrix} O_I \\ O_{II} \end{bmatrix} = \begin{bmatrix} P_I & P_{II} \\ P_{III} & P_{IV} \end{bmatrix} \begin{bmatrix} I_I \\ I_{II} \end{bmatrix}$$

$$O_I = P_I \times I_I + P_{II} \times I_{II}$$

$$O_{II} = P_{III} \times I_I + P_{IV} \times I_{II}$$

In the above example if  $P_I$  and  $P_{III}$  were not required then this case would be identical to the horizontal partitioning case. However, it is not always possible to obtain such a clear cut decomposition.

The above form of decomposition allows the natural partitioning of processes among processors. These decompositions are heuristic in nature and an indepth understanding of the scope and nature of the situation being addressed is necessary. For example, in an aircraft simulation application, the pilot's actions may cause visual and directional changes. One solution is to independently feed all the inputs, based on the pilots actions, to the visual system and the positional system. Each of these systems independently determines changes to the vectors and determines the necessary action to be taken. A natural decomposition would be to first obtain all the inputs, compute the changes to the vectors, and then feed these values to the visual system and position control system. The vision control will then translate

this information to visual updates, and the motion control will translate this information into specific outputs that will be fed into the motion system.

As seen in the above example, a functional decomposition is possible, knowing the nature of the computational aspects. Each process performs a set of well-defined functions that may or may not involve all possible inputs. The results computed by a process is used in conjunction with results computed by other processes by possible intermediate processes to form the final output.

Processes should communicate with one another via messages, and as such processes should rely on the underlying Operating System for an efficient message passing scheme. In addition to an efficient message passing mechanism, the Operating System must provide domain transparency whereby two processes existing on different processors should be able to communicate with one another as if they are executing on the same processor. Moreover the software interface (system services) provided by the Operating System to processes (application software) must be identical regardless of the multiprocessor architecture, be it shared memory, common bus or distributed.

### Logistic Issues

If the implementation involves a set of processes that interact with each other via messages, partitioning processes across processors becomes a logistic issue, provided the Operating System provides transparent remote messaging. When approaching a solution in this manner, the partitioning becomes a matter of performance trade offs.

Too many processes on one processor communicating with one another may result in a situation wherein the processing power of the processor is inadequate. Transparent remote messaging provides a means by which processes may be gracefully allocated to other processors, with the option of adding new processors into the system without having to redo the software. The addition of processors into the system increases the net computing power of the system.

By taking a certain number of processes and partitioning them amongst additional processors, an immediate performance gain is realized per process because fewer processes have to compete for CPU time. There is some additional delay incurred in remote messaging. In determining the partitioning, the additional delay incurred by messages having to cross processor domains should be accounted for. The additional performance realized per process should also be taken into consideration.

Additionally, if the Operating System messaging capability provides multiprocessor architectural independence, then the flexibility gains in terms of configuration is rather extensive. One has to take into consideration the slightly increased delays in message passing, relative to processes executing on the same processor and communicating with one another. Message delays between processes executing on different processors and com-

municating via high speed communication lines (greater than 320M Bits/sec.) is not significantly greater than processes communicating via shared memory, which in turn is not significantly greater than processes communicating via common bus. In effect, one could have a combination of all three multiprocessor architectures co-existing in a system configuration, with processes being allocated to a particular processor based on on timing considerations.

#### An Additional Dimension

In most real-time applications today, one sees implementations that consist of a hierarchical configuration involving micro-processors and mini-computers that add yet another dimension in diversity. The same philosophy discussed in this paper can be extended to encompass multiple processor types, if there is a commonality in the Operating System software interface across the various processors. With the availability of portable real-time Operating Systems that are for the greater part written in a high level language, it has been proven that the same Operating System can be ported onto different processors. With this possible, the application programs can not only be distributed across various multiprocessor configurations involving the same family of processor types, but also be distributed across a multiprocessor configuration involving multiple processor types.

#### Summary

In summary, the basic considerations in implementing real-time software are:

1. The processing requirements are decomposed along functional lines into processes that communicate/co-operate via messages.

2. Additional computing power or resources can then be realized by distributing the processes across multiple processors using transparent messaging schemes. With a comprehensive messaging capability it is possible to achieve a software solution that is independent of the multi processor architecture.
3. Hardware configurations often involve multiple processor types. Using a common Operating System across the various processor types makes the software solution all encompassing, in that the software is independent of processor types as well as multiprocessor architecture.

#### References

1. D. P. Bhandarkar, "Some Performance Issues in Multiprocessor System Design," IEEE Transaction on Computers, May 1977.
2. W. K. Gilio and P. M. Behr, "Making Distributed Multicomputer Systems Safe and Programmable," Proceedings of the International Workshop on High-Level Language Computer Architecture. Nov. - Dec. 1982.
3. N. Quaynor and A. Bernstein, "Operating Systems for Hierarchical Multiprocessor," Proceedings of the Seventh Texas Conference on Computing Systems, Nov. 1978.
4. S. Weeks, "A Design for a Multiple Processor Operating Environment," Digest of Papers, COMPCON 73, March 1973.

Ankur R. Hajare  
MITRE Corporation  
Houston, Texas

#### ABSTRACT

The plans for the Shuttle Procedures Simulator called for more computational power than was available in order to meet future requirements. The three computer systems selected as candidates for meeting these requirements were Univac 1100/80, Univac 1100/40 and a configuration of ten Perkin-Elmer 8/32's. The performance of these systems was measured in terms of their ability to execute a real-time flight simulation. Two benchmarks were used for this purpose. One was a single processor benchmark called KOPBM and the second was a multiprocessor benchmark derived from a simulation software load actually used for training astronauts. KOPBM indicated that a Univac 1100/80 processor was 1.70 times as fast as a Univac 1100/40 processor and that a Perkin-Elmer 8/32 was 0.48 times as fast as a Univac 1100/40 processor. The multiprocessor benchmark, however, showed that a Univac 1100/80 system was 1.18 times as fast as a Univac 1100/40 system with the same number of processors. Thus, the results of the uniprocessor benchmark and the multiprocessor benchmark differed significantly. Subsequent to analysis of the results, the difference in the results of the two benchmarks was attributed to the difference in the memory architecture of the Univac systems and to the computational characteristics of the real-time flight simulation.

### 1.0 INTRODUCTION

#### 1.1 Background

The Shuttle Procedures Simulator (SPS) at the NASA Johnson Space Center (JSC) was used to train astronauts for Space Shuttle flights. The SPS was used for engineering development while the Shuttle Mission Simulator (SMS) complex is used for mission specific training. The revised requirements of the SPS required substantially more computational power than was available. The SPS was to be functionally similar to the SMS. The SMS fixed base and motion base simulators consist of two UNIVAC 1100/44 "host" computers, several Perkin-Elmer Model 8/32 (PE 8/32) Intelligent Controllers (IC's) and various simulation equipment. The standard UNIVAC operating system has been locally modified by UNIVAC personnel to provide a real-time dispatching system for the simulator "frame jobs", written in FORTRAN, that execute cyclically, faithfully reproducing in closed loop model form the Orbiter vehicle environment.

#### 1.2 Objective

The objective of this study was to evaluate computer systems in terms of their ability to execute the real-time flight simulation in SPS. The workload for the SPS computer complex was to consist of the real-time simulation as well as batch

and demand jobs for simulation software development and multi-mission reconfiguration. Measurement of the throughput of batch and demand jobs was excluded from this study because its short time frame did not permit collection of data to characterize the batch and demand workload or the construction of a suitable benchmark.

Three computer systems were evaluated for serving the needs of SPS. The systems selected for evaluation were: (1) A configuration of ten Perkin-Elmer 8/32's, (2) UNIVAC 1100/40 and (3) Univac 1100/80. The SPS computer complex consisted of five Perkin-Elmer 8/32 computers communicating via shared memory. Hence, an expanded Perkin-Elmer 8/32 configuration was an alternative being considered for satisfying the requirements of the SPS. The UNIVAC 1100/40 was selected for this study because SMS already had two such systems in use. Since the UNIVAC 1100/80 is the current high performance member of the UNIVAC 1100 series and was designed to replace and upgrade the older UNIVAC 1100/40, it too was evaluated.

#### 1.3 Approach

Two benchmarks were selected for comparing these systems in terms of executing the real-time flight simulation workload. The first of these two was a single processor benchmark called KOPBM that was immediately available since it has been developed and used for the acquisition of the host computer for the SMS. Although the shortcomings of this benchmark were well known at the time, KOPBM was selected in order to obtain quick, preliminary results within a month. KOPBM was also chosen because the feasibility of developing a better benchmark within the time span of this study had not been established.

The second benchmark selected was a host-only load benchmark which consisted of an actual SMS training load with slight modifications to make it run on standard UNIVAC 1100 series systems. It not only exercised actual flight simulation code but also preserved the interrelationships between the multiple activities within the flight simulation by executing it in real-time.

The UNIVAC 1100/40 and UNIVAC 1100/80 systems differ in the speed and organization of their memory. A UNIVAC 1100/40 can have a combination of primary storage and extended storage. A read from primary storage takes 280 ns and a write to primary storage takes 380 ns. The slower extended storage has a cycle time of 800 ns. The UNIVAC 1100/80 has a 125 ns cache which is interfaced to main storage with a cycle time of 600 ns. A UNIVAC 1100/80 system with more than two processors can have two clusters of cache with each cluster containing up to four segments of 4K words each. Main storage consists of up to eight banks with each one containing either 262K words or 512K words. The limits to performance for each of these systems is dependent upon memory access patterns. A UNIVAC



1100/40 primary storage performs best when simultaneous accesses are made to different 16K word blocks of memory. A UNIVAC 1100/80 main storage performs best when simultaneous accesses are made to different 4K word segments of cache and when all references can be satisfied from cache.

Because of the difference in memory architecture, a single processor benchmark such as KOPBM cannot properly measure the performance of a multi-processor system accessing a common memory. This is because a single processor benchmark does not take into account the performance degradation due to memory contention which can be vastly different in systems with differing memory architectures. The host-only load benchmark took into account the effects of contention for memory by multiple processors.

The real-time flight simulation load in SMS is highly optimized for the memory architecture of the UNIVAC 1100/40. The host-only load benchmark, too, included this optimization. It was not optimized in a similar manner for the memory architecture of the UNIVAC 1100/80.

## 2.0 SINGLE PROCESSOR BENCHMARK

The single processor benchmark used in this study, called KOPBM, was originally used to evaluate computer systems to serve the needs of SMS. KOPBM is a FORTRAN benchmark program designed to measure processor performance for an instruction mix similar to that expected in a real-time flight simulation. Since it is written in FORTRAN, it also tests the FORTRAN compiler's ability to produce efficient code. KOPBM does not test for correctness or accuracy in performing operations; it is a test for speed in performing them.

KOPBM contains the algebraic operations of addition, subtraction, multiplication, division, exponentiation and square roots. It also contains trigonometric functions, logical operations, iterations (DO loops), conditional and unconditional branches and array manipulation using one and two dimensional arrays. It contains nested expression evaluation, thereby testing the FORTRAN compiler's capability to generate optimized code for expression evaluation. All the variables in the KOPBM program are real variables, except for array indices, loop counters and a few logical variables. Hence, KOPBM extensively tests a processor's speed in performing single precision floating point arithmetic operations. KOPBM contains subroutine calls and therefore includes a measure for the efficiency of subroutine linkages.

KOPBM does not perform any input or output operations and therefore it only tests raw computing power instead of a balanced system throughput. The tests were run in an environment that would permit full CPU speed; i.e., with no other activity on the system. Thus, overhead associated with operating system functions such as job swapping was eliminated.

KOPBM is called with a parameter which specifies the number of iterations. Each iteration performs 1,000 FORTRAN operations. The run time can be used to compute the CPU speed in millions of operations per second (MOPS). This measurement of CPU speed is not the same as millions of instruc-

tions per second (MIPS) because the 1,000 FORTRAN operations in KOPBM will normally correspond to more than 1,000 machine instructions. MOPS are better than MIPS for comparing the performance of machines with different instruction sets (such as UNIVAC and Perkin-Elmer). This is because the same computational work can require a significantly different number of instructions on different machines. A machine with a higher MIP rating may require more instructions to perform the operations in KOPBM and thereby yield a lower MOP rating. Therefore, MIPS are a proper measure of relative performance only between software compatible machines, i.e. machines with the same instruction sets.

The three systems studied compare as shown below.

SYSTEM	AVERAGE MOPS	RELATIVE PERFORMANCE
UNIVAC 1100/80	0.762	1.70
UNIVAC 1100/40	0.448	1.00
Perkin-Elmer 8/32	0.217	0.48

## 3.0 HOST-ONLY LOAD BENCHMARK

### 3.1 Approach

SMS software on the UNIVAC host is integrated into a "training load" which performs the real-time flight simulation computations. This real-time simulation software used by SMS is similar in nature to the requirements specified for SPS. Hence, a benchmark consisting of an SMS host training load was excellent for comparing computer systems in their capability for executing the SPS real-time workload. The benchmarking activity using an SMS training load was restricted to UNIVAC 1100/40 and UNIVAC 1100/80 systems because the proposed PerkinElmer 8/32 configuration was not available for testing and conversion of a training load to run on a Perkin-Elmer 8/32 system would have required a large amount of effort.

The SMS host training load consists of "frame jobs" that execute cyclically at frequencies ranging from 25 Hz to 0.5 Hz. The frame jobs communicate with the Perkin-Elmer 8/32 IC's through an interface which was specially built for SMS. A UNIVAC 1100/80 system with such an interface to IC's and with other non-standard SMS equipment such as a microsecond clock does not exist. Hence, it was necessary to determine the feasibility of detaching an SMS training load from the IC's with minimum modifications. The frame jobs that comprise the simulation update variables in a common data pool. The simulation can be started from a "reset point" within a mission by setting the data pool variables to the appropriate values. Feasibility tests were conducted with the objective of finding a reset point from which the host-only simulation would run for a "periodic time slice" (PTS) of 8 seconds and would have a high level of computational activity. During a PTS of 8 seconds

every frame job executes an integral number of times.

During these feasibility tests on a SMS UNIVAC 1100/40 it was found that the simulation would run from reset point 47 for 96 seconds without the IC's. At the end of this period, the simulation went into "autofreeze" mode which meant that it could not run further since some variables had passed critical limits.

Reset point 47 is in a mission phase known as "return to launch site (RTLS) abort". It occurs five seconds after the main engines are cut-off but before the external tanks are released. This phase exercises the maximum amount of code in the dynamic loop and frame job transgressions had been observed during this mission phase demonstrating that this phase heavily taxes the computer system's capabilities. A change was made to the data pool at this reset point to introduce a left roll of 1/2 to 3/4 degrees/second which would continue to increase because nine Reaction Control System (RCS) jets were firing at that time. This was done by using the rotational hand controller (RHC) in the simulator base to fire the RCS jets before performing the datastore. This maneuver increased the level of activity at this reset point even further.

An SMS training load runs under a Frame Time Dispatcher (FTD) which is integrated into the UNIVAC 1100 Series Executive System (EXEC). The FTD was specifically developed for SMS and the operating system used by SMS contains other local modifications. But the benchmark was run under a standard operating system without the SMS FTD even though this meant making modifications to the load. This was done for the following reasons: (1) the FTD was written specifically for a UNIVAC 1100/40 and is machine and operating system dependent, i.e., it would not run on a UNIVAC 1100/80 under the current EXEC level without modifications; (2) the FTD requires a microsecond clock which is not standard UNIVAC equipment that could be obtained on a test UNIVAC 1100/80 system; (3) use of the same standard operating system on both machines would yield a better comparison; (4) running under a standard operating system would be a better test of transportability.

Since the FTD used by SMS could not be used for the benchmark, another Frame Time Dispatcher (FTD2) which ran under an unmodified EXEC was developed for this study. Since FTD2 performs the same scheduling function as FTD with a small difference in overhead, the validity of the benchmark was not adversely affected by the use of FTD2 instead of FTD. The use of the same transportable FTD2 yielded a more equitable comparison since it eliminated any machine dependent optimization.

The SMS simulation load on the UNIVAC 1100/40 host consists of thirteen frame jobs. Six of these frame jobs are run every 40 milliseconds which corresponds to an iteration rate of 25 Hz. These six frame jobs are called high iteration rate (HIR) frame jobs while the remaining seven frame jobs, which are executed at iteration rates between 6.25 Hz and 0.5 Hz are called low iteration rate (LIR) frame jobs. The FTD in SMS uses the custom built Interrupting Microsecond Clock (IMC) to dispatch each frame job at its iteration rate. Since the benchmark was run without the IMC, FTD2 used the

standard millisecond clock for dispatching the frame jobs.

Benchmark runs consisted of a sequence of tests with each test corresponding to eleven PTS of flight simulation. Each test was started from reset point 47 and was therefore a repetition of the same computation as the other tests. FTD2 obtained the execution time of each frame job by reading the standard UNIVAC 1100 Series millisecond clock when a frame job was started and when it completed execution. The execution times of each frame job were accumulated for a complete PTS at the end of which a timing report was printed. This report contained the average and maximum time of each frame job.

A validation report containing certain key flight simulation variables was generated. This report enabled comparison of the values of the key variables produced by the different computer system configurations on which the benchmark was run. The values of these variables were examined by engineers to confirm that a large portion of the real-time simulation software was being exercised. Since each test consisted of eleven PTS's each test produced twelve validation reports (including one prior to the start of the test) and eleven timing reports.

### 3.2 Benchmark Tests

The host-only load benchmark was run on three UNIVAC 1100/80 configurations and on two UNIVAC 1100/40 configurations as listed below.

Configuration 1: UNIVAC 1100/84 (4 x 2)  
(Fig. 3-1)  
CPU's: 4  
IOU's: 2 (IOU0, IOU2)  
SIU's: 8  
Memory: 2.1M words consisting of 262K words each in memorybanks MEM0, MEM1, MEM2, MEM3, MEM4, MEM5, MEM6, MEM7, and MEM8

Configuration 2: UNIVAC 1100/83 (3 x 2)  
(Fig. 3-2)  
CPU's: 3 (CPU0, CPU1, CPU2)  
IOU's: 2 (IOU0, IOU2)  
SIU's: 6 (SIU0, SIU1, SIU2, SIU3, SIU4, SIU5)  
Memory: 1.6M words consisting of 262K words each in memory banks MEM0, MEM1, MEM2, MEM3, MEM4 and MEM5

Configuration 3: UNIVAC 1100/83 (3 x 2)  
(Fig. 3-3)  
CPU's: 3 (CPU0, CPU1, CPU2)  
IOU's: 2 (IOU0, IOU2)  
SIU's: 8  
Memory: 1.0M words consisting of 262K words each in memory banks MEM0, MEM2, MEM4 AND MEM6

Configuration 4: UNIVAC 1100/44 (4 x 2)  
(Fig. 3-4)  
CAU's: 4  
IOAU's: 2

Primary memory: 459K words distributed in 7 banks with 65K words each

Extended memory: 262K words in 2 banks with 131 K words each

Configuration 5: UNIVAC 1100/43 (3 x 2) (Fig. 3-5)

CAU's: 3 (CAU0, CAU1, CAU2)

IOAU's: 2

Primary memory: 459K words distributed in 7 banks with 65K words each

Extended memory: 262K words in 2 banks with 131K words each

### 3.3 Transportability

Besides providing a comparison of relative speeds, the host-only load benchmark tested the transportability of SMS software from a UNIVAC 1100/40 system to a UNIVAC 1100/80 system. This transportability was important because a major advantage anticipated from the use of a UNIVAC 1100 series system in SPS was the ability to use SMS software in SPS.

No problems were encountered in making the benchmark run on any of the configurations tested. The changing values of the flight simulation variables printed in the validation report showed SPS engineers that over ninety percent of the real-time simulation code was exercised during the test. Therefore, it was demonstrated that application software developed in SMS for the UNIVAC 1100/40 systems could be executed on a UNIVAC 1100/80 system.

### 3.4 Analysis of Timing Data

The timing report printed by the benchmark contained execution times for both HIR and LIR frame jobs. These times were obtained by reading the millisecond clock before initiation and after completion of a frame job. Since the HIR frame jobs could not be preempted, the difference between the two readings of the clock was the execution time with a granularity of one millisecond. However, the LIR frame jobs could be preempted by HIR frame jobs. Hence, the values printed in the report were not the true values of the execution times of the LIR frame jobs. These values were, therefore excluded from analysis.

Although the timing obtained from a millisecond clock was coarse, each HIR frame job was run two hundred times during every periodic time slice of eight seconds. Because of the large number of iterations through the HIR frame jobs, the coarseness of the clock did not degrade the results.

The UNIVAC 1100/80 and UNIVAC 1100/40 systems used for the benchmark runs did not have identical mass storage configurations but the accesses to mass storage from the benchmark were made to the same type of disk. The operating systems are on different kinds of disks on the UNIVAC 1100/80 and UNIVAC 1100/40 systems but this did not affect the benchmark runs since the host-only load benchmark did not make the operating system access these disks. There were differences in other peripheral devices on the two systems but that did not affect

the results since the benchmark did not exercise these devices during the timing measurements.

Two UNIVAC 1100/83 configurations were tested, the difference in the two being in the organization and amount of both cache and main memory. Configuration 3 had 1M words of main memory which is more than adequate for the real-time flight simulation. This memory was distributed as 262K words in alternate banks, i.e., it was evenly distributed for better use of the cache. The full 32K words of cache could be used in this configuration. Although configuration 2 had more memory (1.6M words), the additional amount was unnecessary for the workload. The distribution of this memory was unbalanced and the loading of the entire workload into adjacent banks interfacing to the same 4K word segment of cache (SIU) would lead to suboptimal use of cache compared to the balanced case. Configuration 2 had the amount of cache reduced to 24K words. A memory organization such as in configuration 2 is improper for the real-time flight simulation workload. Therefore, the results for configuration 3 are a better representation of the performance of a UNIVAC 1100/83 (3 x 2) system for executing the real-time flight simulation workload. The benchmark was run on Configuration 2 in order to test the sensitivity to memory size and organization.

As shown in Table 3-1, a UNIVAC 1100/84 is 18% faster than a UNIVAC 1100/44 and a UNIVAC 1100/83 is 18% faster than a UNIVAC 1100/43 for executing the HIR frame jobs. Thus, there is a consistency in the relative speeds of the corresponding members of the UNIVAC 1100/80 and UNIVAC 1100/40 series. For both series, a three processor system was 2% slower than the corresponding four processor system. This difference was probably introduced by FTD2 and constitutes the overhead associated with it. On a four processor system the overhead would be absorbed by the fourth processor but on a three processor system it would degrade the execution times of the HIR frame jobs.

Table 3-1 Relative Speeds of High Iteration Rate Frame Jobs

Frame Job	UNIVAC 1100/44	UNIVAC 1100/43	UNIVAC 1100/84	UNIVAC 1100/83 (Con. 3)	UNIVAC 1100/83 (Con. 2)
31	1.00	0.97	1.18	1.14	0.96
21	1.00	0.97	1.13	1.11	0.97
11	1.00	0.97	1.15	1.16	1.04
12	1.00	0.98	1.35	1.32	1.16
22	1.00	0.99	1.09	1.08	0.96
32	1.00	0.97	1.13	1.16	0.94
OVERALL	1.00	0.98	1.18	1.16	1.02

The relative speeds of the configurations tested vary across the six HIR frame jobs by as much as twenty-four percent. Such a variation can be caused by differences in instruction mix, by the amount of input/output or by memory contention in accessing the common data pool. Frame job 12, which does most of the I/O done by the HIR frame

jobs, exhibits a distinctly higher performance gain on a UNIVAC 1100/80 system relative to a UNIVAC 1100/40 system. Particular attention should be paid to the relative speeds for frame job 21 since this frame job is subject to transgressions in SMS. The relative speeds for this frame job differ from the overall figures. For frame job 21 a UNIVAC 1100/84 system is only 13% faster than a UNIVAC 1100/44 system instead of the overall improvement of 18%. Similarly, a UNIVAC 1100/83 is only 11% faster than a UNIVAC 1100/44 instead of the overall improvement speed of 16%. Thus, in both cases, the speed improvement over a UNIVAC 1100/44 system is 5% less when frame job 21 is used as the basis of comparison instead of the overall figures. The smallest speed improvement is in the case of frame job 22 where a Univac 1100/80 system is only 9% faster than the corresponding Univac 1100/40 system.

The average execution times show a high degree of consistency across different tests on the same computer system configuration. The small variation exhibited in these figures is well within the range expected from the granularity of the clock and factors external to the specific frame job.

This analysis has used only the execution times for the HIR frame jobs for the reason stated earlier and the relative speeds presented in the tables are based on these execution times. Although there is a small difference in the capabilities of a UNIVAC 1100/84 and a UNIVAC 1100/83 in terms of their abilities to perform the HIR frame jobs, it should be noted that the LIR frame jobs also need to be completed at the specified iteration rate. A comparison of the relative speeds of the different systems in performing the HIR workload cannot be used to evaluate their relative speeds in performing the complete simulation because the four processor systems have an additional processor which can execute the LIR frame jobs while three processors are executing HIR frame jobs. But on a three processor system, the LIR frame jobs must be executed when one or more of the three processors is relinquished by the HIR frame jobs.

The modifications made to the SMS training load in order to generate the host-only load benchmark reduced memory accesses below the level of the actual flight simulation. This was because IOU (or IOAU) activity was restricted to that necessary for the mass storage I/O performed by the flight simulation. IOU activity resulting from communication with the IC's during actual flight simulation did not exist in the benchmark. Since this difference from the actual simulation existed on the benchmark runs on all the computer system configurations tested, the relative performance figures were not significantly affected. But, if the results of the host-only load benchmark are used for an evaluation of the absolute capacity of UNIVAC 1100/80 systems to perform the flight simulation, this factor could be significant especially if memory contention is the bottleneck in the performance of the system.

In order to preserve the integrity of the test of transportability, the benchmark was run on all configurations without any optimization for the architecture of the UNIVAC 1100/80 series, including optimization of the frame jobs' location in memory. Experience in SMS has indicated that per-

formance gains can be achieved on a UNIVAC 1100/44 by proper placement of the frame jobs in memory. The difference between the performance of the two UNIVAC 1100/83 configurations shows that memory organization is an important factor in the speed of this system too.

The memory size of the frame jobs and the organization of memory in the UNIVAC 1100/80 systems indicate that significant performance gains may be achieved by placing the frame jobs in main memory in a manner that increases the use of the cache. Optimization based on the architecture of the UNIVAC 1100/80 series could be done external to the engineering modules used in the real-time simulation. It could be done within the frame time dispatcher or by a separate processor like the Conflict Avoidance Processor (CAP) used by SMS. The amount of such potential performance gains could not be measured at the time of the study.

#### 4.0 CONCLUSIONS

Two benchmarks were used to measure the relative performance of the computer systems chosen as candidates for serving the needs of SPS. The first benchmark was a single processor benchmark called KOPBM. It KOPBM indicated that a UNIVAC 1100/80 processor was 1.7 times as fast as a UNIVAC 1100/40 processor.

The host-only load benchmark consisted of an actual SMS training load with modifications that were necessary because SMS uses non-standard hardware and software and because the benchmark had to operate without IC's. Hence this benchmark was vastly superior to KOPBM in its representation of the real-time simulation anticipated in SPS.

A UNIVAC 1100/80 system was found to be 18% faster than a UNIVAC 1100/40 system with the same number (3 or 4) processors for executing the HIR workload. This workload consists of three frame jobs executing concurrently. Hence a three processor and a four processor system of the same type performed equally well in executing this workload, except for a 2% difference which can be attributed to overhead introduced by the test. The relative performance of these systems in executing the full simulation will not be the same because the four processor systems have an additional processor to execute the LIR frame jobs whereas on the three processor systems they must be executed by the three processors when they finish processing the HIR frame jobs.

The benchmark was run without any optimization for the UNIVAC 1100/80. It is believed that significant performance gains can be realized by such optimization but the amount of such gains was not measured.

The results obtained from the host-only load benchmark differed markedly from those obtained from KOPBM and provide an indication of the difference in relative performance that can occur in a multiprocessor system compared to a single processor system.

The host-only load benchmark yielded performance measures that were also significantly different from the vendor's claims and from other published results which indicate that a UNIVAC 1100/80

system is 50% to 60% faster than a UNIVAC 1100/40 system with the same number of processors. Performance improvements of 50% to 60% were observed with benchmarks based on general multiprogramming workloads which consist of several independent jobs. A multiprocessing system executing such a workload will encounter far less memory contention than the simulation in SMS which consists of concurrent processes accessing a common data pool. The benchmarks which showed performance improvements of 50% to 60% for the UNIVAC 1100/80 compared to the UNIVAC 1100/40 included a significant amount of input/output including accesses to mass storage as well as memory management overhead such as job swapping. The real-time flight simulation in SMS is much more computation oriented than these benchmarks; it contains a relatively small amount of input/output and incurs no memory management overhead.

In the transition from the 1100/40 to the 1100/80, UNIVAC introduced cache memory. Instead of the 280 ns read cycle memory of the UNIVAC 1100/40 the UNIVAC 1100/80 has a combination of fast cache and slow backing store. The effective speed of this combination depends upon the cache hit ratio. Hence, the relative performance of the UNIVAC 1100/40 and the UNIVAC 1100/80 is a function of cache hit ratio. A workload that yields a high hit ratio (such as one consisting primarily of a large number of iterations through a small loop) will favor the UNIVAC 1100/80.

A hardware monitor at the UNIVAC benchmark site was used to monitor the cache hit ratio during the benchmark runs. According to UNIVAC personnel, the hit ratio for the host-only load benchmark was the lowest ever observed. The real-time flight simulation in SMS can be modeled as a straight-line execution (with forward branching) through 0.5 megawords of code every 40 ms. Such a workload yields a low hit ratio. Some of the difference between the results of the host-only load benchmark and general multiprogramming benchmarks can be attributed to a difference in cache hit ratio. The cache of the UNIVAC 1100/80 is, therefore, not as effective with the simulation in SMS as it is with most workloads.

The cache of the UNIVAC 1100/80 consists of clusters which can be attached to one or two processors. A UNIVAC 1100/80 system with more than two processors has two clusters of cache since one cluster can only be connected to two processors. All three UNIVAC 1100/80 systems on which the host-only load benchmark was run, therefore, had two cache clusters. Since both cache clusters are connected to the same backing store, each can have a copy of the same data in backing store. When data is written to a cache cluster and a copy of it also exists in the other cache cluster, it is invalidated. Hence, the effectiveness of cache is reduced when multiple processors connected to different cache clusters are updating the same pool of data as is the case in the simulation in SMS. Such a situation does not occur when each processor is accessing its own separate data as was the case with multiple copies of KOPBM. This factor can

account for some of the difference in the results of the benchmarks.

Neither the UNIVAC 1100/40 nor the UNIVAC 1100/80 feature virtual memory. This architectural feature would not help the performance of the real-time flight simulation in SMS. The performance of a single job in a virtual memory system is best when all of it is resident in real memory. Virtual memory cannot improve the performance of a single job that is small enough to fit entirely in real memory. In a multiprogramming environment, the memory resource can usually be better utilized by allocating real memory based on dynamic requirements. This can result in improved throughput even when a single job by itself takes longer to complete because of virtual memory. The host-only load benchmark consisted of only one job that was heavily compute bound. It consisted of cyclic execution through approximately 0.5 megawords of memory. In such a case page swapping on a virtual memory system would heavily penalize performance. The performance of such a benchmark with a virtual memory system would be best when there was no swapping, i.e. when the virtual memory feature was totally ineffective. The size of the simulation in SMS does not warrant a virtual memory system because it is small compared to the memory size of today's large computers.

UNIVAC now offers a Scientific Accelerator Module (SAM) as an option on each UNIVAC 1100/80 processor. This option provides faster execution of instructions that occur frequently in scientific computation. At the time the host-only load benchmark was run on the UNIVAC 1100/80 SAMs had been announced but were not available for benchmarking. Instead, UNIVAC provided a hardware measurement tool at the benchmark site that counted instructions in different categories as they were being executed during the benchmark runs. This information was input to a software package that assessed the improvement in performance that could be expected with a SAM. In the case of the host-only load benchmark the improvement claimed by the vendor was 15%. This figure, however, was based on the speed of a single processor. It is believed that the memory system of the UNIVAC 1100/80 was the bottleneck during execution of the host-only load benchmark. In such a situation, a faster processor will not improve the performance of the system and neither will the addition of more processors.

The relative performance of computer systems is very sensitive to workload. Therefore, a benchmark that is used to compare the performance of computer systems must be a true representative of the workload that the computer system is expected to handle. In particular, a multiprocessing workload such as the real-time flight simulation in SMS requires a multiprocessing benchmark. This case also demonstrates that the computational requirements of real-time flight simulation are quite different from the majority of applications and, therefore, general purpose benchmarks are not adequate for the evaluation of computer systems for real-time flight simulation.

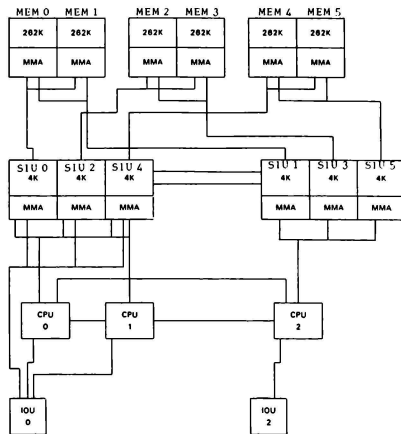


Figure 3-2. UNIVAC 1100/80 System Configuration 2

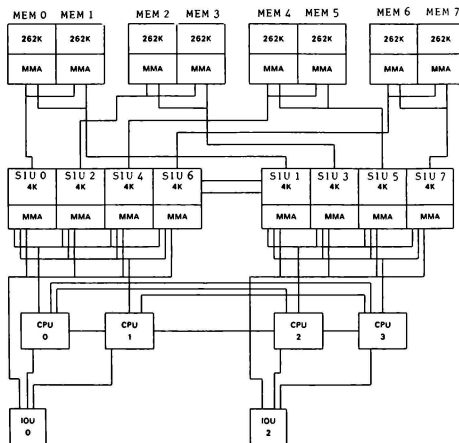


Figure 3-1. UNIVAC 1100/80 System Configuration 1

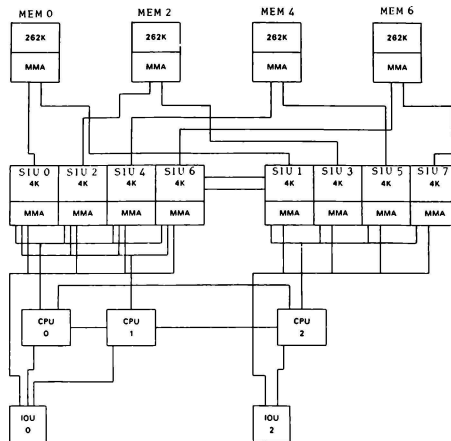


Figure 3-3. UNIVAC 1100/80 System Configuration 3

#### Extended Memory

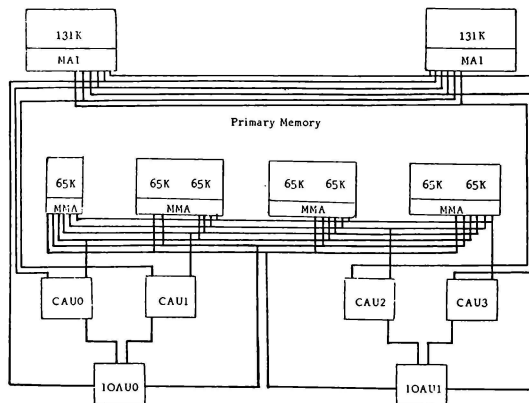


Figure 3-4. UNIVAC 1100/40 System Configuration 4

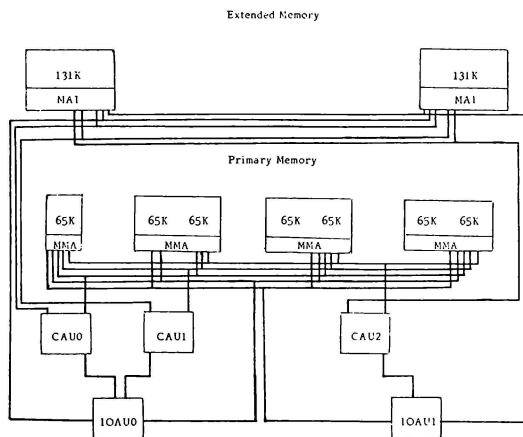


Figure 3-5. UNIVAC 1100/40 System Configuration 5



Richard A. Weeks\*  
Northrop Corporation  
Pico Rivera, California

### ABSTRACT

An investigation of hybrid computer inaccuracies in the engineering flight simulation has been accomplished at the Northrop Corporation - Aircraft Group, Flight Simulation Laboratory in Hawthorne, California. This study was conducted for the United States Air Force under Contract F33615-78-C-3608 with final results presented in Reference 1. Although many error sources are stochastic or random in nature rather than deterministic, and obviously many error sources are directly a function of the computer hardware and its maintained condition, certain types of errors which are present in hybrid simulations can be categorized due to the specific computer configuration utilized.

In this study, four separate computer configurations were mechanized for the investigation of the effect of error sources on a typical man-in-the-loop aircraft simulation problem. Additionally, an all digital airframe mechanization was constructed to address the effects of digital computer frame time on solution accuracy.

### INTRODUCTION

Man-in-the-loop real time simulation, with a sophisticated simulator, requires a large computation facility to provide the capability for effective and detailed mathematical modeling of the air vehicle and its subsystems. Analog computers offer simultaneous real time solution of equations and maintain a continuous solution which makes this method of computation attractive, especially for modern high-speed fighter aircraft flight control system mechanizations. Flight control systems typically involve frequencies which are a decade higher than the airframe. However, as an analog simulation grows in size and becomes more complex, checkout and setup time become lengthy. Also, the size of an analog simulation is usually limited due to the relatively small number of components (amplifiers, potentiometers, etc.) in an analog computer. Furthermore, due to the nature of analog hardware components, error accumulation becomes important relative to the calibrated state of the computer.

Digital computation, on the other hand, allows for rapid setup and repeatable results and can easily support a large scale simulation problem. Digital computation also allows for detailed airframe modeling through extensive nonlinear aerodynamic data tables. However, digital computers require finite time intervals for computation resulting from the serial processing of information. Simultaneous solutions of coupled equations can be achieved in the digital computer through iterative solutions, but would require larger computational time intervals which may have a more adverse effect on the solution accuracy than the serial solution. This is particularly true when

numerical integrations are required during the computational cycle.

Many large simulation mechanizations run in a hybrid fashion, where both analog and digital computing methods are employed. In operating a hybrid computer configuration, the best features of both analog and digital computation are utilized. However, errors and problems associated with both, and the communication link between them, must also be addressed. That is the objective of this paper.

### APPROACH

The objective of this study was to investigate error sources that are inherent in analog, digital and hybrid computation. An extensive evaluation of existing literature was accomplished for identification of computer error sources, whether hardware or mathematical in nature. Table 1 summarizes typical errors encountered in analog, digital and hybrid computation. Initially, error sources were examined analytically for origin and expected level of magnitude. These possible sources of error were then evaluated for the determination of primary cause and subsequent determination of controllable sources. A controllable error source is one which might be deliberately induced or altered for experimental evaluation.

Once the controllable error sources were identified, they were evaluated dynamically with computer mechanizations. An airframe mechanization was selected. Since it has been shown that even if the complete nonlinear equations are solved on the computer, simplified linearized equations can adequately represent the dynamic equations in order to provide an insight into potential computer solution errors (Reference 2). For this reason, a linear airframe model was utilized for the investigation of the effects of error sources on solution accuracy. Furthermore, as presented in Reference 2, it has been shown that short period airframe dynamics tend to be the most sensitive to the effects of computer errors.

This conclusion indicates that a two-degree-of-freedom longitudinal airframe model would be adequate to investigate hybrid computer errors. However, since it was desired to examine the effects of hybrid computer errors relative to both high and low frequency equations, a three-degree-of-freedom longitudinal airframe mechanization was maintained. Therefore, the longitudinal, pitch and vertical acceleration airframe equations were mechanized. Since the airframe pitch attitude is greatly affected by both the short period dynamics and phugoid motion of the airframe, this parameter was utilized extensively to indicate the results.

Four mathematical models of this linear,

\*Member, AIAA

ERROR TYPE	ANALOG	DIGITAL	HYBRID
1. Potentiometer Tolerance	X		X
2. Amplifier Offset	X		X
3. Noise	X		X
4. Circuit Response Characteristics	X		X
5. Capacitor Dielectric Absorption	X		X
6. Truncation		X	X
7. Roundoff		X	X
8. Multiplexer Skewing			X
9. Aliasing (Spectral Folding)			X
10. Word Length		X	X
11. Hold Circuits			X
12. Shared Memory Skewing		X	
13. I/O Link Skewing		X	

Table 1. Typical Computer Error Sources

three-degree-of-freedom airframe were constructed. One was an all analog configuration and the other three were various hybrid configurations. The controlled error sources were then injected into the problem such that their effects on the simulated (numerical) airframe response could be examined. In all evaluations, the numerical response was compared to a closed-form solution of the equations-of-motion representing the airframe.

An additional all-digital airframe mechanization was developed which utilized a high-order predictor/corrector integration technique for the solution of the airframe equations-of-motion. This computer configuration was utilized solely to evaluate the effects of digital computer frame time on the dynamic response of the simulated airframe.

#### GENERAL COMPUTER CONFIGURATION

Before proceeding with a brief description of hybrid computer errors (from an analytical point-of-view), it is worthwhile to describe the computer hardware which was used in the study. Since analog, digital and several types of hybrid test were required, a variety of computing equipment was required to support this study. A small portion of the Northrop Corporation Flight Simulation Laboratory's computer facility was utilized to meet this requirement. As shown in Figure 1, three separate Harris Slash 4 digital computers, a shared common memory between two of the Slash 4 computers, digital computer peripherals, an Electronic Associates Incorporated (EAI) hybrid linkage and Comcor 5000 analog computer were utilized.

The first computer configuration studied utilized the Comcor 5000 analog computer as a stand-alone computing system. The second computer configuration examined was a simple hybrid arrangement with a single Harris Central Processing Unit (CPU), the Comcor 5000 and the EAI hybrid linkage. The Master Digital Slash 4 CPU, Master Hybrid Slash 4 CPU, shared common memory, EAI linkage and Comcor 5000 computer formed the third computer configuration. Finally, the fourth computer equipment setup utilized the Master Digital Slash 4, Multiple System Interface Slash 4, an I/O link, EAI hybrid linkage and Comcor 5000 analog computer. All computer configurations utilized a magnetic (Mag) tape unit peripheral to the Master Digital/Hybrid Slash 4 computers. This

was even true of the all-analog case described earlier. The Mag tape unit was required for purposes of recording data for a subsequent Power Spectral Density (PSD) analysis.

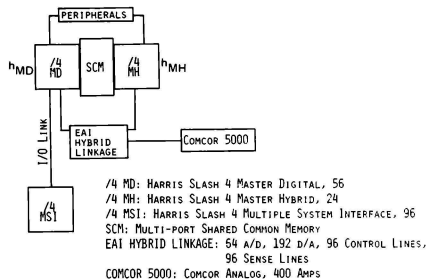


Figure 1. General Computer Configuration

#### ANALOG CONFIGURATION

An analog computer performs computations and makes logical decisions on variables in a continuous manner. Therefore, analog computers are especially suited to the solution of differential equations (i.e., performing integration). There seems to be agreement within the literature that under ideal laboratory conditions, the accuracy of the analog computer can approach 0.01 percent of full scale voltage. However, the accuracy of typical analog computers commercially available tends to range between 0.1 percent and 0.5 percent of the maximum variation on the variables of interest.

With the analog computer, solution accuracy is directly a function of the accuracy of the computing components. Analog computer errors can be divided into two classes: static and dynamic. Static errors are those caused by misalignments, component imbalance and tolerance, incorrect potentiometer settings and equipment malfunctions to name a few. Dynamic errors are caused by inadequate dynamic characteristics of the equipment which in-

clude noise (instantaneous disturbances) and component response characteristics. The net effect is that the computer solution is relative to the machine circuit characteristics rather than the actual equation. These circuits produce shifts in the characteristic roots of the differential equation being solved.

#### HYBRID - SINGLE CPU CONFIGURATION

The hybrid - single Central Processing Unit (CPU) configuration, as typified in Figure 2, provides for the best features of both analog and digital computation equipment to be utilized. However, errors associated with the two methods of computation are encountered as well as the introduction of new error sources generated by the analog/digital and digital/analog communications link (hybrid linkage) between the two.



Figure 2. Hybrid-Single CPU Configuration

Errors associated with analog computers were previously discussed. In contrast to the analog computer, which perform continuous computation, digital computers perform computation, memory storage and logical decisions in terms of variables which appear in discrete form as serial data sequences.

Basically, there are two sources of error in digital solutions, particularly in the solution of differential equations:

- 1) Truncation Errors
- 2) Roundoff Errors

Truncation errors develop from the truncation of an infinite process to give a finite difference approximation to the differential equations being solved. Roundoff errors arise from the limited precision (due to word length) with which arithmetic operations are carried out in the digital computer.

Truncation errors are the result of numerical integration techniques and digital computer frame time. Quite often, the execution time required for digital computation of the many subroutines within the CPU determines the frame time. A numerical integration formula transforms a differential equation into a difference equation. In the process of applying this transformation, many of the higher order terms of the Taylor's Series expansion are neglected or truncated. This procedure specifies the order of magnitude of the truncation error which is a function of the digital computer frame time and the system's time constant. If the higher derivatives of the series are assumed to be small, the truncation error is then decreased by the use of a smaller frame time. If the frame time is too large to handle the highest frequencies in the modeled system, amplitude and phase errors

arise as well as spectral folding or aliasing. In general, a sampling interval of at least twice the frequency of the system being sampled is required (Nyquist or Shannon frequency) although a sampling frequency of 10 to 100 times the system frequency is desirable. In most cases, truncation error can be decreased by using higher-order integration methods. However, since higher-order integration methods take longer to execute, an appropriate compromise must be reached between the order of the integration algorithm and the frame time.

Many different types of numerical integration techniques are available and are widely used in real time flight simulation. Most numerical integration methods become unstable if the frame time is made too large in relation to the time constants of the system being modeled. Up to the time where instability occurs, the selected method may be computing with the required accuracy, but a further slight increase in step-length into the region of instability results in the generation of completely erroneous solutions. Therefore, the significant difference between the stability of a solution and the accuracy of that solution is that when a solution becomes computationally unstable, the errors increase in an unbounded fashion and the result has no physical meaning. However, in a computationally stable solution, the errors are bounded and the results might appear reasonable. This appearance can be extremely deceptive in that the results obtained might not be accurate.

There seems to be an absence of discussions in the literature surveyed on the absolute effects of roundoff error. Generally, roundoff error effects are treated in a statistical fashion, in order to generate the bounds of their effects. Although truncation errors are more amenable to study, these errors do not always dominate. Many simulations are rendered inaccurate because the roundoff error dominates. This is particularly true in single precision computations in which high frequency response systems are modeled.

Theoretically, it is possible to drive the truncation error to zero as the digital computer frame time is driven toward zero. Decreasing the frame time, however, increases the number of computations and therefore increases the roundoff error. As the frame time approaches zero, the roundoff error dominates and the solution becomes unstable. This phenomenon of how the truncation and roundoff error behave in a converse manner is shown schematically in Figure 3. Unfortunately, the optimum selection of the frame time based on truncation and roundoff error considerations is quite difficult to determine in advance and becomes a matter of trial and error with the modeled system.

As shown in Figure 2, the hybrid linkage serves as the communications link between the analog and digital computers. For the purpose of this study, the hybrid linkage refers to analog-to-digital (A/D) data transfer and digital-to-analog (D/A) data transfer. In A/D conversion, the major system components comprising this part of the hybrid loop include:

- 1) Multiplexer
- 2) Sampler
- 3) Quantizer

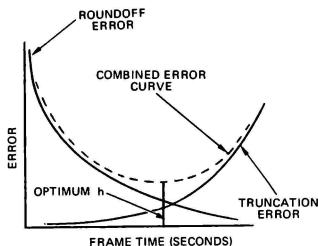


Figure 3. Relationship Between Truncation and Roundoff Errors

For D/A conversion, the system components considered include:

- 1) Digital-to-Analog Converter
- 2) Analog Hold Circuits

The most serious error associated with hybrid computing systems is time delay. This time delay is a combination of the D/A and A/D conversion process and the time required for digital computation. Computing time required for digital computation is a direct function of the problem complexity which is not the case with analog computation.

Multiplexing is the process of allowing a single A/D converter (quantizer) to be time shared among a number of analog input channels for reason of hardware economy. This multiplexing is a prime contributor to the time delay error caused by the hybrid linkage which is commonly referred to as skewing.

Skewing in the multiplex unit causes the data received by the digital computer to represent two different instances in time. One technique for avoiding this problem is to sample and hold all multiplexer inputs. In this manner, all analog channels are sampled simultaneously and then these sampled signals, reflecting the same instant in time, are held for serial input to the digital computer.

Sampling is unavoidable in a hybrid simulation since at some instant in time the continuous analog variables must be converted into a sequence of digital words. Sampling is usually a synchronous process with successive samples being equally spaced in time. Errors in sampling occur due to the sampling operation and the sampler hardware itself. Sampling frequencies are extremely important in obtaining accurate replications of the sampled signal frequency content. Reference 1 describes this in detail and the concept of spectral folding or aliasing.

After an analog quantity is sampled, it undergoes a conversion to a digital word format. This process is known as quantizing. Analog hardware errors associated with quantizing include component tolerance, zero off-sets, and drift. Digitally originated errors include roundoff errors due to limited

word length and digital coding technique. Reference 1 presents an example of how the specific digital code utilized in the quantizer affects the quantizer output.

A major error source in the quantizing process is due to word length employed in the quantizer. Typical word lengths can range from 4 bits to 15 bits, with sign included. The quantizer word length determines the input analog level requirement for the A/D converter output to discretely jump to the next quantum level. Quantization errors become significant when it is not possible to utilize a sufficiently large number of bits in characterizing accurately the continuous input.

An example of a quantized signal is shown in Figure 4. The signal being sampled is a smoothly varying continuous function of time. The quantizer output, however, remains constant while the input signal remains within the boundaries of a quantum level and then changes abruptly by one full level when the signal crosses the boundary. Since at any given instant of time an input signal might be rapidly crossing back and forth over a quantum level boundary, the distortion caused by quantization errors can produce an effect similar to that of an independent source of noise. Therefore, due to the stochastic nature of the quantizer output, most error analyses of quantization take a statistical approach.

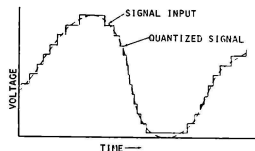


Figure 4. Quantized Signal

The accuracy of a quantizer is always improved by either increasing the sample rate or decreasing the quantization level, or both. For coarse quantization, a rather high increase in sampling rate would be required to improve performance, but a small decrease in quantization level is much more effective.

As previously mentioned, time delay is a major source of error in the A/D conversion process. A series of tests were run to demonstrate the effects of hybrid linkage time delay on solution accuracy. A linear, second-order, simple harmonic ordinary differential equation (whose theoretical solution is a neutrally damped sinusoid) was mechanized. This type of equation is particularly well-suited to this method of investigation, since any time delay induced into the mechanization will change the damping characteristics of the modeled system. The digital processor was free-running, and was used only to read the A/D converter and output to the D/A converter. Therefore, time delay in the hybrid solution would be primarily due to the hybrid linkage. The system frequency and number of A/D and D/A channels were varied to investigate the time delay effects. The results of the test are shown in Figure 5.

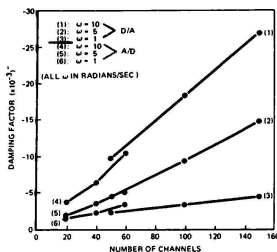


Figure 5. Effect of A/D and D/A Converter Time Delay

As can be seen in Figure 5, the simple harmonic frequency was varied between 1 and 10 radians per second. For a D/A test, only a single A/D channel was utilized; whereas, for an A/D test, only one D/A channel was used. The measure of time delay was in the effective damping factor (relative to critical damping) of the hybrid solution. Note in Figure 5 how the solution consistently diverges (negative damping factor) for all test conditions examined (again, the theoretical solution is neutral stability). System frequencies were kept below 10 radians per second since analog bandwidth and capacitor dielectric absorption tests showed similar (but with less magnitude) trends at higher frequencies.

The purpose of the D/A converter portion of the hybrid linkage system is to translate the sequence of words produced in the digital computer into continuous analog voltages. Electronic analog errors induced by the D/A converter are typified by zero offsets, jitter, and component tolerances. Besides the serious errors induced by linkage time delay (as discussed in the previous paragraphs) another major error source in the D/A conversion process is due to the data reconstruction method (hold circuits). Several types of hold circuits are available for hybrid linkage systems and include: zero-order hold, zero-order hold with data predicted one-half frame time ahead, and first order hold.

The zero-order hold output from a D/A converter represents the reconstructed analog variable which is correct at the beginning of each hold period. Furthermore, at this time the reconstructed data usually represent a delayed output due to hybrid linkage time delay. Although the output is delayed, the zero-order hold circuit causes no phase distortion. Smoothing with a low-pass filter may help but will induce phase shift.

#### HYBRID-MULTIPLE CPU CONFIGURATION WITH SHARED COMMON MEMORY

The hybrid-multiple CPU configuration, with communication between the digital computers through a common area in core, is shown in Figure 6 where  $h$  denotes the digital computer frame time. In this configuration, error sources inherent in the single CPU-hybrid configuration, as discussed in the prior section, are experienced as well as some unique errors due to the common memory usage. In this configuration, it is assumed that only one of the digital processors accesses the hybrid linkage.

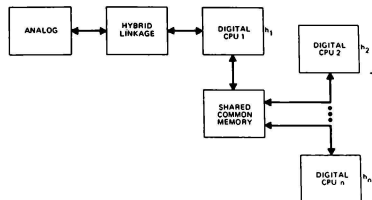


Figure 6. Hybrid-Multiple CPUs With Shared Common Memory Configuration

The most significant additional error source of the computer configuration shown in Figure 6, relative to the hybrid-single CPU case, is due to common memory skewing. Common memory skewing is caused by the free access and modification of the common area of memory by multiple uninterrupted CPUs. When multiple CPUs are used in a parallel uninterrupted fashion, a variable in common memory might be accessed or modified prematurely while attempting to maintain continuity between the parallel processors for a given instant in time. A simple example exemplifies this phenomenon.

Two CPUs are operating at different frame times. CPU No. 1 computes aerodynamic data (table lookup) and executes at 20 milliseconds (msec) while CPU No. 2 computes the aero angles (angle of attack and sideslip angle) and executes at 10 msec. Assume that all of the scheduled CPU time is required for these computations. At the top of the frame, both CPUs start their executions. CPU No. 1 begins aero data generation as a function of angle of attack and sideslip while CPU No. 2 begins generating more current values for the aero angles (say, due to gusts). Every time CPU No. 1 computes an aero function requiring angle of attack or angle of sideslip, the common memory is accessed to retrieve the aero angle parameter. However, at the end of CPU No. 2's frame, CPU No. 2 updates angle of attack and sideslip. However, CPU No. 1 continues generating aero data, only now it is reading a new and different value for the aero angles relative to those read at the top of its frame. This timing mismatch can cause considerable error for fast moving variables.

In a multiple CPU with shared common memory configuration, a careful planning of accessing and placement of data within common memory can reduce this skewing effect. A timing diagram depicting when software modules are executed within the various CPUs, drawn against the same time base, will often times reveal any serious skewing situations and will help in the planning of synchronization of computations. Furthermore, the use of local variables within a program, as opposed to frequent accessing to parameters in common memory will also reduce skewing problems.

#### HYBRID-MULTIPLE CPUs WITH INPUT/OUTPUT LINK CONFIGURATION

For the configuration shown in Figure 7, multiple digital processors communicate through a high-speed parallel data Input/Output (I/O) interface

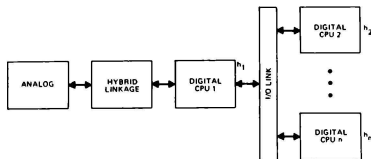


Figure 7. Hybrid-Multiple CPUs with I/O Link Configuration

For uninterrupted CPUs, a similar error to shared common memory skewing occurs. This error, termed I/O link skewing, is in effect similar to a transport delay. That is, for every processor which links up to another processor on a regularly scheduled frame time basis, the receiving processor accepts data which is delayed in time by the transmitting processors frame time. This delay is compounded if many processors are serially linked where the maximum I/O link skewing time approaches the sum of the processors frames times (depending on where I/O transfer requests are placed).

Although the effect of I/O link skewing appears quite severe, typically this type of communication is used for solutions of uncoupled sets of equations. This type of computation is attractive with use of special purpose high-speed digital computers such as Array Processors. When Array Processors are utilized, an I/O Link to that processor can be established several times during the normal frame of an executive CPU. When the Array Processor is accessed, the linking CPU is put into a hold mode since the Array Processor executes at much higher rates. This type of arrangement works quite well when large nonlinear aerodynamic data packages are required and allows the overall structure of the executive CPU to process information in a more serial unskewed fashion.

### SUMMARY OF RESULTS

One of the best methods for investigating error sources is to artificially increase known errors and then measure their effects. Therefore, during the testing for the effects of hybrid computer errors on simulated airframe solution accuracy, a predetermined controlled error source configuration was injected into the problem. The influence of the controlled error source could then be noted.

For the majority of the analysis, a Power Spectral Density (PSD) approach was utilized. The power spectra of a simulated airframe response were generated for airframe pitch attitude, forward velocity, and angle of attack. These power spectra were then related to the theoretical PSD. After a theoretical reference frequency was established, the shift in reference frequency and power magnitude shift at the reference frequency was measured for the airframe variables mentioned above. Figure 8 shows a typical pitch attitude PSD, where curve A represents the theoretical response. A previous study (Reference 3) showed that a shift in power spectrum's local maximum denotes the presence of time delay, and hence an effect of an error source on solution accuracy.

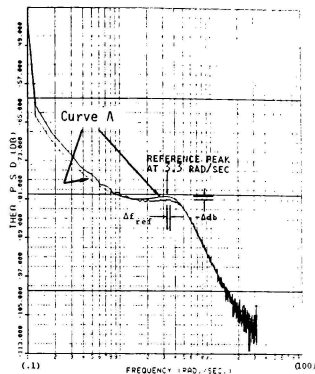


Figure 8. Typical Pitch Attitude Power Spectral Density

In the analog configuration runs, it was found that if key potentiometer settings were set higher than nominal, the pitch attitude power at the reference frequency would drop. Also, the reference frequency would shift to a higher value.

Investigations with the hybrid-single CPU runs indicated a sensitivity of the short-period and phugoid-mode dynamics to time-delay associated with the hybrid linkage operation. The effect of the hybrid linkage quantization resolution was found to increase the reference frequency power for pitch attitude while decreasing power for forward velocity when the linkage word size was decreased to a coarser value. Digital computer frame time influences tend to increase the reference frequency power with increasing frame time, as can be seen in Figure 9. The shift in reference peak frequency denotes a change in the airframe's characteristic frequency response.

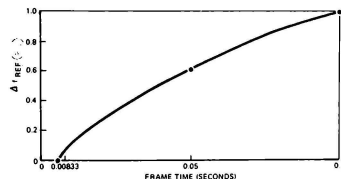


Figure 9. Effects of Frame Time On Airframe Pitch Attitude Response

When dual CPUs were utilized with a shared common memory in a hybrid configuration, it was found that small changes in the reference frequency power occurred due to conversions of the analog elevator surface inputs through the hybrid linkage.

It was found that when one CPU frame time was held constant, an increase in the second CPU frame time produced a decrease in the reference frequency power (see Figure 10). The effects of numerical integration technique on solution accuracy tend to increase both the reference frequency power magnitude and location. Figures 11 and 12 show these effects on peak frequency magnitude and location, respectively, for first order Open Euler (OE), second order Adams Bashforth (AB) and third order Mod Gurk (MG) integration methods.

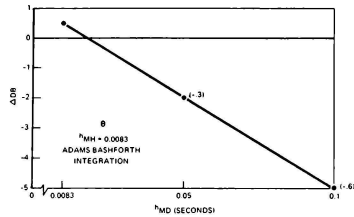


Figure 10. Effects Of Asynchronous Frame Times On Airframe Pitch Attitude Response

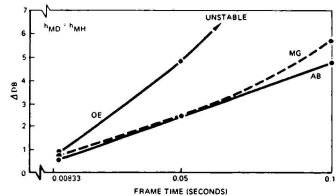


Figure 11. Peak Power Magnitude Shift Due To Frame Time And Integration Method For Pitch Attitude

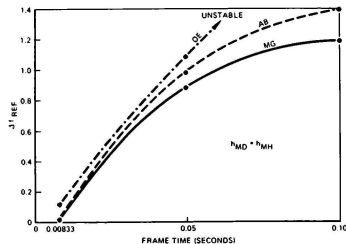


Figure 12. Reference Frequency Shift Due To Frame Time And Integration Method For Pitch Attitude

For the hybrid-dual CPU with an I/O link configuration, it was found that for nearly all integration techniques, the power shift at the reference frequency increases negatively as the frame time increases (see Figure 13). The one exception was for an Open Euler method. However, this method resulted in a reference frequency shift, whereas the other techniques examined did not distort the system frequency appreciably. The 2nd Order Runge Kutta (RK2) method appeared impressive for real time numerical integration with the airframe model utilized in the study. Effects of the hybrid-linkage word-length, in this computer configuration, tended to increase the power frequency magnitude as the quantization coarseness increased, as shown in Figure 14. This trend existed for all numerical integration methods examined.

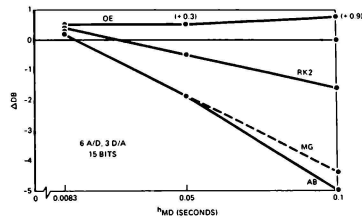


Figure 13. Peak Power Magnitude Shift Due To Frame Time And Integration Method For Pitch Attitude

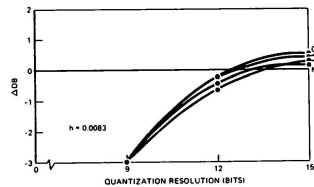


Figure 14. Effects Of Quantization Resolution On Pitch Attitude Response Peak Power Magnitude

Effects of digital computer frame time were studied by constructing an all-digital single-CPU airframe model with 4th order Runge Kutta numerical integrations. Results showed that frame time had virtually no effect on the forward velocity variable while angle of attack and pitch attitude were greatly influenced by computer frame time. Bode plots of the pitch attitude response, as the frame time is increased, are shown in Figures 15 and 16 for gain and phase, respectively. As can be seen in these figures, the frequency response characteristic of the airframe shifts away from the theoretical (zero frame time) as the frame time increases.

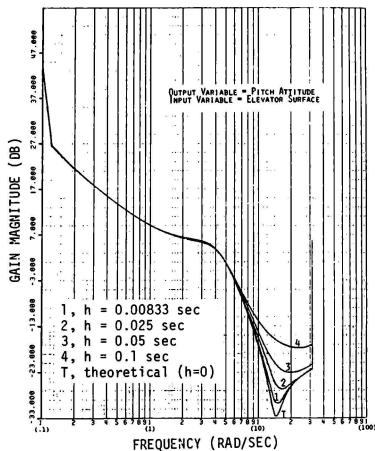


Figure 15. Variation In Bode Gain Due To Frame Time

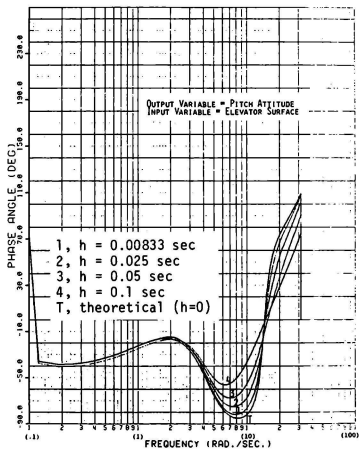


Figure 16. Variation In Bode Phase Angle Due To Frame Time

## REFERENCES

- 1) Weeks, R. A., "Hybrid Computer Errors In Engineering Flight Simulation, AFFDL-TR-79-3091, 1979
- 2) How, R. M., Fogarty, L. E., "Error Analysis of Computer Mechanization of Airframe Dynamics".
- 3) Miller, G. K., et. al., "Evaluation of Several Secondary Tasks in the Determination of Permissible Time Delays in Simulator Visual and Motion Cues", NASA TP-1214, 1978



# USE OF FLIGHT TEST RESULTS TO IMPROVE THE FLYING QUALITIES SIMULATION OF THE B-52H WEAPON SYSTEM TRAINER

Jerome Weiss  
The Singer Company  
Link Flight Simulation Division  
Binghamton, New York

## Abstract

Correlating simulation results to flight test results proved to be a useful tool in assuring high-fidelity flight simulation for the B-52H Weapon System Trainer. The particular correlation described in this paper was limited to the longitudinal flying qualities. Analyses pertaining to the simulation of the engine, aircraft performance, and lateral-directional flying qualities were performed prior to the correlation. The correlation demonstrated the significance of fuel loading and fuel slosh on certain flight test maneuvers. It resulted in modifications to the design data pitching moment coefficient equation and stabilizer angle design. These modifications improved the simulation results to the point where they closely matched with the flight test results.

## Introduction

A high fidelity flight simulation for the B-52H model Weapon System Trainer (WST) was obtained by modifying the simulation design to more closely represent aircraft flight test data. The aircraft response characteristics were obtained from AFFTC-TR-67-30, AFFTC-SD-69-33, and Boeing D3-5393-1 (references 2, 3, and 4, respectively). This comparison was limited to longitudinal flying qualities flight test cases because of the commonality between G and H models. The most significant difference between the H and G models is in the engines and engine nacelles. Differences of approximately 10 percent exist for Basic Drag and Basic Pitching Moment coefficients, with smaller differences in various other coefficient components. These different coefficient components are listed in Table 1. A comparison analysis was previously performed between the B-52G model WST and its flight test data. The resulting modifications from the B-52G WST comparison to the lateral-directional coefficients were incorporated at an earlier date.

Before any flying qualities were analyzed, comparison analyses were performed on the B-52H engine and performance characteristics. The engine analysis verified that thrust, fuel flow, engine pressure ratio, etc., correlated well with flight test data. The aircraft performance analysis concentrated on the aircraft's drag parameters and their correlation to flight manual parameters. The longitudinal flying qualities investigation included trim requirements for

Table 1. MODIFIED AERODYNAMIC COEFFICIENT

COMPONENTS BASED ON BOEING DATA		
$C_{L \text{ BASIC}}$	$C_{D \text{ BASIC}}$	$C_{M \text{ BASIC}}$
$\Delta C_{L \text{ FLAPS}}$	$\Delta C_{D \text{ FLAPS}}$	$\Delta C_{M_{n_z}}$
$\Delta C_{L_{n_z}}$		$\Delta C_{M_{AE}}$
$\Delta C_{L_{AE}}$		$\Delta C_{M_q}$
$\Delta C_{L_q}$		

straight and level flight, trim changes due to aircraft configuration, static longitudinal stability, maneuvering flight, and dynamic short period stability. The comparison of these areas led to modifications of the simulation design and manufacturer's baseline design data. Based on the previous analyses of the engine and aircraft performance, the engine and drag designs were considered frozen. The trim requirements led to an investigation of the stabilizer design because the B-52H uses a movable stabilizer for achieving longitudinal trim. Once acceptable correlation was achieved, this stabilizer design was frozen. The static longitudinal stability and maneuvering flight analyses produced changes to the basic pitching moment coefficient and to the pitching moment coefficient due to elevator deflection. To achieve more desirable dynamic short period stability characteristics, modifications were made to the pitching moment coefficient due to the time rate of change for angle of attack.

These comparative analyses were performed off-line on the Link Software Development Facility (SDF). SDF allowed users to perform analyses at an off-line independent computer complex using simulator software. This facility allowed the simulation software to be executed in the same manner as the actual simulator. This kept required simulator time for analyses to a minimum. Therefore, the majority of the required simulator time was used by the Air Force to verify the results of these analyses.

Close cooperation between the Air Force and Link personnel aided in the selection of flight test cases that were met and identification of key parameters. In some cases with similar conditions and configurations, the flight test results would vary significantly. Continued investigation into these dissimilar test result cases usually led to considering one of these cases as suspect. Link and the Air Force agreed upon suspect cases and these cases were eliminated from these comparisons.

Because of the physical size, large quantity, and distance between the fuel tanks, a limited study of fuel loading and fuel slosh was performed. Since flight test fuel loadings were unavailable, various fuel loadings (for a particular test case) were input for a limited number of static longitudinal stability cases. The effects of the various fuel loadings and their associated fuel slosh could make the difference between acceptable and unacceptable results.

Another limited study was performed for variations in moment of inertia about the y-axis (Iyy) due to various fuel loadings. This study investigated the effects of the various Iyy values on the aircraft's short-period stability characteristics. This analysis showed no significant effect on dynamic short period stability characteristics.

These studies and comparisons were performed primarily at Link's facility in Binghamton, New York, and concluded on-site at Castle Air Force Base, Merced, California.

Incorporating fuel loading and fuel slosh effects, modifications to simulation design and manufacturer's baseline design data led to a satisfactory correlation between the B-52H WST and flight test data. These comparative analyses also demonstrated the important role that accuracy and complete flight test data plays in obtaining a high-fidelity flight simulation of complex aircraft.

#### Fuel Slosh Effects

The B-52H aircraft is capable of carrying approximately 300,000 lb of fuel in 10 different tanks, six along the wings and four in the fuselage. To obtain an accurate simulation, fuel slosh/fuel loading effects must be considered. Reference 4 discusses the fuel slosh effect on longitudinal center of gravity (c.g.) as a function of the aircraft attitude. To better understand this effect on flight test results, a limited study was performed. This study addressed two separate items, trim point c.g. and control surface deflection during a static longitudinal stability test. Five cases were selected from references 2 and 3. These cases included both cruise and power approach configurations with a c.g. variation for each configuration. This analysis was performed on the SDF.

Each flight test case gave initial trim point conditions which included weight, c.g., etc. It was assumed that the c.g. listed on the flight test data was calculated for the aircraft at a zero pitch attitude,  $\theta = 0^\circ$ . Since no fuel loading or trim attitude information existed, several

fuel loadings were obtained for each case at  $\theta = 0^\circ$ . When the trim points were analyzed for these selected test cases, it was found that the pitch attitude usually was not zero. This non-zero trim pitch attitude yielded a shift in the c.g., so that the c.g. would not necessarily be equal to the stated value on the flight test data.

Fuel loading/slosh had definite effects on the control surface deflection for tests where the aircraft experienced significant steady state attitude changes. In static longitudinal stability tests, the amount of elevator deflection required to obtain a particular airspeed varied with fuel loading. In the worst case this variation exceeded  $1^\circ$  of elevator deflection (Table 2). At this particular airspeed, a variation in c.g. of 1.5 MAC was also observed (Table 3). The same test cases were analyzed using the stated c.g. and no fuel slosh effects. Differences greater than  $4^\circ$  of elevator deflection were observed for the same airspeed (Table 4). The no fuel slosh analyses also had no variation in c.g. as the aircraft attitude changed. When fuel effects were accounted for the c.g. could vary as much as 4.2 MAC from the trim c.g. (Table 5) and 1.7 MAC at a particular airspeed (Table 3). The trim c.g. was also observed to vary as much as 2.6 MAC from its stated flight test value for various fuel loadings (Table 5). To correlate simulator results with the flight test results, fuel loadings were selected based on typical fuel burn sequence and with slosh effects activated.

#### Longitudinal Trim

Longitudinal trim was obtained by movement of the horizontal stabilizer. To verify the simulation in obtaining the proper trim stabilizer angle at a given aircraft configuration, three different types of checks were performed. Before these analyses were performed, the simulation

Table 2. VARIATION OF ELEVATOR DEFLECTION  
FOR VARIOUS FUEL LOADINGS

Gross Weight	Configuration	Flight Test Trim C.G.	Mach No.*	$\Delta\delta$ Slosh
319,000	CR	19.0	0.34 0.49	0.25 0.13
407,000	CR	24.9	0.70 0.84	0.40 0.50
319,000	CR	31.2	0.30 0.50	1.10 0.35
281,000	PA	19.0	0.22 0.31	0.60 0.50
262,000	PA	31.3	0.22 0.33	0.90 0.50

\*The two Mach numbers listed per test case are the end points of the static longitudinal stability test.

$\Delta\delta$  Slosh = Variation of elevator deflection at a Mach number due to fuel loadings.

Table 3. VARIATION OF CENTER OF GRAVITY DUE TO

## DIFFERENT FUEL LOADING FOR THE STATIC

## LONGITUDINAL STABILITIES WITH FUEL SLOSH EFFECTS

Gross Weight	Configuration	Flight Test Trim C.G.	Mach No.*	$\Delta$ C.G.
319,000	CR	19.0	0.34 0.49	0.3 0.3
407,000	CR	24.9	0.70 0.84	0.8 0.4
319,000	CR	31.2	0.30 0.50	1.5 0.7
281,000	PA	19.0	0.22 0.31	0.3 1.7
262,000	PA	31.3	0.22 0.33	0.5 0.9

\*The two Mach numbers listed per test are the end points of the static longitudinal stability test.

$\Delta$ C.G. = Variation of c.g. at Mach number due to various fuel loadings.

drag was analyzed and modified as required to match flight test. All three checks were performed with fuel slosh/loading effects taken into account.

The first check was stabilizer angle for all of the initial (trim) points of the static longitudinal stability and maneuvering flight tests from references 2 and 3. An acceptable range of  $\pm 0.5^\circ$  of stabilizer angle was used. Figure 1 shows the comparison of flight test to simulation values. A significant number of data points fell outside of the acceptable tolerance. This plot also showed that if the simulation stabilizer values were offset by  $0.5^\circ$ , virtually all of the data points would fall within the acceptable tolerance band. This was found to be true regardless of the aircraft configuration. The actual reason for the poor baseline correlation may lie in an error in the basic pitching moment coefficient.

An offset was implemented by making a software stabilizer angle (FSTAB) equal to the original stabilizer angle (GSTAB) minus  $0.5^\circ$ . This FSTAB value was used to calculate the stabilizer's contribution to the total lift and pitching moment coefficient equations, replacing GSTAB. A plot of the modified design for stabilizer angles is shown in Figure 2. The four points which did not meet tolerances were at flight conditions similar to points that did meet the tolerance and therefore were considered suspect data points.

Table 4. ELEVATOR DEFLECTION AND TRIM CENTER OF GRAVITY FOR STATIC

## LONGITUDINAL STABILITIES WITH AND WITHOUT FUEL SLOSH EFFECTS

Gross Weight	Configuration	Flight Test Trim C.G.	Slosh Effect Trim C.G. +	Mach No.*	$\bar{\delta}_{e\text{Slosh}}$	$\delta_{e\text{No-Slosh}}$
319,000	CR	19.0	19.2	0.34 0.49	-3.3 3.9	-4.3 4.6
407,000	CR	24.9	25.4	0.70 0.84	-2.3 1.2	-2.8 1.7
319,000	CR	31.2	31.7	0.30 0.50	-2.0 2.5	-3.5 2.7
281,000	PA	19.0	17.0	0.22 0.31	-4.7 2.1	-6.0 3.6
262,000	PA	31.3	28.7	0.22 0.33	-0.1 1.3	-4.5 1.2

\*The two Mach numbers listed per test are the end points of the static longitudinal stability test.

+ This trim c.g. is the average trim c.g. for the various fuel loadings.

$\bar{\delta}_{e\text{Slosh}}$  = Average elevator deflection for various fuel loadings.

$\delta_{e\text{No-Slosh}}$  = Elevator deflection with no slosh effect.

Table 5. VARIATION OF CENTER OF GRAVITY BETWEEN THE TRIM POINT AND THE END

POINT AIRSPEED WITH FUEL SLOSH EFFECTS					
Gross Weight	Configuration	Flight Test Trim C.G.	Slosh Effect Trim C.G.+	Mach No.*	$\Delta C.G.^1$
319,000	CR	19.0	19.2	0.34 0.49	1.7 2.0
407,000	CR	24.9	25.9	0.70 0.84	0.8 1.0
319,000	CR	31.2	31.7	0.30 0.50	2.5 2.1
281,000	PA	19.0	17.0	0.22 0.31	3.6 2.1
262,000	PA	31.3	28.7	0.22 0.33	4.2 1.8

$\Delta C.G.^1$  = Absolute value of the c.g. difference between the trim and end point  
airspeed both having fuel slosh effects.

\*The two Mach numbers listed per test are the end points of the static longitudinal stability test.

+ This trim c.g. is the average trim c.g. for the various fuel loadings.

The second check was the change in stabilizer angle required to trim for various aircraft configuration changes. The difference or delta in stabilizer angle ( $\Delta STAB$ ) was compared to the values in reference 4 or specified by the mastercrew. The mastercrew was a crew of instructor pilots assigned to assess the B-52G Pre-Production Unit (PPU). Table 6 shows the test conditions, change in aircraft configuration, reference, and both simulator and reference delta stabilizer angles. This analysis was performed with the FSTAB modification and fuel slosh incorporated in the software. Also included in

this check was the change in stabilizer angle required to trim during flap extension/retraction (reference 5). During the flap transition the stabilizer deltas were all within the  $\pm 0.5^\circ$  acceptable tolerance band.

As a final check on the stabilizer simulation, several plots of stabilizer vs. elevator deflection, references 2 and 3, at a particular flight condition were analyzed. Again this check was performed for both the original data and modified data. A typical plot of the results from this analysis is shown in Figure 3. This analysis was

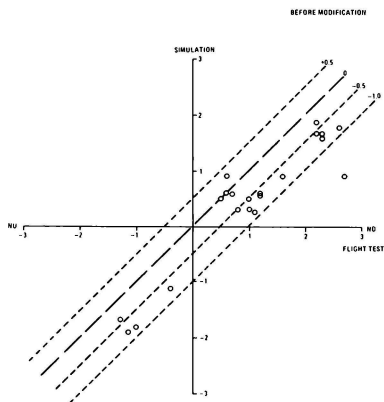


Figure 1 STABILIZER ANGLE CORRELATION - B-52 H PU (CRUISE CONFIGURATION)

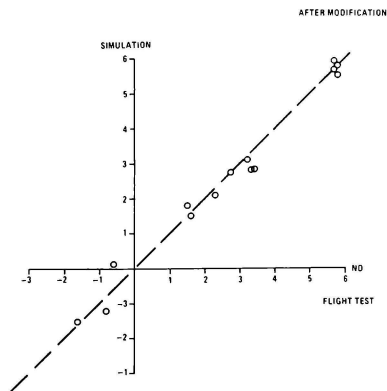


Figure 2 STABILIZER ANGLE CORRELATION - B-52 H PU POWER APPROACH CONFIGURATION

Table 6. SUMMARY OF STABILIZER TRIM ANGLE CHANGE FOR AIRCRAFT

## CONFIGURATION CHANGES

$W \times 10^{-3}$	ALT FLT	C.G. MAC	$V_{IND}$ KTS	FLAPS	GEAR	A/C CONFIGU- RATION CHANGE	$\Delta$ STAB DEG	REF $\Delta$ STAB DEG	REF
450.	1000.	27.7	180.	DN	UP	FLAT RETRACTION	2.9	3.0	4 and 5
293.	4000.	26.0	154.	DN	DN	A/B EXTENSIONS*			
						0 2	0.6	0.5	4
						0 4	2.6	2.8	4
						0 6	3.6	3.6	4
293.	5000.	26.0	250.	UP	UP	GEAR EXTENSION	0.2 0	0.2	MASTERCREW COMMENTS

\*A/B Extensions are given in terms of airbrake level position (page 9.5, reference 1).

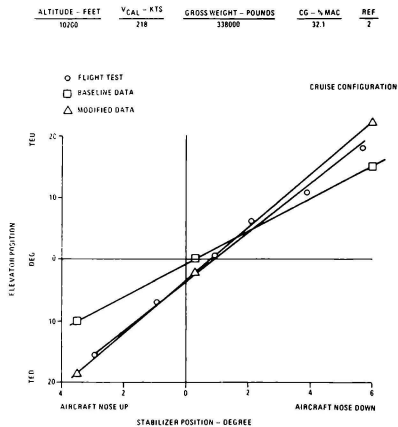


Figure 3 STABILIZER ELEVATOR TRADE-OFF

performed after modifications to pitching moment due to elevator deflection, described in the following section, were made.

## Longitudinal Stability and Control

Three major topics are addressed in this section: static longitudinal stability, maneuvering, flight, and longitudinal short-period dynamic stability. In analyzing each of the above topics, all flight test aircraft configurations (cruise, power approach with no airbrakes, and power approach with airbrakes at position four) were considered. Fuel slosh/loading effects were included in all analyses except

longitudinal short period dynamics. Longitudinal trim and aircraft performance analyses had been completed and all necessary modifications were incorporated before these analyses began.

The first topic analyzed was static longitudinal stability. The acceptable range of elevator deflection in an elevator deflection ( $\delta_e$ ) vs. airspeed or Mach number curve was  $\pm 1^\circ$  from the flight test end point speed value. This tolerance took into account variations due to fuel slosh effects and the uncertainty of the actual fuel loading used during flight test.

The initial analysis was first performed with the aircraft in the cruise configuration. This initial analysis used the baseline coefficient data, reference 1, and its results were plotted and compared to the flight test results from references 2 and 3. The comparison plots  $\delta_e$  vs. M were used in a Slope Matching Technique analysis for all eight cruise configuration static longitudinal stabilities from references 2 and 3. The following observations were made of these plots:

1. Cases at high altitude ( $ALT \geq 35,000$  ft) and high Mach number ( $M > .6$ ), the simulation had good correlation with flight test results.
2. At low Mach number ( $M < .33$ ) and high wing angles of attack ( $\alpha_w > 9^\circ$ ), the simulation elevator deflection tended to flatten out.
3. At high Mach number ( $M > .8$ ), the simulation elevator deflection showed a bucket effect bottoming out at approximately  $M = 0.82$ .
4. In all other tests, the simulation results needed to be rotated clockwise relative to the flight test results. This means that the simulation results were below the flight test values for the deceleration portion of the test and above for the acceleration portion of the test.

Observation 2 led to an investigation of the coefficient component. It was discovered that the shape of the  $C_{m_{BASIC}}$  data curve for  $M=0.3$  in reference 1 did not follow the shape of other low Mach number data curves at high wing angles of attack ( $\alpha_w$ ). This data curve ( $M = 0.3$ , flaps up) was reshaped as shown in Figure 4.

Observation 3 indicated a problem at approximately  $M = 0.82$ . Studying the  $C_{m_{BASIC}}$  reference 1 led to the observation that the shape of the  $M = 0.825$  curve did not follow the shape of its neighboring data curves. A cross plot of vs.  $M$  for various  $\alpha_w$ , Figure 5, was made and suggested a shape modification to both the  $M = 0.825$  and  $M = 0.85$  data curves. These modified curves are also shown in Figure 4. The modified  $C_{m_{BASIC}}$  curves were inserted into the simulation. Rerunning the static longitudinal stability cases showed a significant improvement to the problems discussed in observations 2 and 3.

Observation 1 pointed out that for cases at high altitudes and high Mach number, good correlation existed. Therefore, this portion of the  $\Delta C_{m_{be}}$  data was satisfactory.

The required clockwise rotation of the simulation results, noted in observation 4, was achieved by reducing the values of  $\Delta C_{m_{be}}$  data.

The magnitude of this reduction was determined by the percent difference between the simulation and the flight test average slopes. The reduction of pitching moment coefficient due to elevator deflection required for the different flight test cases was c.g. dependent. This changed the  $\Delta C_{m_{be}}$  data from a function of Mach number and altitude to one of c.g., Mach number and altitude.

Values of  $\Delta C_{m_{be}}$  for areas where flight test conditions did not exist were interpolated from  $\Delta C_{m_{be}}$  values where flight test data did exist. Figure 6 shows the baseline  $\Delta C_{m_{be}}$  data and Figures 7 - 10 show the modified  $\Delta C_{m_{be}}$  data curves. To demonstrate the improvement achieved by these modifications, maximum error plots based on the baseline and modified data are presented in Figures 11 and 12, respectively. These maximum error plots show the largest difference between

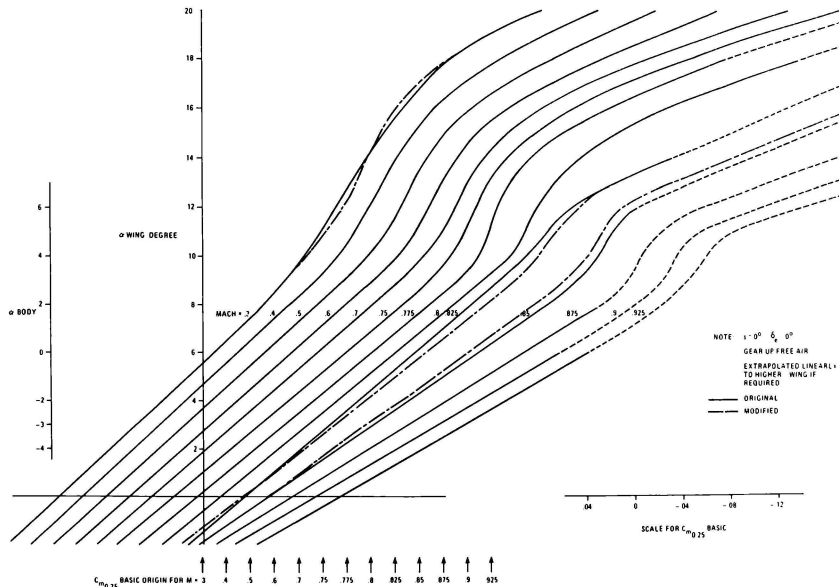


Figure 4 ORIGINAL AND MODIFIED BASIC PITCHING MOMENT COEFFICIENT

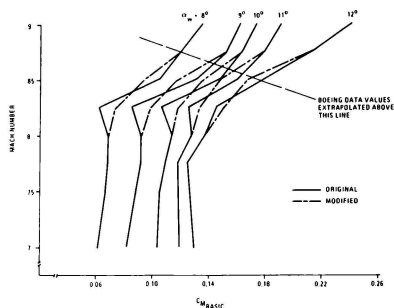


Figure 5 MODIFIED  $M = 0.825$  AND  $0.85$  BASIC PITCHING MOMENT COEFFICIENT

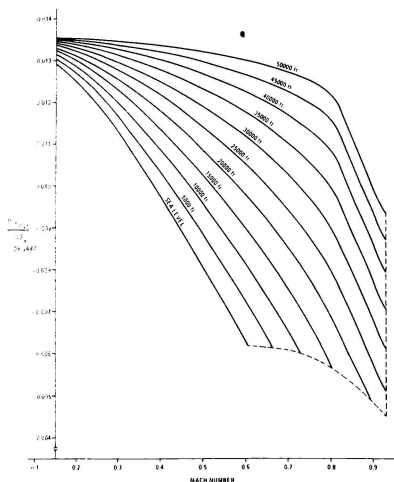


Figure 6 BASELINE  $\Delta C_{m_{\delta_e}}$  DATA

the simulation and flight test elevator deflections for each case analyzed.

After good correlation for static longitudinal stability (cruise configuration) was obtained, the modified  $\Delta C_{m_{\delta_e}}$  was used to investigate

maneuvering flight cruise configuration cases. The modified data also improved the correlation of the elevator deflection vs. normal acceleration ( $\delta_e$  vs.  $g$ ) slopes. This topic is discussed in more detail in the following Maneuvering Flight analysis section.

Static longitudinal stabilities with the aircraft in the power approach configuration was the next area investigated. This investigation was broken into two parts. The first was for airbrakes in the zero position. The second was for the airbrakes in position four. The Slope Matching Technique described for the cruise configuration analysis was also used for both airbrake positions zero and four, power approach configuration analyses.

Since a limited amount of flight data exists for both airbrake positions, similar flight condition cases were plotted to see the correlation between the two flight test reports, reference 2 and 3. Figures 13 and 14 are for airbrakes at position zero and Figures 15 and 16 are for airbrakes in position four. The worst data elevator deflection scatter observed was as much as  $1.5^\circ$  for airbrakes at position zero and  $2^\circ$  for airbrakes in position four.

The analysis of the zero position airbrakes, for the initial baseline data simulation results, indicated that a decrease in  $\Delta C_{m_{\delta_e}}$  was necessary

to obtain acceptable correlation with flight test. An acceptable range of  $\pm 1^\circ$  of  $\delta_e$  at the end point speed was used for acceptable correlation. The original baseline and modified data curves are presented in Figure 17. In areas where no flight test data existed, linear interpolated values were used.

Maneuvering flight test cases in this configuration were analyzed with this modified data and the slope of the  $\delta_e$  vs.  $g$  plots were improved. This topic will be discussed in more detail in the Maneuvering Flight analysis section.

The last section within the static longitudinal stability topic was for power approach with airbrakes at position four. The airbrake zero modified  $\Delta C_{m_{\delta_e}}$  did not yield acceptable correlation.

A problem still existed at high wing angles of attack. It was decided that the way to fix this problem area was to modify Pitching Moment Coefficient due to Spoilers - flaps down ( $\Delta C_{m_{\delta_{sp}}}$ ). This component was selected because it

is a function of wing angle of attack and would not affect any previous analyses. No modification was desired for wing angles of attack below  $8^\circ$ . In this analysis an iterative reshaping technique was used to modify  $\Delta C_{m_{\delta_{sp}}}$  until acceptable correlation was obtained.

Using the modified data curves, the maneuvering flight cases were checked. This modification to  $\Delta C_{m_{\delta_{sp}}}$  yielded acceptable results for two of the three maneuvering flight cases.

The one case that was out of the acceptable elevator deflection range had similar conditions to a case that did meet the elevator deflection acceptable range. Based on this, the flight test data for the case out of the acceptable range was considered suspicious.

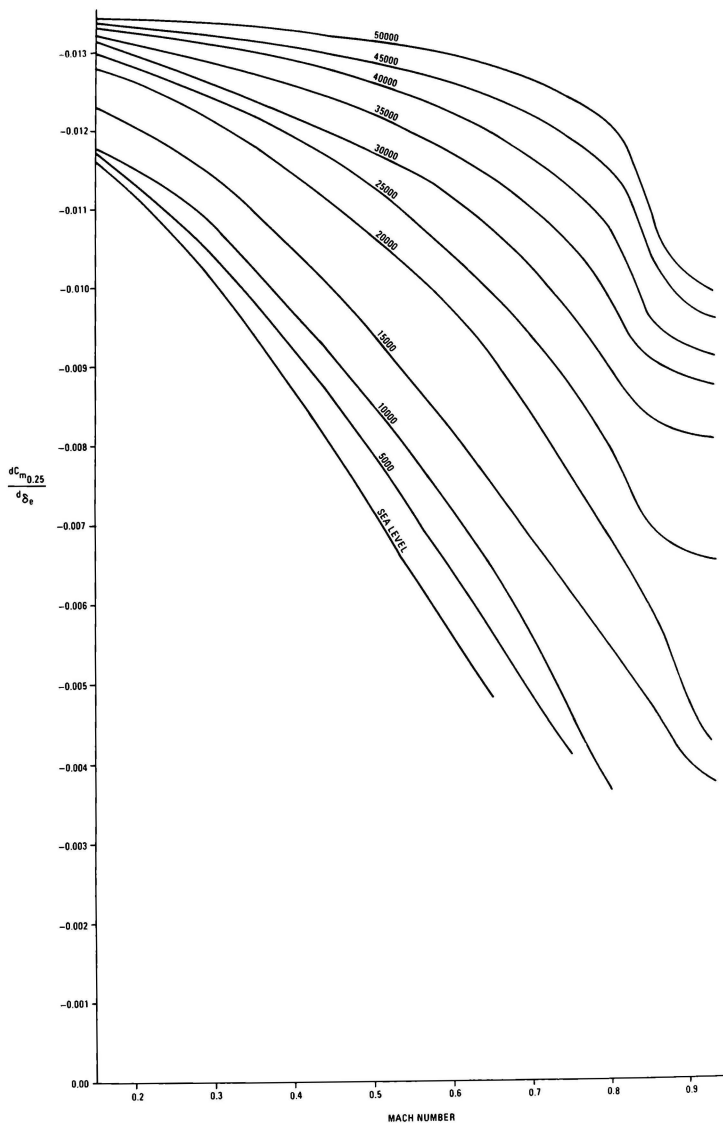


Figure 7 MODIFIED PITCHING MOMENT COEFFICIENT - ELEVATOR EFFECT CG = 16%



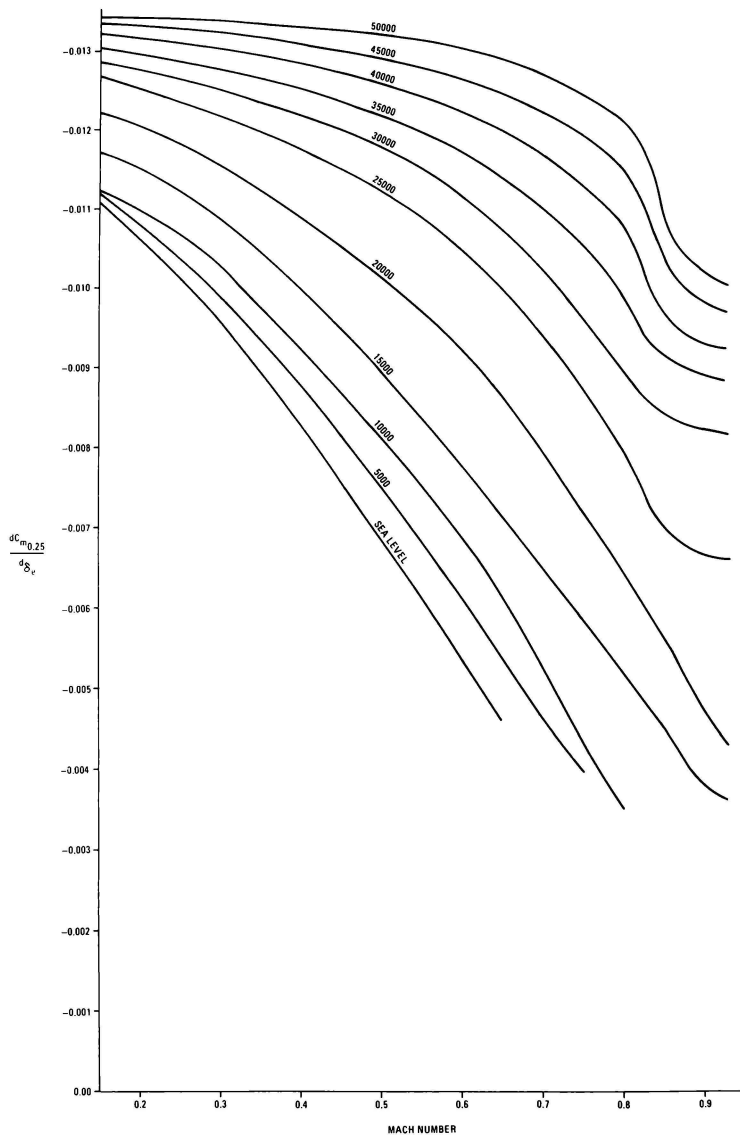


Figure 8 MODIFIED PITCHING MOMENT COEFFICIENT EFFECT CG = 19%

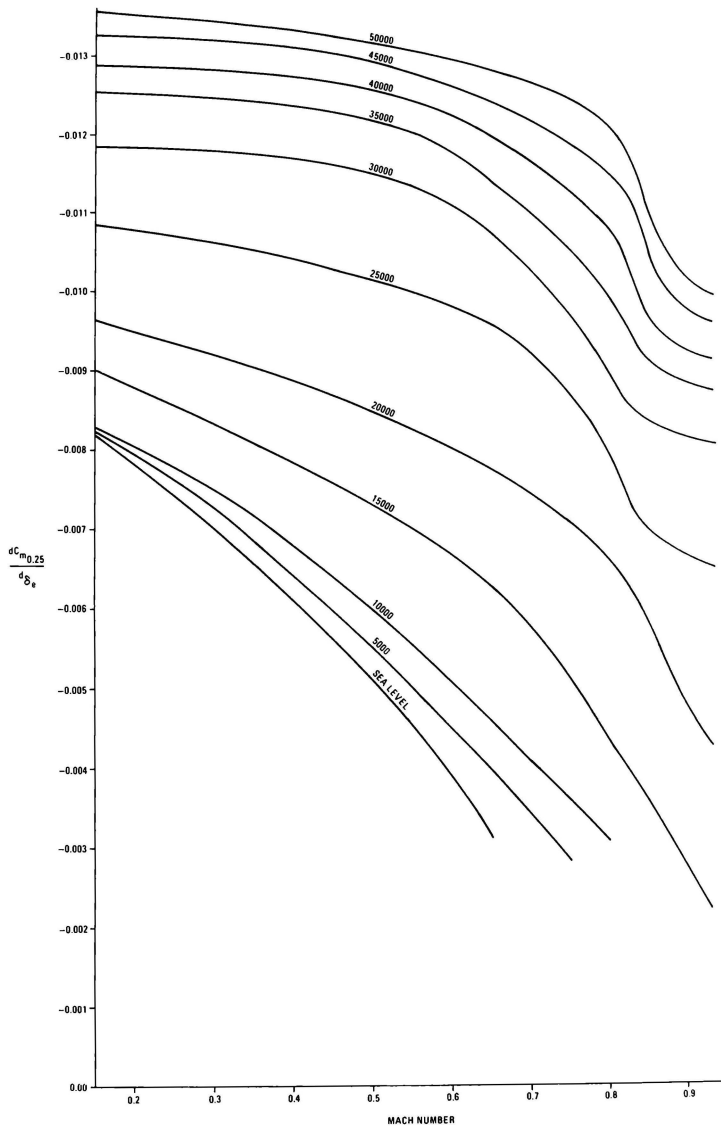


Figure 9 MODIFIED PITCHING MOMENT COEFFICIENT – ELEVATOR EFFECT CG = 32%

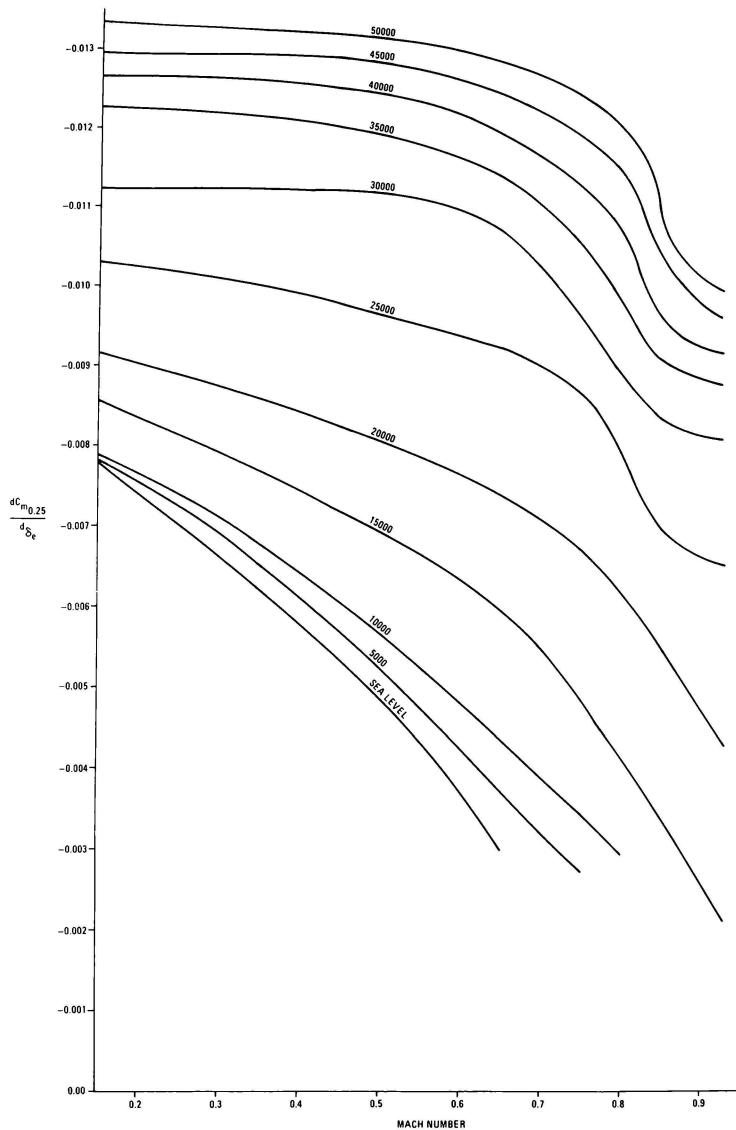


Figure 10 MODIFIED PITCHING MOMENT COEFFICIENT – ELEVATOR EFFECT CG = 35%

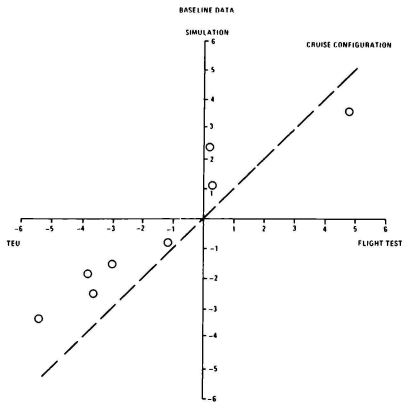


Figure 11 STATIC LONGITUDINAL STABILITY – MAXIMUM ELEVATION ERROR

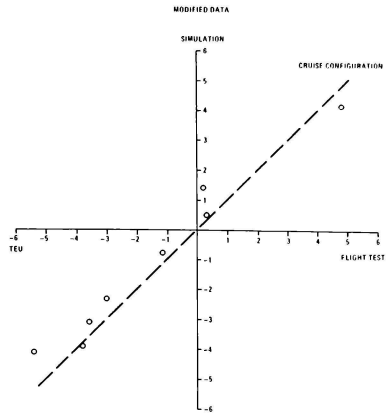


Figure 12 STATIC LONGITUDINAL STABILITY – MAXIMUM ELEVATOR ERROR

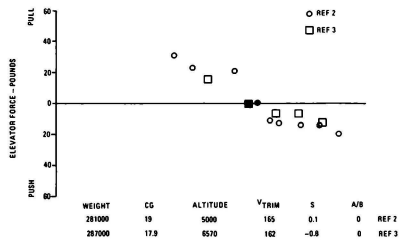


Figure 13 FORWARD CG FLIGHT TEST DATA COMPARISON

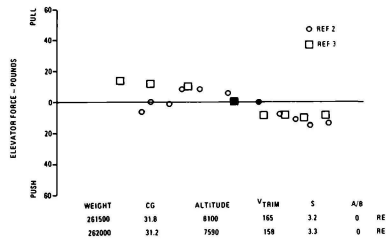


Figure 14 AFT CG FLIGHT TEST DATA COMPARISON

SYMBOL	WEIGHT	ALTITUDE	CG	STABILIZER	$V_{CAL}$	REF
□	275000	5100	18.5	+2.3 N.D.	162	2
△	280500	6710	17.3	+1.6 N.D.	161	3

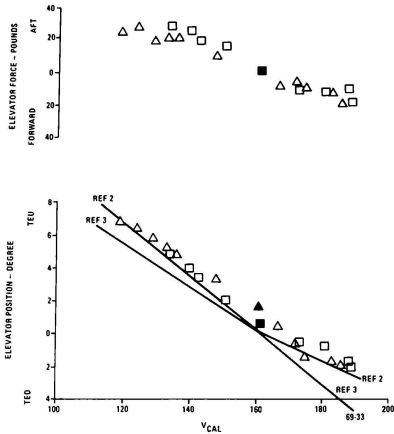


Figure 15 FORWARD CG POWER APPROACH A/B = 4 FLIGHT TEST COMPARISON

SYMBOL	WEIGHT	ALTITUDE	CG	STABILIZER	$V_{CAL}$	REF
△	242500	7100	30.5	+5.8 N.D.	160	3
□	242500	10100	30.7	+5.7 N.D.	164	2

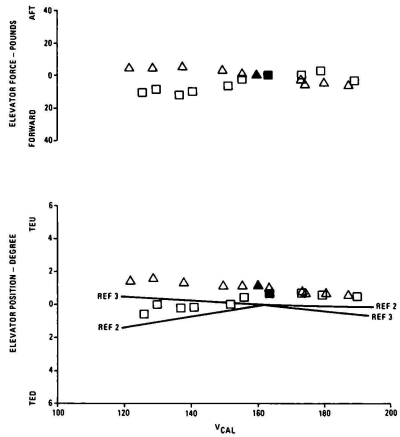


Figure 16 CG POWER APPROACH A/B = 4 FLIGHT TEST COMPARISON

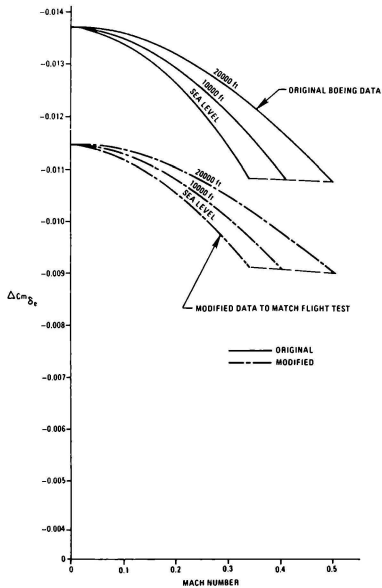


Figure 17  $\Delta C_m \delta_e$  FLAPS-DOWN BASELINE AND MODIFIED DATA

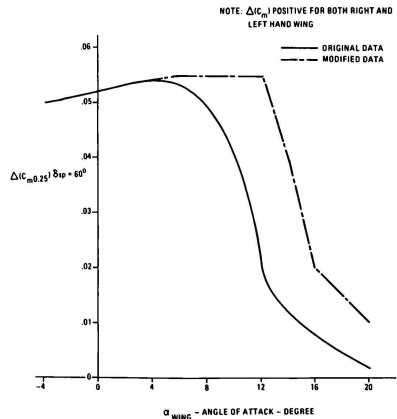


Figure 18  $\Delta C_m \delta_e$  FLAPS DOWN BASELINE AND MODIFIED DATA

The original and modified  $\Delta C_{m_{\delta_{sp}}}$  curves are presented on Figure 18. The improvement achieved by the above modifications to  $\Delta C_{m_{\delta_e}}$  and  $\Delta C_{m_{\delta_{sp}}}$  for power approach with airbrakes at position zero and four can be seen in Figures 19 and 20. These figures are the maximum error plots for static longitudinal stabilities for these configurations.

The second topic analyzed was maneuvering flight, also known as stick force per g. Acceptable elevator deflection range was  $\pm 1^\circ$  of elevator deflection, applied at the last flight test point, on a plot of elevator deflection vs. normal acceleration ( $\delta_e$  vs. g).

The initial baseline cruise data, reference 1, analysis indicated for most cases that the simulation elevator deflection was below the flight test values by more than the  $1^\circ$  allowable deviation. Most of these cases were for low altitudes, similar to observation 4 of the static longitudinal stability analysis. Therefore, the initial attempt to correct this was to apply the modified  $\Delta C_{m_{\delta_e}}$  obtained from the cruise configura-

tion static longitudinal stability analysis. The modified  $\Delta C_{m_{\delta_e}}$  analysis moved the slopes of the  $\delta_e$  vs. g curves to an allowable range. Plots of

the maximum elevator deflection error for the baseline and modified simulation results are shown on Figures 21 and 22.

The power approach analysis was broken into two parts: airbrakes at position zero and four. Both parts of this analysis were performed after their respective longitudinal static stabilities were completed. The same acceptable range of  $\pm 1^\circ$  of elevator deflection was used. As in the static longitudinal stabilities, zero airbrake position elevator deflections for the baseline data simulation results were outside of the acceptable range. These cases were then reanalyzed with the modified power approach  $\Delta C_{m_{\delta_e}}$  from the power approach lon-

gitudinal static stabilities on the off-line SDF. The improvement due to the modified  $\Delta C_{m_{\delta_e}}$  data

curves was sufficient to bring the simulation slopes of  $\delta_e$  vs. g plots to acceptable values.

Only a limited amount of flight test cases existed for maneuvering flight power approach configurations in references 2 and 3. Therefore, both airbrake positions maximum error plots are presented on Figures 23 and 24 for the baseline and modified coefficient components respectively.

The airbrakes at position four analysis was performed after the modification to  $\Delta C_{m_{\delta_{sp}}}$

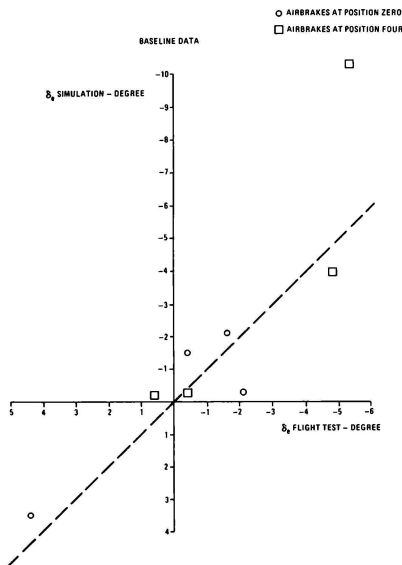


Figure 19 STATIC LONGITUDINAL STABILITY MAXIMUM ELEVATOR ERROR POWER APPROACH CONFIGURATION

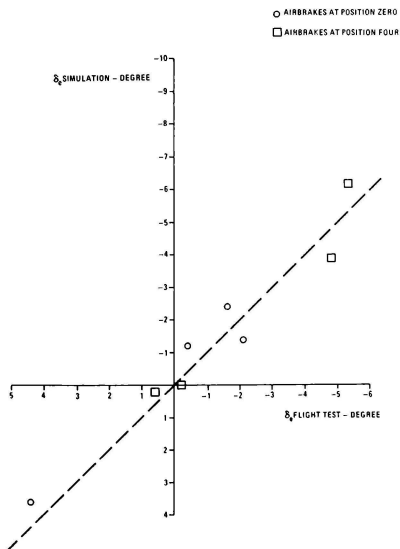


Figure 20 STATIC LONGITUDINAL STABILITY MAXIMUM ELEVATOR ERROR POWER APPROACH CONFIGURATION MODIFIED DATA

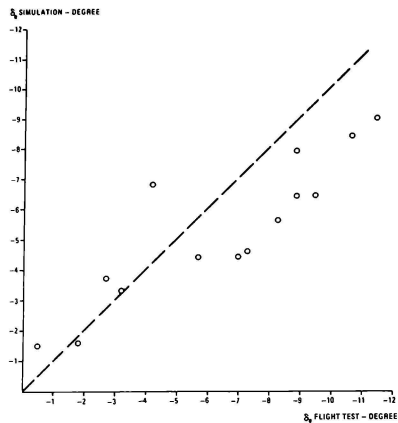


Figure 21 MANEUVERING FLIGHT – MAXIMUM ELEVATOR ERROR CRUISE CONFIGURATION

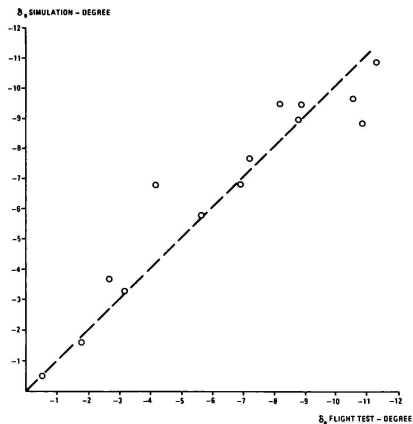


Figure 22 MANEUVERING FLIGHT – MAXIMUM ELEVATOR ERROR CRUISE CONFIGURATION

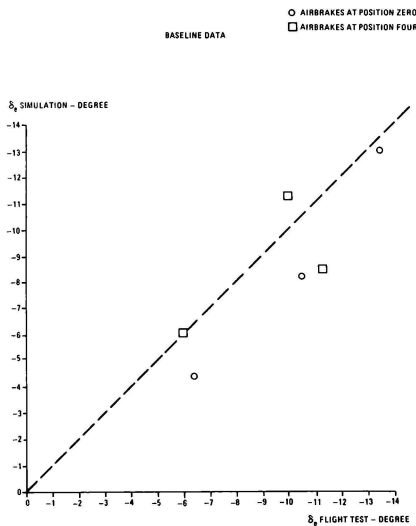


Figure 23 MANEUVERING FLIGHT MAXIMUM ELEVATOR ERROR POWER APPROACH CONFIGURATION

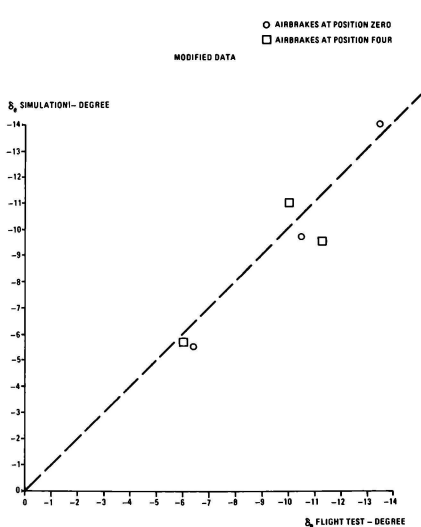


Figure 24 MANEUVERING FLIGHT MAXIMUM ELEVATOR ERROR POWER APPROACH CONFIGURATION

made for the same configuration static longitudinal stabilities. The modification to  $\Delta C_{m_{\delta_{sp}}}$  was such that two of the three  $\delta_e$  vs.  $g$  curve slopes were acceptable.

Maximum error plots can be found on Figures 23 and 24. The one case that was out of the acceptable range had similar conditions to a case that did fall within the acceptable elevator deflection range. Based on this, the flight test data out of the acceptable range was considered suspicious.

The last topic to be analyzed was that of longitudinal short period dynamic stability. As in the other topics, this analysis was handled in two parts based on aircraft configuration, cruise and power approach. Although the analysis treated the cruise and power approach separately, the methodology was the same. Therefore, only one presentation is given, but each modified function for the different configurations is shown separately. Fuel slosh/loading was not included in this analysis because of the fast response time of the aircraft to the elevator input.

The elevator inputs to all of these test cases were modeled as an isosceles triangle of the same amplitudes, slope, and frequency as the actual aircraft input. No elevator overshoot was modeled into the input to the simulation.

Since no fuel loading information for the flight test conditions was available, exact moment of inertia values were not known. A limited study was performed by varying  $I_{yy}$ , the most critical moment of inertia for the short period mode, to investigate its effect on pitch rate ( $q_s$ ) response characteristics. Various fuel loadings were found for a particular case's weight and c.g. with  $\theta = 0^\circ$  (same method as fuel slosh/loading study).  $I_{yy}$  was found to vary as much as 800,000 slug-ft<sup>2</sup>. For this limited study, no significant changes in the first peak characteristics were observed and a maximum variation of 0.3 seconds were found for crossover times. Therefore a value of 8,168,000 slug-ft<sup>2</sup> was used for  $I_{yy}$  analyses. This value of  $I_{yy}$  was calculated from a mid-range weight for a typical fuel burn sequence.

A comparison of the baseline data simulation and flight test (references 2 and 3) responses in pitch rate ( $q_s$ ) led to the observations that pitch damping needed to be increased and the first peak amplitudes needed to be adjusted. This was particularly true for the high dynamic pressure cases. The baseline simulation analysis included all previous flight test correlation modifications to stabilizer angle,  $\Delta C_{m_{\delta_{sp}}}$ ,  $\Delta C_{m_{\delta_e}}$ , and  $\Delta C_{m_{\delta_{sp}}}$ .

The flight test data was so well damped that calculating response frequency and damping ratio was not practical. Therefore, an overlay technique of matching  $q_s$  responses was used instead

of matching frequency and damping ratio. First peak amplitude characteristics and crossover time were of primary importance, followed by second peak amplitude characteristics. The approach used to obtain acceptable response ( $q_s$ ) characteristics was to manipulate Pitching Moment due to Rate of Change for Wing Angle of Attack ( $\Delta C_{m_{\dot{\delta}_e}}$ ).

The traditional pitch damping term, Pitching Moment due to Pitch Rate, was not used because of its effect on maneuvering flight test results. During this analysis, it was observed that the modification required to  $\Delta C_{m_{\dot{\delta}_e}}$  would be a function

of dynamic pressure ( $q$ ). The magnitude of the modification was fine-tuned by using a ratio of first peak amplitude for the unmodified  $\Delta C_{m_{\dot{\delta}_e}}$  and the first peak amplitude of the modified  $\Delta C_{m_{\dot{\delta}_e}}$ .

This process was repeated several times until a function of  $q$  was obtained that produced acceptable response characteristics. To assure that overdamping did not occur, this function was multiplied by the absolute value of the rate of change of elevator position  $|\dot{\delta}_e|$ . The  $|\dot{\delta}_e|$  allowed this function to act only during the elevator input. The  $q$  function along with  $|\dot{\delta}_e|$  was found to be sufficient for acceptable correlation of the first peak amplitude and crossover time characteristics. Some additional restoring moment was necessary for the second peak characteristic correlation. A constant gain was applied to  $\Delta C_{m_{\dot{\delta}_e}}$  in addition to the  $q$  function discussed above.

The constant gain was not multiplied by  $|\dot{\delta}_e|$ . A final adjustment to the  $q$  function was performed to compensate for this constant gain. The final functions are shown in Figures 25 and 26 for the cruise and power approach configurations, respectively. The modified  $\Delta C_{m_{\dot{\delta}_e}}$  equation is shown below:

$$\Delta C_{m_{\dot{\delta}_e}} = \Delta C_{m_{\dot{\delta}_e}}^{\text{original}} \left( K + \frac{f(q) \text{Flaps}}{\text{Up}} \left| \dot{\delta}_e \right| (1 - \delta_{FW}^*) \right) f(q) \text{FLAPS} \left| \dot{\delta}_e \right| \delta_{FW}^* \text{DOWN}$$

where  $\Delta C_{m_{\dot{\delta}_e}}^{\text{original}}$  =  $\Delta C_{m_{\dot{\delta}_e}}$  based on reference 1

$\delta_{FW}^*$  = normalized flap position (0 for cruise, 1 for power approach)

$|\dot{\delta}_e|$  = absolute value at the rate of change of elevator deflection

$f(q)$  = function of dynamic pressure

$k$  = constant gain value equal to 5.0

Comparative plots of the modified and baseline data first peak characteristics, cross-over time and second peak characteristics are presented on Figures 27 through 29(a), respectively. These plots do not contain suspicious data cases.



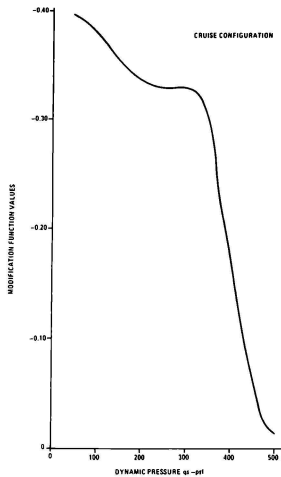


Figure 25 SHORT PERIOD MODIFICATION FUNCTION TO  $\Delta C_{m\alpha}$

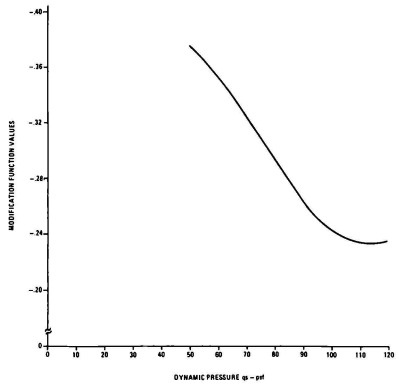


Figure 26 SHORT PERIOD MODIFICATION FUNCTION TO  $\Delta C_{m\alpha}$

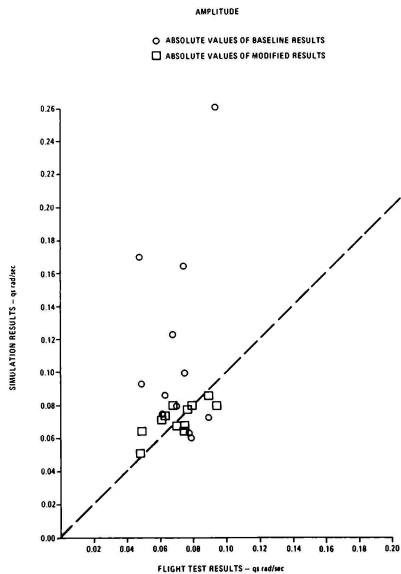


Figure 27 COMPARISON PLOTS FOR SHORT PERIOD DYNAMICS FIRST PEAK CHARACTERISTICS

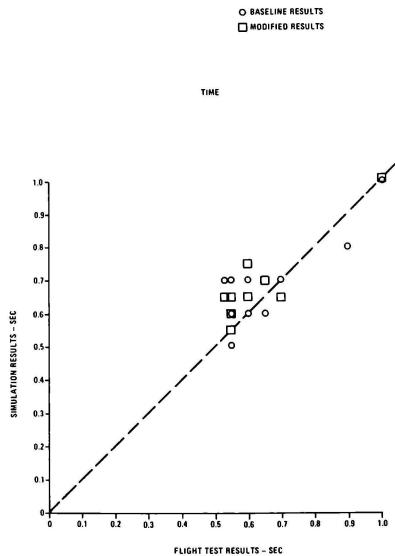


Figure 27 (a) COMPARISON PLOTS FOR SHORT DYNAMICS FIRST PEAK CHARACTERISTICS

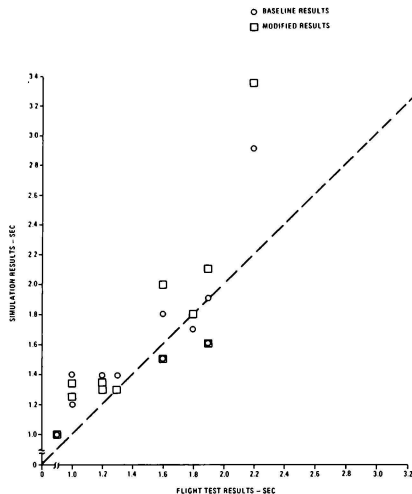


Figure 28 COMPARISON PLOTS FOR SHORT PERIOD DYNAMIC CROSS-OVER TIME

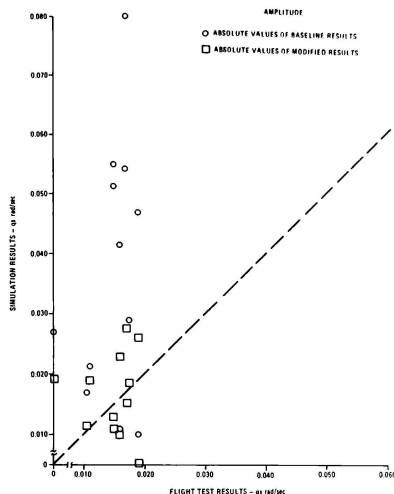


Figure 29 COMPARISON PLOTS FOR SHORT PERIOD DYNAMICS SECOND PEAK CHARACTERISTICS

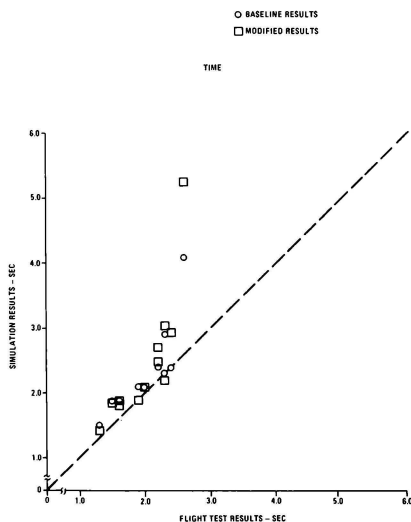


Figure 29 (a) COMPARISON PLOTS FOR SHORT PERIOD DYNAMICS SECOND PEAK CHARACTERISTICS

## Results

Fuel loading and fuel slosh have been found to have a significant effect on maneuvers, trim points, and control surface deflections/forces. Stated flight test c.g. values were assumed to be obtained for a  $\theta = 0^\circ$ . During the performance of the various analyses, the maximum difference between the stated trim c.g. and the simulator trim c.g. was 2.6 MAC. This c.g. shift is due to the fact that an aircraft, at a trim point, does not have to be at  $\theta = 0^\circ$ . Fuel loadings used in these analyses were determined by the following criteria:

1. Use fuselage fuel before wing fuel.
2. The difference between forward and aft main wing tanks should be approximately 7,000 to 10,000 lb with the forward main wing tanks heavier.

Selection of the proper fuel loading can affect the test results. An elevator deflection variation of more than  $1^\circ$  was observed for a particular airspeed during a static longitudinal stability test. Due to the unknown flight test fuel loading the acceptable range was increased to  $\pm 1^\circ$  of elevator deflection at the end point airspeed. It was originally  $\pm 5^\circ$  or  $\pm 1^\circ$  at maximum surface deflection ( $\pm 0.2^\circ$  of  $\delta_{eT}$ ).

Fuel slosh effects were also significant in the outcome of this limited study. The same flight test case was analyzed with fuel slosh effects on and off. A difference of  $4^\circ$  in elevator deflection was observed, with the no-fuel

slosh effects results being higher. This occurred during a static longitudinal stability test because the aircraft c.g. was not stationary. With no-slosh effects the c.g. is frozen at the trim point value. A shift in c.g. from the trim point airspeed to an end point airspeed could be as large as 4.2 MAC. This will affect the aircraft attitude and the amount of elevator necessary to obtain a particular airspeed.

Longitudinal trim was verified in three different areas: stabilizer angle at flight test trim points, changes in stabilizer angle to compensate for a change in aircraft configuration (i.e., flap retraction), and stabilizer vs. elevator tradeoffs for several flight conditions at the cruise configuration. All three areas were matched to the acceptable stabilizer range. The acceptable stabilizer range for all three types of checks was  $\pm 0.5^\circ$  of deflection. The first area of matching flight test trim stabilizer angles was accomplished by introducing an offset of  $-0.5^\circ$  to the simulation original design values. This modified stabilizer value was used in the calculations of lift and pitching moment coefficients. This modified stabilizer design was used for all aircraft configurations. Four out of 36 trim points fell outside of the acceptable range. For all four of these trim points, other trim points having similar flight conditions and aircraft configurations can be found to be within the acceptable range. Lack of exact fuel loading data or an error in the basic pitching moment coefficient could account for these four points not falling within the acceptable range.

Changes in stabilizer angles for changes in aircraft configurations were checked and summarized in Table 6. These checks were made with the  $-0.5$  offset incorporated in the simulation. Correlation between the references and the simulation for flap retraction, airbrake extensions and gear extensions were all found to be well within the acceptable range of  $\pm 0.5$ .

The final check on the longitudinal trim was the stabilizer vs. elevator tradeoffs which were made in the cruise configuration. This check was made with fuel slosh effects, the modified stabilizer design, and with the modified  $\Delta C_{m_{\delta e}}$  for

static longitudinal stability correlation. A significant improvement was obtained, as illustrated in Figure 3.

Longitudinal stability and control was investigated by performing static longitudinal stability, maneuvering flight and longitudinal short period dynamic stability analyses. Modifications to various pitching moment coefficient components was required to obtain satisfactory correlation between the simulation and flight test.

Coefficient components modified for cruise configuration static longitudinal stability were  $\Delta C_{m_{BASIC}}$  and  $\Delta C_{m_{\delta e}}$ . The baseline simulation an-

alyses showed discrepancies for low-speed and high-speed elevator deflections (observations 2 and 3). These discrepancies led to the modification of  $C_{m_{BASIC}}$  for  $M = 0.3, 0.825$ , and  $0.85$

curves. The original and modified curves can be found on Figure 4. These modified curves improved the problems identified in observations 2 and 3.

The Slope Matching Technique led to a solution to the problem described in observation 4. This was accomplished by changing the  $\Delta C_{m_{\delta e}}$  flaps-up

data. Since stabilizer angle values for trim points did correlate well, it was decided that  $\Delta C_{m_{\delta e}}$  would be the way to correct the static longitudinal stabilities and not affect stabilizer trim values. Good correlation was obtained by reducing the magnitudes of the low-altitude  $\Delta C_{m_{\delta e}}$

curves and by changing this coefficient component to a function of c.g. as well as Mach number and altitude. The c.g. dependence is really believed to be associated with lift coefficient due to elevator deflection, but owing to time constraints of the project the modification was made to pitching moment due to elevator deflection.

Figures 11 and 12 show the maximum errors for the baseline and modified analyses respectively. There were a total of eight flight test cases. Three of which did not meet the acceptable range of  $\pm 1^\circ$  of elevator deflection on a  $\delta_e$  vs.  $M$  plot. For two of these tests, similar conditions exist for either another static longitudinal stability or maneuvering flight test case which have good correlation. Therefore these two cases are considered suspect. As will be mentioned later, maneuvering flight tests have good correlation with this same  $\Delta C_{m_{\delta e}}$  modification installed in the

simulation. The third test was believed to be suspicious because on a  $\delta_e$  vs.  $M$  plot, the further aft the trim c.g., the flatter the slope of this curve. This third test did not comply with this trend and therefore was considered suspicious. Figure 30 demonstrates this point.

Power approach configurations was analyzed for airbrakes in the zero position and at position four. A limited amount of data exists for each airbrake position. Plotting the limited flight test data, Figures 6, 7, 8, and 9, demonstrates the type of scatter encountered when comparing various flight test reports. This scatter was greater than the simulation allowable tolerance for matching these flight test cases.

The Slope Matching Technique was used on the airbrakes at the zero position. The baseline data (reference 1) results showed that a rotation of the  $\delta_e$  vs.  $C_{al}$  slope in the clockwise direction was necessary for good correlation with flight test (references 2 and 3). This rotation was accomplished by a 16.5% reduction in the original  $\Delta C_{m_{\delta e}}$  flaps-down data curves. Figure 17 con-

tains the original and modified data curves. After these modified data curves were incorporated into the simulation, all four flight test cases were within the acceptable range of  $\pm 1^\circ$  of elevator deflection at the airspeed end points. It was interesting to note that when a significant difference existed between common flight test

conditions, the simulation results usually lay between the two flight test curves, Figure 31. The worst scatter between common flight test case conditions, in this configuration, was 1.5° of elevator deflection. The simulator met the +1° of elevator deflection acceptable range for both of these cases.

Airbrakes at position four analysis was performed with the airbrake position zero  $\Delta C_{m_{\delta_e}}$  modification incorporated. The modified  $\Delta C_{m_{\delta_e}}$  did not yield acceptable correlation. A problem still existed at high wing angles of attack. This was

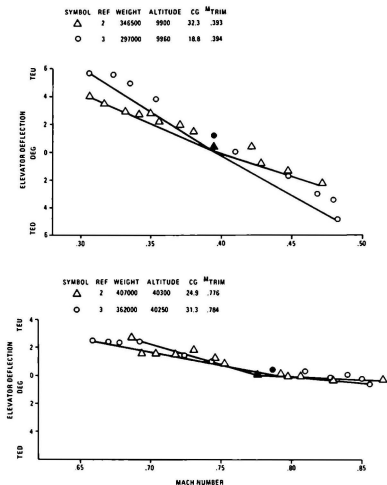


Figure 30 CG POSITION EFFECT ON STATIC LONGITUDINAL STABILITY SLOPE

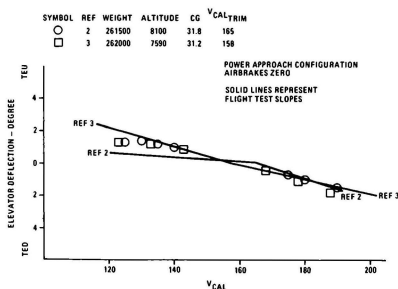


Figure 31 SIMULATOR/FLIGHT TEST COMMON CORRELATION, AFT CG

corrected by modifying  $\Delta C_{m_{\delta_{sp}}}$  for  $\alpha_w$  greater than 8°. This modified  $\Delta C_{m_{\delta_e}}$  and the modified  $\Delta C_{m_{\delta_{sp}}}$

produced acceptable results for all four flight test cases. Although maximum scatter for these common conditions is 2° of elevator deflection, the simulation was within the +1° acceptable range for all cases. Here, as in the airbrake zero cases, the simulation results fell between the slopes of the two flight test cases.

Maneuvering flight (stick force per g) was analyzed in each configuration (cruise, power approach airbrakes position zero and four). Modifications made by static longitudinal stability analyses to  $\Delta C_{m_{\delta_e}}$  and  $\Delta C_{m_{\delta_{sp}}}$  affected the results

of the maneuvering flight results. Therefore, after each static longitudinal stability configuration was satisfied, the corresponding maneuvering flight configuration was analyzed. The baseline cruise configuration data analyses results were similar to those found for the static longitudinal stabilities in that a decrease in  $\Delta C_{m_{\delta_e}}$

would improve the results in a  $\delta_e$  vs. g plot. With the modification made to  $\Delta C_{m_{\delta_e}}$  for satisfac-

tory static longitudinal stability, the analysis was rerun and acceptable results were obtained. Fourteen flight test cases existed for the cruise configuration; eleven met the end point acceptable range of +1° of elevator deflection. All three of these unacceptable tests have conditions and configurations similar to tests that are acceptable. Therefore these three test cases are considered suspicious.

The power approach configuration with airbrakes at position zero, was analyzed after the modification to  $\Delta C_{m_{\delta_e}}$  flaps-down was made for

static longitudinal stabilities. The results of this analysis was that all three flight test cases were matched satisfactorily.

With the airbrakes at position four, the modified  $\Delta C_{m_{\delta_e}}$  was not enough to bring the simulator

into an acceptable correlation with flight test results. High  $\alpha_w$  test points were still a problem. A modification to the  $\Delta C_{m_{\delta_{sp}}}$  data was made

which gave acceptable results for two of the three of the maneuvering flight test cases and all of the corresponding static longitudinal stability test cases. The flight test data for the case out of the acceptable range was considered suspicious. Another flight test case of similar conditions had good correlation with the simulation. A correlation between these two flight test cases resulted in differences beyond the allowable elevator deflection range of +1°.

Longitudinal dynamics was checked by analyzing the short period mode of this aircraft. Initial analyses included all flight test correlation modifications and unmodified baseline values, reference 1, for all other coefficient

components. Due to the well damped characteristics of the aircraft, pitch rate ( $q_s$ ), frequency responses and damping ratios were not calculated. Instead an overlay method of first peak, crossover time, and second peak response characteristics was used to judge acceptability. First peak characteristics and crossover time were of primary importance. The results of initial analysis for the cruise configuration tests are summarized below:

1. Simulation first peak maximum amplitude values were greater than flight test values.
2. Simulation first peak maximum amplitude time values occurred after most flight test cases.
3. Simulation crossover times were usually greater than flight test values.
4. Simulation second peak maximum amplitude values were greater than flight test values.
5. Simulation second peak maximum amplitude time values occurred after flight test cases.

Only three flight test power approach tests existed, one with airbrakes at position zero and two at position four. Their response characteristics from the initial analysis are summarized below:

1. Simulation first peak maximum amplitude values were less than flight test values.
2. Simulation first peak maximum amplitude time values correlated well.
3. Simulation crossover times were usually greater than flight test values.
4. Simulation second peak maximum amplitude values were generally less than flight test values.
5. Simulation second peak maximum amplitude time values were generally greater than flight test values.

A combination of parameters was determined to be necessary to obtain satisfactory results for both cruise and power approach configurations. The introduction of a function of dynamic pressure was necessary to obtain good correlation of the first peak response characteristics. Two separate functions were put into the simulation, one for each configuration, cruise and power approach, Figures 25 and 26.

To assist in obtaining good correlation of crossover time values, the absolute value of the time rate of change of elevator deflection  $|\dot{\delta}_e|$  was multiplied by the above dynamic pressure function. This limited the application of the dynamic pressure function to occur only when a  $|\dot{\delta}_e|$  exists. Generally  $|\dot{\delta}_e|$  became zero, for these short period tests, shortly after the first peak maximum amplitude value occurred.

Second peak amplitude characteristics was aided by the addition of a constant gain. The value of the constant gain was determined to be five. All of these parameters were applied to the

original data values for  $\Delta C_{m_{\alpha_w}}$  by the equation

below:

$$\Delta C_{m_{\alpha}} = \Delta C_{m_{\alpha_{\text{original}}}} (K + [f(q) \text{Flaps} |\dot{\delta}_e| \cdot (1 - \delta_{FW}^*) + f(q) \text{Flaps} |\dot{\delta}_e| \cdot \delta_{FW}^*])$$

Down

where  $F(q)$  = function of dynamic pressure.

$|\dot{\delta}_e|$  = absolute value of the rate of change of elevator

$K$  = constant gain value equal to 5.0

$\delta_{FW}^*$  = normalized flap position

Comparative plots for the baseline and modified first peak characteristics, crossover time, and second peak characteristics are presented on Figures 27 through 29(a) respectively. Sixteen flight test cases, for both aircraft configurations, were analyzed but only twelve are presented on Figures 27 through 29(a). The four cases not presented are considered to be suspicious test cases. All four cases have similar flight conditions to cases that are considered to have satisfactory correlation. Elevator input overshoots or additional elevator input before the  $q_s$  response damped out all believed to be partially responsible for some of the suspicious cases.

A comparison of the two flight test reports, references 2 and 3, showed that the excitation of reference 2 had little or no elevator overshoots. Reference 3 had considerable overshoots on most test cases. It was believed that elevator overshoots increased the slope of  $q_s$  after the first peak maximum amplitude was achieved. This would affect crossover time correlation. The simulation had no overshoots. This was believed to be part of the reason why the correlation with reference 2 is better than with reference 3.

A limited study was performed to examine the effect of  $I_{yy}$  on the simulated short period response characteristics. A variation of  $I_{yy}$  of 800,000 slug-ft<sup>2</sup> was obtained from various possible fuel loadings for a particular test case's gross weight and c.g. No significant variation in first peak amplitude characteristics were observed and a variation of crossover time equal to 0.3 seconds was observed. Since exact fuel loading information does not exist, a single value of 8,168,000 slug-ft<sup>2</sup> was used.

### Conclusions and Recommendations

Simulation design coefficient data is usually a combination of windtunnel test data, predictive analysis and possibly flight test data. Some actual aircraft characteristics may not be taken into account (i.e., empennage aeroelastic effects). A correlation of flight test results against simulation results is a necessary tool to assure a high fidelity simulation. The overall results of such a correlation effort for the

B-52H WST flying qualities led to several modifications to the baseline coefficient data and design. The major conclusions reached by performing this correlation and the limited studies of fuel slosh/loading and Iyy are discussed below:

1. B-52H baseline coefficient data in reference 1 did not satisfactorily represent the aircraft in all components of the longitudinal aerodynamic coefficients. Correlation of flight test to simulation results should be a regular part of any simulations acceptance testing as was performed on the B-52H WST. Without this type of correlation, high fidelity simulation cannot be guaranteed.

2. The Pitching Moment coefficient data for  $C_{m_{BASIC}}$ ,  $\Delta C_{m_e}$ ,  $\Delta C_{m_{\delta_{sp}}}$ , required modification to

obtain good correlation. The equation for the  $\Delta C_{m_z}$  component of pitching moment was modified to supplement the original  $\Delta C_{m_z}$  data for good short

period correlation. The necessary offset to the stabilizer angle design required for good correlation makes the original pitching moment and/or lift coefficients due to stabilizer questionable.

3. Flight test data taken from various references for common conditions and tests may not correlate well between themselves. Sound engineering judgment must be applied to which flight test cases are included in this type of correlation.

4. For the B-52H aircraft fuel loading and fuel slosh are phenomena which cannot be ignored when Longitudinal Trim and Longitudinal Static Flying Qualities are being investigated. These effects could make the difference between acceptable and unacceptable correlation. In the case of short period dynamic fuel loading/slosh effects on Moment of Inertia were found to be insignificant.

It is the general conclusion by both the Air Force and Link that the B-52H WST provides high fidelity simulation of the actual aircraft flying qualities in the areas addressed in this paper. This type of correlation is difficult and time consuming. The following recommendations are made to ease the performance of such a correlation.

1. Detailed aircraft configuration data particularly in the area of Weight and Balance parameters (i.e., fuel loading, trim attitude, c.g., etc.) would remove some of the uncertainty involved in matching flight test results.

2. A common interpretation between the customer and contractor in the flight test data and the parameters of primary importance can expedite these analyses.

3. Start these types of correlations as early in a program as possible to allow for a thorough correlation without impacting schedule milestones.

## References

- Boeing D3-9776-2, "B-52G/H Aerodynamic Characteristics - Mission Simulators (U)". Prepared under contract number F 34601 - 74 - C - 1785.
- Gobert, Don O., and Bowline, Jerry D., "Air Force Evaluation of the B-52G and H Prototype Stability Augmentation and Flight Control System", AFFTC - TR - 67 - 30, February 1968.
- Hood, Frank C., "Evaluation of the B-52G/H Production Stability Augmentation and Flight Control System". AFFTC - SD - 69 - 33, October 1969.
- Boeing D3-5393-1, "Time for Action Again", November 1975.
- Technical Order 1B - 52H - 1, "B-52H Flight Manual", 15 February 1975, Revision 19 August 20, 1979.

## Glossary of Abbreviations and Symbols

A/B	AIRBRAKES (SPOILERS)
A/C	AIRCRAFT
ALT	ALTITUDE
C <sub>D</sub>	AERODYNAMIC DRAG COEFFICIENT
c.g.	LONGITUDINAL CENTER OF GRAVITY
C <sub>L</sub>	AERODYNAMIC LIFT COEFFICIENT
C <sub>M</sub>	AERODYNAMIC PITCHING MOMENT COEFFICIENT
deg	DEGREES
ft	FEET
g	NORMAL ACCELERATION
Iyy	MOMENT OF INERTIA ABOUT THE y AXIS
kts	KNOTS
lbs	POUNDS
M	MACH NUMBER
MAC	MEAN AERODYNAMIC CORD
PPU	PRE-PRODUCTION UNIT
q	DYNAMIC PRESSURE
q <sub>s</sub>	TIME RATE OF CHANGE OF PITCH ANGLE
REF	REFERENCE
SDF	SOFTWARE DEVELOPMENT FACILITY
V <sub>cal</sub>	CALIBRATED AIRSPEED
WST	WEAPON SYSTEM TRAINER
Wt	WEIGHT
$\alpha_w$	WING ANGLE OF ATTACK
$\Delta$	CHANGE IN
$\delta_{FW}$	NORMALIZED FLAP POSITION, 0 - FLAPS UP, 1.0 - FLAPS DOWN
$\delta_e$	ELEVATOR DEFLECTION
$\delta_e$	TIME RATE OF CHANGE OF ELEVATOR POSITION
$\theta$	PITCH ANGLE

## Subscripts

BASIC	BASIC COEFFICIENT
$\dot{\alpha}$	DUE TO RATE OF CHANGE FOR ANGLE OF ATTACK
$\delta_e$	DUE TO ELEVATOR DEFLECTION
$\delta_{sp}$	DUE TO SPOILER (AIRBRAKE) DEFLECTION
AE	DUE TO AEROELASTIC EFFECTS
q	DUE TO PITCH RATE
n <sub>z</sub>	DUE TO NORMAL ACCELERATION
FLAPS	DUE TO FLAP DEFLECTION
IND	INDICATED

Steve K. Butrimas and G. Blair Browder  
Naval Training Equipment Center  
Advanced Simulation Concepts Laboratory  
Visual Technology Research Simulator  
Orlando, Florida

### Abstract

This paper describes by experimental example how a cue synchronization study should be performed on a major flight simulator system. It presents dynamic performance measurements made at the Navy's Visual Technology Research Simulator (VTRS) facility, and shows timing interactions between critical subsystems of the Conventional Takeoff and Landing (CTOL) simulator. It discusses how and why specifications and tests must be developed which determine the cue synchronization and performance requirements for simulation systems.

### Introduction

In any complex simulation system, the degree of cue mismatch resulting from imperfect synchronization is often unknown. This is an obscure component of simulator "fidelity". Since it is difficult to quantify and evaluate, it is often neglected. User opinion evaluation techniques attempt to use the human to integrate and evaluate the interactions by subjective "feel". Other methods use pilot performance as determined by specific computed or recorded measures, and by transfer of training experiments. Such methods, however, look only at overall symptoms which may be the result of many different and overlapping causes. Some of these causes have not been isolated; others have been isolated but not quantified. Subsystem synchronization is a quantifiable set of parameters that are critical measures of overall system performance and should be physically isolated, identified and measured.

### System Description

Major subsystems of the VTRS/CTOL include a T2C aircraft cockpit with G-seat mounted on a six degree-of-freedom motion base and a wide angle dome display. The display consists of a wide-angle background TV projector and a servo-controlled target TV projector. The simulator's displays receive video from either the computer image generation (CIG) system, the closed circuit model board TV system, or other TV special effects equipment.

The simulator's computer system is composed of three Systems Engineering Laboratories (SEL) 32/75 Central Processing Units (CPU). Flight and Visual computers are controlled by an executive computer which also communicates with the Experimentor/Operator control station. The flight and visual computations considered in this report are all performed at a 30 Hz rate.

### Computer Throughput Measurements

The VTRS/CTOL simulator incorporates a linkage system which connects the simulator input cockpit controls (i.e., throttle, control stick, rudder, and toe brakes) to the computers and connects the computers to all simulator output

hardware. The linkage system includes the functions of signal sampling, analog to digital conversion, storage, data transfer, data distribution, digital to analog conversion and signal smoothing. Linkage transport delays (throughput delays) were measured between the analog input stimulus (control movement) and the output to subsystem hardware. The linkage is shown in the system diagram (Figure 1).

Linkage throughput delays were measured over the following transmission routes, some of which apply to Computer Image Generation (CIG), some to the model board Target Image Generation (TIG) and some of which are common to both CIG and TIG operations:

- a. Cockpit control to motion base (leg servos)
- b. Cockpit control to G-seat bellows servos
- c. Cockpit control to Target Imagery Projector (TIP servos)
- d. Cockpit control to TIG (TV probe and gantry servos)
- e. Cockpit control to CIG input and to CIG video output.

The first three linkage routes, the motion base, G-seat and TIP servos are common to both CIG and TIG.

The function of the linkage system is to provide two-way communication between computer memory and simulator hardware. Major components of the linkage are:

- a. The master controller (which is the control center).
- b. System cards (which service the hardware systems), and
- c. The subcontroller (which serves as the interface between the master controller and system cards).

The master controller transfers output data in serial form from an internal buffer memory to the designated system card, and simultaneously accepts input data from the system card and stores it in the buffer memory.

System cards provide analog and digital conversion and interconnection functions required by the system being serviced.

The simulator's computer system consists of three SEL 32/75 computers: one CPU for Executive/Experimentor-Operator operations (EO), one CPU for computation of flight dynamics/kinematics, and the third CPU for visual computations. Computation rate, relative phasing between the

computation frames of the visual and flight CPU's, and their associated linkage transfers are major contributors to throughput delay.

Figure 2 shows the timing relationships between the flight and visual CPU's and their associated linkage transfers of data from hardware to computer memory and from computer memory to hardware. All computational measurements were made with the software operating at an update rate of 30 frames per second (a computation period of 33.3 milliseconds). Computation frames are divided into four subframes, each of 8.33 milliseconds duration. The visual CPU frame lags the flight CPU by two subframes. This flight/visual CPU phasing minimizes lag in the visual computation, since the most recent flight outputs are computed by the end of flight's second subframe and are immediately used by the visual CPU.

There are two linkage data transfer subframes; a flight linkage transfer and a visual linkage transfer (See Figure 3). The control stick input is serviced first in the cycle to minimize delay between stick input and transfer to computer memory. Computer memory is updated during the normal DMA transfer.

Data transfers to the CIG are a serial data transfer from the SEL 32/75 visual buffer memory to the CIG's computer memory. For "CIG only" operation data transfer occurs at the end of subframe 1 of the visual frame (Figure 2). Three-dimensional image computations are performed in the Programmable Data Processor (PDP 11/55) and then data is transferred to General Electric's special purpose image processor (CIG frame II and III hardware) for conversion to a two-dimensional video picture. The basic set-up used for throughput time measurement is shown in Figure 4.

A control stick analog input was generated as a square wave with a frequency of approximately 3.82 Hz, producing step changes every 131 milliseconds. Since four computational frames are of 133 milliseconds duration, the input step changes occurred about two milliseconds out of phase (with the four-frame cycle) and tended to "walk" with respect to each frame. This "walking" of the control stick step input assured the occurrence of minimum and maximum throughput cases. The minimum throughput occurred when the control stick changed state immediately before it was sampled by the A/D. The maximum throughput occurred when the control stick input changed state immediately after the A/D services. Since in this case, the A/D servicing of the input was just missed, a full frame (cycle) must go by before the next A/D sample. Thus, the difference between minimum and maximum throughput was 33.3 milliseconds. A summary of throughput measurements from control stick to each major hardware subsystem is presented in Table 2.

Aerodynamic lags were removed from the flight software so that all transport delay measurements reflected only computer and linkage related throughput lags.

#### THROUGHPUT: CONTROL STICK TO MOTION/G-SEAT

Throughput measurements were made from the cockpit control stick input to the motion base and G-seat analog drive outputs. These analog motion outputs then drive the motion system through the

leg servo pre-filters. The visual computer does not contribute to this throughput delay, since all computation takes place in the flight computer. Motion base drive signals are transmitted during the flight DMA transfer. The G-seat throughput route is the same as that of the motion system. Throughput measurements from control stick input to the motion base drive signals indicated a transport delay of  $55 \pm 17$  msec.

#### THROUGHPUT: CONTROL STICK TO TIP SERVOS

Throughput measurements were made from the cockpit control stick input to the TIP servo analog drive outputs. These analog drive outputs are computed in both the flight and visual computers. TIP servo drive signals are transmitted during the visual DMA transfer. Throughput measurements from the control stick input to the TIP servo drives indicated a transport delay of  $68 \pm 17$  msec.

#### THROUGHPUT: CONTROL STICK TO TV PROBE SERVOS

Throughput measurements were made from the control stick input to the probe servos analog drive outputs. These analog signals drive the probe through pre-filter networks (designed to smooth desampling noise). Computations are performed in both the flight and visual computers with probe drive signals transmitted during the visual DMA transfer. Throughput measurements from control stick input to the probe servos analog drive outputs indicated a transport delay of  $68 \pm 17$  msec.

#### THROUGHPUT: (1) CONTROL STICK TO CIG INPUT AND (2) CIG INPUT TO VIDEO OUTPUT

Throughput from control stick input to video output can be logically divided into two throughput segments, (1) control stick input to CIG data input, and (2) CIG data input to video output. The first detectable video output was defined as the presence of video signal in the first horizontal line of the raster (the first pixel of CIG video). The two throughputs were determined by first measuring the total throughput from control stick to video output, and then by measuring the segment from CIG input to video output. The remaining throughput segment from control stick input to CIG data input was then computed by subtracting the partial throughput from the total throughput.

The flight computer software was modified to cause the aircraft to instantly change position (without aerodynamic lag) upon recognition of change of polarity of control stick input. Two aircraft positions were specified, one at a location where the scene viewed is all-white and the other at a location where the scene viewed is all-black. Thus the stick input caused the visual scene to alternate between total black and total white, providing a readily measurable step change in video output level. Throughput from control stick input to the CIG input (to the PDP-11) was determined to be:

$50 \pm 17$  msec (CIG Mode Only)

$58 \pm 17$  msec (CIG/TIG Mode)

Throughput from CIG input to the first pixel of CIG video output was determined to be 50 msec. Further when total systems response is considered, an additional time period to generate one TV field (17 msec) was added as necessary for



reaching a visual cueing threshold.

Table 1 summarizes all of the linkage and computer system throughput measurements discussed in this section.

#### Hardware Systems Response Measurements

##### Video Systems

In the CIG mode, the target image is generated through computer update of a data base. In the TIG mode, the target image is generated by viewing a model board through a closed-circuit TV system. Images created by either mode are displayed on the screen by a high-intensity TV projector and appropriate optics. The target image is positioned on the screen by servo control of the projector optical elements.

Target image motion is accomplished by servo systems which interface with software generated signals from the visual computer, which in turn, respond to pilot-generated commands from the cockpit controls.

##### Visual Servo Systems Description

##### Servos Common to Model Board Operations

The probe, which houses the TV camera and associated optical systems, is driven over the model board by a three-axis gantry servo. As the TV camera probe is positioned to simulate aircraft position, line-of-sight between the model and focal plane of the camera is maintained by a servo-controlled prism system. Heading and pitch servos keep the model within the field-of-view of the camera while a roll servo maintains desired roll attitude of the received image.

##### Servos Common to CIG and Model Board Operations

Target Image Projection (TIP) servos that drive the gimbaled optical system which displays the target (aircraft carrier, airplane, etc.) image within the dome are common to both CIG and model board operations. Azimuth and elevation servos control position of the image with respect to the observer. A roll servo provides compensation for roll angle induced by combined azimuth/elevation commands.

#### Summary of Servo Systems Evaluation

The following is a summary of the visual system servos evaluated:

##### a. Target Image Projection (In Dome)

- (1) azimuth
- (2) elevation
- (3) roll

##### b. Gantry Rate Servos

- (1) x translation
- (2) y translation
- (3) z translation

##### c. TV Probe (In Gantry Mount)

- (1) heading
- (2) pitch
- (3) roll

(4) command filters (shapes command signals to all probe servos)

##### TIP Servo Performance

Table 1 summarizes the performance of the TIP servos in the frequency domain and time domain. Closed-loop servo performance is presented in the form of bandwidth and step response characteristics. In addition, static repeatability of each servo system is presented.

##### Motion System

The motion platform software accepts inputs of aircraft acceleration velocity and position. It transforms and filters them into six motion drive commands: roll, pitch, yaw, longitudinal, lateral and vertical. The platform position commands are geometrically transformed into leg position commands required to achieve the desired platform position. The platform, in the process of achieving the commanded position, undergoes velocity changes which create the

TABLE 1 - VISUAL SERVOS PERFORMANCE SUMMARY - TIP

		Step Response			
:Bandwidth (1)	: Response	: Damping	: Static	: Range	:
: Hz	: Time (2)	: Ratio	: Repeatability	: Limits	:
:	: (msec)	:	:	:	:
AZ	3.8	67	0.4	+ 0.75 arc min	+95°, -135°
EL	8.5	43	0.5	+0.8 arc min	+65°, -55°
Roll	3.0	55	CTO	+ 1.4 arc min	Continuous

1. -3 db point
2. 63 Percent of Command Amplitudes
3. (CTO) Critical to Overdamped.

desired onset and gravity align acceleration cues.

Tests to determine the character of the onset and subsequent washout of acceleration were performed by issuing step commands in position (heave, in this case). Typical responses to these step commands are shown in Figure 6. The command, position follow pot, command filter output, and acceleration histories are also shown in the figure. The peak heave command of 3.2 inches resulted in a peak acceleration of 0.2G's. The washout acceleration, is about 20 percent of the desired acceleration. Washout of the sustained acceleration is observed to take approximately one second.

For acceleration onset, low frequencies are filtered to provide rapid onset and washout. High frequencies are filtered to prevent stepping and spurious influences, thereby providing a smooth controlled magnitude and duration of onset and washout.

The transport delay and filter effects of the motion system are summarized in Figure 7. The overall acceleration onset response includes transport delay and time for the acceleration to reach 63% of peak. It should be noted that the motion system overall lag will vary depending on the drive philosophy. For example, the system lag for gravity align is much greater than that of acceleration cueing since it does not include the lead acquired by the acceleration cue method of reading actual platform acceleration.

#### The "G"-Seat System

The G-seat contains 29 controllable air bellows elements located in the seatpan, back rest and thigh area, plus a lap belt. The system is open-loop controlled and is designed to provide sustained acceleration cues only. A G-seat test system was constructed and utilized to evaluate G-seat performance as installed in the simulator. An 18 pound load was placed on the seatpan and a linear potentiometer was mounted and attached to provide a measurement of position displacement. The input signal was analog and applied at the motion cabinet input to the control valve.

The throughput time lag for the seatpan cell (No. 10) was 85 msec for both up and down motion. Rise time for both up and down motion was 90 to 100 msec. An example of this response is shown in Figure 8.

#### System Response Summary

A graphic summary of the dynamic response of the VTRS/CTOL computer and hardware systems is presented in Figure 9. Figure 9 shows system performance when operated in a dual mode permitting simultaneous use of the TV model board system and computer image generation (CIG) system. The system dynamic response is a sum of linkage and computer transport delays and output hardware response time. The output hardware response may contain transport delays and/or signal rise time. Throughput delays are measured from control stick input to output hardware commands. Aerodynamic delays are not included in any of the data presented. Output hardware systems shown in Figure 9 are all servo-controlled devices with

the exception of video generation of the CIG picture. Servo response times are defined as the time required for the output to reach 63 percent of the step command. Video generation of the CIG picture includes transport delay within the CIG and a response time defined as the time to complete one TV field.

Since the control stick input can occur anywhere within a basic computation frame of 33.3 milliseconds duration, timing is referenced to an average between worst case (33.3 milliseconds additional time) and best case (0 milliseconds). Thus, an average transport delay time is defined as having tolerance of  $\pm 17$  msec.

With the exception of the G-seat and G-align systems, the average times for computer throughput plus hardware response for the simulation mode of TV model board and CIG is less than 165 milliseconds. However, the G-seat and G-align designs are used for sustained or very low frequency acceleration and thus do not demand fast onset cueing. Other G-seat designs which attempt to provide onset cueing would require improved response.

Early tests showed a dynamic mismatch in visual system performance due to poor servo response in the elevation and azimuth target image project servos. This poor response is shown by dashed lines in Figure 9. System dynamic mismatch was significantly reduced by design improvements on the elevation and azimuth target projector servos.

From Figure 9 the visual systems display a transport delay (plus one video field time) of approximately 120 milliseconds with a tolerance of about  $\pm 17$  milliseconds. The TV probe attitude servos, which are an exception to this, could be readily brought within this tolerance by changing the probe filters. These filters smooth the computer update commands, and were designed for a slower update rate than the 30Hz used in VTRS.

#### Design Features Resulting in Enhancement of Cue Synchronization

The following design features, incorporated into the VTRS/CTOL simulator, minimized system delays/lags and provided dynamic matching of visual and motion systems:

1. The linkage, which distributes all signals between the computer and simulator systems, has an optimum sequence with respect to its DMA transfer of data between the linkage memory and the computer's memory which occurs near the end of each computation frame. Immediately after this DMA data transfer, all linkage output cards are serviced to minimize output time lag. In this simulator there are many more time critical outputs than inputs. The delay of critical inputs was overcome by a special servicing of the stick and throttle linkage system card which converts their voltage to a digital word just prior to the DMA transfer of data into the computer. All other inputs have the added frame delay.

2. Since certain flight dynamic outputs such as aircraft position and attitude are required as inputs for visual computations, the visual computation frame (33 msec) must follow the flight

computation frame. To minimize any time delays from this, all critical flight subroutines were placed in an optimum calling order and "up front" in the flight computation frame. As a result, the visual computer is phased behind the flight computer by only 16.7 msec, or 1/2 frame, rather than waiting 33.3 msec until the next frame.

3. In the "CIG only" mode of operation, subroutines in the visual computer are optimized in calling order, for minimization of transport delay. As a result, critical visual subroutines are computed at the beginning of the visual computation frame and sent to the CIG computers at the end of only one subframe of 8.33 msec.

4. Subroutines computed at rates below the basic 30 Hz of flight and visual, and subroutines that are not a link in the dynamic response chain, are placed towards the end of the computational cycle.

5. The Experimentor Station subroutines are placed in the executive computer and are computed in parallel with flight and visual. Thus, they do not add to response time.

6. For smoother visual presentation, the CIG computer is provided with predicted values of eyepoint position/attitude and point-of-interest direction cosines in between actual computer values of these parameters. The net result is a 60 Hz image presentation, with field one generated from computed parameters and field two generated from the predicted parameters.

7. Hardware response of systems such as the target projection servos was increased and then "tuned" such that the times from control stick input to hardware response closely matched the time from stick input to CIG video outputs.

8. The motion platform acceleration cues lead visual position as in the real world. This desired feature is a result of driving platform position with aircraft acceleration and servicing it with the flight linkage transfer which leads the visual linkage transfer by 6.7 msec.

### Conclusion

The form of, and requirements for, the synchronization tests, such as discussed here, are dependent on the system tested.

The number and interrelationships of computers, the type of display system, number of channels, and the like will affect the test design as well as the equipment needed to perform them. For example, the dimensions and performance of motion platforms will require nonstandard strategic placements of accelerometers and proper scaling and computation to read out the desired platform accelerations.

A set of synchronization tests needs to be a standard element in the procurement process, such as aerodynamic performance and computer loading.

This set of tests should be well specified and tailored to the particular system and characteristics that need to be addressed.

The basic tests should be available and selectable for ready incorporation into specifications. Since at present they are not, an effort should be mounted to design a menu of tests and standardize (packaged as much as possible) a set of test equipment to perform them.

However, test, and test procedures are incomplete unless a specification design goal is available that prescribes the "acceptable" performance. Therefore, performance requirements and specifications should be assembled from the existing literature and research pursued to define the data that is not available for incorporation into specifications and The Test Procedures and Results Report.

For example, a cue synchronization analysis of the software flow could result in repartitioning or blending the software into new modules which would consist of sections of existing modules in the flight, visual, or linkage groups. Furthermore, during development and construction, such tests should be performed to obtain concrete data on system performance and provide detailed guidance to help create an optimally designed system.

In summary, it is recommended that a cue synchronization analysis be performed on all proposed simulation systems. Then, the critical characteristics that are identified by this approach can be optimized to enhance the total system performance and define the final system configuration by determining the cue synchronization performance and tests that must be specified.

TABLE 2

LINKAGE THROUGHPUT MEASUREMENTS

Control stick to Motion Base and G-seat	55± 17 msec
Control Stick to TIP Servos	68± 17 msec
Control Stick to TV Probe and Gantry Servos	68± 17 msec
Control Stick to SEL/PDP-11 Data Transfer (CIG only mode)	50± 17 msec
Control Stick to SEL/PDP-11 Data Transfer (CIG/TIG mode)	58± 17 msec

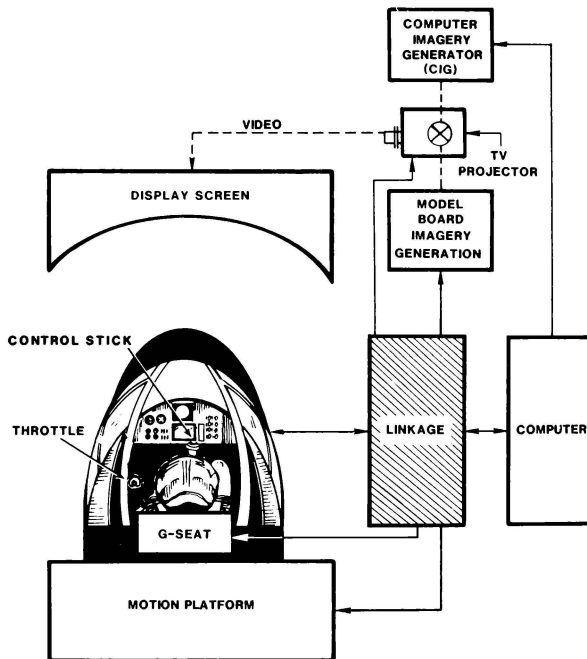


Figure 1. VTRS System Diagram



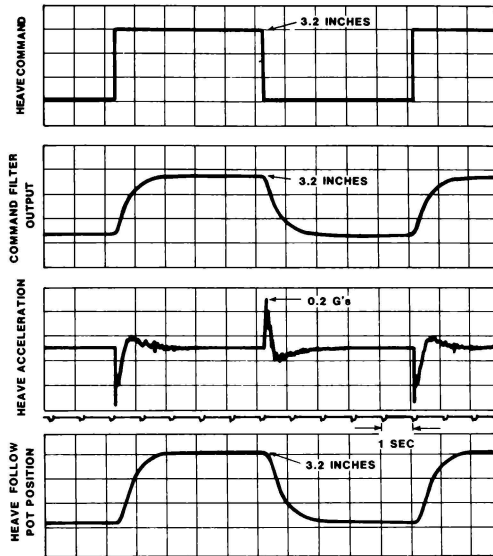


Figure 6. Motion System Heave Step Response

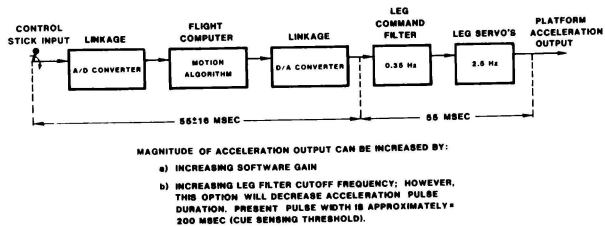
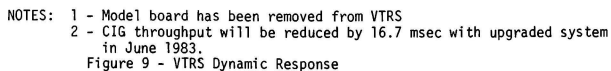
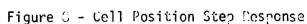


Figure 7. Onset Acceleration Response



Richard A. Weeks\*  
Northrop Corporation  
Pico Rivera, California

### ABSTRACT

This paper describes a real time simulation of mission environments for use in developing, synthesizing and analyzing complex avionics systems for fighter aircraft. The problem is one of creating an operationally correct environment for a pilot to operate in such that he is properly task loaded. Proper task loading insures the proper integration of the avionics subsystems (on an operation level) so as to verify that the mission objectives will be fulfilled.

### INTRODUCTION

There has been constant growth in digital avionics systems for fighter aircraft over the last several decades. Particularly the past decade has revealed an extreme sophistication of these systems in terms of airborne hardware and software. Hardware has been continually improved so as to provide higher computing speeds and larger memories while packaging size has decreased. Overall, system architectures are being standardized in the areas of higher ordered programming languages (MIL-STD-1589), instruction sets (MIL-STD-1750) and interprocessor communication (MIL-STD-1553). All of this standardization leads to easier integration of new systems as this digital avionics growth continues.

Another area of constant growth and improvement in militarized systems is in the area of cockpit controls and displays. With the inclusion of powerful on-board computing equipment in aircraft, a tremendous amount of information can be processed simultaneously and therefore can be portrayed to the pilot simultaneously. This wealth of constantly changing data can run the pilot into an "information overload" condition unless the information displayed is presented in an efficient manner. Misinterpreted display information can culminate into a catastrophic situation and/or a failure to meet mission objectives. Just as critical to the display development is the area of controls. Complex systems of automation or semiautomation (multiple actions based on a single command) have been incorporated into today's avionics. As with complex displays, complex controls are not acceptable, particularly in a fast-paced fighter cockpit environment. However, maximum efficiency and safety can be derived through rigorous man/machine/environment engineering evaluations of the total system concept with the human operator.

Efficient man/machine interaction requirements have provided the emphasis for detailed modeling and simulation of avionic systems, particularly in the area of controls and displays. This interaction is further enhanced by providing an accurate simula-

tion of the operational environment to which the pilot will be subjected. This real time simulation of the mission environment can be effectively utilized to investigate the intricate interactions of avionics systems with the key element of the system - the human pilot.

### SIMULATOR FACILITIES

Before describing the elemental simulations which integrate to provide an operational mission environment, a brief description of supporting facilities at Northrop is presented. These facilities can best be subdivided into the Visual Flight Simulator (VFS), Video Radar Landmass Simulator (VRLMS), Digital Image Generator (DIG) and digital computer complex. When used jointly, these facilities (and associated software) provide a correlatable mission environment for the development and investigation of complex aircraft avionics systems referred to as an Avionics Mission Simulator.

### VISUAL FLIGHT SIMULATOR

The VFS is the most recently developed simulator in use at Northrop's Aerospace Sciences Laboratory in Hawthorne, California. It is a device in which a high-fidelity simulated crew station is supported by a fixed pedestal which is centered within a 24-foot spherical dome. An exterior view of the VFS and supporting electronics equipment is shown in Figure 1. The interior of the dome acts as a screen for projected visual targets, earth/sky and terrain images. The simulated crew station accurately replicates an actual cockpit design. Currently, F-20 and F/A-18L cockpits can be installed in the VFS within a matter of hours due to a unique interchangeable cab feature which has been designed into the VFS.

The F-20 and F/A-18L simulator cockpits are configured primarily with fully flight-qualified avionic control and display hardware and functionally operate as the actual aircraft would. Figures 2 and 3 show simulator cockpits for the F-20 and F/A-18L. To accommodate the rapid changeover of these sophisticated cockpits, each is equipped with its own set of Intel 8080 microcomputers. These microcomputers act as the central data input/output device processor for all cockpit electro-mechanical controls and displays (flight instruments, switches, indicator lights, etc.) and link with the main computing system for the passage of data. Electronic displays use dedicated transmission lines with each cockpit retaining its own unique display electronic set.

\*Member, AIAA



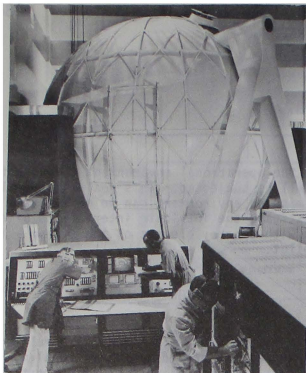


Figure 1. Visual Flight Simulator



Figure 2. Simulated F-20 Crew Station

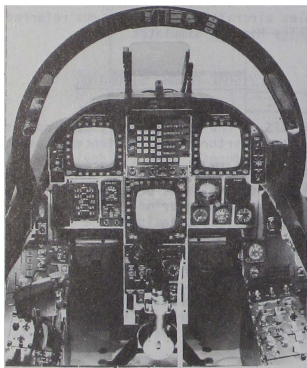


Figure 3. Simulated F/A-18L Crew Station

Inside the VFS, an array of projection systems are used to display targets, terrain and earth/sky visual images. All projectors are located above and behind the pilot's head.

A dedicated target projector displays a primary (and usually interactive) airborne target which is produced by a high intensity projection of an image which is generated from viewing a 3-dimensional target model with a closed circuit television camera. The target model is gimballed and computer controlled so as to continuously provide proper line-of-sight geometries and attitudes to the pilot.

An earth/sky image is provided by a single projection system which utilizes two color transparencies and point light sources. One transparency/point light source projects a red-brown earth hue whereas another transparency/point light source projects a blue shade for a sky reference. Along the lower portion of the sky transparency is a mountain reference which rotates to allow for accurate turn-rate cueing. The earth/sky projection system uses a 4-axis gimbal system which permits a continuous all-attitude reference.

A third projection system is used for displaying terrain images. This system is comprised of 3 projectors which jointly supply a 50 degree vertical by 150 degree lateral field-of-view projection, fixed to the aircraft axes system. The terrain images are generated by a Singer-Link Digital Image Generator (DIG) which provides extremely detailed landmass and ground-based cultural features. Typical (DIG) images are shown in Figure 4. The DIG will be described more completely in a following section.

#### VIDEO RADAR LANDMASS SIMULATOR

In response to the growing trend of providing imaging radar capability on fighter aircraft, the Northrop Aerospace Sciences Laboratory conceived, developed and implemented the Video Radar Landmass Simulator (VRLMS). This facility produces the required radar video imagery for the mapping modes of typical airborne radar systems. As will be described later in the operational scenario sections, the radar imagery produced by the VRLMS is completely correlated with scene provided by the Singer-Link DIG.

Simulated radar video is produced by the viewing of a Synthetic Aperture Radar mosaic by

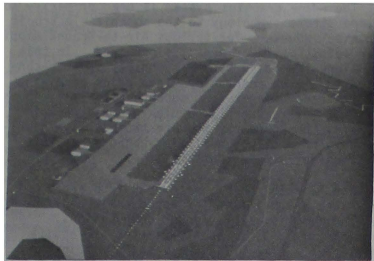


Figure 4. DIG Images

a high-resolution video camera (See Figure 5). The mosaic is scaled at 1:75,000 and equivalently encompasses approximately 500 nautical miles by 111 nautical miles of continuous radar imagery. The video camera is attached to a mobile gantry which is capable of moving 3-dimensionally relative to the mosaic. Generally, the gantry tracks aircraft position over the mosaic. However, if a Doppler

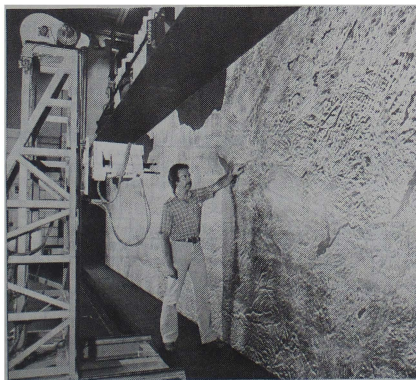


Figure 5. VRLMS

Beam Sharpening radar patch mode is selected, the gantry can be slaved to a specific "area-of-illumination" at any time and subsequently return to the aircraft's position over the mosaic. The camera is also gimbaled to provide imagery rotation due to aircraft heading change.

Complex blanking hardware is utilized to preprocess the camera video image prior to mixing it with vector-graphic symbology for display on a head-down electronic display. This blanking hardware shapes the radar video depending upon the pilot selected operating mode, azimuth scan, maximum range and antenna depression angle.

#### DIGITAL IMAGE GENERATOR

As was mentioned in the VFS section, the DIG provides extremely detailed landmass and ground-based cultural features which are projected inside the VFS dome. The DIG data base encompasses a 400 nautical mile by 400 nautical mile area which contains a number of high-detail features such as air-bases, targets, rivers, cities, lakes, mountains and coast lines. For example, Griffiss, Plattsburg and Pease Air Force Bases as modeled in extreme detail such that even objects such as ground-based antennas show up in their correct geographical location. The entire mountain region between Griffiss and Plattsburg is also accurately modeled, which provides an excellent corridor for terrain-following tasks. All natural and cultural ground-based features are placed accurately within the data base to create the illusion of "real world" flying. Target images include airborne threats (or friendly), surface-to-air missile sites, anti-aircraft artillery sites and tank convoys.

The DIG is comprised of special purpose digital computing equipment which allows for real time operation. Data base management is accomplished through a general purpose Perkin-Elmer (P-E) 8/32 minicomputer. The P-E determines what area within the data base can actually be seen by the pilot flying the simulator. This "regional" area is paged off of a hard disc storage device into local P-E memory. The area which is within a 10 - 20 mile viewing distance from the local aircraft position is then sent to the special purpose digital computing equipment for real time processing of the active visual scene and display via the projection system in the VFS.

#### COMPUTER COMPLEX

In supporting avionics system development and integration in the simulator, a large number of mathematical models must be generated. These mathematical models simulate the operational characteristics of the various avionic subsystems. The computing system utilized for the programming of these avionic subsystem models is configured primarily with Harris Slash 4 and H-800 minicomputers. Additionally, Floating Point Systems AP-120B Array Processors, Adage 4135 stroke graphics and Intel 8080 microcomputers are linked into the main Harris computing complex to accomplish special purpose computation tasks required in the simulation. Figure 6 shows the Harris computing system. Air-



Figure 6. Harris Computing System

frame dynamics, avionics and flight control system computations are accomplished efficiently within 5 Harris Slash 4's which are configured as a Master Digital Central Processing Unit (CPU), Master Hybrid CPU and 3 slave CPU's. The Master Digital CPU utilizes a virtual memory whereas the other CPU's function solely on resident memory. All Harris CPU's are tied together with a shared common memory which permits effective software partitioning and unrestricted information flow between processors.

The Master Hybrid CPU provides the processing for most of the radar avionics subsystem modules. However, this CPU is also utilized to communicate with a hybrid interface which is required to drive the simulator visual and audio system. In a similar fashion, besides processing avionics subsystem software models, the Master Digital CPU links digitally with the H-800 minicomputer which acts as the host for the Adage graphics system. Figure 7 schematically shows the functional layout of the various processors in the computer complex.

The Adage graphics system is used primarily to provide stroke symbology to the cockpit electronic displays. However, for various Air-to-Ground mapping radar modes, a video format is required. In this situation, the Adage stroke symbology is scan-converted to a high resolution video prior to mixing with the radar imagery and subsequent display in the cockpit. For reasonably complex graphic cockpit displays, the Adage can produce two displays simultaneously on a flight qualified cathode ray tube (modified for use in the simulator).

The Floating Point Systems AP-120B array processors are utilized for aerodynamic coefficient and function table lookup computations. Functions of 1, 2, 3 and 4 variables are easily computed in a time efficient fashion within the AP-120B based on parameter data passed from a slave Harris Slash 4 CPU. The AP-120B airframe computation (which usually encompasses 50,000-150,000 data points) can be accomplished in a matter of several milliseconds. Computed aerodynamic parameters are then passed back to a slave Harris Slash 4 CPU for use in the airframe equations-of-motion computation.

As shown in Figure 7, the Intel microcomputers are digitally linked to the H-800. These Intels serve as the input/output interface for all cockpit flight instruments with the exception of the electronic displays and flight control stick. The flight control stick communicates with the Harris Master Hybrid Computer through a high bandwidth hybrid (analog/digital) interface since the stick signals are distributed to additional processors (such as the AP-120B) once arriving in the Harris Master Hybrid computer.

#### CREW STATION CORRELATION

The following sections contain descriptions relating the correlation of mission simulation segments, such that when combined, an entire full mission scenario is achieved. The segments described are broken down into Navigational, Air-to-Air and Air-to-Ground scenarios. However, a baseline correlation between the airframe, engine and flight control simulations and cock-

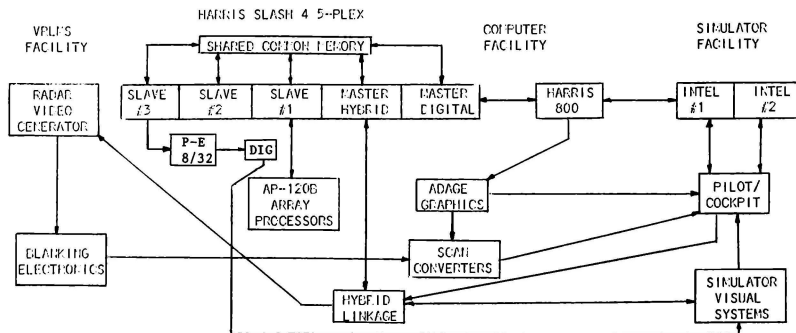


Figure 7. Facilities Functional Flow Schematic

pit controls and displays is inherent in all mission segments.

Stick and throttle movements create an interaction with the airframe, engine and flight control system simulations in order to create changes in aircraft attitude, position and velocity. All of these aircraft motions can be seen as responses in the visual, target and earth/sky scene projections as well as in all cockpit instrumentation. For example, a throttle movement will affect the engine mechanization which in turn creates responses in all engine parameters such as engine speed, fuel flow, oil pressure, exhaust gas temperature and hydraulic pressure. Furthermore, this throttle movement would change the thrust force which affects the total force on the airframe causing an acceleration on the aircraft's translational movement. This acceleration induces a velocity change which would then be reflected on the aircraft's electronic display readouts and flight instruments (such as the airspeed indicator).

As mentioned earlier, the simulated crew stations are completely operational. Hence, cockpit workload in the simulator is similar to that of the actual aircraft. This cockpit operation fidelity supports the concept of the mission environment in that all functions within the cockpit itself are correlated. As an example, in the F/A-18L cockpit, when the A/A master mode switch is depressed, all applicable electronic displays in the cockpit (such as the left/right multi-purpose and head-up electronic displays) configure for an A/A attack. Also at this time, certain multi-function switches in the cockpit also become configured to command A/A attack functions. Hence, one single switch action provides the stimulus for other cockpit switching and display functions to occur. This type of cockpit procedural correlation contributes to the simulation of the mission environment by providing mission-like switchology.

#### NAVIGATION MISSION ENVIRONMENT SIMULATION

Navigation (NAV) mission environment simulation requires a large number of elemental simulations to provide the operational characteristics of the NAV avionics subsystems. The NAV environment encompasses the entire mission from engine start, preflight tasks, takeoff, enroute navigation to landing. Obviously, for the development of new Avionics Systems, the simulation of the NAV aids (Tactical Aircraft NAV (TACAN), Instrument Landing System, etc.) are essential for creation of a realistic NAV mission environment. To be effective, the NAV aid models must correlate with appropriate cockpit operations and the electronic displays.

A key electronic display during NAV operations is the Electronic Horizontal Situation Indicator, or EHSI. Figure 8 shows a typical EHSI display where active NAV aids appear as small symbols within the compass symbol. The compass display is scaled (usually by pilot selection) such that the distance to the NAV aid can be approximated by the position of NAV aid symbol relative to the interior of the compass symbol. In Figure 8, the numeric 40 at the upper right hand part of the display indicates that when a NAV aid symbol lies on the interior edge of the compass symbol, the aircraft is approximately 40

nautical miles from that NAV aid. For example, the small symbol with the arrow through it near the center of the EHSI display in Figure 8 represents a selected TACAN station. The pilot has selected this station from an aeronautical chart or instrument approach plate. Note that this symbol is about one-quarter the distance from the center of the display which indicates that the aircraft is about 10 nautical miles from the TACAN station. Hence, in the simulation of the NAV mission environment, all display/cockpit interactions are provided such that an operationally correct scenario is maintained.

The second key element in the providing of correct cueing in the NAV simulation is in the outside visual scene presentation. The Singer-Link DIG was described earlier and becomes an important part of the NAV mission simulation. In the example above, as the pilot approaches the TACAN station, the small TACAN station symbol approaches the center of the EHSI display (where a reference airplane symbol is placed).

As the pilot navigates toward the station, he can look outside the cockpit and see a DIG representation of the TACAN station. This TACAN station is located spacially in the DIG data base so as to be accurately correlated with the NAV mathematical model. Hence, cockpit/external world cross-checks can be accomplished in the simulator. This cross-checking is much more dramatic during simulated instrument landing approaches. Here, the pilot is flying the approach on head-down instruments and eventually transitions head-up to pick up the runway in front of him for landing. Also, the NAV systems (such as the Inertial NAV System) can be corrupted (errors introduced) so as to accomplish overfly updates and realign the navigation system.

As described above, the main elements of the NAV mission simulation include the NAV model (with all the simulated on-board/earth-based transmitters/receivers and strapped-down inertial systems), the cockpit instrumentation and the external visual scene generator. All of these elements are utilized in Northrop's Avionics Mission Simulators for the development of the aircraft avionics systems and are completely correlated to insure accurate operations. Furthermore, all elements are correlated with the real world such that actual aeronautical charts and instrument approach plates can be employed. Lastly, the data bases are extensive such that an uninterrupted mission from takeoff to landing can be accomplished.

#### AIR-TO-AIR MISSION ENVIRONMENT SIMULATION

Air-to-air (A/A) mission environments are relatively easy to simulate. The main emphasis in the creation and correlation of the various A/A mission elements is in the matching of target trajectories with the radar display. Most A/A radar displays present "processed" data, hence the simulation of ground clutter has been eliminated. Therefore, the typical A/A radar display merely portrays the relative geometry of the A/A engagement.

Figure 9 shows a typical A/A radar display in the Northrop Avionics Mission Simulator. Target returns are denoted by the small boxes near the center of the display. The lateral and vertical positions



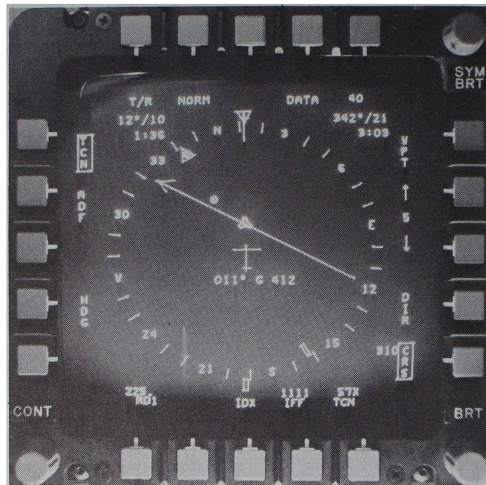


Figure 8. EHSI Display

of the target box on the display, relative to the scales at the bottom and side of the display depict target inertial off-boresight-axis angle and range, respectively. As the attacking (ownship) aircraft turns to the right, the target boxes move to the left on the display. Similarly, as the attacking aircraft accelerates relative to targets, the target boxes move towards the bottom of the display. As targets approach the bottom of the display, (which indicates zero range), the pilot can look head-up to visually acquire the targets.

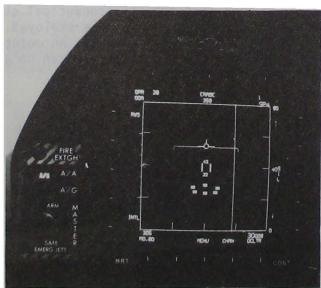


Figure 9. Typical A/A Radar Display

The above description relates the primary mission environment simulation concept during A/A scenarios - the correlation of airborne targets and the A/A radar display. The visual acquisition of multiple airborne targets through the use of radar search and tracking tasks presents an extremely realistic environment of pilot operation in the simulator. In the simulation, up to six targets have been displayed visually simultaneously.

The illusion of an air-to-air engagement is further enhanced by the destruction of targets during an attack. For example, if a radar target is attacked "beyond visual range", the target return will be removed from the radar display when the missile impacts the target. This target return removal denotes target breakup and the pilot flying the simulator realizes that a kill has been achieved.

Other cues provided during A/A mission scenarios which contribute to the mission environment include Head-Up Display feedback of selected weapon launch envelopes, missile seeker position and radar antenna pointing angles as well as typical audible sounds encountered during an attack. These sound cues range from missile seeker search and lock-on tones to missile launch and gunfire.

#### AIR-TO-GROUND MISSION ENVIRONMENT SIMULATION

The simulation of Air-to-Ground (A/G) mission environments for the development of sophisticated integrated avionics systems is by far the most difficult to create. The A/G mission not only involves intricate control and display functions during weapon delivery, but also involves the use of ad-

vanced sensors such as A/G imaging radar (Real Beam Ground Map and Synthetic Aperture), forward looking infrared, low light level television and moving maps. Furthermore, due to the increasing threat of surface defenses, an A/G mission usually will require use of Electronic Warfare (EW) devices during the penetration phase enroute to a target area. Northrop has successfully accomplished the simulation of typical A/G missions by providing correlated visual/radar/EW environments for operation in its Avionics Mission Simulator.

As was mentioned above, the control and display functions during A/G operations are more complex than those during NAV and A/A operations. A/G weaponry options are extensive and require the programming and storing of the delivery options into weapon delivery programs. Options typically involve delivery mode (computed release time, computed impact point, manual, etc.), fuzing type (electrical, mechanical, nose, tail, etc.), quantities to be released, multiples to be released in order to fulfill the quantities selected as well as many other options or suboptions. All of these programming functions are provided in the Northrop simulations as an integrated part of the overall mission scenario. Other cockpit switchology functions such as target designation, sensor modeing and EW operations are accurately represented to faithfully simulate A/G missions.

To provide insight into the required correlation of the various elemental A/G mission simulations, a typical A/G mission segment (as flown in the simulator) is described below. The scenario begins with the selection of the A/G master mode. Immediately, the electronic displays reconfigure for A/G attack. Usually A/G Real Beam Ground Mapping Radar and Stores Management are presented on Head-Down Displays while the Head-Up Display presents weapon delivery information for the selected weapon.

As the pilot enters the hostile area, an aural warning can be heard alerting him to the fact that he is being scanned by enemy Surface-to-Air radars. A glance at the Radar Warning Receiver Azimuth Indicator indicates the bearing and range to the threat.

As the mission progresses, these radars may eventually enter a tracking mode with subsequent Surface-to-Air Missile (SAM) launch. All SAM threats are intelligent in that they are under computer control and can launch their defensive weapons if the penetrating aircraft enters a lethal zone. All SAM launchings are scored to determine if a kill has been achieved on the penetrating aircraft. The penetrating aircraft is usually equipped with electronic countermeasures and other conventional countermeasures (chaff and flare). Combinations of countermeasures as well as evasive maneuvers are taken into account in scoring a successful SAM kill. It might also be noted that when a SAM sight is overflow, the pilot can visually acquire the sight which is usually depicted by a radar site and associated missile launchers. This visual scene always correlates with the electronic display on the Radar Warning Receiver Azimuth Indicator.

Using the Inertial Navigation System (INS), the pilot navigates towards the designated target area. Typically, a target is assigned as an INS waypoint. As the target area is approached, the pilot may formally designate a target for attack by using his Real Beam Ground Mapping (RBGM) radar display. On the RBGM radar display, the pilot may be able to

pick out the actual target or may simply designate a point near the target by cross-correlating prominent features on the radar display with a map of the area.

Once a target is designated, the pilot can transition the attack to the Head-Up Display (HUD) where a target designation cue is displayed showing where the target has been designated in the HUD coordinate system. As the pilot looks through the HUD target designation cue, he acquires the target visually. Often, the pilot redesignates the target visually by manually slewing the target designator around on the HUD until the symbol accurately overlays the target. The attack continues until weapon release has been successfully accomplished.

The above description indicates how the simulation of A/G mission environments involves many elements all of which are correlated with each other. INS navigation transitions the pilot into the target area while providing for the deception, avoidance and countering of intelligent ground based threats. Correlation of the EW environment and displays with the visual projection of the threats through the DIG system is preserved. As the target was approached, it was shown how the imaging radar simulation provided a head-down display which was also completely correlated with the DIG visual projection of the target area. The target designation (whether through the radar display or visually through the HUD), the operation of the weapons systems and eventual deployment of these weapons all play together as an operational scenario.

#### CLOSURE

This paper describes how Northrop has produced a correlatable mission environment for the investigation of the man/machine/environment interactions in an aircraft with a sophisticated avionics system. Navigation, Air-to-Air and Air-to-Ground mission environments were described. In general, Air-to-Air mission environments are the easiest to simulate with the Air-to-Ground environment being the most difficult. The facilities used to support this type of simulation were also described. Facility requirements are extensive, but when coupled with appropriate software which models the aircraft avionics/flight control systems, a powerful tool emerges for understanding the complexities of an advanced aircraft integrated avionics system. Understanding this complexity, and providing effective controls and displays for the human operator to comprehend and communicate with this complex system, enhance safety and probability of mission success.

THE MAN-VEHICLE SYSTEMS RESEARCH FACILITY:  
A NEW NASA AERONAUTICAL R & D FACILITY

David C. Nagel\*  
Robert J. Shiner\*\*  
NASA-Ames Research Center  
Moffett Field, California

### Abstract

A new flight simulation facility nearing completion at the NASA Ames Research Center is described. The facility is intended to support aeronautical human factors research and consists of a new building, two full mission flight simulators and an air traffic control simulator. Special features of the new facility are described which make it particularly well suited for human factors research.

### I. Introduction

Flight simulators have become increasingly indispensable tools used by those doing research in aeronautics and astronautics. Indeed, short of the flight test, the modern simulator is often used to provide final verification of the proof of concept for new avionics, controls, or other systems designed to enhance the efficiency or performance of advanced air- and space-craft.

At the same time, simulators are gradually replacing the use of aircraft for the training of flight crews, in some cases for reasons of economy, but also because certain kinds of training can be done in simulators which are impractical or even dangerous in the actual aircraft. A central issue in simulation, whether it be used for research or training, is that of fidelity. For training applications, the requirements for fidelity are straightforward in concept if not in practice; a high degree of fidelity is only useful if it provides an effective training environment. There is no *a priori* requirement for a given degree of fidelity, only for that which will produce the most rapid and long lasting training benefit.

For simulators used for research, the requirements are somewhat different. One wishes to generalize the results of studies done in the simulator to the actual aircraft and flight situation. Here the *a priori* requirements for fidelity are more stringent because, by nature, research is used to explore the unknown; each study is at least to some degree different.

Contemporary aeronautical human factors research may provide the most stringent requirements yet for certain kinds of fidelity. Here the emphasis is on determining how flight crew members behave in normal and off normal situations: how they make decisions, manage workload, communicate among themselves and with ground personnel, and how they solve problems and process information. Research done by Ruffell-Smith and his colleagues at Ames have pointed clearly to the need for a high degree of operational fidelity if the goal is for test crews to behave in simulators like they do in the actual flying situation. A high degree of operational fidelity can be achieved through full mission simulation of a functionally complete aircraft. If this is done, the test crew can made to perform the full range of behaviors in realistically complex flight scenarios. Ruffell-Smith showed that if care is taken in the process, test crews do indeed perform in a remarkably similar fashion to those in actual flight, including making the same kind and number of errors during the course of a flight.

When a new research facility for aeronautical human factors research was being planned at the Ames Research Center some five years ago, the Ruffell-Smith results and related findings influenced the definition of requirements to a large degree. The aeronautical human factors research program at Ames is broadly structured to address the problems with today's aviation system as well as the issues raised by the introduction of new technologies in the future. To provide capabilities in both areas, two flight simulators were planned: one to be representative of current technology and the second to be representative of technology of the future. In the latter case, it was determined that the best period to target was the decade beginning with the mid-1990's, since research done now and in the next few years could reasonably be expected to have some impact on aircraft and aviation system design for new generation aircraft of that era, but not before. To provide the operational fidelity needed, it was determined that air traffic control, both today's and anticipated future systems, should be simulated so that flight crewmembers might experience aircraft missions in their full operational context.

\* Research Scientist, Man-Vehicle Systems

\*\* Research Division, Member ATAA

Operations Manager, Man-Vehicle Systems  
Research Division, Member ATAA

It is intended that the facility support a range of studies of aeronautical human factors, and that it be available to the aviation community at large in addition to the researchers at Ames. Its capabilities, design philosophy, and features are described below.

## II. Design and Construction Approach

The detailed requirements for the facility and its simulation systems were developed primarily by the research staff of the Ames Research Center and several organizations outside Ames through a series of study contracts. Detailed requirements for the air traffic control simulator, for example, were developed by the Department of Aeronautics and Astronautics. The Advanced Concepts Flight Simulator (ACFS) was developed jointly by a team from Ames, the NASA Langley Research Center, and the Lockheed-Georgia Company, who, as described below, developed the overall conceptual design of the advanced aircraft on which the simulator was then based. An interesting aspect of this activity was the depth to which it was necessary to carry this design so that a simulator capable of full mission operation could be developed.

To reduce the overall resources required to complete the facility design and construction, it was decided early that NASA would act as the prime contractor and system integrator. A design and construction team was formed, headed by Rodger Hayes of the Ames engineering staff. The conventional technology simulator was purchased from the Link Division of the Singer Company, the air traffic control simulator was developed by the Massachusetts Institute of Technology with government funding, and the advanced simulator was developed, as mentioned previously, jointly with the Lockheed-Georgia Company and the Langley Research Center. A number of simulator support systems (e.g., a sophisticated audio system) and other special aircraft electronic systems for the ACFS were designed and constructed by the engineering staff at Ames. Software for the facility was developed partly through purchase from the Singer Company, partly through efforts of the Ames in-house software support contractor, Informatics General Corporation, partly through government-funded development at M.I.T., and partly through joint project sharing with Lockheed-Georgia and NASA-Langley. Software integration assistance is also being obtained from the Singer Company. To minimize both the risk and the amount of time required to develop the simulation facility, hardware and software were purchased and modified, whenever possible.

## III. Facility Elements

### Building

The facility building is shown in cutaway form in Fig. 1. Comprising approximately 13,000 square feet in size, it is intended to house the three major simulator systems, computers and other support equipment, control areas, and office space for personnel responsible for operating and maintaining the facility. A smaller office area is reserved for visiting research staff. A unique feature of the building is a flight crew "ready" or "briefing" area located adjacent to the flight simulator high bay area. This location is intended for use as a staging area for crews, e.g. where they may be given "pre-flight" briefings, or where they may be housed for brief periods of up to 24 hours or so if experimental needs dictate. This area is relatively self-contained with toilet and shower facilities as well as a small refrigerator, stove, and sink for simple meal preparation.

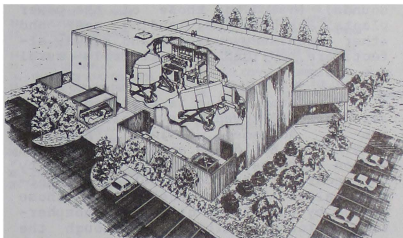


Fig. 1 The MVSRF Building.

### Conventional Technology Flight Simulator

We chose as the current technology flight simulator the Boeing 727 Series 200 aircraft. This particular aircraft was chosen as a model because of its predominant representation in the fleet; more than 1800 727 aircraft have been built by the Boeing Company. Although the last of the 727 series will be built during the next year or so, it is likely to comprise a substantial proportion of the domestic transport fleet for many years to come. Additionally, a large number of B727 flight crews are domiciled in the San Francisco Bay area. These crews potentially provide a substantial population from which to draw test crews for studies done in the simulator.



The flight simulator itself, a version of the AST design series built by the Singer Company, is typical of the most modern full mission training simulators employed by many airlines, but modified to enhance its suitability for research. The modifications are almost exclusively in the areas of simulator control and data collection. The simulator provides all modes of operation including preflight, pushback, engine start, taxi, take-off, climb, cruise, descent, approach for landing, flare, touchdown, and park. The crew compartment is a full-scale replica of a current airline cockpit equipped for domestic operation; all switches operate as they do in the aircraft. All functional systems are simulated as fully as practical and are modeled in accordance with aircraft data. All normal, and many abnormal, procedures and conditions can be simulated.

Changes in aircraft attitude, thrust, drag, altitude, temperature, gross weight, center of gravity, and configuration are accurately modeled, as are various ground effects. The latter include tire and brake effects under various runway conditions. Cockpit sounds, including those of the power plants, aerodynamics, landing gear and other machinery noises, and runway effects are provided by a flexible aural cue system.

Simulator motion is provided by a six-degree-of-freedom "synergistic" system of advanced design. Actuator lengths of 60 inches and wide bandwidth motion response provide the capability to accurately reproduce motion cues often called "disturbance" cues; those caused by turbulence or other atmospheric and ground conditions. Although the coordinated motion cues associated with normal control maneuvers can be simulated to some degree, the disturbance cueing abilities are of the greatest interest in this facility; NASA-Ames has several other large amplitude motion platforms in operation with which coordinated motion cues may be reproduced with a very high degree of fidelity for manual control or handling qualities studies.

A hydraulic control-loading system simulates the characteristics of the aircraft's primary flight controls - wheels, columns, and rudder pedals. Changes in the amount of movement and force on the controls are a function of aircraft acceleration, velocity, configuration, center of gravity and the type of control system peculiar to the aircraft. It is expected that the simulator will be eligible for FAA Phase 2 certification in accordance with FAR Part 121, Appendix H requirements.

## Advanced Technology Simulator

The advanced concept generic aircraft was formulated and sized on the basis of projected user needs in 1995 and a hypothetical technology cutoff date of 1998. This concept led to the design of a hypothetical aircraft with the capacity to carry 200 passengers, with twin engines, speed and range of 78 Mach and 2500 miles, all-electric controls and actuators, fly-by-wire or light flight control systems, load alleviation, advanced airfoil and airframe characteristics based on the use of composites for primary and secondary structures. A complete description of the design process and a very detailed description of the entire flight station have appeared elsewhere.<sup>2</sup>

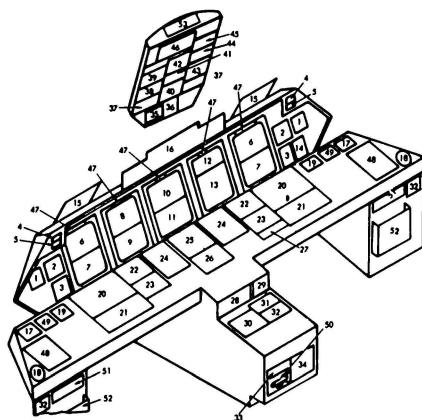
The baseline flight station is designed for operation by a two-pilot crew and configured so that all controls required for operation of the aircraft are accessible by both pilots. All controls and displays are placed in a convenient location for the pilots on the main instrument panel, a nearly horizontal surface or "desk top" over the pilots' knees, glare shield, center console, or abbreviated overhead or side consoles. Fig. 2 shows the baseline layout of the various flight station components.

The main instrument panel contains five vertically oriented 13-inch diagonal, full color shadow mask cathode ray tube (CRT) displays mounted side by side, which function as multi-function electronic displays. The majority of the information for the pilots is presented through these five displays, three of which are equipped with touch panel overlays for data or control entry. The desk top contains nosewheel steering controls, McFadden side-arm electro-hydraulic controls, control-display units, an integrated comm/nav system, electronic throttles, parking brake, rudder pedal adjust, coffee cup holders, and ash trays.

Controls for the automatic flight control system, auto-throttle engage, altitude alerting systems, barometric pressure and radar altimeter set knobs, and the master caution and warning lights are located on the glare shield. The abbreviated overhead console contains controls for the fire control system, engine start, flight control system, head-up displays, interior and exterior lights, landing gear, brake system, oxygen system, cockpit voice recorder, auxiliary power unit, adverse weather system, and emergency circuit breakers. The center console contains controls for an alternate trim system, wing flaps, global positioning system,

radar, printer, a data transfer module for entering pre-recorder flight and navigation data into the flight management computer system, and an emergency landing gear release. Side pedestals contain oxygen and smoke mask storage units, microphone and headset jacks, drawers for storing papers, and other storage areas for charts and maps.

For the most part, the dark cockpit philosophy is used throughout. Most of the controls are of the lighted push-button variety which are easy to use, offer a clean, uncluttered appearance, and eliminate protrusions. While the switch labels are readable under any lighting conditions likely to be encountered in the cockpit, the drive circuitry is such that the switch lights are only illuminated under abnormal circumstances.



Voice generation capability is also used for the Advisory, Caution and Warning System (ACAWS) system to augment visual information appearing on the center CRT display. Again, in the simulator, system design is very flexible. The system, with hardware and software both developed at Ames, is based on the use of a Digital Equipment Corporation PDP11/34 computer, and allows the experimenter to synthesize a large number of voice or other auditory messages, to edit these into desired sequences, store them magnetically, and play them back to the flight crew at appropriate times. Thus, a wide variety of ACAWS system philosophies can be studied in a realistic operational context.

- |                                |  |
|--------------------------------|--|
| 1. MASTER CRT BRIGHTNESS       | 27. ACARS/SELCAL CONTROL               |
| 2. CLOCK                       | 28. ALTERNATE TRIM CONTROL             |
| 3. WING FLAP INDICATOR         | 29. WING FLAP CONTROL                  |
| 4. MASTER WARNING LIGHT        | 30. OPS CONTROL                        |
| 5. MASTER CAUTION LIGHT        | 31. RADAR CONTROL                      |
| 6. FLIGHT DISPLAY              | 32. MIC AND HEADSET JACK               |
| 7. NAVIGATION DISPLAY          | 33. DATA TRANSFER MODULE RECEPTACLE    |
| 8. ENGINE POWER                | 34. PRINTER                            |
| 9. ENGINE STATUS               | 35. LAND LIGHTS AND ADV WX             |
| 10. ACARS                      | 36. LANDING GEAR CONTROL               |
| 11. CDTI                       | 37. HEAD UP DISPLAY CONTROL            |
| 12. CHECKLISTS                 | 38. FLIGHT CONTROL SYSTEMS CONTROL     |
| 13. SYSTEMS SCHEMATICS         | 39. ENGINE START CONTROL               |
| 14. ENGINE STATUS              | 40. LANDING GEAR/BRAKE PANEL           |
| 15. FUEL QUANTITY INDICATOR    | 41. CABIN ADVISORY LIGHTS              |
| 16. HEAD UP DISPLAY            | 42. INTERIOR LIGHTING CONTROLS         |
| 17. GUIDANCE AND CONTROL PANEL | 43. APPL/EXTERNAL POWER                |
| 18. COFFEE CUP HOLDER          | 44. OXYGEN/EMERGENCY DEPRESS           |
| 19. ASH TRAY                   | 45. COCKPIT VOICE RECORDER             |
| 20. SIDE STICK CONTROLLER      | 46. FIRE CONTROL PANEL                 |
| 21. FMC CDU                    | 47. CRT ALTERNATE SOURCE CONTROLS      |
| 22. NAV DISPLAY CONTROL        | 48. NOSEWHEEL STEERING & PARKING BRAKE |
| 23. TRANSMIT/MONITOR CONTROL   | 49. RUDDER PEDAL ADJUST                |
| 24. THROTTLES                  | 50. EMER GEAR RELEASE                  |
| 25. COMM/NAV FREQ DISPLAY      | 51. STORAGE DRAWER                     |
| 26. COMM/NAV FREQ ENTRY        | 52. MAP CASE                           |
|                                | 53. EMER CIRCUIT BREAKERS              |

Fig. 2 Advanced Concepts Flight Station Layout

A flight management computer is simulated and available to the flight crew of the advanced aircraft. In the baseline design, the computer supports the following functions: operating system, flight planning, navigation and steering, performance management, display formatting, navigation and communication tuning support, system test and monitoring, and a voice command and response system. The latter system is, in the simulator, a very flexible and general purpose voice command and response system with the capability of emulating a variety of voice synthesis techniques. An off-the-shelf voice recognition module, built by Interstate Electronics, provides speaker dependent recognition accuracies of better than 99% for 100 word, isolated utterance, vocabularies.

As noted before, primary and secondary flight information is displayed on five 13 inch CRT's arrayed across the front of the main instrument panel. The two outboard displays contain primary flight and navigation information, the two in-board displays engine and systems status, data link information, weather, approach charts, checklists, and graphic representations of aircraft functional systems states. Through the use of the touch panel overlay control systems, built in this case by Elographics, the pilots may interact with the aircraft systems, e.g. change the state of a fuel valve from on to off. The center CRT presents visual ACARS information and a cockpit display of traffic information (CDTI). In developing the display formats, special attention was paid by the Lockheed design team to the problems of color coding, symbology, and

symbol logic to meet requirements of consistency, and generally accepted human factors principles for the display of visual information.

The displays are generated by five general purpose, high performance raster graphics systems manufactured by Ikonas, Inc., now a division of Adage. The systems have software programmable resolutions which may vary from 512x512 to 1024x1024 pixels. The Ikonas systems are capable of refresh at 60 Hz rates in low resolution mode or 30 Hz, non-interlace, for high resolution displays. Display update times are dependent on the display function and content. Maximum rates of between 10 and 15 per second are feasible. Raster systems of this sort currently provide the most flexible capabilities for display generation since they support area fill, full color, and general programmability. Inherent disadvantages of such systems for display of graphic information, such as spatial or temporal aliasing, may be partially overcome through software techniques (e.g. anti-aliased vector generation). Although current technology raster systems suffer these deficiencies, and may not be the best current choice for actual aircraft application, they were picked over purely calligraphic displays or hybrid calligraphic-raster systems because they do a better overall job of supporting the wide variety of display studies envisioned for this facility.

To make the alteration of existing displays or the creation of new displays much more efficient, the Informatics software development team at Ames has created an interactive dynamic display editor (termed AIDDE for Ames Interactive Dynamic Display Editor). Using this tool, and several other pieces of software necessary for adding dynamics and linking the display formats to the aircraft simulation models, a designer (or sophisticated experimenter) may design and implement a completely new display format within a period of several days. During the design phase, AIDDE is interactive and the designer may quickly see the effects of design changes before developing the final display implementation code.

An important point is that the baseline ACFS design is just that: a baseline. It is intended as a starting point for investigations of automation, display characteristics, and for wide ranging studies of advanced aircraft systems and issues. Special attention has been placed on making the software system flexible, modular, and well documented. Many changes in the design of the interface between the pilots and the aircraft can be implemented by changes in the display formats; others may require more fundamental alterations of

the underlying simulation or system models and flight deck hardware. In either case, however, the ACFS is designed for change, while maintaining the capability to support full mission operation.

#### Air Traffic Control Simulator

The air traffic control (ATC) simulator is primarily intended to enhance the realism of the missions for the simulator flight crews. The ATC environment is a significant contributor to the workload, and therefore to the performance, of crews in flight. The usefulness of a full-mission simulator is greatly affected therefore by the degree of realism of the ATC model. Following initial discussions with NASA, Professors Antonio Elias and Robert Simpson and Dr. John Pararas of the Department of Aeronautics and Astronautics at the Massachusetts Institute of Technology developed detailed requirements for an ATC simulator that fills this broad need. For today's technology environment, ATC primarily consists of dynamically changing verbal messages, from air to ground and reverse, and from the pilots of one aircraft to another. In order to generate the appropriate messages to test crews in a simulated flight, ground controllers must have the ability to track the progress of the simulated flight, as well as that of other flights that are simulated to occur in the same "airspace". In the MVSRRF ATC simulator, the dynamic nature of ATC is achieved through the use of "operators" or controllers manning the equivalent of an ATC controller station, and controlling both the test aircrew and a number of other pseudo aircrew whose actions may interfere with the test crew's actions. The latter aircrew are implemented via so-called "pseudopilot" stations. With one such station a single individual may control the activity of up to 20 different aircraft. These aircraft then appear on the controllers' displays as though they were real aircraft flying in the same simulated ATC "sector."

In order to maximize the kinds of studies that can be done and to minimize the preparation necessary to conduct a piloted simulation study with ATC, the MVSRRF ATC simulator may be operated in any of three modes: standalone, without participation by the other simulators; single-cab mode, with either the advanced or conventional cab actively participating in the study; and dual-cab mode, with both cabs actively participating.

To increase the simulation flexibility, the ATC simulator provides three independent controller stations. These stations can be reconfigured from one simulated geographical area to another in less than 60 seconds, allowing the simulated control position to "leapfrog" in order to follow the progress of a mission. Single-controller operation is also possible for simpler missions, with some loss of realism. An example controller display format is shown in Fig. 3. The training required of the controller operators has been reduced by providing more information (i.e. range rings, named intersections and airways, and additional aircraft "tag" information) than is the practice with current NAS and ARTS systems displays. Each controller has available controls for the range of the display and its area of interest and may perform some minor display editing (i.e. moving the position of an aircraft tag) during the course of a simulation. A radar sweep of four seconds is simulated and up to five previous radar "hits" may be displayed to give the controller operator better estimates of track history.

The three controller displays are generated by a single Sanders Graphic 7 calligraphic display system driving separate monochrome display monitors. Color display monitors may easily be added in the future if that becomes desirable. The system is sufficiently fast to update nearly the maximum number of aircraft across the three displays during a four second simulated radar sweep, although it is considered highly unlikely that this would ever be required. Each controller operator is also provided a keyboard, to control the display characteristics as previously noted, and to simulate digital datalink messages for simulation of future ATC environments.

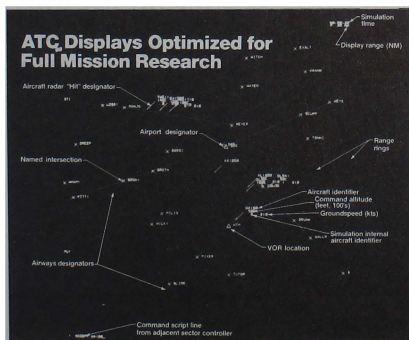


Fig. 3 Simulated Controller Display Format.

A pseudopilot display format is shown in Fig. 4. Information concerning the "active" aircraft under the pilot's control is shown in the upper left portion of the display. The display is implemented on a Texas Instruments 940 display terminal, which supports independent scrolling of various regions on the screen. Two such scrolling regions are used here. One region contains the current flight plan for the aircraft currently selected by the pilot. Selection is done by pressing a single special function button from among a number of buttons stretching across the top of the pseudopilot keyboard. A second scrolling region contains the sequence of previous pseudopilot commands for reference and confirmation by the pilot. Other display regions show pilot identification, the state of the simulation, simulation time, and error messages. Once an aircraft is selected, the pseudopilot may issue commands for that aircraft by typing appropriate messages on the terminal keyboard; e.g. "UA171 DES 40" means United Flight 171 descend to 4000 feet. Each pseudopilot has control of up to 20 aircraft; only 12 of these are designated as "audio aircraft", or those where the pseudopilot may verbally communicate with the simulator aircrew or a controller station. The remainder are typ-

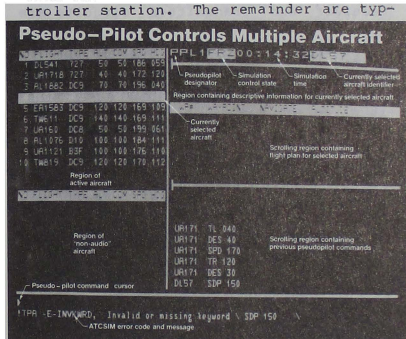


Fig. 4 Simulated Pseudo-Pilot Display Format.

ically used during handoff maneuvers from one controller's sector to another.

As noted earlier, from the pilots' point of view and for today's technology ATC system, the most obvious interface between ground and air and air to air is a sequence of verbal messages. In actual flight, these typically arrive via the aircraft VHF communication receivers which must be tuned to the correct frequency for a given region of airspace in order for a message to be received. The

system is dynamic and one important activity of a flight crew is the retuning of the receivers as the flight progresses. In order to make the test simulation realistic, the audio information must be "managed" in the simulation so that proper messages are heard - or not - at the appropriate times. A special audio distribution system was designed and built at Ames to perform this function under control of the ATC simulation computer. The system has a number of unique features. Foremost among these is the ability to change the characteristics of the audio channels to disguise the voices of the controllers and pseudopilots. The audio distribution system does this by detecting and shifting the fundamental voiced pitch of the speaker up and down the frequency scale. Since the most reliable method of identifying a speaker is through analysis of the voiced sounds, pitch shifting results in a remarkably effective disguise of the voices of the controllers and pilots, from the vantage of the test crews. Other circuits allow the voice channels to be degraded in systematic and repeatable fashions to further enhance the utility of the simulator for ATC-related research. Finally, logic and switching circuitry manage the assignment of audio "loops" so that receiver and transmitter circuits are only completed if the proper frequency selection is done in the simulator cockpits. The entire system is controlled by a microprocessor which receives commands from the ATC simulation computer.

#### External Visual Display

One of the more compelling features of the modern flight simulator is often the display of the external visual environment. In the MVSRF, external visual scenes are created by a night-dusk computer generated visual system built by the Link-Miles Company of England. The IMAGE II visual system is a compact flight simulator attachment which presents color scenes representing the outside world which normally depict specific airports and their surroundings, as view at dusk or night from the cockpit. Generic enroute visual scenes are also simulated.

Night scenes include light points, horizon glow, and runway markings and textures in the area illuminated by the simulated aircraft's landing lights. In dusk conditions, ground surface and building textures are shown in addition to the light points. At all times, occulting or the occluding of lights, surfaces, and horizon glow by intervening surfaces is simulated. The system is capable of the simulation of a variety of reduced visibility conditions: fog, cloud layers, scud, and so forth. The

IMAGE II may also simulate and display other visual air and ground traffic, which may be accurately modeled to depict a particular aircraft type. As described later, information concerning the location of this other "visual-traffic" is passed to each simulator and to the visual systems by the air traffic control simulator.

A four window, three channel display system is used to support B727 simulations. Such a system typically provides an instantaneous field of view of approximately 90 degrees horizontally and 30 degrees vertically. The CRT image is collimated by spherical mirror/beamsplitter optics so that it appears to the test crew at near optical infinity. For the ACFS, a two window single channel system is used for an approximate 45 degree by 30 degree field of view in the advanced cab.

A unique feature of the Ames IMAGE II system is the ability of the system to transition from a terminal area data base (170 Nmiles square) to an enroute database without perceptible visual effects. The enroute data base, which consists of random light points, and strings and other cultural features, may be controlled to create aircraft flights of arbitrary length, another feature of considerable importance in completing the illusion of full mission flight.

#### Facility Integration

Fig. 5 shows the major functional elements of the MVSRF and their inter-connectivity. The flight simulators employ System Engineering Laboratory (SEL) Model 32/77 computers to perform the calculations of the equations of motion, aircraft systems models, and so forth. The SEL 32/70 series computers have 32 bit processors, perform very fast floating point calculations, and allow multiple processors to share a common memory system. The B727 simulator utilizes a SEL 32/7780 configuration which comprises four independent processors and a central shared memory. The ACFS uses a 32/77, which has two processors, but which is augmented by a VAX 11/780 computer that performs graphics pre-processing and certain other I/O functions. The ATC simulation computer is a VAX 11/750. All four main simulation computers are tied together with high speed DMA parallel I/O channels as well as slower serial channels, which primarily function to support the transfer of command information. The simulations operate at a basic rate of 30 times per second, but with some calculations taking place at fractional frame rates.

The ATC computer is slaved to one or the other of the SEL computers, from which it receives command information. It responds in turn with information concerning the states of all other aircraft in the simulated airspace and environmental information (pressure, temperature, and so forth) in addition to simulation time. Graphics generation and display systems (see below) are used to implement the interface between experimenter and the simulation systems. A central data switch system provides access to any of the simulation computers from terminals located throughout the facility building.

The two flight simulators and the air traffic control simulator necessarily maintain information concerning the geographical and navigation features of the simulated airspace. For example, both the aircraft simulators and the ATC simulator use information concerning the location of radio navigation aids, VOR stations and so forth, as well as a common coordinate system, to simulate the function of navigation systems. Within the MVSRLF, the common database is distributed and that portion required by each simulator resides and is used locally. Integration must be done carefully to ensure that the database is consistent across simulators. This integration process is also required so that the visual system databases are internally consistent as well as consistent with the navigation databases.

#### MVSRLF Integration

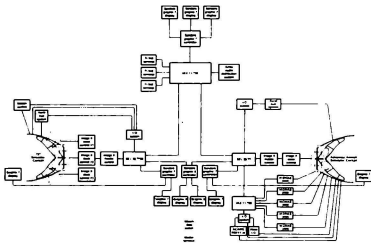


Fig. 5 MVSRLF Computer System Integration.

#### Experimenter Interface

##### Experimenter Station.

It is assumed that most investigators will wish to observe, record, and quantify many aspects of flight crew behavior during studies in the MVSRLF. The aim of the facility is to permit fine-grained evaluations of individual and crew performance under the widest variety of circumstances. The experimenter station design is such to permit control of the various aspects of a simulation, including data collection, to display the status of the simulators and the simulated flight as it progresses, and to facilitate communication with the various actors in the simulation.

Two experimenter stations are provided, one for each of the flight simulators. They are collocated (see Fig. 6) and may be reconfigured to support experiments involving simultaneous operation of both flight simulators. Each experimenter station contains two computer graphic display systems, keyboards and terminals for interacting with the simulation computers, status lights and emergency controls, communication systems, and other equipment useful or necessary for controlling the flight simulators and conducting simulation experiments. Each experimenter's laboratory also contains an audio station so that experimenters may communicate with the simulator flight crews during an experiment or with observers located "on-board". Under certain circumstances, the experimenters can act as air traffic controllers or as pilots of other aircraft, to reduce the number of personnel

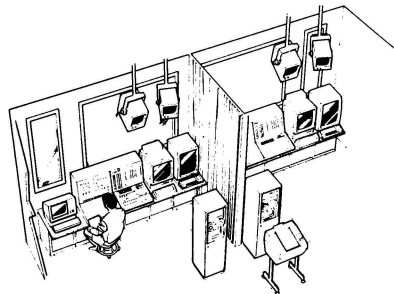


Fig. 6 MVSRLF Experimenter Laboratory.

required to conduct certain simulations. In addition to the main experimenter consoles or stations, two additional stations are located aboard each of the flight simulators. Each of these is equipped with a graphic system, keyboard, and other controls and communication systems, and may be used to perform most of the functions that are possible in the remotely located stations.

#### Data Collection

Data collection within the MVSRF is very flexible. Each of the flight simulator data variables within a global datapool may be sampled according to the needs of the experiment or simulation. While there exists an upper limit to the total amount of data which may be sampled and stored, this limit is large. Typical practice will be to sample and store a differing number of variables for each phase of flight, and to time code these samples to facilitate later analysis. Following completion of a simulation, the data file will be available for postexperimental analysis. For certain applications it is possible to take a "snapshot" of the simulation, that is, sample every variable in the datapool so that the simulator may be re-initialized to a previous state. The capability also exists to "replay" a limited portion of a simulation. The latter capability may be most important during flight crew training exercises.

The ATC simulator maintains a separate data collection capability. ATC simulation data also are time stamped and may be merged with the data from the piloted simulators following completion of a given simulation or experiment. The timing and occurrence of voice communications and the communications themselves may also be recorded for later comparison or correlation with the objective simulation data. Other measurements of crew behavior and performance can be made as experimental needs dictate. Closed circuit TV monitoring and recording are possible, if required. Direct observation and monitoring of flight crew behavior and performance are also possible from within each of simulator cabs through the use of the on-board experimenter station. Data thus recorded can be integrated with the remaining simulation data.

#### Script System

To make simulations repeatable and in some cases to facilitate the automatic creation of certain simulation events, a flexible scripting system was developed, initially for the ATC simulator by the MIT team, but subsequently expanded for application for the two flight simulators as well so that a single integrated mechanism is available for simulation control. The development of a script

may be done off line, with storage of the script in a computer file for later use in controlling the events of the simulation. Each script consists of a series of script "lines", with the following syntax:

```
<trigger-directive> ==>
    <action-directive>; <data>
```

Trigger directives may be either time-specified, event specified, or value-specified. A time-specified event is further defined as one occurring at some particular time, before some particular time or after some particular time. Event-specified triggers are typically defined in terms of simulated distance from some geographical or cultural feature in the simulation (e.g. a waypoint, sector boundary, or airport), or in terms of the activity of one of the simulation actors (e.g. a particular pseudoaircraft in the ATC simulation). Value-specified triggers allow events to be defined in terms of values of simulation variables in the global datapool. Prior to runtime, the trigger directives are scanned and the time-specified directives stripped from the remainder, sorted, and stored. The event-specified and value-specified triggers cannot be sorted but are stored in sequential fashion. During a simulation, both trigger buffers are scanned to see if the conditions specified by each trigger is true or false. If true, the action directive associated with that particular trigger is implemented.

Within the ATC simulation, the action directive is typically a command to deliver a text line to one of three terminal types: the command console, a controller terminal, or a pseudopilot terminal. The text lines (which are specified in the <data> field of each script line) may have one of three functions:

(1) to simply show some information to the "user" of that terminal (a "display only" line), (2) to place a command line on the actor's terminal input area which can then be entered by the actor by just pressing the "enter" key (termed a "validated line"), or (3) may be sent to the terminal for automatic entering, without actor action (this case is termed an "automatic" line).

Basic simulator control can be effected in this fashion, e.g. by sending the automatic line, FREEZE, to the ATC command terminal. Alternatively, messages may be sent to the various simulation actors to "key" their behavior at various points in the simulation. For example, a pseudopilot may be commanded to change the heading of a particular aircraft under his control when the test aircraft passes a certain waypoint.

The trigger directives may be nested to allow quite complex contingencies to control simulation events. Event directives for the flight simulators are similar to those for the ATC system, with the exception that they generally refer to specific aspects of simulator control. For example, a particular fuel system malfunction may be triggered by a sequence of other simulation events. Using this flexible, event-driven system, simulation events may be reproduced time after time for other test crews. The script mechanism also allows the experimenter to alter the manner in which simulation data is collected and stored for later analysis. Although it is typical for an entire script to be created prior to a simulation and automatically processed by the script processing system, it is also possible to insert new script lines during the course of a simulation (or training session) if so desired. Each of the three simulators may also be operated "manually" from the experimenter stations; that is, direct commands to RUN, FREEZE, and so forth may be directly entered and used to control the course of a simulation.

#### IV. Summary

The MVSFRF will make possible the creation of realistic single- and multiple aircraft, part- and full-mission scenarios. This flexibility will permit the study and analysis of many kinds of interactions among flight crew members, between air and ground, and between the crew members and aircraft systems. Such studies will be possible in the contexts of both today's aviation environment as well as those of future decades. The overall goal of such studies is to reduce the incidence of human error in the operation of the National Aviation System, and to increase the efficiency of operations by matching the characteristics of aircraft and control systems in an optimal fashion to those of the human participants in the system.

Construction of the MVSFRF will be completed at the end of calendar year 1983. Inquiries regarding usage of the facility should be forwarded to the second author of this paper.

#### References

1. H. P. Ruffell-Smith. A Simulator Study of the Interaction of Pilot Workload with Errors, Vigilance, and Decisions. NASA Technical Memorandum 78482, 1979.
2. W. R. Paden, Jr. and G. A. Sexton. Applying Advanced Technology to Flight Station Design. Presented at the 13th Council of Aeronautical Sciences/AIAA Aircraft Systems and Technology, Seattle, Washington, 22-27 August, 1982.



C. G. Horattas and R. P. Adkins  
Goodyear Aerospace Corporation  
Akron, Ohio

### Abstract

This paper discusses data base requirements for simulating the sensor environment used in typical military aircraft. Certain mission characteristics can be capitalized upon to effect some relief in the enormous demand on data base coverage and detail, while maintaining the high degree of realism and fidelity needed to provide adequate training.

### Introduction

The quality of flight simulation usually is judged by the quality of the simulation of the sensors employed during flight training (i.e., out-the-window visual, radar, infrared and electro-optical).

The quality of sensor simulation is in turn judged by the fidelity of reproduction of visual cues using data that is derived from a variety of sources, (Defense Mapping Agency (DMA), reconnaissance, satellite, intelligence, etc.) and available in a variety of formats.

The primary function of flight simulators is to train crew members. The amount and rate of training transfer to the trainee depends on the realism with which sensors are simulated. Re-creating sensor images that are identical with real world would be the ultimate level of simulation and would provide the same training obtained by flying real aircraft. However, real world fidelity cannot yet be achieved, therefore, certain trade-offs and constraints must be tolerated.

The data base from which the sensor imagery is derived is an extremely important component of the simulation system. Data selection criteria can be established based on specific requirements of the mission and of the sensors to be simulated.

Understanding the specific aspects of the training mission leads to the conclusion that adequate flight and tactical training can be obtained without the need for whole world/real world data.

This paper describes some aspects of the real mission that could help reduce both the quantity and the quality of data needed for simulation.

### The Tactical Mission

#### General

The typical air-to-ground mission relies on precise navigation, penetration tactics, and self-contained target acquisition and weapon delivery to achieve acceptable performance and to assure destruction of the target. The air-to-ground mission involves an attack against pre-briefed targets whose geo-coordinates are established prior to the mission and against targets of opportunity present

at the ingress and egress to the target area. The various ranges, terrain type, weather, enemy detection and jamming, and altitude profiles encountered in the air-to-ground mission require the pilot to utilize all sensors at his disposal during some phase of the mission. The air-to-ground mission will, in most cases, require low altitude, nap-of-the-earth flying to avoid detection by enemy radar; as such, the pilot task loading increases to the point where the pilot has little opportunity to make major corrections in his flight plan. This is the main reason why pre-briefing of a mission is so important; such pre-briefing provides the pilot with all navigational and tactical information that he will require for a successful mission. The pilot may have to make minor in-flight corrections to compensate for variables that cannot be accurately predicted during pre-briefing and, if the cumulative error exceeds certain limits, the pilot may opt to abort the mission. Navigational pre-briefing provides the pilot with an exact flight plan: checkpoints, initial point, and target latitudes and longitudes, time between checkpoints, fuel consumption between checkpoints, wind velocities, weather conditions, etc. To the pilot, the tactical portion of pre-briefing is just as important. Tactical intelligence provides him with enemy deployment and surveillance along the flight path and in the vicinity of the target, increasing the probability of his survivability and that of the aircraft.

The air-to-ground mission consists of ten distinct phases; these phases are shown on Figure 1 and listed as follows:

- 1 Takeoff
- 1-2 Climb
- 2-3 Cruise
- 3-4 Descent/Preliminary Target Acquisition  
(Cross Front Edge of Battle Area (FEBA))
- 4-5 Run-In To Target
- 5-6 Pop-Up/Target Detection
- 6-7 Target Acquisition & Weapon Delivery
- 7-8 Weapon Guidance Assistance
- 8-9 Damage Assessment
- 9-10 Run-Out/Target Of Opportunity

### Types of Missions

The air-to-ground missions can be classified into three main types: close air support, battlefield interdiction, and deep interdiction. Table 1 compares parameters of the three types of missions:

Table 1 - Types of Missions

TYPE OF AIR TO GROUND MISSION	TIME FROM FEBA TO TARGET (MINUTES)	DISTANCE FROM FEBA TO TARGET (NM)
Close Air Support	0-2	0-5
Battlefield Interdiction	0-5	0-20
Deep Interdiction	20-30	100-200

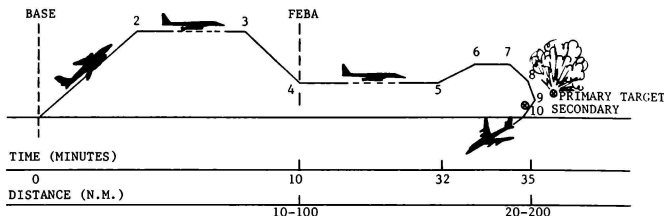


FIGURE 1 - Deep Interdiction Mission Profile

The Close Air Support Interdiction Missions penetrate up to five miles inside of the FEBA and are designed to attack and destroy stationary targets that are deployed in positions for fighting.

The Battlefield Interdiction Mission extends up to 20 miles inside the FEBA and the mission is designed to disrupt enemy supply lines.

The Deep Interdiction Mission is more removed from the actual fighting than the other two types of missions, and accordingly, the tactics of the pilot change from battlefield to one of penetration and navigation. This mission is the most demanding so far as sensors are concerned and will be discussed more extensively. The deep interdiction mission operates inside of the FEBA in ranges in excess of the battlefield region and normally in the 100 to 200 nautical mile range. It is directed against strategic targets, to disrupt the enemy's assembly and staging areas, to disrupt the enemy's lines of communications, and to provide harassment that will effectively inhibit the enemy's ability to mount an attack.

The deep interdiction mission imposes stringent navigational requirements on the pilot and forces him to a defensive posture from the FEBA to the target. To assure his reaching the target, the pilot must fully utilize the aircraft's sensors to cope with low altitude flying.

#### Sensor Requirements

##### General

Due to the stringent mission requirements and possible adverse weather conditions, it is necessary for U.S. aircraft to possess an array of sensors for use in navigation, target detection, weapon release, etc. in all kinds of weather. Sensor suites may vary from aircraft to aircraft, but there is one thing in common - they all possess some combination of the three basic sensors: radar, electro-optical (EO), and forward looking infrared (FLIR). Nearly all present day aircraft possess at least one of the basic sense modes; however, it is becoming apparent that there will soon be a need

for all three sensors to be incorporated in a single fighter attack aircraft.

##### Sensor Utilization

How and when a sensor is utilized depends on many parameters: mission profile, terrain, weather, sensor characteristics, target type, jamming and detection, pilot preference, etc. Defining when a sensor may be used is rather ambiguous; it is easier to define when a specific sensor may not be used. Nominally in any mission profile, EO and FLIR operational ranges are less than ten miles; radar however, is capable of ranges in excess of 200 miles. Resolution also plays a major role in selection of a particular sensor; for example, one would not select a range resolution of 2000 feet when wanting to detect a target of less than 100 feet.

Mission profile may also restrict the operational range of a sensor. If the mission is low level, it is not practical to get large ranges from the sensors at such a shallow depression angle; not only may there be line-of-sight interference, but as the depression angle approaches zero, the range cells at far range become infinite in length. If the mission is to be flown over large bodies of water, then FLIR may not be used due to its high susceptibility to humidity. EO is not useful in darkness - even low-light level television (LLLTV) is ineffectual below quarter moon illumination.

Target type plays a key role in selection of a sensor. EO and FLIR are passive sensors, they do not illuminate a target by active emanation of power, rather they are merely receivers of energy emitted by the target.

Weather, heavy rains and snow affect radar; high humidity affects FLIR; smoke and fog affect EO; the atmosphere itself provides an attenuating factor for the sensors; every sensor has its shortcomings. Fortunately, these areas of deficiencies are not overlapping to the extent that all sensors are affected the same; rather, the pilot must make the determination as to which sensor shall be best utilized for the prevailing conditions.

The spectral sensitivity of the individual sensor determines the transmissivity in weather conditions of rain or fog. EO sensors are affected most by inclement weather conditions due to the reflection and absorption as a function of wavelength. FLIR is predominantly an "after-dark" or low light level sensor. The sun, an emitter of high energy infra-red, causes the FLIR sensor to saturate, but in certain conditions, FLIR may be used during daylight hours. Radar is unaffected by fog, clouds, or smoke but is susceptible to heavy rainfall and to active enemy jamming. Of the three basic sensors, radar alone is susceptible to detection because it provides its own emanation of power; the others are merely passive receivers of energy emitted by the target.

Table 2 represents the array of sensors available aboard current aircraft and when they are used during deep interdiction missions.

#### High Resolution Ground Mapping

Tactical/strategic aircraft radar is currently being enhanced in two distinct ways. The first is Doppler Beam Sharpening (DBS). This is a technique that allows the forward motion of the plane to aid in the construction of a radar image by recording the phase generated by the doppler phase shift. Synthetic Aperture Radar (SAR) also uses the forward motion of the aircraft, not to generate doppler shifts but to synthetically increase the length of the antenna thus increasing its resolution (since the resolution of the radar is proportionally related to the antenna length). Both of

these types of radar are included in the processing equipment on board tactical/strategic aircraft. Although the processing is not strictly realtime (SAR requires the time of forward motion to generate its synthetic antenna, DBS requires the time of forward motion to generate the doppler phase shifts), it provides displays in adequate time, rendering both SAR and DBS as viable tactical warfare devices.

#### Simulated Mission Requirements

##### General

Simulated missions can be classified in two main categories: 1) those used to gain and maintain proficiency by crew members in the use of on-board avionics and 2) those full missions used to familiarize the crew with specifics of a particular mission.

In the first category, the sensor simulation is required to merely provide typical displays. In this type of mission the emphasis is on the use of sensor and the interpretation of its displays. Data base requirements and processing requirements could be minimal because it is only generic information, not necessarily related to ground truth data that is required.

The latter type of training mission is gaining popularity in recent years as can be seen by the weapon system trainers presently under development. This mission allows the crew to fly full training

Table 2 - Sensor Utilization

MISSION PHASE SENSOR	CRUISE NAVIGATION STEPS 2-3	PRELIM TARGET ACQUISITION STEPS 3-4	RUN-IN TO TARGET STEPS 4-5	TARGET DETECTION STEPS 5-6	TARGET ID WEAPON DELIVERY STEPS 6-8	DAMAGE ASSESS STEPS 8-10
TELEVISION			X	X	X	X
LOW LIGHT LEVEL TELEVISION			X	X	X	
FORWARD LOOKING INFRARED			X	X	X	X
LASER DESIG/RANGER				X	X	
LASER SPOT TRACKER				X	X	
REAL BEAM GROUND MAP	X	X	X		X	
DOPPLER BEAM SHARPENED	X		X			
SYNTHETIC APERTURE RADAR	X	X	X	X		
GROUND MOVING INDICATOR		X		X		
BEACON	X					
TERRAIN FOLLOWING/AVOIDANCE			X			
RADAR WARNING RECEIVER	X	X	X	X	X	X
AIR-AIR RADAR	X					
STORED MAPS	X	X		X	X	X

missions that would not be possible in the actual aircraft due to several factors:

1. Areas of interest may not be accessible because they are in hostile territory.
2. Repeated training missions over an objective may endanger the aircraft and the crew.
3. Repeated training missions over an objective will divulge strategic information.
4. It is costlier (fuel and ordnance savings).
5. Mission cannot be stopped and resumed at will to recover from an error.
6. Certain training scenarios involve high risk when performed in the actual aircraft.

The full mission training puts far more demands on data and processing resources than the ordinary training mission. The simulator must carry on-line and process on-time sufficient amounts of data to re-create the real world environment to the degree required by the specific sensor. Added to this stringent requirement is the requirement for longer missions under adverse conditions (low altitude, inclement weather, etc.). The result is an enormously large data base that is quite difficult to store and to process.

Fortunately, certain characteristics of the real mission can be capitalized on to provide a more manageable data base.

For maximum training transfer, the training mission must include as many of the pertinent features of the real mission as possible. Some of these features may impose great burdens to the simulated environment and to the cue generation equipment, while others may, if properly evaluated, facilitate such tasks. For example, it is known that prebriefing establishes the ingress and egress to the objective.

Realizing that the mission follows pre-established flight paths can result in concentration of data base storage and processing resources to a particular set of data indigenous to the pre-established corridor. This conclusion can result in considerable savings of resources and, in some cases, can become the difference between success or failure in the simulation of the mission.

The fact that low altitude, and/or nap-of-the-earth flying is limited to the FEBA enclosed area (approximately 10 nm from the objective), can be used to great advantage to reduce the high resolution data base requirements to that area about the target or waypoint.

The fact that a pop-up maneuver is used sparingly and when used involves but a few (5-6) seconds, limits the data base to that of the viewable area, and the number of features within the data base to that which could be discerned by the viewer. Knowing that the pilot will concentrate on the specific item or group of items that comprise his objective (way-point, initial point, target, etc.), can reduce the number of features that need be contained in the data base.

## Data Base Requirements

### General

Each sensor to be simulated has unique characteristics that set it apart from others. The data base area of coverage, resolution, and format, as well as utilization may be different not only between sensors but between modes of operation of the same sensor. At the same time, it is necessary for two or more sensors covering the same area to provide scene correlation. This can be best achieved by providing for a unitized data base which can support all sensors, (e.g. Defense Mapping Agency (DMA) Digital Data Base (ddb) with enhancements). This unitized data base can be processed in an off-line data base management system and formatted into a unique on-line data base suitable for each sensor.

### Background

Since the days of Project 1183, the DMA Digital Land Mass Simulation (DLMS) Level I Digital Data Base has been the primary source data for sensor simulation. Prior to this, radar simulation was accomplished using transparencies and flying spot scanners. It was not easy to teach terrain following and low level flight techniques, nor was the data base adequate to resolve individual features, or portray the height of cultural features. Transparencies and scanners represented a costly and time-consuming project in terms of data base update and maintenance. While there had indeed been some early digital radar landmass simulators, they utilized a special contractor-generated digital data base. Project 1183, which consisted of two major development efforts, concluded that the DMA DDB is practical for sensor simulation. This conclusion has since been substantiated by the use of DMA DDB in a number of recent simulators.

As the requirements for sensor simulation have increased, so has the level of sophistication of the DDB. Level I DDB evolved to Level II, Level V, Level X, and the Standard Linear Format (SLF) with future specifications currently under development. There are many advantages to using the DMA DDB, ranging from providing a common source reference, to providing sufficient information density as a baseline for enhancement. The one major weakness, which will continue to plague DDB users in the near future, is the sparsity of the detail data needed to represent the world at a level commensurate with sensor requirements, particularly high resolution sensors.

### Simulated Mission Data Base

Pre-planned missions could be effectively used to limit the DDB to a level that could be within the realm of today's technology. Certain observations could be made that balance the desired versus the realistic data required for a training mission.

Gaming Area. The aircraft range and type of training to be performed defines a gaming area that would contain all training missions to be performed by a training facility. Some of the data base defining this gaming area may be available through DMA. The remaining data will have to be added by a variety of embellishment techniques.

Mission Corridor. Realizing that the aircraft will always fly a pre-established flight path as explained earlier, a corridor can be defined which will contain that data base which is potentially viewable by the sensor. This corridor would be sufficiently wide to allow for the sensor-typical ranges of operation and could include all checkpoints and targets.

Way-point Patch. The data between waypoints is of little interest for training, except that they must provide typical images with relatively low world truth content. Since this area is by far the largest area, some data compression schemes can be employed. Polygon surfaces are one common scheme of data base compression. High order splines and other stochastic and probabilistic methods of generating artificial imagery have been explored in the last few years. The prime criteria to be considered is the visible regions. For this reason, terrain elevation is a very important true world attribute to be preserved.

Feature and Detail. At the waypoints, a pre-defined area of several nautical miles about the specific waypoint must be considered. This area allows for error in aiming of the sensor. The data base within the waypoint area may need to support multiple resolutions and levels of detail for sensor and mode selection. The data base within the waypoint area could consist of two specific types of data: 1) The item or group of items that comprise the checkpoint itself must be modeled with true world data, scaled, oriented and merged into the background, and 2) the remaining data could be comprised of generic data derived from libraries or function generating algorithms. This generic data is needed to add fidelity to the scene and can be generated by various methods, such as synthetic breakup, three-dimensional modeling, etc.

#### Data Base Enhancement

It is necessary to enhance the DMA DDB to increase data content and density to a level sufficient to meet current and projected requirements. There have been many such attempts in the past, starting with early radar and Computer Image Generation (CIG) simulations in which the entire data base was synthetically derived, to today's technology in which the DMA DDB is manually or semi-automatically enhanced. These enhancements began as total manual inputs to the DMA DDB, (e.g., an operator monitoring a CRT, utilizing input devices such as joy sticks, track-balls, digitizing tables, etc.) to manipulate the DDB. As technology and knowledge increased, so did the efficiency of the operator/computer/DDB interface. More and more formerly manual processes have been automated to the point where the operator is now primarily responsible only for those decisions which are not practical to be performed by the computer.

Beginning with the DMA Level 1 data base, the Data Base Management (DBM) facility needs to proceed in two directions of processing. First, to create detail that extends the resolution down to eight feet for SAR, (less for EO type sensors) and second, to compress the data base so as to minimize both the data storage and the on-line data processing needs.

The first process attempts to replace the Level I area cells with an array of cells that

cover less area and provide description for more features. This direction could be sufficient for all image generation if we had infinite storage and processing resources. Since this is not the case, it is necessary to resort to means of containing the quantity of data and the amount of processing needed to recover the image. Several schemes for accomplishing this have been considered. Unfortunately, each scheme works only in limited situations and does not meet the needs of all sensors and all aspects of the training mission. A combination of techniques, which could approach an acceptable compromise is: By using a data compression scheme to describe the average terrain that is only incidental to the mission; and, emphasizing of those areas that have a direct impact on the mission (such as waypoint and target items).

The addition of detail and increase in resolution call for processes that involve digitization of topography obtained from maps, reconnaissance and satellite photographs, and other intelligence sources. The digitization process must be of sufficiently high sampling rates to preserve the integrity of the data base. Other processes involved in the addition of detail are scaling, rotation, translation, and merging of data. All these processes must be carried out in an off-line DBM Facility and as automatically as possible.

Non-essential, but desirable data are those features that add to the fidelity and quality of the image. This data base could be generated by stochastic and probabilistic arithmetic processes such as higher order splines and "fractals" or by geometric surfaces which combine a multitude of cells into a single entity (polygonization). Polygons have been successfully used in generating visual scenes as well as EO sensor images. The transformation required to generate polygons from pixels must be as automatic as possible. Algorithms that compare one cell to its neighbor using all essential criteria to create larger cells and ultimately large areas that preserve the common features are in use today. In addition, a reverse process (inverse transform) which changes polygon data into pixel format is essential.

The techniques described increase the data content of the DDB, but they don't necessarily provide assurances that such increase in data has added to the fidelity of the prospective image. It is possible, by analyzing the mission, to ascertain what data is critical to training performance. Once this is established, those data base items which are of interest to the trainee need to be considered first in the enhancement process. Subsequently, data base items that are not of prime interest to the trainee, but are necessary to enhance the quality and realism of the scene must be added. These latter items, since they would not directly affect the performance of the mission, could be implemented using generic data.

A figure of merit can be established for the high resolution patch analogous to the signal-to-noise ratio used in communications. This figure of merit will be the ratio of number of true world features to the number of generic features. This figure of merit would allow an automatic fill of the available area; the density would depend on this figure of merit. The figure of merit will be established by observing the checkpoint image in the DBM facility.

### Conclusion

It is possible to provide adequate sensor simulation using real world data without need of entire world data base. Using specific corridors for the simulated missions and/or specific high resolution patches which contain the mission check-points and target areas, a training mission can be pre-planned by the training officer, very much as is the full tactical mission, by following pre-established way-points and ingress and egress routes.

High resolution patches can be created around pre-established way-points and target areas to simulate high resolution sensors images. Finally, an interactive graphics language and a user-friendly operating system could provide a highly automated DEM facility, which can provide data bases for simulating all sensors in all modes of operation required for a cost effective, state-of-the art simulator.

### Bibliography

Faintich, Marshall B., Gough, John; "Increased Sensor System Capability as a Result of Improvement to the Digital Landmass System (DLMS) Data Base", 1981 Image Generation/Display Conference II, pages 181-196.

Hall, Ernest L., Gonzalez, Rafael C.; "Multi-sensor Scene Synthesis and Analysis", 1981 Rome Air Development Center RADC - TR-81-255.

Bunker, M., Heesch, R., "Airborne Electro-optical Sensor Simulation", 1975 Air Force Human Resources Laboratory AFHRL - TR-75-35.

McHugh, Conrad J., Maj. USA; "The Role of the Air Assault Division on the European Battlefield", 1975 Master's Thesis, U.S. Army Command and General Staff College, AD-A093778.

Fox, H. R., Helser, G. L., Kim, F. M., Kinnaman, R. L., Wallace, M. R.; "Integrated Strike Avionics", 1980 Air Force Wright Aeronautical Laboratories AFWAL - TR-801145.

Greening, Charles P.; "Significant Non-Target Effects on Target Acquisition Performance", 1977 Proceedings of the 1977 Image Conference, pages 35-47.

Hoog, Thomas W., Stengel, John D.; "Computer Image Generation Using the Defense Mapping Agency Digital Data Base", 1977 Proceedings of the 1977 Image Conference, pages 203-217.

DuPuis, T. A.; "Simultaneous Sensor Presentation Techniques Study", 1977 Office of Naval Research ONR - CR213-142-1F.

Richard J. Crosbie\*  
Naval Air Development Center  
Warminster, Pennsylvania 18974

### Abstract

This paper discusses the experimental derivation of human response transfer functions and their application to the development of a control algorithm for the recently completed NAVAIRDEVCEV centrifuge based Dynamic Flight Simulator (DFS). Centrifuge experiments are described in which human perceived angular response to the individual and combined component angular stimuli of rotating linear acceleration vectors and angular accelerations were measured. Analyses of the data revealed that human response to the combined stimuli could be predicted by adding the predicted response to the individual component stimuli. This knowledge was subsequently used in the development of a control algorithm for the DFS in which one component angular stimulus was used to counter-influence the other component angular stimulus. The human response transfer functions were used in this development to compare the predicted angular response perceived by the DFS pilot, with the predicted angular response perceived by the simulated aircraft pilot to the same control inputs. This provided a powerful and ingenious method for initially tuning the control algorithm prior to manned operation, by adjusting certain parameters within it to achieve maximum agreement between the two pilots.

### Nomenclature

$\theta^{\text{ap}}$	Pilot perceived angular response in pitch at 1 g
$\phi^{\text{ap}}$	Pilot perceived angular response in roll at 1 g
$\theta^{\text{ap}}$	Pilot perceived angular response in pitch at G
$\phi^{\text{ap}}$	Pilot perceived angular response in roll at G
G	Pilot's resultant G level in multiples of g (accel. of gravity)
G'	Magnitude and direction of G but delayed by approx. 1 sec.
S	Derivative with respect to time
$\theta^{\text{vp}}$	Pilot perceived angular response in pitch to vector rotation
$\phi^{\text{vp}}$	Pilot perceived angular response in roll to vector rotation
$\theta^{\text{v}}$	Vector angular displacement in pitch
$\phi^{\text{v}}$	Vector angular displacement in roll
$\theta^{\text{p}}$	Pilot perceived angular response in pitch to combined pitch stimuli
$\phi^{\text{p}}$	Pilot perceived angular response in roll to combined roll stimuli
R	Radius of centrifuge
$\alpha$	Angular displacement of outer gimbal (roll)
$\beta$	Angular displacement of inner gimbal (pitch)
$g_r$	Radial acceleration of centrifuge arm
$g_t$	Tangential acceleration of centrifuge arm
$G_x$	Transverse acceleration on Pilot
$G_y$	Lateral acceleration on Pilot
$G_z$	Longitudinal acceleration on Pilot
G	Resultant acceleration on Pilot

\*DFS Program Manager  
Member AIAA

### I. Background

The NAVAIRDEVCEV has recently completed the development of the world's first full system total G-force environment Dynamic Flight Simulator (DFS).<sup>1</sup> Using the NAVAIRDEVCEV unique human centrifuge (figure 1) as a force/motion base, the DFS provides the tri-service and industrial communities with a simulator capable of reproducing, under pilot control, the potentially disabling and disorienting multi-directional G force environment associated with controlled and uncontrolled flight of current and future high performance military aircraft. It has particular application in programs where rapidly applied, high sustained G profiles are involved. Such profiles are generated during air combat maneuvers (ACM), missile evasive maneuvers, close air support, and weapons delivery.

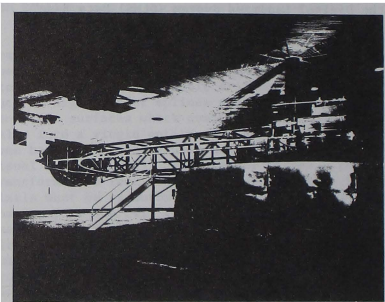


Fig. 1 NAVAIRDEVCEV Human Centrifuge.

The challenge in this unique centrifuge method of ground based flight simulation lies in the extension of force generation requirements beyond that of any previous simulation. A major problem exists, however, in generating the total G force environment of an aircraft which flies in an unlimited six degrees of freedom (DOF) flight regime with a device mounted in a dual gimbal system and confined to move in a fixed radius circle.

Previous studies have shown that problems occur when the simulator pilot attempts to fly the DFS through certain maneuvers because of unrealistic and often disturbing angular artifacts produced by rotations of the centrifuge gondola about its pitch and roll axes.<sup>2,3</sup> These gondola rotations, which occur during periods of transient G and are often quite rapid, are necessary to follow the rotating G vector and to provide the proper linear acceleration to the pilot seated therein.

This G Force method formed the basis for the original centrifuge control algorithm which has historically been used for psycho-physiological research studies, and was designed to provide precise G force control on a centrifuge subject. If this method were used to control the centrifuge for flight simulation studies, however, it would produce disturbing angular artifacts on the simulator pilot and would, without modification, limit the use of the DFS for pilot controlled flight simulation studies.

A new centrifuge control algorithm has been developed therefore, which reduces these angular artifacts by emphasizing perceptual rather than physical realism. As an essential aid in developing this new algorithm, transfer functions were experimentally derived which describe human perceptual response to the individual and combined component angular stimuli of angular accelerations and rotating linear acceleration vectors about the pitch and roll axes. This approach is in agreement with the recommendations made in the AGARD Advisory Report No. 159 which states, "In the vestibular field, the models of dynamic processing of combined linear and angular acceleration cues in terms of perceived orientation could be brought to bear on the design of more efficient motion platform algorithms."<sup>4</sup>

## II. Definition of Human Perceptual Response Models

Since the DFS will incorporate a well structured visual display system as well as a force-motion system, the simulator pilot will be exposed to three primary inputs as shown in figure 2: visual, tactile/kinesthetic, and vestibular.<sup>5</sup> The tactile/kinesthetic and vestibular receptors are two subclasses of the proprioceptive human reception system and mediate such sensibilities as sense of position, sense of movement, pressure sense, and equilibrium. Previous centrifuge studies have demonstrated that angular stimulation for these proprioceptive receptors can be separated into two components, angular acceleration and rotating linear acceleration vectors.<sup>6,7</sup>

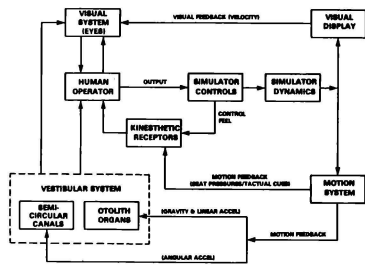


Fig. 2. Visual and Motion Closed-Loop Human Sensing System.

In one particular study, measurements were made of human perceptual responses (about the roll, pitch, and yaw axes) to the separate and combined oscillatory stimuli of angular accelerations and sweeping linear acceleration vectors.<sup>8</sup> These measurements were primarily concerned with the amplitude attenuation and phase angle shift of the perceived angular response about each axis. Careful analyses of these data revealed that, when the mean phase angle shifts of the perceived responses across subjects, for each component stimulus, were taken into account, the scaled sum of these responses could be used to predict the perceived response across subjects to the combined stimuli.

Figure 3 provides a diagrammatical representation of three possible ways these component angular stimuli may combine to create the perception of roll angular rotation. Normal rotation occurs in a constant gravitational field, and as such, is represented by the third situation. The vestibular semicircular canals are classically identified as being stimulated by angular accelerations as in the second situation, while the vestibular otolith organs along with the tactile/kinesthetic receptors are classically identified as being stimulated by rotating linear acceleration vectors, as in the first situation.

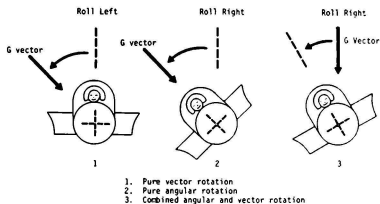


Fig. 3. Diagrammatical Representation of Three Possible Ways a Pilot May Perceive Angular Rotation.

Ignoring, for the time being, the considerable effect which visual stimulation is known to have on a pilot's perceived angular motions, this effort is concerned primarily with the stimulation and response characteristics of the pilot's proprioceptive receptors. The visual stimuli will be introduced later after every effort has been made to control the DFS in such a manner that the DFS pilot's perception of his angular motions match that of the aircraft pilot.

## III. Measurement of Human Perceptual Response

In an initial centrifuge study, four volunteer subjects, two male and two female, were exposed on the NAVAIRDEVCON centrifuge to G profiles operating from 1.25 G base to peaks of 2 or 3 G, and having on-set and off-set times of 2 or 4 sec. The sustaining time at peak for each run was 20 sec. Variations in the shape and phasing of angular accelerations and sweeping linear acceleration vectors were generated during the



on-set and off-set portions of the G-profile by altering the phase and amplitude of the gimbal drive signals in a preselected manner.

Following a period of training, the subjects, seated and tightly strapped in a darkened gondola, were requested to track their perceived angular orientation about either the pitch or roll axis for 20 sec. before exposure, during the transient and steady-state portions of the acceleration exposure, and for 20 sec. after the acceleration was terminated. Since all of the runs were below the subject's tolerance levels and little or no straining was involved, each subject was able to undergo several runs consecutively. An interval of at least one minute was provided between runs.

The tracking, which employed a cross-model matching method, required the subject to move a control stick in such a manner as to keep its perceived orientation in the upright direction. Thus he would move the stick forward during perceived backward motions and move it backward during perceived forward motions. The control stick was located on the subject's right arm rest and required wrist motion only to move it in either the pitch or roll directions. While tracking, the subject was requested to verbally report the direction of his perceived motion. This information was used to confirm or correct the direction in which he moved his stick. The stick motions were recorded and used as the primary measurement of the subject's sensory response to each particular angular stimulus.

The first series of runs involved the continuous measurement of the subject's perceptual response to pure angular accelerations. In these runs the gondola was controlled in pitch and roll in such a manner as to vector out lateral and transverse accelerations on the subject over the entire G profile. During these runs the subjects were initially instructed to ignore rolling cues and to respond only to perceived angular pitch motions. They subsequently were instructed to ignore pitching cues and to respond only to perceived angular roll motions. The resulting data were then analyzed across subjects and used to formulate the following transfer functions which describe human angular perceptual response about the pitch and roll axes to angular accelerations in the presence of a coordinated G field.

$$\theta'_{ap} = \beta \frac{12.48S}{S^2 + 15.0S + 50.0} \quad (1)$$

$$\phi'_{ap} = \alpha \frac{12.48S}{S^2 + 12.5S + 25.0} \quad (2)$$

$$\theta_{ap} = \frac{\theta'_{ap}}{G^1} \quad (3)$$

$$\phi_{ap} = \frac{\phi'_{ap}}{G^1} \quad (4)$$

where

$\theta'_{ap}$  and  $\phi'_{ap}$  represent the perceived angular responses to angular displacements,  $\beta$  and  $\alpha$ , about the pitch and roll axes respectively, in a constant but coordinated 1 g field, and  $\theta_{ap}$  and

$\phi_{ap}$  represent the same responses in a varying but coordinated G field.  $G^1$  represents the magnitude of the varying G field delayed by approximately 1 sec. The simulated responses to angular displacements  $\beta$  and  $\alpha$  are shown in figures 4 and 5, respectively.

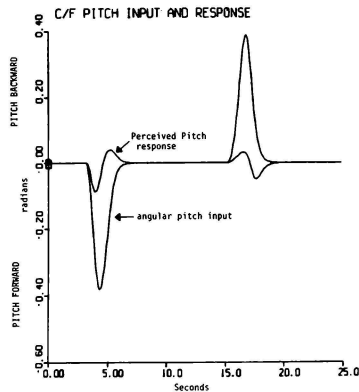


Fig. 4. Simulated Perceived Angular Response to Angular Displacements about the Pitch Axis in a Varying but Coordinated G Field.

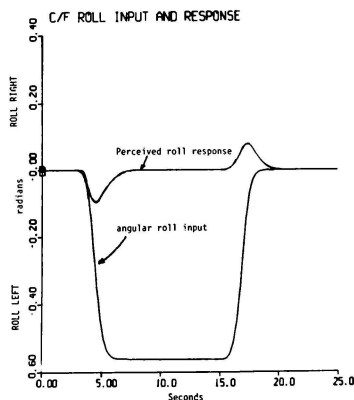


Fig. 5. Simulated Perceived Angular Response to Angular Displacement about the Roll Axis in a Varying but Coordinated G Field.

During the second series of runs, continuous measurements were made of the subject's perceived angular response to pure rotations of the linear acceleration vector. The vector rotations were provided by blanking the control signals to the inner gimbal over the entire G profile. The resulting data were then analyzed across subjects and used to formulate the following transfer functions, which describe the human angular perceptual response to rotating linear acceleration vectors about the pitch and roll axes.

$$\text{evp} = \text{ev} \frac{2.66S + 2.0}{S^2 + 10.2S + 2.0} \quad (5)$$

$$\text{dpv} = \text{dv} \frac{6.66S + 5.0}{S^2 + 10.5S + 5.0} \quad (6)$$

$$\text{ev} = \text{Sin}^{-1} \frac{G_x}{G} \quad (7)$$

$$\text{dv} = \text{Tan}^{-1} \frac{G_y}{G_z} \quad (8)$$

where

evp and dpv represent the perceived angular responses to rotating linear acceleration vectors which rotate through the angles ev and dv about the pitch and roll axes, respectively. The simulated response to a given vector rotation about the pitch axis is shown in Figure 6.

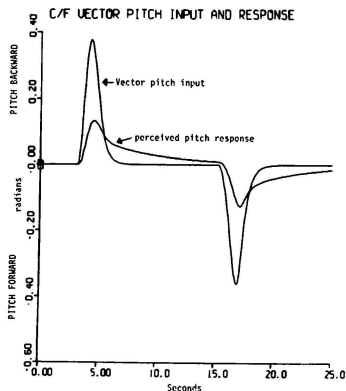


Fig. 6. Simulated Perceived Angular Response to Vector Rotation about the Pitch Axis in a Varying G Field.

While equations (1) and (2) may be considered as representing transfer functions of the semi-circular canals, equations (5) and (6) are probably not purely vestibular or otolithic alone, but include many tactile/kinesthetic cues as well. This is acceptable in this case, because the environment in which the functions are to be

applied is the same environment in which the functions were derived.

It is of interest to note that the transfer functions,  $\text{evp}$  and  $\text{dpv}$ , describe a rate function response to the angular displacement commands,  $\delta$  and  $\alpha$ , respectively. The transfer functions,  $\text{evp}$  and  $\text{dpv}$ , on the other hand, describe a delayed proportional function response to the vector angular displacement commands. This difference in the shape and timing of the two types of angular response functions is extremely critical when they are subsequently added, as in equations (9) and (10) below, to describe human perceptual angular response to combined component stimuli.

The final series of runs involved the measurement of the subject's sensory response to various sizes and shapes of combined angular stimuli. For the pitch axis, this effect was obtained by programming the inner gimbal drive signal to lead or lag, in 0.5-sec. steps, the drive signal which would produce vector coordination in the previously described G profiles. Additional shaped stimuli were obtained by repeating this sequence with the gimbal drive signal attenuated by 50 percent. Similarly, for the roll axis, the effect was obtained by programming the outer gimbal drive signal to lead or lag, in 0.5-sec. steps, the drive signal which would produce vector coordination in the same G profiles. The subject's measured sensory responses were then compared with the predicted responses obtained by adding the scaled individual responses of each component stimulus. In this respect the following equations apply:

$$\text{ep} = \frac{\alpha' \text{dp}}{G} + \text{evp} = \text{eap} + \text{evp} \quad (9)$$

$$\text{dp} = \frac{\phi' \text{ap}}{G} + \text{dpv} = \text{dap} + \text{dpv} \quad (10)$$

where  $\text{ep}$  and  $\text{dp}$  represent the subject's perceived angular response about the pitch and roll axes to combined component angular stimuli.

Figure 7 shows a typical record which provides remarkable evidence that the stimuli are indeed additive. Here the control of the inner gimbal is purposely delayed from that required to follow the rotating resultant G vector. This results in the gondola subject being initially stimulated by a backward vector rotation followed by a forward angular rotation. As seen in the bottom two recordings, the subject's measured angular response to these combined stimuli matched the predicted angular response obtained by adding the predicted response to each component stimulus.

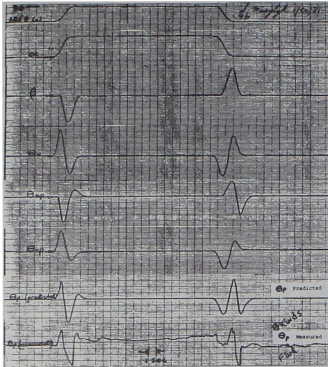


Fig. 7. Typical Data Record Showing Subject's Predicted and Measured Angular Response to Combined Stimuli about the Pitch Axis.

Further evidence is provided by figures 8 and 9 which show the predicted response in solid lines and the average subject's response in dashed lines to combined stimuli of various shapes generated during the transient on-set and off-set periods of a 2 or 3 G profile. It is interesting to note that most of the changes in the combined stimuli were due to changes in the rotating linear acceleration vector since little, if any, changes occurred in the angular acceleration. While little is mentioned in this paper concerning the measurement and comparison of roll axis data, similar results were obtained.

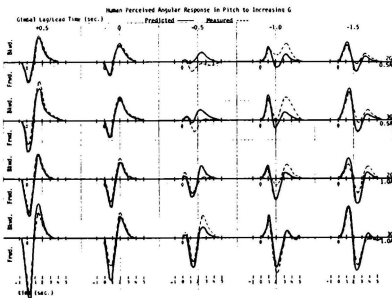


Fig. 8 Human Perceived Angular Response in Pitch to Combined Stimuli during G On-set. Predicted \_\_\_\_\_; Measured -----.

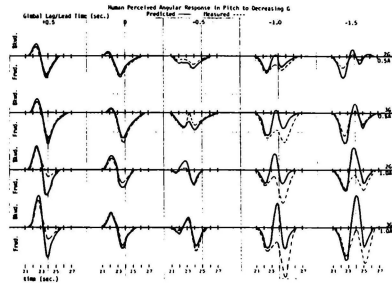


Fig. 9. Human Perceived Angular Response in Pitch to Combined Stimuli during G Off-set. Predicted \_\_\_\_\_; Measured -----.

#### IV. Proposed Control Algorithm - Defined and Simulated

The NAVAIRDEVCON human centrifuge has an enclosed 10-ft. spherical gondola, mounted in a controllable two-gimbal system at the end of a 50-ft.-long main arm. The gimbal system (figure 10) consists of an outer gimbal which rotates about a horizontal axis perpendicular to the centrifuge arm, and an inner gimbal which rotates about an axis in the plane of the outer gimbal and perpendicular to its axis. The two gimbal drive motors, along with the main centrifuge drive motor, are all independently controlled, thus providing three degrees-of-freedom in the programming and operation of the centrifuge. These are normally used to control the three linear accelerations,  $G_x$ ,  $G_y$ , and  $G_z$ , on a centrifuge subject.<sup>9</sup>

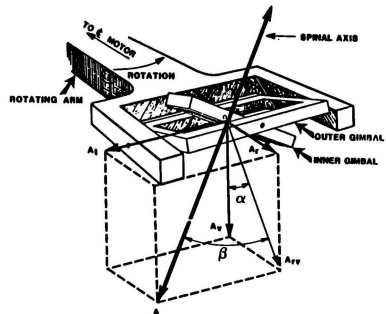


Fig. 10. Centrifuge Gimbal Construction and Acceleration Parameters.

The limited three degrees of freedom of the DFS are obviously insufficient to permit objective fidelity with the six degrees-of-freedom (three linear and three angular) of a simulated aircraft. Therefore, as with all simulators, efforts had to be directed toward achieving perceived motion fidelity. For the DFS, this required that a control algorithm be developed which, in response to simulator pilot control inputs, programs the two gimbals to move in sufficient harmony with the centrifuge arm as to provide an acceptable degree of perceived angular motions to the pilot with little or no significant sacrifice in the required linear accelerations imposed on him.

The basic scheme for developing this new control algorithm was formulated when it became evident that the two component stimuli of angular accelerations and rotating linear acceleration vectors were additive. The implications of this remarkable finding supports the concept that one component stimulus could be programmed to counter influence the pilot's perception of the other component stimulus. Thus, by delaying and attenuating the gimbal drive command signals derived by the G force control algorithm during periods of G transition, the resultant linear acceleration vector through the pilot would rotate in a direction opposite to that of the gimbal rotation and mask the pilot's perception of either rotation. The previously derived human response transfer functions proved to be an invaluable tool in deriving the proper gimbal drive commands signals to achieve this neutralizing effect. This effect was eventually obtained and verified during a series of centrifuge tests in which the subjects indicated by their tracking and their verbal reports that there perception of angular motions during periods of G transition was substantially reduced.

The transfer functions were further utilized to define and quantify the specific aircraft angular parameters which should be added to these modified gimbal command signals to minimize any difference between the projected DFS pilot's perceived angular response and the projected aircraft pilot's perceived angular response.

Following the direction described above, and referring to figure 10, the following new centrifuge control algorithm was derived:

$$\dot{\omega} = \frac{1}{R} \sqrt{G^2 - 1 - R^2 \omega^4} \quad (11)$$

$$\omega = \int \dot{\omega} dt \quad (12)$$

$$\alpha = \sin^{-1} \frac{G_y}{G_{rv}} - \left( \tan^{-1} Gr \right) \left( \frac{1.0}{0.2S + 1} \right) + .4 \int \dot{\rho} dt \quad (13)$$

$$\beta = \tan^{-1} \frac{G_x}{G_y} + \left( \sin^{-1} \frac{G_z}{G_{xz}} \right) \left( \frac{0.5}{0.8S + 1} \right) + .5 \dot{q} \quad (14)$$

where

$$G_{rv} = \sqrt{G_r^2 + 1}; G_{xz} = \sqrt{G_x^2 + G_z^2} \quad (15)$$

$$G_z = G_t \cos \beta + G_r \sin \alpha \sin \beta - \cos \alpha \sin \beta \quad (16)$$

$$G_y = G_r \cos \alpha + \sin \alpha \quad (17)$$

$$G = G_t \sin \beta - G_r \sin \alpha \cos \beta + \cos \alpha \cos \beta \quad (18)$$

$$G = \sqrt{G_x^2 + G_y^2 + G_z^2} \quad (19)$$

$$G = \sqrt{G_r^2 + G_t^2} + 1 \quad (20)$$

The major difference between this control algorithm and the previous G force control algorithm is the addition of the terms shown under the brackets in equations (13) and (14). The terms under the first bracket essentially place a delay in the control signal to each gimbal drive system and a 0.5 attenuation in the inner gimbal signal. The terms under the second bracket provide angular motion commands of the simulated aircraft.

The potential benefits of these changes were observed in a second centrifuge study in which projected DFS pilot perceived angular responses were compared with projected aircraft pilot perceived angular responses for identical aircraft control inputs using first the previous G force control algorithm and then the new proposed control algorithm. These control inputs are open loop computer generated and do not require active pilot participation. Block diagrams depicting the method used for projecting and comparing these angular responses and the human angular sensing models are shown in figures 11 and 12 respectively. The control inputs were such as to cause the simulated aircraft to roll to the left and pull a 3.0 G turn within 2 sec., hold for 5 or 10 sec., and then return to straight and level flight in 2 sec.

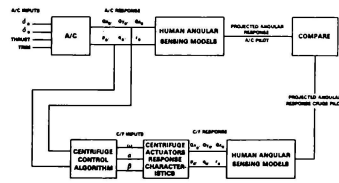


Fig. 11. Diagram Depicting Method for Using Human Angular Response Models in Comparing Motion Perception of Simulation Pilot vs. Aircraft Pilot.

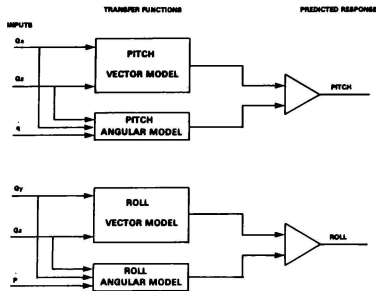


Fig. 12. Block Diagrams of Human Angular Sensing Models.

Figure 13a shows the projected aircraft pilot's responses in dashed lines and centrifuge pilot's responses in solid lines, superimposed for comparison, using the previous G force control algorithm. Note the large reversals in the centrifuge pilot's response during the G on-set and off-set periods which were principally responsible for much of the pilot induced oscillations (PIO's) experienced in many of the previous DFS programs. These results are in contrast to the remarkable similarity between the perceived responses of the centrifuge pilot and the aircraft pilot, about their pitch axes as shown in figure 13b, when the new centrifuge control algorithm is used. In comparing the predicted roll responses for the previous G force control algorithm, figure 14a, the centrifuge pilot's response is observed to be in the same direction as the aircraft pilot's response, but significantly out of phase with it. Again the new control algorithm, as seen in figure 14b, is able to bring close agreement between the two responses.

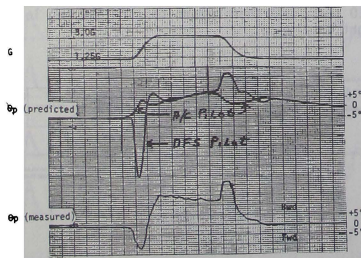


Fig 13a. DFS Controlled by G-Force Control Algorithm.

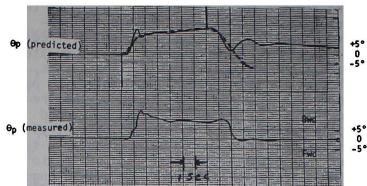


Fig. 13b. DFS Controlled by New Centrifuge Control Algorithm.

Fig. 13. Angular Response in Pitch of DFS Pilot vs. A/C Pilot during a Bank Left G Maneuver.  
DFS Pilot \_\_\_\_\_; A/C Pilot -----.

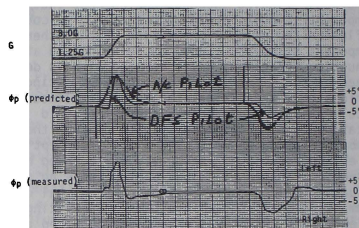


Fig. 14a. DFS Controlled by G Force Control Algorithm.

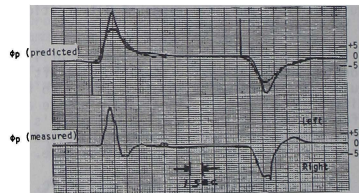


Fig. 14b. DFS Controlled by New Centrifuge Control Algorithm.

Fig. 14. Angular Response in Roll of DFS Pilot vs. A/C Pilot during a Bank Left G Maneuver.  
DFS Pilot \_\_\_\_\_; A/C Pilot -----.

Perhaps an even more dramatic benefit of the new control algorithm is obtained when the simulated aircraft is controlled to roll right in a similar G profile. For the previous G force control algorithm the difference was an outright reversal between the centrifuge pilot's sensory response in roll and the aircraft pilot's as shown in figure 15a. This is to be expected since the centrifuge pilot is rolled to his left by the outer gimbal during G on-set. For the new control algorithm, the sensory responses between the two pilots, figure 15b, were as close as they were when the aircraft roll was made to the left.

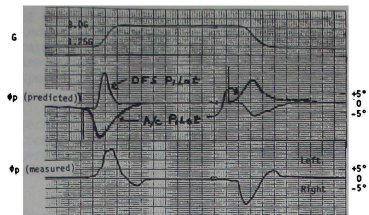


Fig. 15a. DFS Controlled by G Force Control Algorithm.

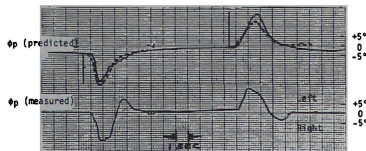


Fig. 15b. DFS Controlled by New Centrifuge Control Algorithm.

Fig. 15. Angular Response in Roll of DFS Pilot vs. A/C Pilot during a Bank Right G Maneuver.  
DFS Pilot \_\_\_\_\_; A/C Pilot ----.

Figures 13 through 15 provide further evidence of the accuracy with which the transfer functions are able to predict the centrifuge pilot's perceived angular response to the combined component angular stimuli of angular accelerations and rotating linear acceleration vectors. This accuracy is determined by comparing the measured angular responses at the bottom of each chart with the predicted centrifuge pilot's responses about the pitch and roll axes for each of the many conditions included in these tests.

Admittedly, more data are required, using a greater variety of subjects over a wider range of conditions, before the given transfer functions should be accepted as final. The method of reducing the effect of the angular acceleration in the presence of a large G field by dividing it by the delayed value of the G itself is probably an oversimplification. Other investigators have indicated that the linear acceleration vector acts to stabilize the angular response. Benson et al reported a considerably more rapid decay of post rotational nystagmus when a linear acceleration vector is introduced in the plane of the corresponding semicircular canal.<sup>10</sup> Also during this study, several responses were observed which indicated that the subjects, on occasion, did respond to one or another of the stimuli individually. Nevertheless, sufficient evidence has been accumulated during these and other experiments to warrant the application of the derived human response transfer functions in the initial development of control algorithms for all motion base platforms. This application can occur either prior to placing the simulator pilot in the control loop or, after placing the pilot in the control loop, prior to mounting the pilot

and the simulator on the motion base. Final tuning of the algorithms, however, must await analysis of the simulator pilot's response to his own control inputs, with all systems in full operation, including the visual systems.

## V. References

1. Crosbie, R. J., and Eyth, J., Jr., "A Total G-Force Environment Dynamic Flight Simulator," Paper presented at AIAA Aerospace Sciences Meeting, Reno, NV, 10-13 January 1983.
2. Eney, J. A., "Moving Base Simulation of the F-14 Stall/Spin," NADC-73085-30, 6 June 1973.
3. Fortenbaugh, R., "Assessment and Control of the Undesired Components of Human Centrifuge Acceleration Response to a Single Axis Command," NADC-AM-6923, 12 June 1969.
4. AGARD Advisory Report No. 159, "Fidelity of Simulation for Pilot Training," (AGARD 1980), 17.
5. Puig, J. A., "Sensory Interaction of Visual and Motion Cues," Naval Air Training Center Commemorative Technical Journal, November 1977.
6. Cohen, M. M., "Elevator Illusion: Influences of Otolith Organ Activity and Neck Proprioception," Perception and Psychophysics, 11, 1972, 433-436.
7. Cohen, M. M., Crosbie, R. J., and Blackburn, L. H., "Disorienting Effects of Aircraft Catapult Launchings," Journal of Aerospace Medicine, 44(1), January 1973, 37-39.
8. Cohen, M. M., "Human Performance During Exposure to Combined Linear and Angular Accelerations," NASA Contract MPRT-8477C.
9. Crosbie, R. J., "Directional Control of Accelerative Forces in Centrifuge by System of Gimbals," Journal of Aviation Medicine, December 1956, 27, 505-511.
10. Benson, A. J., et al, "Interaction of Linear and Angular Accelerations on Vestibular Receptors in Man," Journal of Aerospace Medicine, February 1966, 144-154.



## DESIGN OF A REAL-TIME CGSI SYSTEM

Dorothy M. Baldwin, Physicist  
Advanced Simulation Concepts Division  
Naval Training Equipment Center  
Orlando, Florida

Brian F. Goldiez, Systems Engineer  
U.S. Army Project Manager for Training Devices  
Orlando, Florida

Carl P. Graf, Sr. Principal Research Scientist  
Honeywell Systems and Research Center  
Minneapolis, Minnesota

Abstract

A hybrid system, CGSI, is being developed which will merge the attributes of video disc technology and Computer Generated Imagery (CGI). Initial non-real time feasibility has been demonstrated and reported on. Detailed design of a limited real-time system is being conducted. The basic design is modular with a parallel pipeline architecture. This real-time design is the topic of this paper.

IntroductionRequirements and Applications

The rapid development and increased use of sophisticated imaging sensors in conjunction with the real world visual scene have expanded the capabilities of most military systems. Figure 1 illustrates the complexity of the simulation problems for: a) the Navy's F/A-18 cockpit, and b) a scene taken from the window of an Army helicopter flying nap of the earth (NOE). The new capabilities require simulations to evaluate and verify system operations before production, to train the

operators before assignment and to maintain proficiency. This simulation and training is more difficult and important because: the information content of imaging sensors is high, the data is now novel to the observer, and the operator workload is very high. Testing and training with the actual equipment in the real environment is valuable. However, high equipment cost, high maintenance cost, availability of fuel, risk factors, and lack of suitable conflict scenarios reduces test and training efficiency. The great challenge of simulation today is the simulation of high fidelity multiband imagery sensor correlated with the out-the-window simulated visual scene.

Hybrid system concepts such as Computer Generated Synthesized Imagery (CGSI) offer near-term solution for simulating sophisticated sensors and correlated visual-sensor imagery. Because of the high potential payoff from the real-time implementation of CGSI, NAVTRAEQUIPCEN, with support from FM TRADE, funded Honeywell's Systems and Research Center in 1981 to provide a non-real time demonstration of CGSI for a NOE flight and a preliminary design for real-time implementation



(a) Reprinted from Naval Aviation News,  
Nov. 1982



(b) Helicopter NOE flight, view out the window.

Fig. 1 Simulation Complexities

of GSGI.<sup>1, 2</sup> In addition to displaying individual objects in a scene, the system is capable of displaying groups of objects, imagery as seen from various sensors and adding special effects.

The system design is modular with a parallel pipeline architecture to allow one to configure a system with as many object generators or pipelines as necessary to provide adequate scene detail.

Although the initial non real-time feasibility has been demonstrated, additional work is necessary and being pursued to provide a real-time capability (i.e., a minimum update rate of 30 Hz). This work is currently funded by NAVTRABQUIPCEN and PM TRADE with some support from the Air Force Human Resource Laboratory. Detail design of a limited system is being conducted with completion in April 1983. Fabrication of a single pipeline will be completed in August 1983. GSGI pipeline processors will be interfaced to NAVTRABQUIPCEN's Visual Technology Research Simulator (VTRS) facility in 1984 for evaluating GSGI concepts and for demonstrating simulation of coordinated multisensor displays (visual and FLIR).

The GSGI system is a candidate for a competitive flyoff for next generation visual technology for the AH-64 simulator. The U.S. Army visual requirements encompass weapons effects and delivery, wide field of view displays to support nap-of-the-earth flight, multiple viewpoints, multiple sensors and multiple magnifications through a telescoping system. These requirements are felt to be one of the most demanding in the simulation industry today. The Honeywell GSGI system could provide a capability to meet these requirements. The GSGI system has potential application for providing air-to-ground capability in the Navy's F/A-18 Hornet fighter/attack aircraft simulators and for filling nap-of-the-earth training requirements on the CH-53 D/E and CH-46 helicopter simulators. One of the extremely attractive features of this approach is the potential for utilizing GSGI to retrofit existing GGI systems and enhance the scene content. The Air Force's interest in this development results from the need for high fidelity simulation for air-to-ground attack missions.

#### GSGI Background

The strength of Computer Generated Imagery (CGI) is its ability to generate surface representations. A real or artificial surface can be measured to get elevations at specified points, usually at intersections of a uniform grid. The scene can be constructed in a computer by connecting the sample elevations and placement of objects (trees, rocks, shrubs, houses, roads, etc.). The weakness of CGI is

the lack of fidelity and detail; the objects appear cartoonish.

Computer Synthesized Imagery (CGI) uses high fidelity photographs of real scenes. The objects in the scenes are not represented individually; nor is the scene modeled by elevation profiles. Usually the scene is held static, while single objects, like aircraft or tanks, move within the scene. The high-fidelity CGI scenes are limited to the viewpoint of the camera. That is, one cannot drive through a scene unless a series of through-the-scene photographs is used.

Computer Generated Synthesized Imagery (GSGI) combines the best features of both technologies: CGI and GGI. A scene is constructed by placing individual high-fidelity CGI objects on a specified GGI surface. A GSGI scene is constructed much like a GGI scene. The surface elevations and object locations are laid out on a uniform grid. The individual objects used in the scene are transformed for perspective and size. This includes size, position, rotation, warp, and intensity transformations on the image. The surface may be a GGI texture or a series of CGI surface inserts. The GSGI scene may be constructed with imagery from any portion of the spectrum—visual, infrared, millimeter, or radar frequencies.

#### GSGI System Overview

Figure 2 is a functional overview of a real-time GSGI system.

- o **Data Base Construction.** The data base consists of two very different types of data: the object library and the gaming area. The object library contains images of objects and surfaces, and transmissivity masks of special effects from one to many bands of the spectrum. This allows the simulation of various sensors. The gaming area data base provides the information necessary for placing the contents of the object library, objects, surfaces, and special effects on a grid or gaming area. The objects in the library may be either stationary or capable of movement.
- o **Vehicle Simulation Computations.** The vehicle simulation computations, based upon the vehicle math model and control inputs, determines the locations and viewing direction of the visual or sensor system for the primary vehicle.
- o **Systems Interface.** The I/O of the vehicle simulation system and I/O of the GSGI system must interface in an efficient manner.



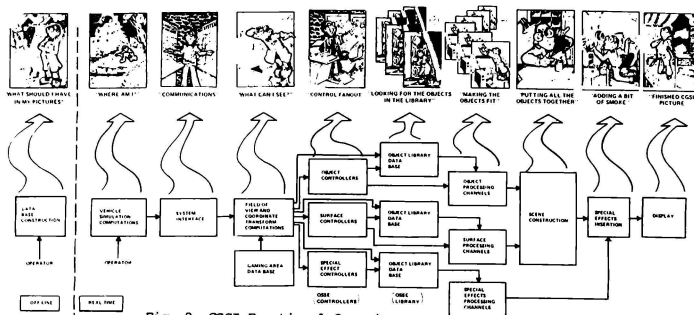


Fig. 2. GSSI Functional Overview.

- **Field of View (FOV) and Coordinate Transform Computations (OSSE).** The FOV processor determines the presence of objects, surfaces, and special effects in the scene under construction. The output of a transformation matrix (V) converts the real-world coordinates to screen coordinates.
- **Object/Surface/Special Effects Controllers.** The controllers fan out and process the control functions generated during the FOV computation. The processed control functions are passed to the object/surface/special effects processing channels.
- **Object/Surface/Special Effects Library.** The library stores the images used to construct a scene. The controllers command the selected images which are passed to the processing channels.
- **Object/Surface/Special Effects Processing Channels.** The individual processing

channel pipelines process one object, surface or special effect per channel. All the processing channels operate in an identical manner: large object, small object, surface or special effect. That is, the object, surface, special effect processing channels change a stored image (normal perspective) to scene conditions (screen coordinates) by changing image, position, size, rotation and warp. Image intensity is modified based upon range and object type.

- **Scene Construction.** The scene construction module takes the individual image from each processing channel, separates the image from the background, and assembles the scene based upon range. The high frequency edges generated by assembling a scene from individual images are smoothed matching edge and internal frequencies.
- **Special Effects.** Special effects are added after the generation of the scene based upon range.

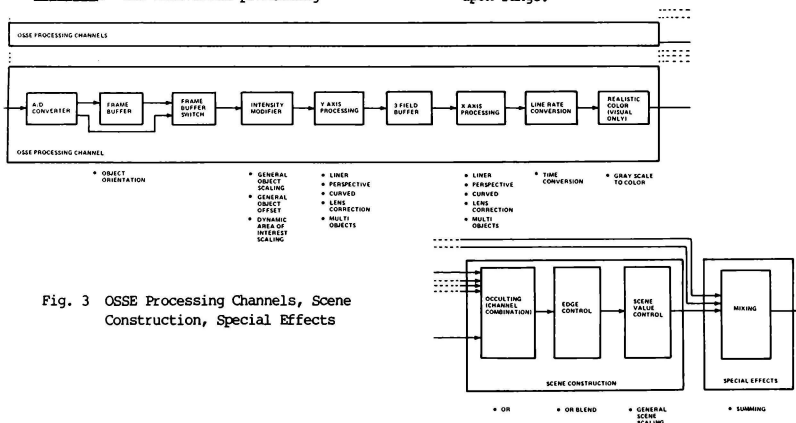


Fig. 3 OSSE Processing Channels, Scene Construction, Special Effects

### CGSI Real-Time Functional Overview

The preceding sections presented a CGSI introductory overview. This section examines the detailed functions available in CGSI simulations. Figure 3 is an expansion of the OSSE Processing Channels, Scene Construction and Special Effects shown in Figure 2. The remaining parts of Figure 2, not shown in Figure 3, either provide control functions or data storage functions which do not modify the image. It is the intent of this design to allow the system to produce any type of imagery; i.e., visual, IR, MMW, SAR, radar, etc.

### OSSE Processing Channels

The OSSE processing channels prepare each object, surface or special effect (OSSE) for insertion in the scene as the scene is constructed on a pixel-by-pixel basis. Systems under consideration contain from four to more than one hundred OSSE channels. Some systems may require all of the capabilities reviewed and others may require only a selected number.

**A/D Conversion.** A high speed A/D module converts the analog video imagery to digital data. The module operates near 10 MHz and provides 8-bit, or 256 gray-shade, output.

**Frame Buffer.** The frame buffer is used to store images that are not changing. This includes small 2D objects, surfaces and special effects. The warping process may compress data if the image is rotated beyond 50 or 60 degrees. By using a high speed memory design with access in both the X and Y axis, one image may be rotated a full 360 degrees.

**Frame Buffer Switch.** The frame buffer switch allows the imagery to be held in the frame buffer for repeated use of 2D objects, surfaces and special effects. After an OSSE is stored in the frame buffer, the optical disc may supply imagery to other channels. For dynamic 3D objects, the frame buffer switch allows the imagery to be taken directly from the optical disc without any delays. The frame buffer switch is controlled by the OSSE controller.

**Intensity Modifier.** The intensity modifiers modify the intensity of a scene in both global and local manners. Global changes use a look up table (LUT) and provide the following:

- o **General Object Scaling.** This changes the slope of the gray scale. The change may be linear or non linear.
- o **General Object Offset.** This raises or lowers the general intensity of the object. As an example, these changes may be associated with ranges. That is,

an object at a great distance is more saturated, bluer and darker than the same object at a very short range. Local modifiers change just part of any object by using multiplier modifiers in a real time basis.

- o **Dynamic Area of Interest Scaling.** This changes each pixel by a slightly different value to obtain a slope or gradient. As an example, an object may be modified to represent the sun shining on the side of a tree as shown in Figure 4.

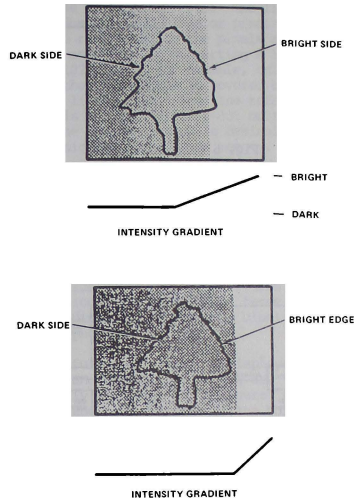


Fig. 4 Intensity Gradient.

**Y Axis Processing.** The algorithm for distorting an object operates in two passes as shown in Figure 5. Before explaining the Y axis functions, an overview of the warping function is presented. The warping algorithm contained in the pipeline operates in two passes; first the Y axis and then the X axis. Figure 6 shows the warp function components. The field microprocessor determines the offset (starting location), the magnification (change of line length) of the first line in each axis and selects the field memory buffers. The line microprocessor determines the delta (Δ) offset and delta (Δ) magnification of each line.

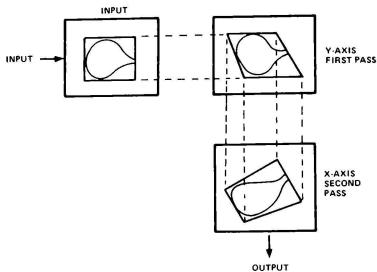


Fig. 5 Warp Processing.

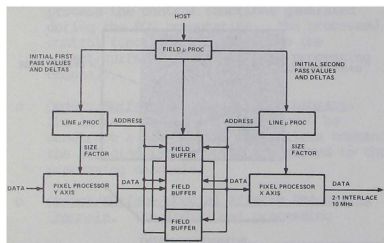


Fig. 6 Warp Function.

The field microprocessor operates in a 16 millisecond cycle and the line microprocessor in a 63 microsecond cycle. The pixel processors operate on the pixel streams in a 100 nanosecond cycle or 10 MHz.

During the first pass of the Y axis, each line in the row may be distorted in one or more of the following manners (Figure 7):

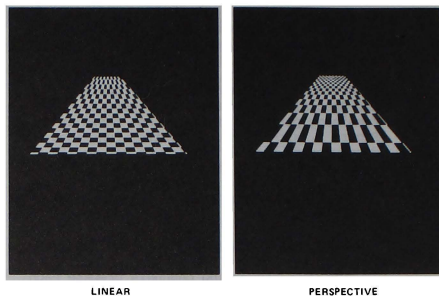


Fig. 7 Runway Applications.

- o **Linear.** The pixels in the image in the Y axis are scaled in a linear manner by using an offset and magnification. The offset is a constant for the entire frame and the magnification is constant for each line. This approach makes a long runway curve up at both ends. See Figure 7a.
- o **Perspective.** The pixels are scaled in a nonlinear manner. Each offset and magnification is different due to the nonlinear range variable. This approach keeps the internal detail of a flat surface in correct perspective. The runway does not curl up at the ends. See Figure 7b.
- o **Curved.** A hemisphere may be distorted to appear flat (a common technique used in map making). By using nonlinear offsets and magnification, the distorted flat surface may be restored to sphere from any desired view angle. The tank turret shown in Figure 8 is an excellent example.

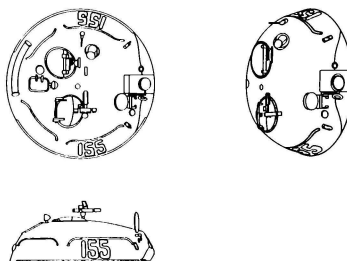
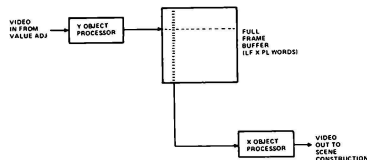


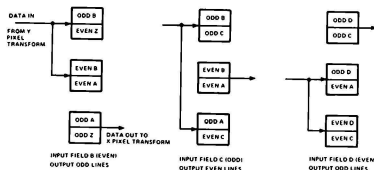
Fig. 8 Tank Turret.

- o **Lens Correction.** Lens and spherical projection surfaces may require distortion corrections. Major distortion corrections may be made at the offset level and minor corrections made at the magnification level.
- o **Multi-Objects.** Most scenes contain many small objects and only a few large objects. To obtain maximum use of a pipeline, many small objects (4, 9, 16, 25) may be processed rather than one large object. This is achieved by changing the offset and magnification factors each time a new object is encountered in a line which would require a perspective warp algorithm.

**Three Field Buffer.** The three field buffer allows the Y axis processed image to be read into two field buffers, one for odd pixels and the second for even pixels. The third field buffer allows either odd or even fields to be processed in the X axis processor. This configuration is shown in Figure 9.



(a) Conceptual Frame Buffer



(b) Data Flow in Frame Buffer.

Fig. 9 Three-Field Buffer.

**X Axis Processing.** The techniques used in the X axis can be identical to those used in the Y axis which includes the following functions:

- o Linear
- o Perspective
- o Curved
- o Lens Correction
- o Multi-Objects

In addition, for potential applications where perspective distortions in the real world are not identical to the X and Y axis, the X axis processing could use algorithms which differ from the algorithms used in the Y axis. This case could occur with dome projection display systems or Synthetic Aperture Radar (SAR) imaging systems.

**Line Rate Converter (LRC).** Various applications require different line ratios. The standard pipeline operates at 525 video lines. The line rate converter changes the line rate of 525 lines to 875 or 1024 lines by changing the pixel clock rate. The line rate converter does not add lines or pixels; it only changes the rate at which the pixels are clocked in and out. In converting a 525 line system to 1024 lines, for example, only one fourth of the 1024 system is covered by a single 525 line output. The line rate converter is a first-in/first-out buffer (FIFO). The implementation is basically that of a very high speed two-part memory. Object image data is written into the memory in the 512 x 512 format at a 10 MHz pixel rate. At the same time, scene image data is read from the memory in the 1024 x 1024 (or 875 x 875) format at a maximum 40 MHz pixel rate.

**Realistic Color.** The CGSI approach has been developed to provide monochrome; realistic color; or true color capability. True color is provided through the creation of three spectrally distinct (red, green, blue) for each full color photograph.

When a full color image is displayed, the red, green and blue object images are independently processed and delivered to the red, green and blue channels of the color display system used. One can see that full color is bought for a price: three times as many processing channels are required relative to the number needed to generate a monochromatic version (e.g., IR) of the same object image.

Near perfect color is achievable in a much more economical manner. Most OSSES contain only shades of one or two colors. Consider green leaves and camouflaged targets. To obtain realistic color, each object is stored as a black and white image. Associated with each image is a red, green and blue LUT conversion that assigns up to 256 colors to gray shade levels of the image. The 256 colors that are achievable may be 256 shades of one hue—for example, shades of green to create a high fidelity color image of a bush—or 256 distinct hues.

#### Scene Construction

The scene construction module assembles the individual objects being processed into a single scene (or picture). Near objects

occlude detail objects. Figure 10 demonstrates the warping and assembling of a house in a scene based upon range.

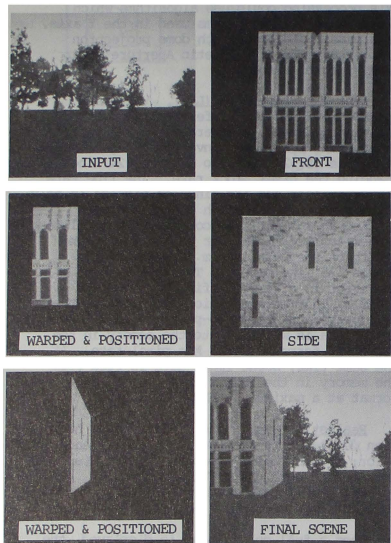


Fig. 10 Construction Scenes.

**Occlusion.** The pipeline combiner or function used on a "binary tree" selection algorithm forms the heart of the scene construction module. Video data from multiple sources (or pipelines) is combined on a pixel by pixel basis. Near pixels occlude more distant pixels. The term "pipeline" is used here to refer to a source of video data. Each of these sources may be expanded to include one or more colors. As shown in Figure 11, the object switch element accepts (objects and surfaces) video data and range information from either the OSSE controller or the previous object switch. The object switch then outputs the selected video pipeline and the appropriate range of that channel.

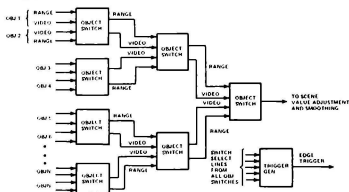


Fig. 11. Object Switch.

**Edge Control.** During the processing, the individual object in the OSSE processor, background pixels at the edge of the object, may become mixed with the object pixels. If the background is dark, a dark halo is formed around the object. This artifact is easily removed by adding a pixel around the perimeter of the object during threshold processing when the OSSE library is being constructed. It is this extra pixel that becomes mixed with the background during OSSE processing. In constructing a scene, in the visual domain, the edge control process uses the mixed pixel to determine the amount of the adjacent object pixel and the amount of the adjacent background pixel used to generate a new mixed pixel. In the IR and other sensor domains, a Gaussian spread function is used across several of the edge pixels to match heat, sensor roll off and other edge effects.

Scene Value Control. The scene value adjustment is used where scene-wide intensity corrections are required. Such corrections may be applied to compensate for day/night lighting, haze and rain. These are typically initial conditions, or very slowly changing conditions.

## Special Effects

These translucent objects (smoke, fog, dust, shadows, haze, etc.) overlay the solid objects. These objects are stored as a mask which defines the outline, shape and transmissivity factor. The mask determines the combining percent of object/special effects. A second variable controls the intensity or color of the special effect object. The warp algorithm is used to distort the special effects and a series of frames are used to generate the motion.

The data (the mask) in the object library determines the percent of background objects present and the percent of special effects present by the following equation:

$$\text{Pixel Value (gray level)} = B + T (S - B)$$

This is shown in Figure 12. A series of special effects are described to demonstrate the capability of the system.

Dynamic Dust/Smoke. A dust/smoke mask defining the outline and transmission factors is generated by an artist based upon picture and mathematical characteristics of the dust/smoke. The top and bottom must be in the same location and have the same width as shown in Figure 13. Next a series of frames ( 480) are generated. Each line is incremented one or more lines in the Y axis when the frames are played back. This produces a continuous circulatory loop. This is shown in Figure 13.

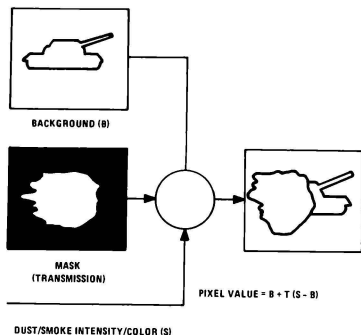


Fig. 12. Dust Smoke Algorithm

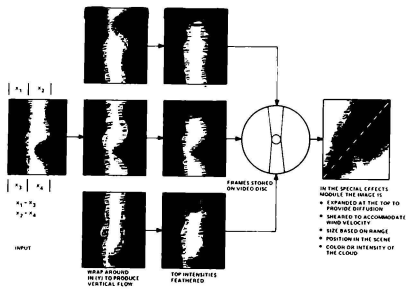


Fig. 13. Dynamic Smoke.

Next, the top of the dust/smoke cloud in each frame is featured to match the dispersant of the smoke in the atmosphere. The frames are stored in sequence on a video disc as shown in Figure 13. The warp algorithm, Figure 13, in the special effects processor is used to:

- o Expand the top to simulate diffusion
- o Shear the image to accommodate wind velocity
- o Size the cloud based upon range
- o Position the cloud in the scene

An initial condition parameter sets the color or intensity of the cloud. The rate at which the dust/smoke fumes are played back determines the rate of flow.

**Shadows.** Shadows are treated as translucent objects like dust and smoke. The transmission masks for shadows are generated from images in the object library. The transmission mask, a shadow, is created by setting all the pixels in an object to one gray level. The gray level determines the transmission of the shadow. In the gaming area, the four reference points of an object are projected to the surface. The new points on the surface are shadow reference points. The shadow, transmission mask, is warped to fit the scene based upon the shadow's reference points, Figure 14.

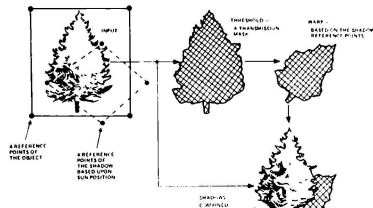


Fig. 14. Shadows.

**Glint and Glare.** Typically, glint and glare are computed from the surface normal data. However, in a CGSI system, unless the objects are developed from CGI nodal data, the normal data is not available. To produce glint and glare, a sector mask is developed based upon the glint and glare bright areas produced by different sun angles, Figure 15. The sectors in the mask are gray level. That is, when stored in the object library, sector 1 may have a luminance value of 8, sector 2 a value of 16, etc. The sun angle table data sets the look up tables in the object processor. If the sun is in sector 2, the input value of 16 in the look up table sets the output glint and glare values to a predetermined level. The remaining output values in the lookup table are zero. The result is a bright spot in sector 2. As the turret moves or the sun moves, the sector changes. In this procedure, dynamic glint and glare is based upon sun and vehicle movement.

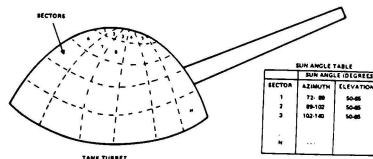


Fig. 15. Glint and Glare.

## Hardware Overview

The high data rates of the video data, 10 MHz, requires special purpose hardware where the flow of imagery is involved. However, the controllers of the special purpose hardware may be an off-the-shelf microprocessor. Figure 16 shows a possible implementation configuration using off-the-shelf components.

simulator (VTRS) facilities in 1984 for evaluating GSSI concepts and for demonstrating simulation of coordinated multisensor displays (visual and FLIR).

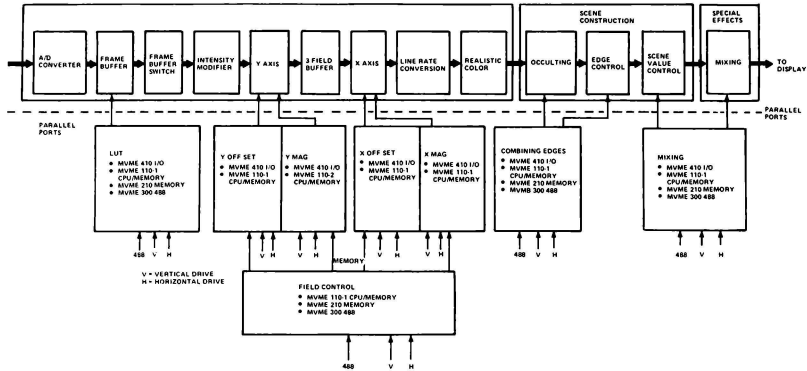


Fig. 16 Possible Control Hardware

## Conclusions

Real time implementation of GSSI offers high potential payoffs in terms of meeting requirements for high fidelity, coordinated sensor simulation. The current program has triservice funding and is on schedule. Fabrication of a single pipeline is scheduled for completion in August 1983. At least two GSSI pipeline processors will be interfaced to NAVTRAEQUIPCEN visual technology research

## References

1. Graf, C., Marvel, O., Fairchild, K., Sedler, M., Sefkow, D. Extend GSSI, Naval Training Equipment Center, Orlando, Florida, 32813, March 1983. (Government Distribution Only)
2. Graf, C., Baldwin, D. Computer Generated/Synthesized Imagery (GSSI), Proceedings of Fourth Interservice/Industry Training Equipment Conference, November 16-18, 1982, pp 549-558.

D. F. Crane\*

NASA Ames Research Center, Moffett Field, California

Abstract

A piloted aircraft can be viewed as a closed-loop, man-machine control system. When a simulator pilot is performing a precision maneuver, a delay in the visual display of aircraft response to pilot-control input decreases the stability of the pilot-aircraft system. The less stable system is more difficult to control precisely. Pilot dynamic response and performance change as the pilot attempts to compensate for the decrease in system stability, and these changes bias the simulation results by influencing the pilot's rating of the handling qualities of the simulated aircraft. Delay compensation, designed to restore pilot-aircraft system stability, was evaluated in several studies which are reported here. The studies range from single-axis, tracking-task experiments (with sufficient subjects and trials to establish statistical significance of the results) to a brief evaluation of compensation of a computer-generated-imagery (CGI) visual display system in a full six-degree-of-freedom simulation. The compensation was effective — improvements in pilot performance and workload or aircraft handling-qualities rating (HQR) were observed. Results from recent aircraft handling-qualities research literature which support the compensation design approach are also reviewed.

Introduction

There is a trend toward the use of computer-generated imagery (CGI) systems to generate flight-simulator visual scenes. CGI visual systems offer important advantages, including large field of view, ease of scene modification, and independent motion of scene elements, for example, combat targets. CGI systems construct an image from a description of the scene stored in a computer. The image construction time, though short (~100 msec), introduces a delay into the pilot-aircraft system. Several authors<sup>1,2</sup> have reported simulation problems traced to time delays in visual-system cueing. The multimillion dollar simulator evaluated by Decker<sup>3</sup> was rated unsatisfactory for training pilots to perform precision flight tasks — at least in part because of CGI delays.

Crane<sup>4</sup> analyzed the pilot-aircraft system as a closed-loop, man-machine control system and documented (for a single-axis tracking task) the change in pilot performance and workload and the change in pilot-aircraft system stability for a range of visual-display delays. Based on this analysis and extrapolating the data from the single aircraft configuration evaluated, Crane concluded that when a simulator pilot was performing a precision maneuver

... a delay in the visual display of aircraft response to pilot control input

has a number of deleterious effects. The immediate effect of the delay is to decrease the stability of the pilot-aircraft system. . . . Simultaneously, pilot dynamic response and system performance change as the pilot attempts to compensate for the decrease in system stability. Most importantly, the changes in pilot dynamic response and system performance can bias the results of the simulation by influencing the pilot's rating of the handling qualities of the simulated aircraft. The decrease in system phase margin ( $\Delta\phi_m$ ) is given by the product of system crossover frequency ( $\omega_c$ ) and display delay ( $t_d$ ), ( $\Delta\phi_m = \omega_c t_d$ ). The importance of a delay increases with the ratio of (the resulting)  $\Delta\phi_m$  to  $\phi_m$ , the design phase margin. Since  $\omega_c$  and  $\phi_m$  are dependent on the specifics of a simulation (aircraft dynamics, display, controller, task, etc.), the importance of a particular delay also depends on the simulation specifics. A given delay will be most troublesome when a pilot is attempting to precisely control a responsive aircraft (high  $\omega_c$ ) and when the design phase margin of the pilot-aircraft system  $\phi_m$  is relatively small.

The predicted variation of aircraft handling-qualities rating (HQR) with delay and bandwidth has been observed in recent studies of the effects of delay in aircraft control systems. Figure 1, reproduced from Ref. 5, summarizes data from several sources. The data exhibit the predicted degradation of HQR with delay and bandwidth. Variation in the design phase margin ( $\phi_m$ ) for the various aircraft configurations evaluated would explain the observed spread in HQR at a given bandwidth, which was also predicted. This relatively large "flight control system delay" data base is relevant here for three reasons. First, visual-display delay and control-system delay are equivalent with regard to their effect on HQR: a simulator pilot, observing aircraft response to control inputs on a visual display, cannot distinguish between the two sources of delay. Second, the data confirm the need for compensation to minimize HQR bias due to display delay, especially when the ratio ( $\Delta\phi_m/\phi_m$ ) approaches unity. Third, the data support the "pilot-aircraft system" analysis of visual display-delay effects. The approach to visual-display delay compensation evaluated here is based on the same analysis.

Ricard and Harris<sup>5,7</sup> reported the results of an evaluation of a number of visual-display delay compensation filters; however, constraints in the filter selection process limit the applicability of those data.<sup>8</sup> The compensation designed using the Optimal Control Model<sup>6</sup> was not experimentally evaluated. Crane<sup>9</sup> applied classical control-system design principles to the pilot-aircraft system to guide selection of compensation for visual-display delay and evaluated the compensation in an experiment wherein pilots performed a single-axis tracking task using an oscilloscope display. This paper

\*Research Scientist.

This paper is declared a work of the U.S. Government and therefore is in the public domain.



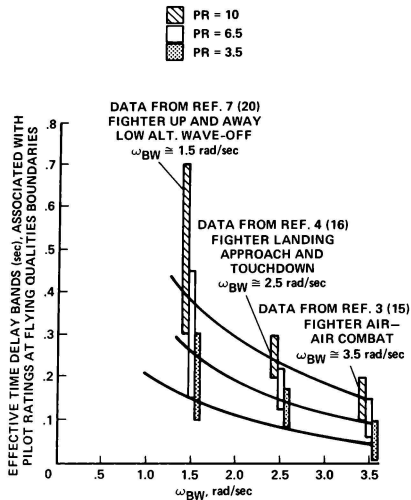


Fig. 1 Time-delay bands associated with flying-qualities boundaries versus bandwidth (from Ref. 5).

reviews 1) the compensation design, experimental design, data, and conclusions from that study and 2) the experimental design and data from recent evaluations of display-delay compensation applied to a CGI visual display system.

#### Control System Delays: Analysis and Compensation

The effects of time delay in closed-loop control systems can be readily determined by conventional control-system design methods. Figure 2a is a block diagram of a simple control system; Fig. 2b is a sketch of the open-loop transfer function of the system. Figure 2b identifies two important system parameters: crossover frequency ( $\omega_c$ ) and phase margin ( $\phi_m$ ). Crossover frequency is that frequency at which the transfer function amplitude ratio "crosses" from greater than unity to less than unity (i.e., crosses the zero decibel line). Crossover frequency is a measure of system bandwidth or responsiveness. Phase margin is defined as the amount by which the system phase angle at  $\omega_c$  exceeds  $-180^\circ$ . Phase margin is a measure of system stability. Figure 2b also illustrates the change in the system open-loop transfer function when a delay is inserted into the system. The delay transfer function  $G_D$  has an amplitude ratio that is identically 1 and a phase given by the expression  $\phi_D = -\omega t_d$  (where  $\omega$  is frequency and  $t_d$  is the delay). The effect of the delay is to decrease the phase margin and stability of the system.

The decrease in system phase margin ( $\Delta\phi_m$ ) is given by the product of system crossover frequency ( $\omega_c$ ) and display delay ( $t_d$ ) ( $\Delta\phi_m = \omega_c t_d$ ). The ratio  $\omega_c t_d / \phi_m$  is here called the Trouble Index

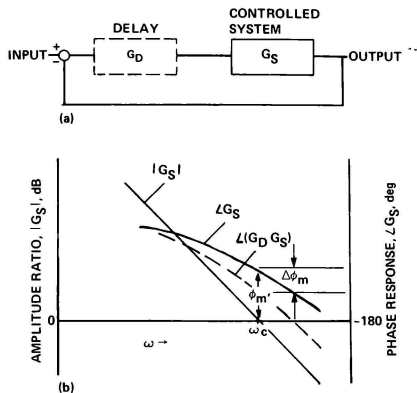


Fig. 2 Closed-loop control system. a) Diagram of simple control system; b) open-loop transfer function.

(TI) because the reduction in system stability due to delay is proportional to the TI. The TI emphasizes the fact that system characteristics ( $\omega_c$ ,  $\phi_m$ ) moderate or exaggerate the importance of a given delay.

Figure 3 shows the amplitude and phase response of the lead filter,  $G_f$ :

$$G_f = K_D(T_n S + 1) / (T_d S + 1) \quad (1)$$

It should be noted that 1) filter phase lead is a function of frequency and filter pole-zero separation; and 2) filter amplitude ratio is a function of frequency - the filter "gain distortion," defined here as the ratio  $|G_f(\omega_p)| / |G_f(\omega_z)|$ , is also proportional to filter pole-zero separation. It is especially important to note that phase lead is purchased at the cost of gain distortion.

When the system transfer function is known, design of a lead filter to compensate for a

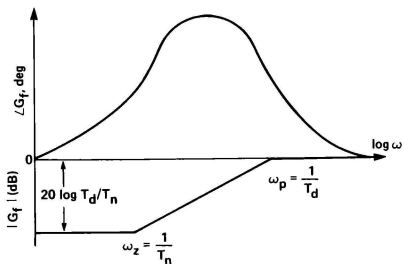


Fig. 3 Lead-filter amplitude and phase response.

specific delay  $t_d$  is straightforward. One need only locate the filter zero at  $\omega_c$  and solve for  $T_d$  from Eq. (2), which equates the filter phase lead ( $\phi_f$ ) at  $\omega_c$  to the delay phase lag at  $\omega_c$ :

$$\phi_f|_{\omega=\omega_c} = \tan^{-1}\omega_c T_n - \tan^{-1}\omega_c T_d = \omega_c t_d \quad (2)$$

Figure 4 illustrates the design.

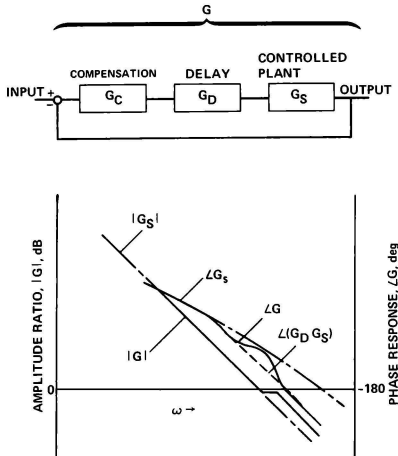


Fig. 4 Delay compensation with a lead filter.

This approach restores system stability while maintaining system accuracy (proportional to system gain) and responsiveness (proportional to  $\omega_c$ ). The resulting increase in system gain at frequencies  $>\omega_c$  is not normally a problem, because system amplitude ratio and input and disturbance signal power usually decrease rapidly at frequencies  $>\omega_c$ . The preceding review of a classical method of control system compensation is strictly applicable to constant-parameter linear systems.

McRuer<sup>10</sup> and others have shown that pilots performing precision tracking tasks can often be modeled as quasi-linear describing functions. This suggests that a modification of the procedure described above may be effective for man-machine control-system compensation. In piloted simulation, some distortion in system amplitude ratio is the price one must pay for the phase lead required to restore system stability. However, the gain distortion must be tailored to minimize change in system responsiveness, tracking accuracy, and pilot workload.<sup>9</sup>

These considerations led to the following design rules:

- 1) Minimize compensation-filter-gain distortion by providing the minimum lead required and by locating the lead at the frequency ( $\omega_c$ ) at which the lead will be most effective in restoring system stability.

- 2) Distribute the attendant system gain distortion (over frequency) so as to minimize gain-distortion effects on system responsiveness ( $\omega_c$ ), pilot workload, and tracking accuracy.

Where a first-order lead filter is used, the filter zero is placed at  $\hat{\omega}_c$ , estimated crossover frequency. The filter time-constant  $T_d$  is computed from Eq. (2) to restore phase margin; the constant  $K_p$  is chosen such that the filter gain at  $\hat{\omega}_c$  is unity. Results of evaluations of this approach to display-delay compensation will be reviewed in the next section.

Recent aircraft handling-quality research again provides data that are relevant here. Many researchers<sup>11-13</sup> have investigated the question "How can one construct a low-order representation of aircraft dynamics equivalent, with regard to HQR, to a more complex high-order representation?" Wood and Hodgkinson<sup>14</sup> examined pilot rating differences between pairs of configurations in previous NT-33 data.<sup>15,16</sup> Each pair of configurations consisted of an unaugmented low-order response and a high-order system formed by adding terms to the low-order response. Wood and Hodgkinson summarized the pilot rating data with envelopes of "maximum unnoticeable added dynamics." Figure 5 is reproduced from Ref. 17, where it was observed that the data show "pilots were most sensitive to changes in the dynamics in the region of crossover."

The display-delay compensation design rules attempt to minimize change in pilot-aircraft dynamics in the region of crossover in order to restore system stability and maintain system responsiveness.<sup>4</sup> The Wood and Hodgkinson<sup>14</sup> data imply that approach is required to minimize bias in HQR due to delay or delay compensation. The TI explains the sensitivity of HQR to change in aircraft dynamics in the region of crossover and further suggests that the Wood envelopes should be considered functions of the system characteristics ( $\omega_c$ ,  $\phi_m^*$ ) of particular aircraft rather than absolute "maximums."

#### Compensation Evaluation Experiments

##### Oscilloscope Display: Single-Axis Tracking Task

The tracking task used in the first experimental evaluation of the proposed compensation is diagrammed in Fig. 6. The pilot's task was to manipulate a side-arm controller to maintain the simulated light, fixed-wing jet aircraft in a wings-level attitude in the presence of turbulence. The subjects were experienced helicopter pilots with recent flight time in military reserve or commercial helicopters. Attitude error (or delayed attitude error or compensated and delayed attitude error) was displayed on an oscilloscope with a 5-in. CRT; no other instruments were used.

There were three experimental conditions: BASELINE, DELAYED, and COMPENSATED: they differed only in the processing of the aircraft attitude

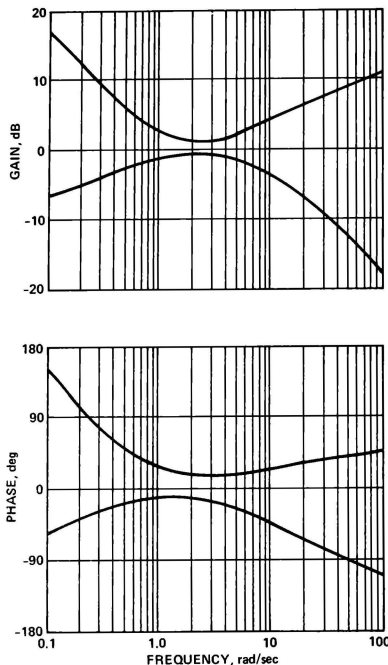


Fig. 5 Envelopes of maximum unnoticeable added dynamics — from Wood and Hodgkinson<sup>14</sup> (reproduced from Ref. 17).

error signal,  $\phi_e$  (Fig. 6). During BASELINE trials, attitude error was displayed on the oscilloscope without further processing ( $G_C = 1$ ,  $G_D = 1$ ). During DELAYED trials, the attitude error signal was delayed 0.108 sec before being displayed. During COMPENSATED trials, the attitude error signal was filtered in accordance with Eq. (1) and then delayed 0.108 sec before being displayed. The data from this experiment are unique because the negligible delay of the oscilloscope display made possible acquisition of "no delay," BASELINE, data.

The pilot describing function was computed using the program described by Shirachi and

Shirley.<sup>18</sup> The program computes the pilot's average (over the trial) amplitude and phase response at each disturbance frequency. The pilot-aircraft open-loop transfer function was computed from the following:

$$G = G_C G_D G_P G_A \quad (3)$$

where

$$G_C = \begin{cases} 1 & \text{Condition B,D} \\ 0.85 (0.555S + 1) / (0.372S + 1) & \text{Condition C} \end{cases}$$

$$G_D = \begin{cases} 1 & \text{Condition B} \\ \exp(-0.108S) & \text{Condition C,D} \end{cases}$$

$G_P$  = pilot-describing function (measured)

$G_A$  = aircraft transfer function

$S$  = Laplace transform operator

Crossover frequency and phase margin were estimated by interpolating the open-loop transfer function data. Compensation parameters were based on crossover frequency estimates from preliminary BASELINE trials. The attitude error signal ( $\phi_e$ , Fig. 6) was squared and integrated over each trial as a measure, integral-squared error (ISE), of pilot performance. Average (over trials) integral-squared error (ISE) is plotted versus experimental condition in Fig. 7. When averaged over pilots, ISE was 38% larger for the DELAYED condition than for the BASELINE condition. The average increase in ISE was reduced to 19% for the compensated condition.

Pilot phase response summed over the six disturbance frequencies and averaged over trials is plotted versus experimental condition in Fig. 8. The average (over pilots) decrease in lag (increase in lead) between the BASELINE and DELAYED conditions was 28°. The increase in pilot lead is an indication of an increase in pilot workload,<sup>19</sup> which would bias the results of a simulation by influencing the pilot's rating of the handling qualities of the simulated aircraft. The average increase in lead was reduced to 9° for the COMPENSATED condition. Complete details of the experiment and additional experimental data were reported in Ref. 9, which concluded that

1) The compensation was effective. When using the compensated display, measures of pilot performance and workload approached "no-delay" values.

2) Pilot-to-pilot differences in dynamic response were small enough that compensation based on average pilot dynamics improved performance and/or workload measures for all pilots.

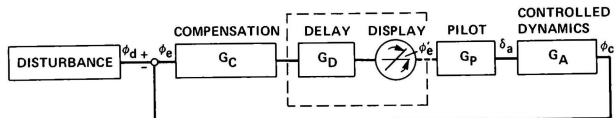


Fig. 6 Diagram of tracking task used in the experiment.

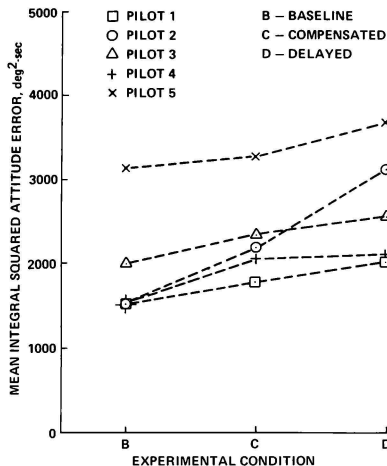


Fig. 7 Mean-integral-squared attitude error as a function of experimental condition: oscilloscope display.

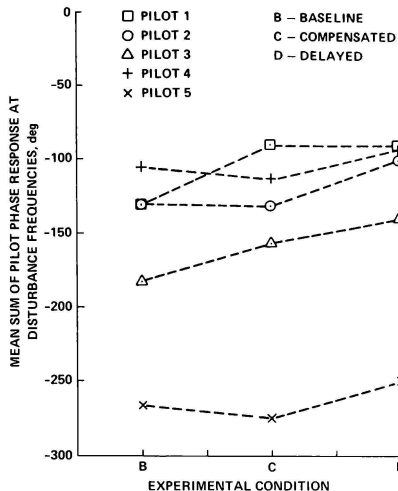


Fig. 8 Mean sum of pilot phase-response at disturbance frequencies as a function of experimental condition.

#### CGI Display: Single-Axis Tracking Task

The CGI system used here (Model F-111, manufactured by Link Division, Singer Corporation) has three major subsystems: a general-purpose computer, special-purpose image-generator hardware, and video electronics. Figure 9 is a timing diagram of a simulation which includes the CGI visual display system.

The aircraft dynamics computer and the CGI system computer are not synchronized. The frame time of the CGI processor is fixed at 33.3 msec. The minimum frame time of the dynamics computer (18 msec in this simulation) increases with simulation complexity. The dynamics processor samples

pilot control inputs, integrates the equations of motion, applies lead compensation (described here) to selected variables, and transfers pilot position and attitude and position and attitude rate-of-change information to the CGI system. The CGI computer uses the rate information to extrapolate the position and attitude data to the time corresponding to the beginning of each frame. An updated image is displayed every 33.3 msec. However, as a result of the CGI system "pipeline" architecture, three frames (~100 msec) are required to generate and display the image corresponding to each new pilot position.

The tracking task (Fig. 6) was also used in a preliminary evaluation of CGI system delay

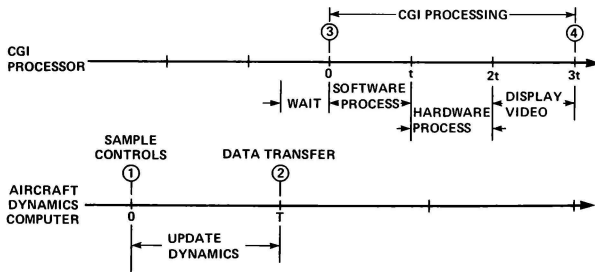


Fig. 9 Simulation timing diagram.

compensation. The simulated aircraft was positioned 30 ft over the runway threshold and constrained to move only about the roll axis. The pilot's task was to manipulate a center-stick controller to maintain the simulated aircraft in a tight, wings-level attitude, as if on a landing approach. The maximum value of the turbulence-like roll-attitude disturbance was  $13^\circ$ . The CGI system displayed attitude information to the pilot on color CRT monitors positioned as shown in Fig. 10. The pilot viewed the image through collimating optics.

There were two experimental conditions: DELAYED and COMPENSATED. During DELAYED trials the image was delayed as a result of the inherent delay of the CGI system. No compensation was used ( $G_C = 1$ , Fig. 6). During COMPENSATED trials the attitude signal was filtered in accordance with Eq. (1) before transfer to the CGI system. The pilot describing function, the pilot-aircraft open-loop transfer function, crossover frequency, and phase margin were computed as described earlier. Compensation parameters were based on crossover frequency estimates from preliminary trials.

The compensation was again effective for all pilots. With the COMPENSATED display, pilots improved their performance with reduced levels of workload and control activity. Measures of pilot performance and control activity are plotted versus experimental condition in Figs. 11 and 12, respectively.

Average phase margin in the DELAYED condition was improved (increased  $10^\circ$ ) relative to the earlier study primarily because of the large field of view in this study. Complete details of the experiment and additional experimental data will be reported elsewhere.

#### CGI Visual System: XV-15 Simulation

A brief evaluation of CGI visual-display delay compensation in the context of a complete six-degree-of-freedom simulation was recently completed. Motion cues were provided by the Ames Research Center Vertical Motion Simulator, a six-degree-of-freedom motion system with  $\pm 30$  ft of vertical travel.

The aircraft simulated was the XV-15. The XV-15 is a proof-of-concept aircraft which features a rotor system that can be oriented such that it can be flown as a helicopter or as a conventional aircraft.<sup>19</sup> As noted earlier, analysis of the pilot-aircraft system indicates that a given display delay will be most troublesome when a pilot is attempting precise control of a responsive aircraft (large  $\omega_{\phi}$ ) with relatively low inherent stability (small  $\phi_m$ ). For the compensation evaluation tests the roll-axis stability and control augmentation system (SCAS) was turned off, mimicking a SCAS system failure. This resulted in an XV-15 configuration with reduced lateral stability — relatively susceptible to the destabilizing effect of visual-display delay. The lateral control breakout force was set to zero and the lateral control-force gradient was reduced because these control characteristics were more familiar to the commercial helicopter pilots used for the initial tests.

In preliminary tests, the roll-axis pilot describing function ( $G_{p\phi}$ ) was computed from XV-15 roll-axis tracking-task data as described previously. The pilot-aircraft roll-axis open-loop transfer function was estimated as the product of  $G_{p\phi}$  and a linear approximation of the aircraft roll-axis dynamics. Crossover frequency was

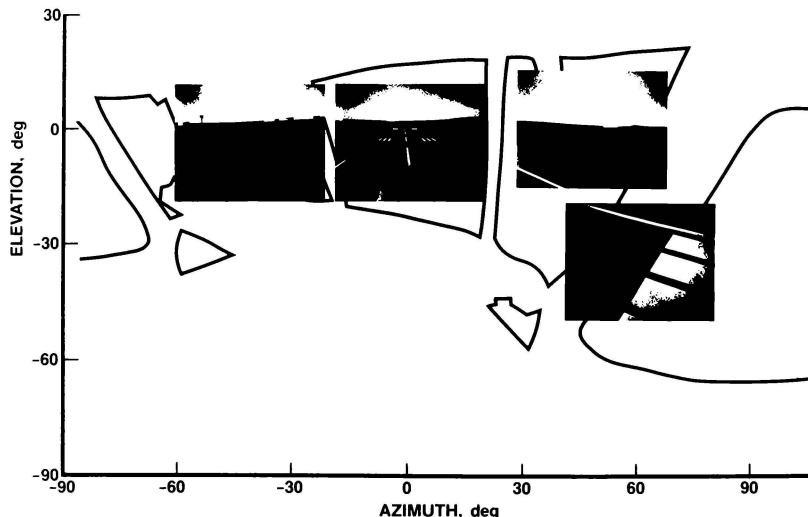


Fig. 10 Simulator field of view; elevation and azimuth angles are measured from pilot's eye position.

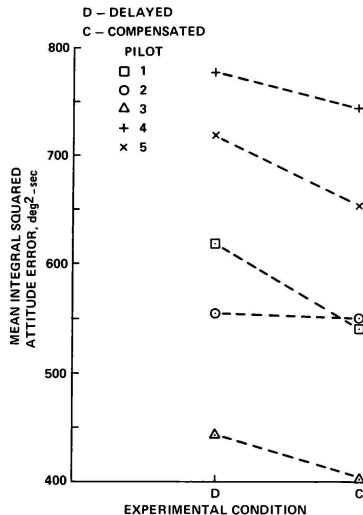


Fig. 11 Mean-integral-squared attitude error as a function of experimental condition: CGI display.

estimated by interpolation of the open-loop transfer function data. Compensation-filter parameters were computed from the estimates of crossover frequency ( $\omega_c = 1.8$  rad/sec) and display delay ( $t_d = 108$  msec), as described earlier. Only the roll-attitude signal was compensated before transfer to the CGI.

The piloting task was selected to expose lateral-axis handling-qualities deficiencies. The XV-15 simulation (helicopter configuration, roll-axis SCAS off) was initialized approximately 10 ft above a road. The pilot was briefed to "sidestep briskly to the opposite side of the road and stabilize lined up precisely with the edge of the road," then to "repeat the task to the opposite side of the road and continue back and forth across the road in this manner." Pilots considered the task to be a good test of lateral handling qualities. Figure 13 illustrates the inner (attitude) and outer (position) lateral-control loops closed by the pilot. The inner loop has the higher bandwidth and is therefore more susceptible to delay-induced instability. Outer-loop precision depends on inner-loop stability.

After practicing the task with the visual display both compensated and uncompensated, the pilot made evaluation runs. Figure 14 is a copy of the strip-chart record of the consecutive evaluation runs by an Ames Research Center test pilot who had extensive XV-15 experience. For the "no-compensation" case, the pilot reported that several cycles of control were required to dampen attitude

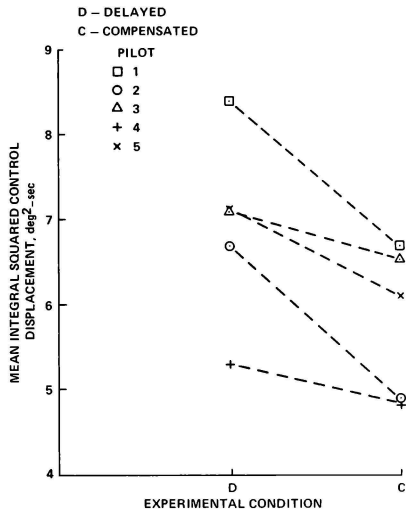


Fig. 12 Mean-integral squared-control displacement as a function of experimental condition.

oscillations after each sidestep across the road and rated the aircraft handling qualities a seven on the Cooper-Harper scale. The compensated case was judged to be more like the XV-15 (SCAS off); the configuration was rated a six on the Cooper-Harper scale. The strip-chart record confirmed the pilot's report: in the "no-compensation" case, objectionable, lightly damped oscillations in the lateral control, roll-rate, and roll-angle traces are apparent (e.g., shaded area, Fig. 14).

Another pilot also reported an improvement in handling-qualities rating when performing a similar hover task with the compensated display. These results, though limited in scope and number (by the simulator schedule), are consistent with the more detailed single-axis data reviewed previously. The XV-15 data illustrate the distortion in aircraft handling-qualities ratings which can result from visual-display delay and the use of compensation to restore system stability and handling characteristics.

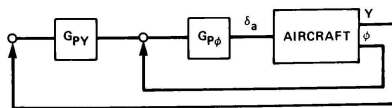


Fig. 13 Loop structure for precision lateral sidestep task:  $G_{p\phi}$  and  $G_{p\psi}$  are pilot describing functions for roll-attitude control and lateral position control, respectively.

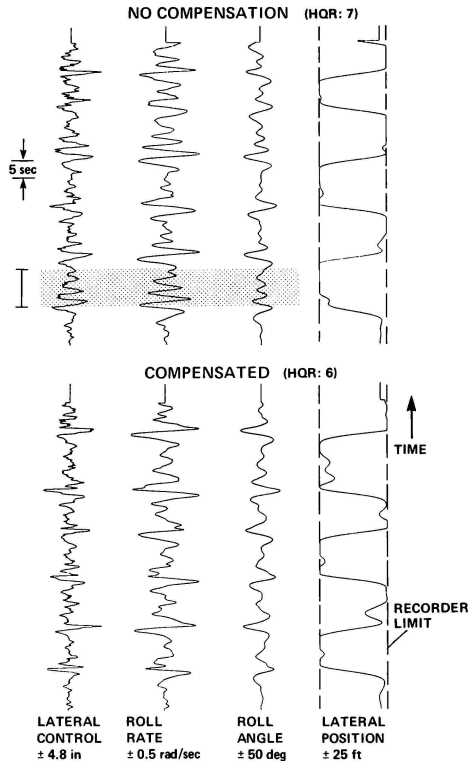


Fig. 14 Compensation evaluation results: XV-15 model, roll SCAS off, precision sidestep maneuver.

#### Concluding Remarks

Analysis of the pilot-aircraft system as a closed-loop, man-machine control system clearly indicates that a reduction of system stability is the immediate effect of visual-display delay. The reduction in system stability influences pilot workload and performance and therefore biases aircraft handling-quality ratings (HQR). The Trouble Index (TI) is defined as the ratio of the change in system phase margin (due to delay) to the nominal system phase margin. The TI predicts (for a given delay) a degradation of HQR with system bandwidth — moderated or exaggerated by the system nominal phase margin. The predicted variation of HQR with delay and bandwidth is seen in Fig. 1 in Weingarten's summary<sup>5</sup> of data from several sources on the effects of delay in aircraft control systems. These data are important here because they support the analysis upon which the delay compensation is based and

because they greatly extend the "delay-effects" data base.

Visual system display-delay compensation, designed to restore pilot-aircraft system stability, was previously shown effective in an experiment using an oscilloscope display.<sup>9</sup> Results of two evaluations of CGI visual-display system compensation are reported here. In each case, the compensation was effective; improvements in pilot performance and workload or HQR were observed. Once again, recent aircraft handling qualities data are relevant. The delay compensation approach attempts to minimize changes in pilot-aircraft dynamics in the region of crossover frequency. The Wood-Hodgkinson "envelopes of maximum unnoticeable added dynamics" (Fig. 5) imply that approach is required to minimize bias in HQR due to delay or to delay compensation. The TI explains the sensitivity of HQR to change in aircraft dynamics in

the region of crossover and further suggests that the Wood-Hodgkinson envelopes<sup>14</sup> should be considered functions of the system characteristics ( $\omega_c$ ,  $\phi_m$ ) of particular aircraft rather than absolute "maximums."

Additional research is required to 1) evaluate compensation effectiveness over a comprehensive range of aircraft dynamics and flight tasks and 2) evaluate the effect of possible control manipulator nonlinearities on compensation effectiveness.

As noted in the text, the "pilot-aircraft system" analysis of display-delay effects provides insights into the Weingarten and Wood and Hodgkinson summaries of aircraft handling-qualities data. The approach shown here to be effective for simulator visual-display delay compensation may also be useful when designing compensation for aircraft control system delay.

### References

- <sup>1</sup>Larson, D. F. and Terry, D., "ASUPT Visual Integration Technical Report," Technical Report ASUPT 82, Singer-Simulation Products Division, Binghamton, N.Y., 1975.
- <sup>2</sup>Gum, D. R. and Alberty, W. B., "Time Delay Problems Encountered in Integrating and Advanced Simulator for Undergraduate Pilot Training," Journal of Aircraft, Vol. 14, 1977, pp. 327-332.
- <sup>3</sup>Decker, J. F., "Qualification Operational Test and Evaluation of the FB-111A Weapon System Trainer Visual System Attachment," Final Report, Project 77-SAC-331, USAF Strategic Air Command, 1980.
- <sup>4</sup>Crane, D. F., "Time Delays in Flight Simulator Visual Displays," Proceedings of the Summer Computer Simulation Conference, Seattle, Wash., 1980.
- <sup>5</sup>Weingarten, N. C. and Chalk, L. R., "In-Flight Investigation of Large Airplane Flying Qualities for Approach and Landing," Proceedings of the AIAA Atmospheric Flight Mechanics Conference, San Diego, Calif., Aug. 1982.
- <sup>6</sup>Ricard, G. L. and Harris, W. T., "Time Delays in Flight Simulations: Behavioral and Engineering Analysis," Proceedings of the AIAA Flight Simulation and Technologies Conference, Arlington, Tex., 1978.
- <sup>7</sup>Ricard, G. L. and Harris, W. T., "Lead/Lag Dynamics to Compensate for Display Delays," Journal of Aircraft, Vol. 17, No. 3, 1980.
- <sup>8</sup>Baron, S., Lancraft, R., and Caglayan, A., "An Optimal Control Model Approach to the Design of Compensators for Simulator Delay," NASA CR-3604, 1982.
- <sup>9</sup>Crane, D. F., "Flight Simulator Visual-Display Delay Compensation," Proceedings of the Winter Simulation Conference, Atlanta, Ga., 1981.
- <sup>10</sup>McRuer, D. T. and Krendel, E. S., "Mathematical Models of Human Pilot Behavior," AGARD-AG-188, 1974.
- <sup>11</sup>Hodgkinson, J. and LaManna, W. J., "Equivalent System Approaches to Handling Qualities Analysis and Design Problems of Augmented Aircraft," AIAA Paper 77-1122, Hollywood, Fla., Aug. 1977.
- <sup>12</sup>Smith, R. E., "Equivalent System Verification and Evaluation of Augmentation Effects on Fighter Approach and Landing Flying Qualities," Calspan Report 6241-F-3, Aug. 1979.
- <sup>13</sup>Mitchell, David G. and Hoh, Roger H., "Low-Order Approaches to High-Order Systems: Problems and Promises," Journal of Guidance, Control, and Dynamics, Vol. 5, No. 5, Sept.-Oct. 1982, pp. 482-489.
- <sup>14</sup>Wood, J. R. and Hodgkinson, J., "Definition of Acceptable Levels of Mismatch for Equivalent Systems of Augmented Aircraft," MDC Report A6792, Dec. 1980.
- <sup>15</sup>Neal, T. Peter and Smith, Rogers E., "An In-Flight Investigation to Develop Control System Design Criteria for Fighter Airplanes," AFFDL-TR-70-74, Vol. 1, Dec. 1970.
- <sup>16</sup>Smith, Rogers E., "Effects of Control System Dynamics on Fighter Approach and Landing Longitudinal Flying Qualities," Vol. 1, AFFDL-TR-78-122, Mar. 1978.
- <sup>17</sup>Hoh, R. H., Mitchell, D. G. et al., "Proposed MIL Standard and Handbook - Flying Qualities of Air Vehicles," AFWAL TR 82-3081, Nov. 1982.
- <sup>18</sup>Shirachi, D. and Shirley, R., "The Effect of a Visual/Motion Display Mismatch in a Single Axis Compensatory Tracking Task," NASA CR-2921, 1977.
- <sup>19</sup>Dugan, D. C., Erhart, R. G., and Schroers, L. G., "The XV-15 Tilt Rotor Research Aircraft," NASA TM-81244, 1980.
- <sup>20</sup>DiFranco, D. A., "In-Flight Investigation of the Effects of Higher Order System Dynamics on Longitudinal Handling Qualities," AFFDL TR 68-90, 1968.







